
Dipartimento di Matematica e Fisica
Ph.D Course in Physics
XXXVI Cycle

Thesis Title:

Optimizing the Search for Neutrinoless Double Beta Decay

Liquid Argon Instrumentation for Background Suppression in
LEGEND-200 Experiment

Ph.D Candidate:
Nina Burlac

Supervisor:
Prof. Giuseppe Salamanna

Co-Supervisor:
Dr. Valerio D'Andrea

"In the matter of physics, the first lessons should contain nothing but what is experimental and interesting to see. A pretty experiment is in itself often more valuable than twenty formulae extracted from our minds"
(Albert Einstein)

The search for neutrinoless double beta ($0\nu\beta\beta$) decay is a topic of broad and current interest in modern physics. Its detection would imply the violation of lepton number conservation as predicted to occur in many extensions of the Standard Model. Among many experiments in the field, the LEGEND-200 experiment is searching for $0\nu\beta\beta$ decay in ^{76}Ge isotope, using about 200 kg of High-Purity Germanium (HPGe) detectors. The detectors are operated bare within a cryostat filled with Liquid Argon (LAr), serving as cooling medium and an active shield. LAr scintillates upon interaction with ionizing radiation, a feature utilized in LEGEND-200 to reject background events with coincident energy deposition in the LAr and HPGe detectors. The rejection capability is given by the implementation of the LAr instrumentation. This thesis work details the assembly, commissioning and subsequent integration of the LAr instrumentation with HPGe detectors in the LEGEND-200 setup. The front-end electronics of the LAr instrumentation has been successfully integrated achieving a remarkable overall noise level of $250\ \mu\text{V}$. The signals from the LAr instrumentation has been investigated leading to three category of pulses. A dedicated setup has been used to study the scintillation time profile of LAr, resulting in a triplet lifetime of $1.147\ \mu\text{s}$. SiPM coincidence rates of the LAr instrumentation suggest a uniform scintillation light production in the LAr. Additionally, the thesis presents the development of a novel signal processing algorithm for the LAr instrumentation. An optimum filter has been developed to effectively account for the noise levels of the experiment and has been integrated in the LEGEND-200 analysis framework. It achieves an excellent 95.8% accuracy in energy reconstruction and an efficiency for single photoelectron peak reconstruction of 99.7%. This achievement allows LEGEND-200 to effectively suppress 92.2% of ^{42}K background events in coincidence with the HPGe detectors while maintaining a 95% signal acceptance. By utilizing the first LEGEND-200 dataset, corresponding to an exposure of 10.1 kg·yr, one background event remains after applying all cuts, including the LAr veto. This corresponds to a background index of 4.1×10^{-4} cts/(keV·kg·yr). This reflects the successful commissioning of the LAr instrumentation and affirms the overall readiness of LEGEND-200 for the acquisition of physics data. Beyond that, the present work introduces innovative algorithm for particle and background tagging using LAr instrumentation signals. This demonstrates the capability of the LAr instrumentation, employed not only as a veto but as an independent detector. A pulse shape discrimination technique has been developed and applied to select a sample of events from ^{39}Ar and ^{42}Ar β decays. A preliminary analysis has been conducted to determine the specific activity of ^{39}Ar using a simplified model, resulting in 1.109 Bq/kg, and to establish a framework to study the activity of ^{42}Ar , a crucial background component in LEGEND-200 experiment.

La ricerca del decadimento doppio beta senza emissione di neutrini ($0\nu\beta\beta$) è un argomento attuale di notevole interesse nella fisica moderna, poiché la sua scoperta implicherebbe la non conservazione del numero leptonico. Tra i numerosi esperimenti dedicati a questa ricerca, l'esperimento LEGEND-200 si concentra sul decadimento $0\nu\beta\beta$ dell'isotopo ^{76}Ge , utilizzando circa 200 kg di rivelatori di germanio ad alta purezza (HPGe). Questi rivelatori operano all'interno di un criostato riempito di argon liquido (LAr), che oltre a fornire raffreddamento funge anche da schermo protettivo. Il LAr emette scintillazioni quando interagisce con radiazioni ionizzanti, caratteristica utilizzata in LEGEND-200 per discriminare gli eventi di fondo che causano depositi di energia coincidenti con i rivelatori HPGe. Tale capacità di discriminazione è ottenuta grazie all'utilizzo della strumentazione LAr. Questo lavoro di tesi fornisce una descrizione dell'assemblaggio, della messa in funzione e dell'integrazione della strumentazione LAr con i rivelatori HPGe di LEGEND-200. L'elettronica di front-end della strumentazione è stata integrata con successo, raggiungendo un notevole livello di rumore complessivo pari a $250 \mu\text{V}$. L'analisi dei segnali provenienti dalla strumentazione ha portato all'identificazione di tre categorie di impulsi. È stato utilizzato un setup dedicato per studiare il profilo temporale di scintillazione del LAr, risultando in un tempo di vita del tripletto di $1.147 \mu\text{s}$. I tassi di coincidenza dei SiPM della strumentazione LAr indicano una produzione uniforme di luce di scintillazione nel volume di argon liquido intorno ai rivelatori HPGe. Inoltre, la tesi presenta lo sviluppo e l'integrazione di un nuovo algoritmo di elaborazione dei segnali per i SiPM, che utilizza un filtro ottimo per gestire in modo efficace i livelli di rumore dell'esperimento. Tale algoritmo ha raggiunto una precisione del 95.8% nella ricostruzione dell'energia e un'efficienza nella ricostruzione del picco di singolo fotoelettrone del 99.7%, consentendo a LEGEND-200 di sopprimere il 92.2% degli eventi di fondo dovuti al ^{42}K in coincidenza con i rivelatori HPGe, mantenendo al contempo un'accettazione del 95% dei segnali. Utilizzando il primo set di dati di LEGEND-200, corrispondente a un'esposizione di $10.1 \text{ kg}\cdot\text{yr}$, un solo evento di fondo rimane dopo l'applicazione di tutti i tagli, incluso il LAr veto, risultando in un indice di fondo di $4.1 \times 10^{-4} \text{ cts}/(\text{keV}\cdot\text{kg}\cdot\text{yr})$. Oltre a ciò, il lavoro introduce un algoritmo innovativo per l'identificazione di particelle utilizzando i segnali della strumentazione LAr, dimostrando la capacità di quest'ultima di essere utilizzata come un rivelatore indipendente. È stata sviluppata e applicata una tecnica di discriminazione della forma dell'impulso per selezionare gli eventi dai decadimenti β dell' ^{39}Ar e dell' ^{42}Ar . Infine, è stata condotta un'analisi preliminare per determinare l'attività specifica dell' ^{39}Ar , risultando in 1.109 Bq/kg , e per stabilire una base per lo studio dell'attività dell' ^{42}Ar , un componente di fondo cruciale nell'esperimento LEGEND-200.

Contents

Abstract	i
Riepilogo	iii
Introduction	1
1 Neutrinos and Physics Beyond the Standard Model	3
1.1 Present neutrino knowledge	3
1.1.1 Neutrino oscillation phenomenon	4
1.2 Neutrino mass enigma	6
1.2.1 Dirac neutrinos	6
1.2.2 Majorana neutrinos	7
1.3 Current limits on neutrino mass	9
1.4 Neutrinoless double beta decay	10
1.4.1 Theoretical considerations	10
1.4.2 Experimental considerations	14
1.5 Present and future efforts on $0\nu\beta\beta$ decay search	16
1.6 Pros and cons of Germanium for $0\nu\beta\beta$ decay search	19
2 The LEGEND Experimental Program	21
2.1 LEGEND goals	21
2.2 LEGEND-200 experiment	22
2.2.1 Experimental setup	22
2.2.2 HPGe detectors	24
2.2.3 Data acquisition system	26
2.2.4 Active background reduction techniques	28
2.2.5 Data processing	30
2.3 LEGEND-200 status	31
2.3.1 Performance	31
2.4 Towards LEGEND-1000 experiment	34
3 LEGEND-200 LAr Instrumentation	37
3.1 Argon isotopic composition	37
3.2 Argon scintillation mechanism	39
3.3 LEGEND-200 LAr purification	41
3.4 LAr instrumentation	43
3.4.1 WLS fiber shroud and SiPMs	43
3.4.2 LAr instrumentation installation	46
3.4.3 SiPM voltage determination	48
3.5 Front-end electronics	49

3.5.1	FE design	50
3.5.2	Integration in LEGEND-200	52
3.6	SiPM pulses	54
3.6.1	Decay time distributions	56
3.6.2	LAr instrumentation dynamic range	59
3.7	LAr scintillation profile	60
3.7.1	LAr instrumentation and source setup	60
3.7.2	Time profile analysis	61
3.8	LAr instrumentation response studies	63
3.8.1	Majority trigger schemes	64
3.8.2	Two-fold coincidence	66
3.9	Current status of LAr instrumentation	67
4	Optimum Filter Synthesis for SiPM Charge Estimation	71
4.1	SiPM charge estimators	71
4.2	DPLMS optimum filter	74
4.2.1	Overview on DPLMS method	74
4.2.2	DPLMS filter synthesis	76
4.2.3	SiPM processing chain	78
4.3	Charge reconstruction efficiency and SPE resolution	79
4.4	LAr instrumentation performance	82
4.5	LEGEND-200 background index	85
5	LAr Instrumentation for $^{39}\text{Ar}/^{42}\text{Ar}$ Activity Estimation	87
5.1	Previous measurements of ^{42}Ar specific activity	87
5.2	LEGEND-200 ^{42}K background mitigation	88
5.3	LAr instrumentation data for ^{42}K activity estimation	90
5.3.1	Event trigger evaluation	90
5.3.2	LAr energy distribution	92
5.4	^{39}Ar energy distribution study	93
5.4.1	LAr instrumentation LY and resolution	94
5.4.2	^{39}Ar activity estimation	96
5.5	Pulse shape discrimination in LAr	99
5.5.1	Event PSD distribution	100
5.6	$^{42}\text{Ar}/^{42}\text{K}$ activity estimation	101
5.6.1	Light yield and resolution cross-check from ^{40}K gamma line	102
5.6.2	β/γ spectrum fit	104
5.6.3	Discussion	106
	Conclusions	109
	A Thorium and Uranium Chain	111
	B HPGe Detector Configuration	113
	C LEGEND Liquid Argon Purification System	115
	D Connections of Front-End Electronics	117
	E LAr Instrumentation Front-End Stability Tests	119

F	SiPMs Working Principle	123
G	LAr Instrumentation SiPM Super-Pulses & Decay Times	129
H	Pulser Crosstalk and Muon Events from LAr Instrumentation	135
I	LAr Energy Distribution: DPLMS vs Hypercurrent	139
J	Alpha Contamination	141
	Acronyms	143
	Ringraziamenti	147
	Bibliography	149

The discovery of the neutrinoless double beta ($0\nu\beta\beta$) decay would reshape our fundamental understanding of neutrinos and of matter in the Universe. The search for $0\nu\beta\beta$ decay tests whether there is a fundamental symmetry of Nature associated with lepton number, probes the quantum nature of neutrinos, and allows the measurement of their effective mass. It is the only practical way to demonstrate if neutrinos are their own antiparticles, that is, if neutrinos have a Majorana mass. The discovery of Majorana neutrinos would open the door to new physics beyond the discovery of neutrino oscillation, and would signify a paradigm shift in our understanding of the origins of mass and matter. The neutrino non-zero mass impacts the evolution of the Universe from the beginning of time to the formation of large-scale structures in the present epoch, and Majorana neutrinos play a key role in viable scenarios that explain the matter-antimatter asymmetry in our Universe.

Among several experiments in the field, the LEGEND-200 experiment, at Laboratori Nazionali del Gran Sasso (LNGS) of INFN, operates about 200 kg of germanium detectors, made from material enriched in ^{76}Ge , in a Liquid Argon (LAr) cryostat. The experiment aims to probe the $0\nu\beta\beta$ decay of ^{76}Ge isotope with a sensitivity on the half-life of about 10^{27} yr (at 90% CL), which translates in a range of the effective Majorana neutrino mass of $m_{\beta\beta} < (34 - 78)$ meV. To achieve such results LEGEND-200 requires a background decreased by a factor of 3 below the measured levels of its predecessors using germanium detectors. Therefore, the experiment needs a careful selection of highly radiopure materials and the development of efficient background suppression techniques. Among the active techniques employed by LEGEND-200 for background suppression is the use of the LAr instrumentation, which allows to veto background events in coincidence with HPGe detectors.

My thesis work covers three main aspects related to the LAr instrumentation. A significant part has been dedicated to the installation and commissioning of the LAr instrumentation. Once the system has been integrated in the LEGEND-200 setup, the work has been moved to the development of signal processing routines aimed to the improvement of the LAr instrumentation performance. After the start of LEGEND-200 data taking, the main focus of my work has been shifted to explore the potential of the LAr instrumentation, that allowed to perform studies on the observed background independent of the germanium detectors.

In particular, throughout the commissioning phase of the LEGEND-200 experiment, my responsibilities included assembling and testing the LAr instrumentation, integrating the new front-end electronics, and analyzing the corresponding test and commissioning data. Several tests have been performed to check the stability and the noise level of the

overall setup. Specifically, I worked on realization of different shielding and grounding schemes of differential lines between the SiPM detectors and the front-end electronics in order to reach a remarkable noise level. The optical response of the LAr instrumentation system has been investigated taking ^{39}Ar decays as a benchmark.

In the second part of this thesis I worked on the development of a digital filter for the events energy reconstruction. This marked improvement in noise separation from SiPM signals and contributed to an enhancement in the performance of the LAr instrumentation. Furthermore, an investigation has been conducted on the effectiveness of background suppression by the LAr instrumentation when coinciding with HPGe detectors.

The last part of the thesis work is dedicated to the analysis of the energy distribution spectrum obtained with the LAr instrumentation. This involves estimating both the light yield and resolution of the LAr instrumentation. Furthermore, employing a simplified fitting model allowed a preliminary estimation of the specific activity of ^{39}Ar and establish a framework to study the ^{42}Ar specific activity.

The thesis is structured as follow. Chapter 1 provides an overview of various aspects of neutrino physics, with a specific focus on the nature (Dirac and Majorana) of neutrino mass. Both theoretical and experimental considerations are discussed on the $0\nu\beta\beta$ decay, a powerful approach to gain insights about the neutrino nature and mass.

Chapter 2 outlines the experimental goals of the LEGEND program and provides comprehensive details regarding the LEGEND-200 experimental setup. The primary background sources and the innovative techniques applied for their active suppression are also presented. The ongoing status of the LEGEND-200 experiment, along with the first performance results, are also reported.

Chapter 3 provides an overview of the LAr instrumentation and details the work performed during the installation and commissioning, offering insights into the front-end electronics of the LEGEND-200 LAr instrumentation. It includes an investigation of the pulse shapes generated by the LAr instrumentation, studies of the LAr scintillation profiles and a discussion on pulse coincidence rates of the SiPM from the LAr instrumentation.

Chapter 4 illustrates a novel signal processing algorithm for SiPM, describing the synthesis of an optimum filter based on the DPLMS method. This method allows efficient treatment of the noise observed in the SiPM traces. The chapter demonstrates the algorithm effectiveness in reconstructing SiPM charge and outlines the efficiency of background suppression of the LAr instrumentation when coinciding with HPGe detectors.

Chapter 5 presents a technique for pulse shape discrimination which has been developed and implemented to identify events from ^{39}Ar and ^{42}Ar β decays, two naturally occurring radioactive isotopes in the LAr. A preliminary analysis has been conducted to determine the specific activity of ^{39}Ar using a simplified model and to establish a framework for studying the activity of ^{42}Ar , a critical background component in the LEGEND-200.

Appendix A details the Th and U decay chain, while Appendix B encompasses the LEGEND-200 detector configuration. In Appendix C, the scheme of the LEGEND liquid argon purification system is presented. The connection schemes of the front-end electronics of the LAr instrumentation can be found in Appendix D. The stability test results of the front-end electronics of the LAr instrumentation are reported in Appendix E. Appendix F illustrates the working principle of the SiPM. Additional plots of the SiPM super-pulses and decay times are provided in Appendix G. Examples of pulser crosstalk and muon events from the LAr instrumentation are included in Appendix H. The comparison between the LAr energy distribution calculated with the developed digital filter and the default charge estimator is illustrated in Appendix I. A preliminary distribution of α contamination is shown in Appendix J.

CHAPTER 1

Neutrinos and Physics Beyond the Standard Model

Neutrinos remain the most enigmatic elementary particles known to science. Within the framework of the Standard Model (SM), they are considered fundamental particles, and the way they interact has shaped their theoretical formulation over time. Despite the passage of ninety years since Wolfgang Pauli initial hypothesis and almost seventy years since their first experimental detection, several fundamental properties of neutrinos continue to elude us, such as their precise mass and their nature. Additionally, compelling evidence suggests that the unknown neutrinos attributes may be linked to new physics mechanism beyond the SM (BSM).

This chapter provides an extensive description of various aspects of neutrino physics. Section 1.1 examines the fundamental characteristics of neutrinos with a particular focus on neutrino oscillation phenomenon, that provided the initial insights into non-zero neutrino masses. Section 1.2 is focused on the nature (Dirac and Majorana) of neutrino mass. The current limits on neutrino mass, considering different detection techniques, are presented in Section 1.3. The second part of the chapter (Section 1.4) is dedicated to the neutrinoless double beta ($0\nu\beta\beta$) decay, a highly powerful method to gain crucial information about the neutrino nature and mass. Both theoretical and experimental considerations will be discussed. The significant experiments conducted over the years will be briefly summarized in Section 1.5. Since this thesis focuses on the search for $0\nu\beta\beta$ decay using germanium detectors, Section 1.6 will provide a comprehensive overview of the advantages and disadvantage associated with the selection of these specific detectors.

1.1 Present neutrino knowledge

Neutrinos first captured scientific attention through explorations in the study of β radioactive decay. Initially, it was believed that only one particle was emitted in the final state, and a monochromatic energy spectrum of the β particle was expected. However, in 1914, Chadwick made a significant observation: the energy spectrum was continuous, challenging the conservation of energy, momentum, and angular momentum [1]. It wasn't until 1930 that Pauli postulated the existence of a third particle in the β decay [2], even though the technology at that time couldn't detect it.

Four years later, Fermi formulated the theory of weak interaction [3], offering a theoretical explanation for Pauli hypothesis. The "discovery" of the neutrino was eventually confirmed in 1956 when Cowan and Reines experiment detected electron antineutrinos

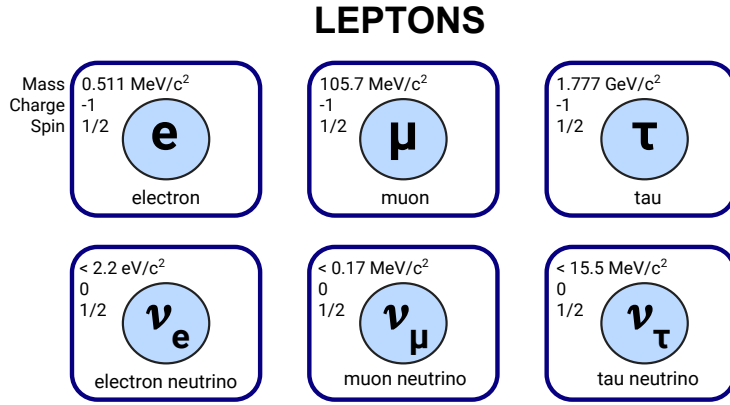


Figure 1.1: Leptonic sector of the SM. For each particle the mass, electric charge and spin are indicated.

emitted alongside electrons during nuclear decay inside a reactor [4].

Following the discovery of the muon in 1937, Pontecorvo proposed the existence of another flavor of neutrino: the muon neutrino, associated with the muon [5]. This prediction was validated in 1962 through Lederman, Schwartz and Steinberger experiment [6]. Subsequently, with the identification of the third charged lepton (1975), called tau, the corresponding tau neutrino was observed in 2000 by the DONUT experiment [7]. This completed the picture of the SM with three types of neutrinos and their corresponding charged leptons.

As shown in Figure 1.1, the leptonic sector of the SM is made of six fermionic particles with a spin of $1/2$, categorized into three groups: electrons, muons, and taus. Complementing these, there are also their corresponding six antileptons, possessing identical characteristics but with opposite electric charges. According to the SM, the neutrino is a fermion with no charge and no mass. However, this last property is a challenging research topic in particle physics. Thanks to the observation of the neutrino oscillation phenomenon [8, 9], we know that there exist at least two neutrino mass eigenstates with non-null mass eigenvalues, but the nature and the size of their mass are still open issues in the neutrino sector BSM.

1.1.1 Neutrino oscillation phenomenon

The concept of neutrino mixing, similar to what is observed in the quark sector, was initially proposed by Maki, Nakagawa, and Sakata in 1962 [10]. However, it was not until seven years later, with the work of Gribov and Pontecorvo [11], that the first connection to potential neutrino flavor oscillations was established. This flavor oscillation, similar to the quark flavor oscillation described by the Cabibbo-Kobayashi-Maskawa (CKM) matrix, becomes a possibility only if neutrinos have non-zero mass.

The basic assumption for neutrino oscillation is that the weakly interacting flavor eigenstates ν_l , with $l = e, \mu, \tau$, are not identical to the three neutrino mass eigenstates (ν_i) ($i = 1, 2, 3$) with mass m_i . The relationship between flavor and mass eigenstates can be represented as a superposition of one another, which can be formulated as:

$$\nu_l = U \nu_i, \quad (1.1)$$

where U is the Pontecorvo-Maki-Nakagawa-Sakata (PMNS) mixing unitary matrix. The

PMNS matrix can be expressed in its standard parametrization as:

$$U = \begin{pmatrix} c_{12}c_{13} & s_{12}c_{13} & s_{13}e^{-i\delta} \\ -s_{12}c_{23} - c_{12}s_{23}s_{13}e^{i\delta} & c_{12}c_{23} - s_{12}s_{23}s_{13}e^{i\delta} & s_{23}c_{13} \\ s_{12}s_{23} - c_{12}c_{23}s_{13}e^{i\delta} & -c_{12}s_{23} - s_{12}c_{23}s_{13}e^{i\delta} & c_{23}c_{13} \end{pmatrix} \times \begin{pmatrix} 1 & 0 & 0 \\ 0 & e^{i\frac{\alpha_{21}}{2}} & 0 \\ 0 & 0 & e^{i\frac{\alpha_{31}}{2}} \end{pmatrix}. \quad (1.2)$$

where $c_{ij} = \cos \theta_{ij}$, $s_{ij} = \sin \theta_{ij}$; δ is the Dirac phase responsible of the charge conjugation parity (CP¹) violation, while α_{21} and α_{31} are the two Majorana phases responsible of the CP violation and are physical only if neutrinos are Majorana particles (see Section 1.2.2). The observable oscillation, however, does not depend on the Majorana phases. Assuming the existence of three neutrinos, the matrix is expressed by six physical parameters: three mixing angles $\theta_{21}, \theta_{31}, \theta_{32}$ and three phases δ, α_{21} and α_{31} .

The probability of neutrino oscillation depends on the neutrino energy (E), the distance between source and detector (L), and the elements of the PMNS matrix. The probability that a neutrino produced with flavor l can be detected with flavor l' is given by:

$$P_{l \rightarrow l'} = \delta_{ll'} - 4 \sum_{i>k} \text{Re}(U_{li}^* U_{l'i} U_{lk} U_{l'k}^*) \sin^2 \left(\frac{\Delta m_{ki}^2 L}{4E} \right) + 2 \sum_{i>k} \text{Im}(U_{li}^* U_{l'i} U_{lk} U_{l'k}^*) \sin^2 \left(\frac{\Delta m_{ki}^2 L}{2E} \right) \quad (1.3)$$

where $\Delta m_{ki}^2 = m_k^2 - m_i^2$ is the squared mass difference between the mass eigenstates k and i .

Note that flavor oscillations can only manifest when $\Delta m_{ki}^2 \neq 0$, which means that m_k must not be equal to m_i , and at least one of the mass eigenstates must satisfy the condition $m_k \neq 0$. Neutrino oscillation experiments exclusively probe the mass squared differences Δm_{ki}^2 , the three mixing angles θ_{ij} and the CP violating Dirac phase δ . They are neither sensitive to the absolute mass scale nor to the Majorana phases α_{21}, α_{31} , i.e. no conclusion can be drawn about the Majorana or Dirac nature of the neutrinos (Section 1.2).

Experimental confirmation of neutrino oscillations has been observed in various contexts, including solar [12], atmospheric [13], reactor [14], and accelerator [15] neutrinos. These experimental data have provided insights into the elements of the PMNS matrix and the absolute values of the mass squared differences.

Neutrino mass ordering

The determination of the neutrino mass hierarchy is a central and challenging research topic in particle physics. By utilizing the Mikheyev-Smirnov-Wolfenstein (MSW) effect in the propagation of solar neutrinos [16], the sign of Δm_{21}^2 has been determined as positive, meaning $m_1 < m_2$ [17]. However, the sign of Δm_{31}^2 remains undetermined as it necessitates the observation of muon neutrinos over very long distances. Consequently, there are two possibilities for the hierarchy of neutrino masses:

- Normal hierarchy: $\Delta m_{31}^2 > 0, m_1 < m_2 < m_3$;

¹CP-symmetry states that the laws of physics should be the same if a particle is interchanged with its antiparticle (C-symmetry) while its spatial coordinates are inverted (P-symmetry).

- Inverted hierarchy: $\Delta m_{31}^2 < 0$, $m_3 < m_1 < m_2$.

Prospective long-baseline reactor oscillation experiments like DUNE [18] and T2HK [19] are dedicated to establishing the sign of Δm_{31}^2 with a notably high level of statistical significance. Very sensitive neutrino oscillation experiment is also JUNO [20], built to investigate the neutrino mass ordering and the possibility of CP violation of neutrinos.

1.2 Neutrino mass enigma

Within the framework of the SM, the masses of charged fermions are attributed to their Yukawa couplings with the Higgs field. These interactions result in a mass component when the Higgs boson acquires a vacuum expectation value during the electroweak symmetry breaking process. In contrast, the origin of neutrino masses is less certain and more speculative due to the various potential mechanisms involved [21].

In the minimal SM version that excludes the introduction of right-handed neutrinos and includes only the standard $SU(2)_L$ doublet Higgs boson, there is no viable mechanism for generating mass terms for neutrinos through Yukawa couplings, as is the case for charged fermions. Hence, it is frequently asserted that, within the SM, neutrinos are considered to have strictly zero masses. From this standpoint, the observed non-zero neutrino masses, inferred from diverse experimental observations, constitute the initial compelling experimental proof necessitating the inclusion of physics BSM.

1.2.1 Dirac neutrinos

The most straightforward approach to give mass to neutrinos involves the incorporation of right-handed neutrinos and their coupling through a Yukawa interaction. Following the electroweak symmetry breaking process, this yields the resulting neutrino mass term:

$$-\mathcal{L}_m = m_D(\bar{\nu}_R\nu_L + \bar{\nu}_L\nu_R), \quad (1.4)$$

which in principal is not diagonal in flavor space, but it can be diagonalized via a bi-unitary transformation, such that:

$$U_L^\nu m_D U_R^{\nu\dagger} = \text{diag}(m_1, m_2, m_3). \quad (1.5)$$

Defining the mass-eigenstates as $\nu_{iL,R} = (U_{L,R}^\nu)_{i\alpha}\nu_{\alpha L,R}$, the Dirac neutrino fields becomes:

$$\nu_i = \nu_{iL} + \nu_{iR}, \quad (1.6)$$

and thus the Dirac mass term can be rewritten as:

$$-\mathcal{L}_m = \sum_i m_i \bar{\nu}_i \nu_i. \quad (1.7)$$

For each neutrino mass eigenstate, the fields ν_i contain four degrees of freedom, accounting for both left and right neutrino chiralities as well as their corresponding antineutrinos. Furthermore, this term upholds the global lepton number symmetry, which corresponds to the transformation $\nu_i \rightarrow e^{i\theta}\nu_j$.

While this method for generating neutrino masses is quite straightforward, its primary limitation arises from the fact that the Higgs vacuum expectation value (VEV) is at the electroweak scale (around 10^{11} eV). To achieve neutrino masses below 1 eV, the Yukawa

couplings must be exceedingly tiny, falling well below 10^{-11} , which is significantly smaller than the smallest known Yukawa couplings for charged fermions (around 10^{-6}). In the absence of a compelling explanation for such a vast hierarchy between the Yukawa couplings of neutral and charged fermions, Dirac neutrino masses appear to be unnaturally small.

1.2.2 Majorana neutrinos

The two experimentally observed neutrino states with electron flavor are the left-handed electron neutrino, generated in a β^+ decay, and the right-handed electron antineutrino, produced in a β^- decay. These states can be conveniently described using Weyl spinors, which possess well-defined chiralities and thus contain only two degrees of freedom. Consequently, one can contemplate the possibility of expressing a mass term with the necessary $L \leftrightarrow R$ transition using just two degrees of freedom. This concept was initially proposed by Majorana in 1937 [22]. According to his hypothesis, the mass eigenstate of the neutrino field and its antiparticle field coincide, similar to what occurs with particles like the photon or the neutral pion π^0 , which are identical to their antiparticles.

Majorana attempted to characterize the massive neutrino by solely using the left-handed field. He achieved this by expressing ν_R in terms of ν_L through the application of the charge conjugation operator²:

$$\nu_R = C\bar{\nu}_L^T = \nu_L^C. \quad (1.8)$$

In this way the neutrino field becomes:

$$\nu = \nu_L + \nu_R = \nu_L + \nu_L^C, \quad (1.9)$$

that means $\nu^C = \nu$ or that neutrino and antineutrino are the same particle. In this way the Majorana mass terms for left-handed neutrino becomes:

$$-\mathcal{L}_m = \frac{1}{2}m_L(\bar{\nu}_L\nu_L^C + \bar{\nu}_L^C\nu_L). \quad (1.10)$$

It exists an analogous term for ν_R introducing the mass m_R . Taking into account the relation (1.9), the mass term can be rewritten as:

$$-\mathcal{L}_m = \frac{m_L}{2}\bar{\nu}\nu, \quad (1.11)$$

and one can see that this mass term does not preserve any $U(1)$ phase symmetry, violating the so-called lepton number by 2 units.

In summary, there are two possible scenarios to consider:

- if ν_R exists, it is feasible to have both mass terms (Dirac and Majorana);
- if ν_R does not exist, and the neutrino is exclusively left-handed, a Dirac mass is not possible, and only a Majorana mass is viable, which results in a violation of lepton number conservation by 2 units.

²Under charge conjugation (C) a particle transforms into its respective antiparticle, that carries opposite sign in all charge-like quantum numbers.

See-saw mechanism

Various models have been proposed to account for neutrino mass, including the Zee and supersymmetric models [23, 24]. The simplest and most natural way to introduce the very small neutrino masses in the SM is the see-saw mechanism [25].

The most comprehensive Lagrangian, encompassing both Dirac and Majorana terms, can be written as:

$$-\mathcal{L}_M = \frac{1}{2}(\bar{\nu}_L^C \ \nu_R)M \begin{pmatrix} \nu_L \\ \bar{\nu}_R^C \end{pmatrix} + h.c., \quad (1.12)$$

where the mass matrix M is:

$$M = \begin{pmatrix} m_L & m_D \\ m_D & m_R \end{pmatrix}. \quad (1.13)$$

Choosing $m_L = 0$ and $m_R \gg m_D$, the mass eigenstates which result from the diagonalisation of this mass matrix are two Majorana fields with masses:

$$\begin{aligned} m_{light} &\simeq \frac{m_D^2}{m_R}, \\ m_{heavy} &\simeq m_R \left(1 + \frac{m_D^2}{m_R^2} \right) \simeq m_R. \end{aligned} \quad (1.14)$$

The eigenstate associated with m_{light} is mostly the familiar left-handed light Majorana neutrino, while the one associated with m_{heavy} is mostly the heavy sterile right-handed partner.

Since $m_D/m_R \ll 1$, then $m_{light} \ll m_D$, and hence the lightness of the known neutrinos is related to the heaviness of the sterile state ν_R . This is the famous type I see-saw mechanism: when one state mass increases, the other decreases. It offers an elegant solution to the question of why the neutrino mass is significantly smaller than that of the other charged leptons.

The assumption that $m_L = 0$ is a natural one, as a Majorana mass term for the left-handed chiral field ν_L would break both the symmetries and the renormalizability of the SM. For example, when the Dirac neutrino mass is $O(10^2)$ GeV, and the scale M is on the order of $\sim 10^{15}$, the resulting neutrino mass is $m_\nu \sim 0.01$ eV. This value aligns with experimental data and is considered a plausible scale for the neutrino mass.

Synopsis

The presence of a Majorana mass term results from the oscillations between particles and their corresponding anti-particles, causing the violation of the lepton number conservation. Consequently, investigating instances of lepton number non-conservation may provide insights into the nature of neutrinos.

Majorana neutrinos, with their intrinsic property of violating the lepton number, play a crucial role in leptogenesis scenarios. They contribute to the creation of a lepton asymmetry in the early universe. These lepton asymmetries, arising from the potential decay of heavy neutrinos with CP-violating phases in the early universe, can be transformed into the observed baryon asymmetry through sphaleron processes³ [26]. This offers a potential explanation for the prevalence of matter over antimatter in our universe.

One of the most promising process for probing the neutrinos Majorana nature, and thus the lepton number violation, is the neutrinoless double beta decay (Section 1.4).

³Sphalerons are non-perturbative quantum field theory phenomena capable of altering the difference between baryon and lepton numbers.

1.3 Current limits on neutrino mass

The limits on neutrino mass are determined through various experimental methods and studies. Cosmological measurements provide the most robust limits on the sum of the three neutrino masses [27]:

$$\Sigma = \sum m_i < 0.12 \text{ eV}, \quad (1.15)$$

but it's important to note that these limits are contingent on the specific cosmological model. To mitigate the model-dependent factors, direct kinematic approaches, like Kurie-plot analyses, stand out as the most model-independent method for investigating neutrino mass, yielding limits on the effective electron neutrino mass:

$$m_\beta = \sqrt{\sum_i |U_{ei}^2| m_i^2}. \quad (1.16)$$

Recent constraints from the KATRIN experiment have set an upper limit on effective electron neutrino mass of $m_\beta < 0.8 \text{ eV}$ [28].

By exploring variations in neutrino oscillation parameters within their 3σ ranges, it becomes feasible to construct plots for the effective Majorana neutrino mass ($m_{\beta\beta}$, defined in Equation (1.19)), the effective neutrino mass (m_β) from β decay kinematics, and the sum of neutrino masses (Σ), accessible by cosmology, as depicted in Figure 1.2.

The left panel of Figure 1.2 delineates the parameter space available for $m_{\beta\beta}$ as a function of the lightest neutrino mass (m_{light}). In the context of the normal ordering scenario, m_{light} corresponds to m_1 , whereas in the inverted ordering scenario, it corresponds to m_3 . These ordering scenarios occupy distinct regions in the parameter space; however, at higher values of m_{light} and correspondingly elevated values of $m_{\beta\beta}$, the two bands degenerate.

The central panel of Figure 1.2 showcases the connection between $m_{\beta\beta}$ and m_β while considering the anticipated sensitivity of the KATRIN experiment. In the hypothesis of normal ordering, $m_{\beta\beta}$ can potentially approach zero, whereas in the case of the inverted ordering scenario, there exists a minimum value of approximately 0.013 eV. This minimum value represents a significant target for ongoing and forthcoming neutrinoless double beta ($0\nu\beta\beta$) decay experiments.

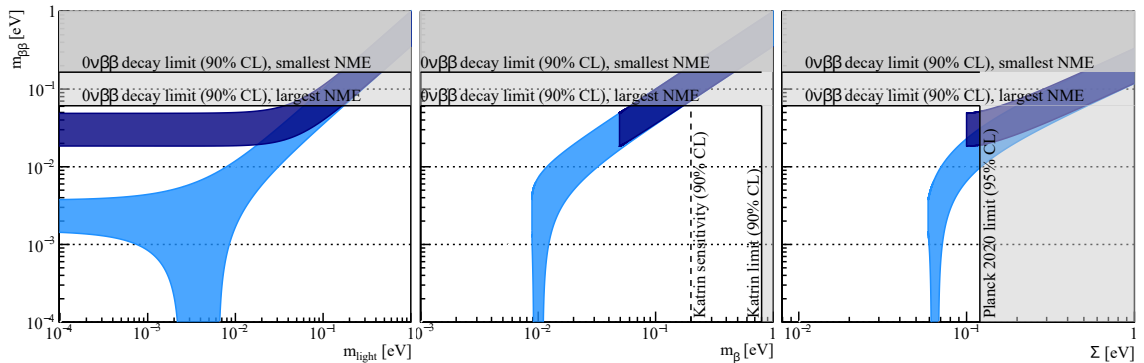


Figure 1.2: The parameter space allowed for $m_{\beta\beta}$ is shown as a function of m_{light} , m_β and Σ . The light-blue and dark-blue bands show the parameters spaces allowed for the normal ordering and the inverted ordering scenario, respectively. The grey-shaded areas show the parameter space already excluded, taking the limit on $m_{\beta\beta}$ from KamLAND-Zen [29], the m_β limit set by KATRIN [28], and the constraint on Σ from Planck [27]. Adapted from [30].

Lastly, the right panel of Figure 1.2 illustrates the relationship between $m_{\beta\beta}$ and Σ , incorporating the cosmological constraints on Σ .

In summary, as of now, there are only upper limits on all three observables related to neutrino mass, leaving the absolute neutrino mass scale shrouded in uncertainty. Nevertheless, the collective objective of upcoming experiments dedicated to the search for $0\nu\beta\beta$ decay is to enhance sensitivity to a level approaching 10^{28} yr, thereby enabling a definitive examination of the parameter space where $m_{\beta\beta}$ exceeds 10 meV, as depicted in Figure 1.2. This particular region aligns with the parameter space allowed in the inverted ordering scenario. Consequently, these future experiments hold the potential to detect the $0\nu\beta\beta$ decay, assuming that neutrinos exhibit Majorana properties and that the mass hierarchy follows an inverted configuration.

1.4 Neutrinoless double beta decay

The $0\nu\beta\beta$ decay search is a topic of broad and current interest in modern physics. The experiments searching for $0\nu\beta\beta$ decay have the potential to provide information on some fundamental questions, including the precise values of neutrino eigenstate masses, the ordering of neutrino mass states, and even the potential for discovering CP violation in the lepton sector. Additionally, this ‘‘matter-creating’’ process would not only validate but also offer insights into leptogenesis scenarios, which seek to elucidate the universe asymmetry between matter and antimatter.

1.4.1 Theoretical considerations

The double beta ($\beta\beta$) decay is a second-order weak nuclear decay process with the longest lifetime ever observed. The idea of such a decay was first suggested by Maria Goeppert-Mayer in 1935 [31]. The two-neutrino mode of the $\beta\beta$ ($2\nu\beta\beta$) decay is a nuclear transition in which two neutrons are simultaneously converted into two protons with the emission of two electrons and two antineutrinos, as depicted in Figure 1.3 Left.

This process may be observed experimentally in scenarios where single beta decay is prohibited due to energy conservation constraints or significantly suppressed due to a substantial spin change. It becomes viable only when the initial isotope is less stable than the resulting product, and both must be more stable than the intermediate nucleus. These conditions are met exclusively by certain even-even nuclei (even number of protons and neutrons). There are 41 isotopes for which this happens (35 $\beta^-\beta^-$ and 6 $\beta^+\beta^+$) and the $2\nu\beta\beta$ decay has indeed been directly observed in about a dozen of them, such as in ^{48}Ca , ^{76}Ge , ^{100}Mo , ^{136}Xe and ^{130}Te , which have lifetimes of the order of 10^{19} - 10^{22} yr [32].

In 1939, Wendell H. Furry presented a new $\beta\beta$ decay mode: the neutrinoless double beta ($0\nu\beta\beta$) decay [33]. As in the $2\nu\beta\beta$ decay, in the $0\nu\beta\beta$ decay a nucleus with Z protons decays into a nucleus with $Z + 2$ protons and the same mass number A , accompanied by the emission of two electrons but no antineutrinos (Figure 1.3 Right):

$$(A, Z) \rightarrow (A, Z + 2) + 2e^-. \quad (1.17)$$

Furthermore, in contrast to the $2\nu\beta\beta$ decay, the $0\nu\beta\beta$ decay violates the law of lepton number conservation by two units. While several extensions of the SM propose mechanisms to account for this decay, in accordance with the Schechter-Valle theorem [34], all realizations of relation (1.17) are linked to a Majorana neutrino mass. The conventional

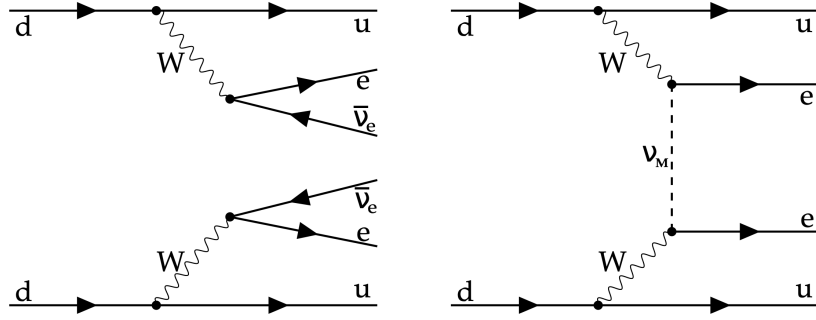


Figure 1.3: **Left:** double beta decay with the emission of two antineutrinos. **Right:** the neutrinoless double beta decay with the exchange of massive Majorana neutrino.

interpretation of the $0\nu\beta\beta$ decay can be categorized as a mediation process involving massive Majorana neutrinos [35].

Following the Fermi golden rule, the rate of the $0\nu\beta\beta$ decay, in the assumption that the decay is mediated only by the two massive Majorana neutrinos, can be factorized as [36]:

$$\Gamma^{0\nu} = \frac{1}{T_{1/2}^{0\nu}} = G^{0\nu}(Q_{\beta\beta}, Z) |M^{0\nu}|^2 \left(\frac{m_{\beta\beta}}{m_e}\right)^2 \quad (1.18)$$

where $T_{1/2}^{0\nu}$ is the half-life of the $0\nu\beta\beta$ process, $G^{0\nu}$ is the phase space factor, $M^{0\nu}$ is the nuclear matrix element (NME) and m_e is the electron mass. The expression features also a key quantity, the effective Majorana mass of the electron neutrino, defined as:

$$m_{\beta\beta} = \left| \sum_{i=1}^3 U_{ei}^2 m_i \right|, \quad (1.19)$$

where U is the PMNS mixing and m_i are the mass eigenvalues of the three neutrinos. In this way, by studying the $0\nu\beta\beta$ decay, it is possible to measure the half-life and then estimate the neutrino Majorana mass.

Phase space factor

The phase space factor $G^{0\nu}$ can be considered almost independent of the mechanism when two electrons are emitted during the process. It is of the order of 10^{-15} yr^{-1} and can be calculated to a satisfying degree of accuracy (0.1%) [37, 38]. $G^{0\nu}$ scales with the end-point energy of $2\nu\beta\beta$ decay to the fifth power ($Q_{\beta\beta}^5$). The so called Q-value or end-point energy, $Q_{\beta\beta} = M_i - M_f - 2m_e$, is given by the difference of initial (M_i) and final mass (M_f) of the nuclei involved and the mass of the two electrons ($2m_e$). It defines the maximal kinetic energy of the two electrons in the final state of the $2\nu\beta\beta$ decay. The $0\nu\beta\beta$ signal is expected at this energy. In general, values of $Q_{\beta\beta}$ are measured experimentally. In Table 1.1 numerical values of $G^{0\nu}$, Q-value and natural abundance of target isotopes, currently being pursued by leading $0\nu\beta\beta$ decay experiments, can be found.

Nuclear matrix element

The main source of systematic uncertainty on $T_{1/2}^{0\nu}$ is introduced by $M^{0\nu}$ [39, 40]. The calculation of these matrix elements is a challenging task due to the complex nature of nuclear structure: it involves several nuclear physics ingredients, including the nuclear

Isotope	$G^{0\nu}$ (10^{-15} y^{-1})	$Q_{\beta\beta}$ (keV)	nat. abundance (%)
⁴⁸ Ca	24.81	4267.98(32)	0.187
⁷⁶ Ge	2.363	2039.061(7)	7.8
⁸² Se	10.16	2997.9(3)	9.2
⁹⁶ Zr	20.58	3356.097(86)	2.8
¹⁰⁰ Mo	15.92	3034.40(17)	9.6
¹¹⁶ Cd	16.70	2813.50(13)	7.6
¹³⁰ Te	14.22	2 527.518(13)	34.5
¹³⁶ Xe	14.58	2457.83(37)	8.9
¹⁵⁰ Nd	63.03	3371.38(20)	5.6

Table 1.1: Phase space factor $G^{0\nu}$ from [37], Q-value and natural abundance from [30] for $0\nu\beta\beta$ candidate isotopes (see Section 1.4.2).

wave functions, the two-body nuclear Hamiltonian, and other factors that describe the nuclear structure. Exact calculations for the $0\nu\beta\beta$ isotopes are currently not possible, leading to various approximations and truncations. Several nuclear structure models and techniques have been employed to calculate these matrix elements, marking substantial progress in their evaluation over the past decade. In Figure 1.4 a comparison between the values of the NMEs calculated with the different models is illustrated. The models predict NME values with 2-3 factors of difference for the candidate nuclei, which has to be taken into account when making predictions about experimental sensitivities and when comparing $0\nu\beta\beta$ searches with different isotopes.

In literature, the NME is commonly redefined by taking out the contribution of the axial-vector coupling constant g_A^2 : $M^{0\nu} = g_A^2 M^{0\nu}$. Typically, the value of g_A^2 for the free neutron is employed, ranging between 1.25 and 1.27. A challenge arises when comparing predicted and measured $2\nu\beta\beta$ decay half-lives of various isotopes, consistently smaller than the estimated values. A potential explanation lies in the "quenching" of g_A^2 , either induced by limitations in the calculation or by the omission of non-nucleonic degrees of freedom:

$$g_A^{eff} = g_A \cdot A^{-\gamma}, \quad (1.20)$$

where γ varies from 0.12 to 0.18, depending on the employed nuclear model [41]. Considering $0\nu\beta\beta$ decay, the question arises whether the value of g_A^2 is quenched in a manner similar to $2\nu\beta\beta$ decay or not. Currently, there is no universally agreed-upon answer, and the question remains a subject of debate. Since the correct value of g_A^2 is an open issue, this introduces significant uncertainty into the determination of $m_{\beta\beta}$ from the $0\nu\beta\beta$ rate formula of expression (1.18).

Effective Majorana mass vs $G^{0\nu}$ & $M^{0\nu}$

Various calculations of $M^{0\nu}$ and $G^{0\nu}$ for all $\beta\beta$ candidates are compared in [42]. The results depicting the effective Majorana mass limits as a function of a renormalized specific phase space and the squared nuclear matrix element are presented in Figure 1.5 for selected $\beta\beta$ candidates. A nearly uniform inverse correlation between phase space and the square of the nuclear matrix element is observed. Consequently, no $\beta\beta$ isotope demonstrates a clear preference or disadvantage; all exhibit approximately the same sensitivity to $0\nu\beta\beta$ decay per unit mass.

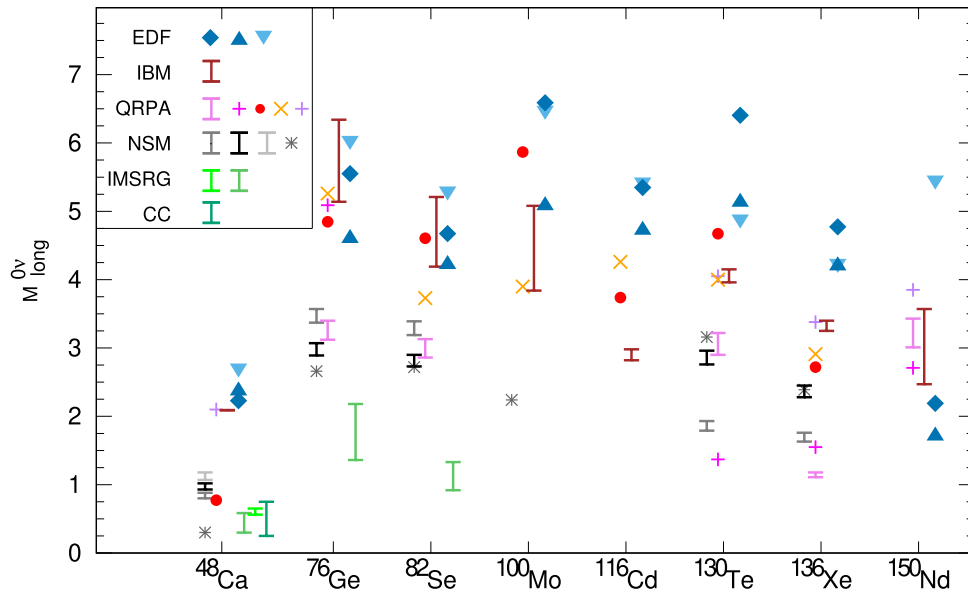


Figure 1.4: Predictions of NME values for light-neutrino exchange from different many-body models. Figure from [30].

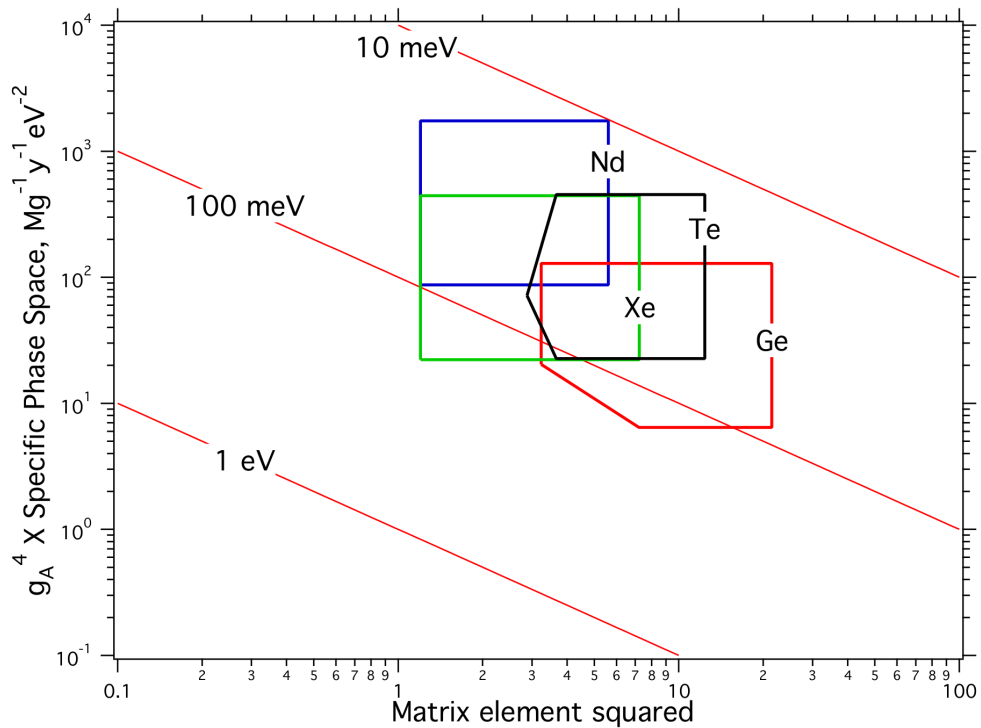


Figure 1.5: Limits on effective Majorana neutrino mass in relation to the specific phase space and squared matrix elements for the $\beta\beta$ candidates: ^{76}Ge , ^{130}Te , ^{136}Xe , and ^{150}Nd . The vertical span represents the range of g_A^2 , which differs for the adopted models, leading to non-rectangular boundaries. The lines indicate the effective $m_{\beta\beta}$ that would correspond to a count rate of 1 event per tonne per year. Figure taken from [42].

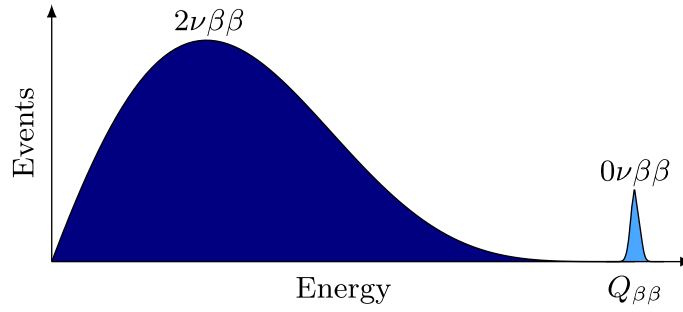


Figure 1.6: Illustration of $2\nu\beta\beta$ and $0\nu\beta\beta$ decay spectra. Image from [30].

1.4.2 Experimental considerations

From the experimental point of view, the most direct approach in the search for a $0\nu\beta\beta$ decay signal consists in the detection of the two emitted electrons. The recoil energy of the nucleus is negligible and the energy is almost entirely carried away by the two electrons. Therefore the $0\nu\beta\beta$ decay signal will manifest as a characteristic peak in the energy spectrum at $Q_{\beta\beta}$ of the decay process. Figure 1.6 shows an illustration of the two-electrons spectra: a monochromatic peak at $Q_{\beta\beta}$ is expected for the $0\nu\beta\beta$ decay, while the $2\nu\beta\beta$ process has a continuous spectrum with $Q_{\beta\beta}$ as end point.

An important aspect in the search for the $0\nu\beta\beta$ decay is the choice of the isotope. The first requirement is a high $Q_{\beta\beta}$ of the $\beta\beta$ emitter; an ideal choice would be $Q_{\beta\beta}$ larger than 2.6 MeV, which represents the end point of the dominant natural gamma radioactivity. Another fundamental requirement is high isotopic abundance of the $\beta\beta$ emitter; the majority of candidate isotopes have a natural isotopic abundance $< 10\%$ (Table 1.1), the only exception being ^{130}Te with 34.5% of natural isotopic abundance. For these reasons, among the 35 nuclei capable of undergoing $2\nu\beta\beta$ decay, 9 isotopes emerge as particularly promising candidates for the $0\nu\beta\beta$ decay search: ^{48}Ca , ^{76}Ge , ^{82}Se , ^{96}Zr , ^{100}Mo , ^{116}Cd , ^{130}Te , ^{136}Xe and ^{150}Nd .

Detecting the $0\nu\beta\beta$ decay is extremely challenging due to the inevitable presence of background events from radioisotopes. Stringent low-background techniques must be employed due to the significantly higher environmental radioactivity levels compared to the expected decay rate. Firstly, experiments need to be conducted underground to shield the detectors from cosmic rays. Subsequently, a shield with minimal radioactivity, along with detector materials with low intrinsic contamination, must be employed to neutralize natural radioactivity. The residual background contamination can be eliminated through either event topology discrimination or the implementation of a secondary detector operating in anti-coincidence with the primary detector (e.g. muon veto, scintillation light detection, neutron moderator). Moreover, the source material of the detector itself must not only contain a substantial fraction of the $\beta\beta$ decay isotopes but must also maintain a high level of purity.

Neutrinoless double beta decay sensitivity

The sensitivity of an experiment searching for the $0\nu\beta\beta$ decay is expressed by a "detection factor of merit" ($S^{0\nu}$) defined as the process half-life corresponding to the maximum signal that could be hidden by the background fluctuations (at a given statistical CL^4 n_σ). It can

⁴Confidence Level.

be expressed as [43]:

$$S^{0\nu} = \frac{\ln(2) \cdot N_A \cdot \epsilon \cdot a}{m_A \cdot n_\sigma} \sqrt{\frac{M \cdot T}{BI \cdot \Delta E}}. \quad (1.21)$$

This expression highlights the role of the experimental parameters used on the search for $0\nu\beta\beta$ decay:

- the detection efficiency ϵ is a critical parameter and it depends on the experimental technique; the highest detection efficiency is typically achieved in a detector = absorber configuration, where the isotope is by itself, or at least directly embedded in, the detector material;
- the isotopic abundance a of the $\beta\beta$ emitter: as mentioned before, the natural isotopic abundance of many $\beta\beta$ emitters is $< 10\%$, consequently, isotopic enrichment procedures are employed, contributing to an increase in the overall costs of the experiment; only ^{130}Te may offer a use without enrichment, but even here, enrichment may provide a substantial enhancement in the ratio of detector mass to isotope mass;
- the target mass M : expanding the target mass usually corresponds to a parallel increase in expenses;
- the experimental lifetime T ;
- the Background Index BI , defined as the rate of background events per unit of energy in the region of interest, mass and time; it depends on the chosen experimental technique and the radio-purity of materials; furthermore, it can be also improved through the implementation of additional selection criteria and techniques designed to discriminate signal from background events;
- the energy resolution ΔE of the detector, defined as the Full Width at Half Maximum (FWHM) at $Q_{\beta\beta}$: $\Delta E = \text{FWHM} = 2\sqrt{2\ln(2)}\sigma$, where σ is the expected standard deviation of the $0\nu\beta\beta$ decay peak; it is a crucial parameter also to minimize the background produced by the $2\nu\beta\beta$ decays.

Background-free condition

Of particular interest is the situation where BI is so low that the number of expected background events is less than one count in the energy region around $Q_{\beta\beta}$, the so-called “background-free” condition. The advantage of such a condition lies in the linear increase of the sensitivity $S^{0\nu}$ with the experimental exposure (mass \times lifetime) [43], instead of the square root as in the expression (1.21):

$$S^{0\nu} = \frac{\ln(2) \cdot N_A \cdot \epsilon \cdot a}{m_A \cdot N_s} M \cdot T. \quad (1.22)$$

where N_s is the number of observed events in the region of interest around $Q_{\beta\beta}$. Therefore, the optimal experimental conditions are achieved when a zero-background limit is upheld for the majority of the experimental runtime.

1.5 Present and future efforts on $0\nu\beta\beta$ decay search

Starting from the middle of the 20th century, numerous experiments have been carried out to investigate double beta decays. Different isotopes and detection approaches have been employed to track particles and measure the sum of the energies of the two emitted electrons. The main technologies used within the field can be classified as: scintillator detectors, semi-conductor detectors, cryogenic bolometers, Time Projection Chambers (TPCs) and tracking calorimeters.

The status of the $\beta\beta$ decays search is in continuous evolution: many experiments are running, under construction or proposed. Several experimental approaches are now available to search with high sensitivity and low backgrounds for $0\nu\beta\beta$ decay in a variety of isotopes covering the entire region of the inverted mass ordering and beyond. Lower limits for the $0\nu\beta\beta$ half-life were established in last years by KamLAND-Zen, GERDA, MAJORANA, EXO-200, CUORE and CUPID experiments.

Table 1.2 lists the most stringent $0\nu\beta\beta$ decay limits currently available (limits above 10^{24} yr are reported), including half-life lower limits and upper limit ranges on the effective Majorana neutrino mass. Whereas Table 1.3 highlights the discovery sensitivity on $0\nu\beta\beta$ decay half-life for 10 years of lifetime and the corresponding sensitivity on $m_{\beta\beta}$ of the next-generation experiments, which will reach a 3σ sensitivity higher than 10^{27} yr. The following list of experiments is not exhaustive; however, it aims to provide an overview of the key projects and experimental techniques currently available.

Scintillator detectors

Liquid scintillators are frequently chosen for extensive, multi-ton rare event searches. They operate by emitting characteristic light during the de-excitation of the scintillator molecules, which is then detected by an wide array of photosensors, usually after undergoing wavelength shifting. By employing meticulous purification and vetoing techniques, it is possible to achieve exceptionally low background levels. These detectors offer a cost-effective approach to increase the isotope mass, particularly when $\beta\beta$ isotopes are incorporated into the scintillator mixture, making them particularly suitable for repurposing in solar/reactor neutrino experiments. Nevertheless, their energy resolution is limited, typically around few % level.

KamLAND-Zen experiment involves employing a nylon balloon filled with liquid scintillator enriched in ^{136}Xe . The first phase, KamLAND-Zen-400, yielded strong half-life limits, despite unexpected background due to the Fukushima nuclear disaster. The sec-

isotope	$T_{1/2}^{0\nu}(10^{25}\text{yr})$	$m_{\beta\beta}(\text{meV})$	experiment
^{136}Xe	> 23	$< 36 - 156$	KamLAND-Zen [44]
	> 3.7	$< 129 - 555$	EXO-200 [45]
^{76}Ge	> 18	$< 79 - 180$	GERDA [46]
	> 8.3	$< 113 - 269$	MAJORANA [47]
^{130}Te	> 2.2	$< 90 - 305$	CUORE [48]
^{82}Se	> 0.46	$< 263 - 545$	CUPID-0 [49]
^{100}Mo	> 0.18	$< 280 - 490$	CUPID-Mo [50]

Table 1.2: Recent experimental lower limits on the $0\nu\beta\beta$ decay half-life for light Majorana neutrino exchange and upper limit ranges on $m_{\beta\beta}$, both at 90% CL, with the corresponding experiments. Note that only recent result reaching above 10^{24} yr are reported.

isotope	$T_{1/2}^{0\nu}(10^{27}\text{yr})$	$m_{\beta\beta}(\text{meV})$	experiment
^{76}Ge	> 1.5	$< 27 - 63$	LEGEND-200 [52]
	> 13	$< 9 - 21$	LEGEND-1000 [53]
^{100}Mo	> 1.1	$< 12 - 34$	CUPID [54]
^{136}Xe	> 7.4	$< 6 - 27$	nEXO [55]
	> 2.2	$< 12 - 50$	NEXT-HD [56]
	> 1.1	$< 17 - 72$	Darwin [57]
	> 1.1	$< 17 - 71$	KamLAND2-Zen [44]

Table 1.3: The discovery sensitivities on the $0\nu\beta\beta$ decay half-life and the corresponding sensitivity on $m_{\beta\beta}$ of next-generation $0\nu\beta\beta$ experiments. Note that only experiments that will reach a discovery sensitivities above 10^{27} yr are reported.

ond phase, KamLAND-Zen-800, achieved world-leading half-life limits [44] (see Table 1.2). The KamLAND-Zen collaboration is planning a follow-on phase, KamLAND2-Zen, which will deploy approximately 1 ton of enriched xenon, aiming to significantly reduce background by improving energy resolution and implementing upgrades such as new light concentrators and photomultiplier tubes, leading to a background reduction by a factor of 20 and enhanced sensitivity.

SNO+ is a successor to the SNO experiment, utilizing its infrastructure. Its setup involves filling SNO acrylic sphere with around 780 tons of liquid scintillator containing tellurium, while the surrounding SNO water filled cavity serves as a water Cherenkov active veto. The project follows a multi-stage plan. Initially, it will use about 1.3 tons of ^{130}Te with an expected energy resolution of about 7% FWHM@ $Q_{\beta\beta}$. In a subsequent phase, the goal is to increase the ^{130}Te mass to 6.6 tons and improve the energy resolution to 5%. This ambitious initiative is projected to yield a sensitivity on $T_{1/2}^{0\nu} > 10^{26}$ yr [51].

Semiconductor detectors

Semiconductor detectors, primarily using High-Purity Germanium (HPGe), are integral to the search for $0\nu\beta\beta$ decay. These detectors offer exceptional energy resolution ($< 0.1\%$), enabling the precise measurement of particle energies, critical for distinguishing rare signal events from background radiation. Enriched isotopes, such as ^{76}Ge , are often used to enhance sensitivity. Techniques like pulse shape discrimination and operation in cryogenic environment are employed to reduce background contamination and noise.

GERDA and MAJORANA Demonstrator experiments used p-type HPGe detectors enriched in ^{76}Ge isotope. MAJORANA focused on refining background reduction techniques within the traditional approach of operating germanium detectors in a vacuum environment, while GERDA pioneered an innovative approach involving liquid argon. The GERDA experiment achieved the highest sensitivity on the half-life, of 1.8×10^{26} yr at 90% C.L., collecting more than 100 kg·yr of total exposure in a “background-free” regime [46]. The MAJORANA experiment achieved the best energy resolution of 0.12% FWHM@ $Q_{\beta\beta}$ [47].

By combining technological expertise and experience from both previous experiments, the LEGEND program is expected to reach a design sensitivity two orders of magnitude greater than its predecessors. In particular, LEGEND-200 experiment aims to reach a sensitivity on the half-life of 10^{27} yr by operating about 200 kg of HPGe detectors [52]. Together with its scientific purpose, it will also serve as a testing ground for all R&D solutions in view of LEGEND-1000 experiment. The latter aims for discovery potential beyond 10^{28} yr [53, 58]. Since this thesis work focuses on the LEGEND project, additional

details will be provided in Chapter 2.

Cryogenic bolometers

Cryogenic bolometers operate at extremely low temperatures, close to absolute zero, and are designed to measure temperature changes caused by the energy deposited by particles. Cryogenic bolometer experiments for $0\nu\beta\beta$ decay typically involve high-purity crystals or scintillating materials, sensitive thermometers like superconducting thermistors or transition-edge sensors and shielding to minimize background radiation. Signal generation is slow, taking milliseconds, but they achieve excellent energy resolutions (about 0.1%) at MeV energies. Scintillating crystals can collect light signals for particle discrimination. Multiple detectors can be used in a granular array but require complex cryogenic infrastructure.

The leading experiment, CUORE [48], employs TeO_2 bolometers operating at 10 mK and within a radiopure lead shield, cooled in a helium dilution refrigerator. CUORE has demonstrated the feasibility of a ton-scale bolometric experiment, achieving an impressive energy resolution of 0.3% FWHM@ $Q_{\beta\beta}$. However, the experiment currently lacks particle identification and faces a background from surface alpha particles. The CUPID experiment [54] is planned to succeed CUORE in the same cryostat, using isotopically modified Li_2MoO_4 crystals and implementing particle discrimination. The goal of CUPID is to explore the inverted hierarchy region of neutrino mass, achieving a sensitivity of $T_{1/2}^{0\nu} > 10^{27}$ yr.

Time projection chambers

TPCs detect and characterize particles using scintillation and ionization channels. TPCs reconstruct positions and energies of particles, with ionization-to-scintillation ratios aiding particle identification. Xenon is often the medium of choice due to its low background. TPCs offer remarkable energy resolution, close to 1% for liquid xenon and down to about 0.5% for high-pressure gas TPCs in electroluminescence mode. Self-shielding properties of xenon can reduce background, but outer regions may need additional shielding.

The up-to-date best $0\nu\beta\beta$ decay result of a TPC is achieved with the EXO-200 experiment [45]. EXO-200 comprises a cylindrical TPC containing liquid xenon enriched in ^{136}Xe . The anti-correlation between ionization and scintillation signals from ^{136}Xe facilitates the reconstruction of event topology, energy, position, and particle type, allowing to achieve a resolution of about 3% FWHM@ $Q_{\beta\beta}$. The upcoming nEXO experiment [55] is set to employ five tonnes of enriched liquid xenon, aiming to increase the energy resolution below 2% and attain a sensitivity of $T_{1/2}^{0\nu} \sim 10^{28}$ yr after 10 years of data taking.

The NEXT experiment [56] uses a high-pressure gaseous xenon TPC with an electroluminescent region. NEXT-White, a proof-of-principle detector with 5 kg of ^{136}Xe , demonstrated an energy resolution of $\sim 1\%$ at $Q_{\beta\beta}$ and tracking performance capable of distinguishing electron track events, reducing background by a factor of 27. NEXT-100, the second stage of the project, contains 87 kg of ^{136}Xe , with a projected background index of 4×10^{-4} cts/(keV·kg·yr). NEXT-HD is a future ton-scale phase of NEXT, with an expected significant reduction in background, by replacing PMTs with an all-SiPM light readout at both TPC ends and using wavelength-shifting fibers to enhance further the light collection. The main goal is to reach a sensitivity of $T_{1/2}^{0\nu} \sim 10^{27}$ yr.

DARWIN experiment [57] is a dual-phase natural-xenon TPC with electroluminescent readout, designed for direct searches for Weakly Interacting Massive Particle (WIMP)

Dark Matter. This detector also possess sensitivity to $0\nu\beta\beta$ decay, even with natural xenon targets. However, the instrumentation required for the detection of nuclear recoils from WIMPs naturally leads to higher levels of external background compared to detectors optimized for $0\nu\beta\beta$ decay experiments. DARWIN will use 40 tons of Xe and aims for a discovery sensitivity of $T_{1/2}^{0\nu} \sim 10^{27}$ yr.

Tracking calorimeters

Tracking calorimeters are also specialized detectors used in the search for $0\nu\beta\beta$ decay. They differ in having distinct source and detector components, which minimizes self-absorption within the source. A thin-foil source material is employed to mitigate absorption issues, surrounded by a low-density gas tracker that reconstructs electron paths. These detectors provide detailed topological information about particle interactions and energy measurements, enabling the study of the underlying decay mechanism. Although tracking calorimeters are efficient, they have limitations when it comes to handling mass.

NEMO-3 [59], the most sensitive tracking calorimeter to date, set competitive constraints on various target isotopes. Its successor, SuperNEMO [60], follows similar design principles and is in preparation. SuperNEMO includes a SuperNEMO Demonstrator with 7 kg of ^{82}Se and a full-scale experiment featuring multiple modules with a total ^{82}Se mass of 100 kg. By reducing the background to 20%, SuperNEMO aims to a 10-year discovery sensitivity of $T_{1/2}^{0\nu} \sim 10^{24}$ yr and $T_{1/2}^{0\nu} \sim 10^{25}$ yr for SuperNEMO-D and SuperNEMO, respectively.

1.6 Pros and cons of Germanium for $0\nu\beta\beta$ decay search

Germanium detectors are particularly suitable for $0\nu\beta\beta$ decay search, despite some theoretical disadvantages. The decay rate, expressed by Equation (1.18), depends on the phase space factor ($G^{0\nu}$), resulting in an expected half-life higher than many other $0\nu\beta\beta$ candidates, as illustrated in Figure 1.7. Additionally, the maximal value of $M^{0\nu}$ for ^{76}Ge is over 2.5 times larger than the minimally predicted one, introducing significant uncertainty to $T_{1/2}^{0\nu}$. This uncertainty has to be taken into account when making predictions about experimental sensitivities and when comparing $0\nu\beta\beta$ searches with different isotopes. From an experimental standpoint, the $Q_{\beta\beta}$ value is relatively low compared to the endpoint of natural gamma radioactivity (Table 1.1), and germanium detectors require isotopic enrichment due to low natural abundance, contributing to the overall cost of the experiment. However, this cost challenge is a common issue across all $0\nu\beta\beta$ experiments.

Despite these theoretical and experimental challenges, germanium detectors offer compensatory advantages. The relatively long expected half-life of $0\nu\beta\beta$ decay is partly compensated by the exceptional energy resolution achievable with germanium detectors, a crucial factor in sensitivity of a $0\nu\beta\beta$ experiment, as demonstrated by Equation (1.21). Given that $2\nu\beta\beta$ decay acts as an irreducible background source for $0\nu\beta\beta$ decay searches, the excellent energy resolution becomes essential to distinguish the expected peak from the tail of the $2\nu\beta\beta$ decay distribution (Figure 1.7 Right). Additionally, germanium detectors exhibit high detection efficiency, being both the source and detector of the $\beta\beta$ emitter, and possess intrinsic radiopurity. The background rejection ability of germanium detectors, stemming from their proven technology with a long history in $0\nu\beta\beta$ search [61], play a pivotal role in discriminating signal-like events from backgrounds. This discrimination power facilitates the efficient reduction of the background index, achieving the background-free condition.

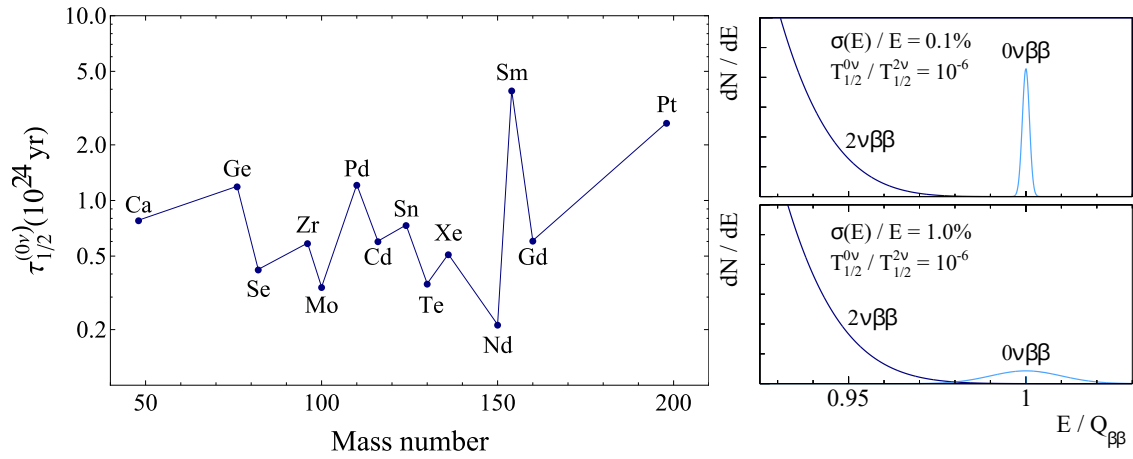


Figure 1.7: **Left:** expected $0\nu\beta\beta$ half-lives for different candidate isotopes. Figure from [62]. **Right:** summed electron energy spectrum for $2\nu\beta\beta$ decay and $0\nu\beta\beta$ decay with two different energy resolutions for the $0\nu\beta\beta$ peak. Adapted from [63].

CHAPTER 2

The LEGEND Experimental Program

The LEGEND (Large Enriched Germanium Experiment for Neutrinoless double beta Decay) collaboration works to develop the largest ^{76}Ge -based $0\nu\beta\beta$ decay experiment in history. The collaboration was born from the synergy of the GERDA and MAJORANA collaborations, and additional new international institutions. The experimental program will be phased: LEGEND-200 and LEGEND-1000 will search for $0\nu\beta\beta$ decay in ^{76}Ge isotope, using about 200 kg and 1000 kg of High-Purity Germanium (HPGe) detectors, respectively. LEGEND-200 is currently taking data with about 140 kg of HPGe detectors at Laboratori Nazionali del Gran Sasso (LNGS) of INFN¹ in Italy.

The chapter unfolds with a discussion of the experimental goals for both LEGEND phases (Section 2.1). It then provides more detailed information about the LEGEND-200 experiment (Section 2.2), main focus of this thesis work, covering aspects such as the experimental setup, HPGe detectors descriptions and an overview on data acquisition system. Primary background sources, the innovative techniques applied for their active suppression and the LEGEND-200 data processing are also presented. The Section 2.3 contains an update on the current status of LEGEND-200 experiment and performance results. Finally, in the Section 2.4, a brief description of the next-generation experiment, LEGEND-1000, is presented.

2.1 LEGEND goals

The primary goal of the LEGEND collaboration is to build upon the achievements of the GERDA and MAJORANA experiments, exploring a new background regime within the region of interest, centered around the $Q_{\beta\beta} = 2039$ keV, for ^{76}Ge isotope. LEGEND staged approach provides a low-risk path to world-leading sensitivity. Its expected sensitivity to a $0\nu\beta\beta$ decay signal in ^{76}Ge as a function of exposure (mass \times time) is shown in Figure 2.1 and is described below.

The goal of the first phase, LEGEND-200, is to reach a background index of 2×10^{-4} cts/(keV \cdot kg \cdot yr) or 0.5 cts/(FWHM \cdot t \cdot yr) at $Q_{\beta\beta}$ of the decay². With such a low background level, LEGEND-200 will attain a 3σ discovery sensitivity on $T_{1/2}^{0\nu}$ of the order of 10^{27} yr with 1 t \cdot yr of exposure over a period of 5 years of data taking. The 3σ discovery sensitivity

¹Istituto Nazionale di Fisica Nucleare.

²1 cts/(keV \cdot kg \cdot yr) = $\Delta E \cdot 10^3$ cts/(FWHM \cdot t \cdot yr), ΔE of 2.5 keV has been considered.

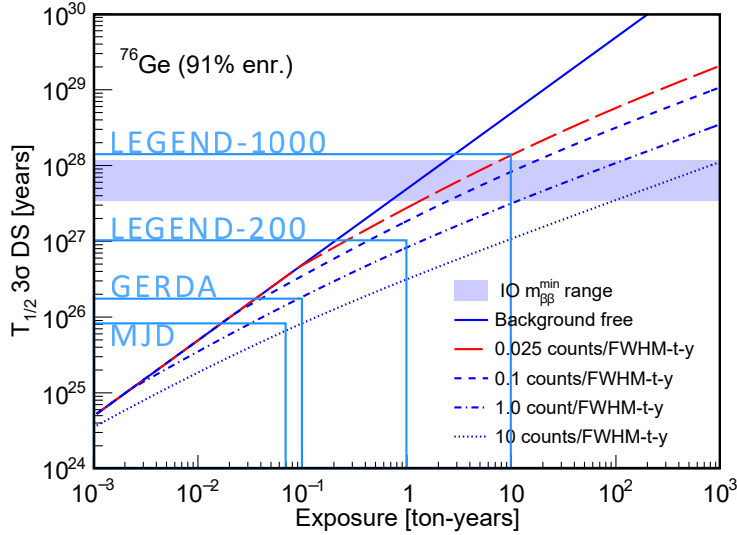


Figure 2.1: LEGEND sensitivity to the measurement of a $0\nu\beta\beta$ decay signal in ^{76}Ge isotope as a function of exposure for a 3σ (99.7% C.L.) discovery sensitivity and previous results from GERDA and MAJORANA experiments. The maximum expected BI scenario is indicated by the red dashed line. Adapted from [53].

of LEGEND-200 will translate to an upper limit on the effective Majorana mass ($m_{\beta\beta}$) in the range of 34-78 meV [52]³.

LEGEND overarching goal is to reach a 3σ discovery sensitivity across the entire remaining parameter space for the inverted neutrino mass ordering, assuming that light left-handed neutrino exchange dominates. The LEGEND-1000 experiment is expected to surpass the signal-to-background discrimination achieved by current-generation experiments. The background target for LEGEND-1000 is a BI of less than 1×10^{-5} cts/(keV·kg·yr) or less than 0.025 cts/(FSHM·t·yr). With this reduced background, LEGEND-1000 will attain a half-life discovery sensitivity of 1.3×10^{28} yr, corresponding to an upper limit on $m_{\beta\beta}$ in the range of 9-21 meV over a span of 10 years of data taking [53].

2.2 LEGEND-200 experiment

The LEGEND-200 experiment takes place at LNGS of INFN, benefiting from the natural shielding effect of the rock overburden (3500 m water equivalent), which effectively attenuates the hadronic components of cosmic ray showers and decreases the muon flux by six orders of magnitude. During this phase, about 200 kg of HPG ^{76}Ge detectors (about 70 kg from GERDA and MAJORANA, and 130 kg of newly produced p-type detectors) are employed within a modified infrastructure inherited from the GERDA experiment.

2.2.1 Experimental setup

The LEGEND-200 setup follows a multi-layer approach in order to minimize the main background sources. Figure 2.2 Left shows an artistic representation of the LEGEND-200 experiment and its components are discussed below.

³Assuming the current matrix element calculations and an un-quenched axial-vector coupling constant.

⁴The impurities concentration is $\sim 10^{-13}$ atoms/Ge.

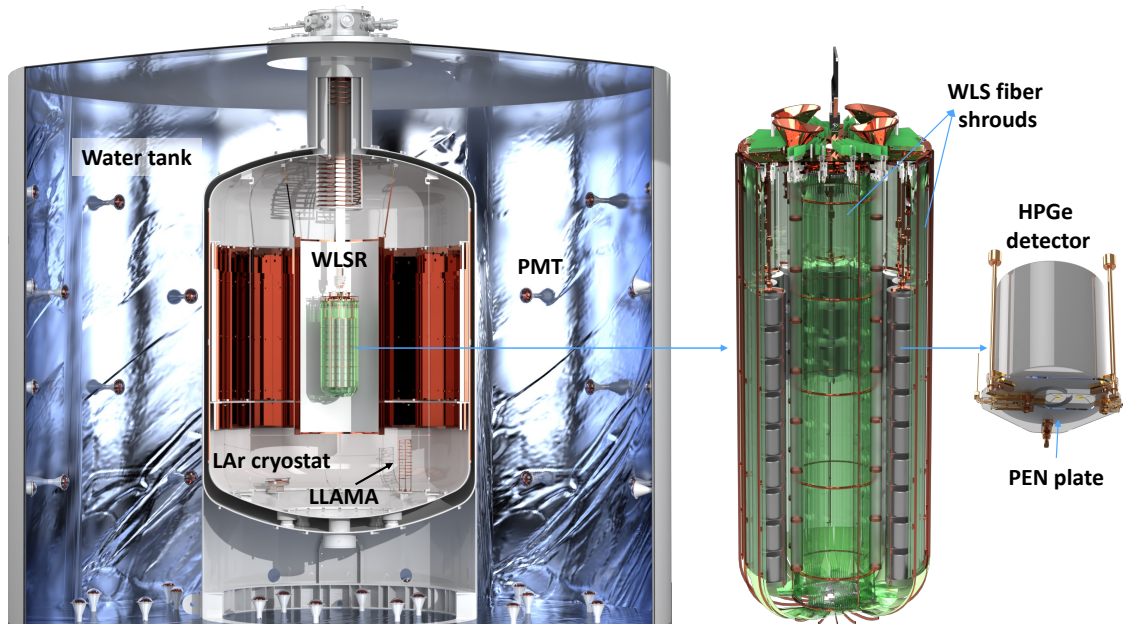


Figure 2.2: Left: Artistic view of LEGEND-200 setup. Right: HPGe detector strings surrounded by the LAr instrumentation and an HPGe detector element. Main components are marked. Images credit to P. Krause.

A 10 m-diameter and 8 m-height tank with 590 m³ of ultra-pure water shields from neutron and gamma backgrounds. It works also as a muon veto for residual cosmic muons through the detection of Cherenkov light with 66 encapsulated PhotoMultiplier Tubes (PMT) [64, 65].

Inside the water tank a 4 m-diameter vacuum-insulated stainless steel cryostat with 64 m³ of purified Liquid Argon (LAr), at a temperature of about 89 K, is present. The internal walls are covered with a 6 cm low-background copper layer to shield the γ radioactivity originating from the steel. The ultra-pure LAr acts as cooling medium for germanium detectors⁵ and additional shield for external radiation [64, 66]. At the bottom of the cryostat, the LEGEND LAr Monitoring Apparatus (LLAMA) is placed, allowing to monitor the purification levels of the LAr continuously. The system consists of a 85 cm-height copper frame; an ²⁴¹Am light source, contained in a triangular shaped copper vessel and equipped with Silicon-PhotoMultipliers (SiPM), is positioned at the base of the frame support and 13 peripheral SiPMs are located at different distances to the light source. Off-line analysis is applied in order to provide the LAr optical properties [67].

The center of cryostat contains a 1374 mm-diameter and 3 m-height cylinder, made of copper-tetrax foil coated internally with TetraPhenyl Butadiene (TPB), called WaveLength-Shifting Reflector (WLSR) [68]. The WLSR is designed to separate the innermost LAr volume (about 6 t of LAr), working as further shielding for detector systems and as a reflector of the LAr scintillation light (see Section 3.4). Inside the WLSR the LAr instrumentation is present. It is composed of two concentric WaveLength-Shifting (WLS) fiber shrouds, which surround the HPGe detector (Figure 2.2 Right), coupled to SiPMs on both ends. The LAr instrumentation plays a key role in detecting background events that deposit energy in the LAr volume surrounding the HPGe detectors. Further details of the system will be elaborated upon in Chapter 3, as it is the central focus of this dissertation.

⁵The germanium detectors narrow energy band-gap of 0.67 eV require cryogenic cooling to operate effectively, minimizing thermally induced current.

The HPGe detectors are mounted on supports made of active PolyEthylene Naphthalate (PEN), a scintillating plastic material known for its ability to improve background rejection [69], and are arranged in 12 strings. In order to uphold a high radiopurity of components near the detectors array, low-mass MAJORANA-style components have been employed and underground electroformed copper has been introduced to mitigate the impact of the ^{238}U and ^{232}Th decay chains and the cosmogenic activation of ^{60}Co in copper [70]. Each HPGe string is placed inside a TPB-coated nylon cylinder, called Nylon Mini Shroud (NMS), to limit the volume of LAr around them from which radioactive ions, such as ^{42}K (see Section 5.2), can be captured by electric fields on the detector surfaces [71].

The assembly of HPGe detectors, surrounded by LAr instrumentation, takes place within an ISO7 clean room, inside a glove box. The nitrogen atmosphere in the glove box facilitates clean handling and deployment. After the installation the LAr instrumentation and HPGe strings are lowered to the cryostat through a lock system.

The High-Voltage (HV) supply is realized by 160 6 kV HV power-supplies from CAEN⁶. An asymmetric 3-pole RC filter, designed for LEGEND-200, is employed to eliminate AC noise from the DC voltage. The signals from HPGe and SiPM detectors are driven via 10 m long Kapton flat-band cable to the outside of the lock where they are digitized by a flash analogue-to-digital (ADC) converter, see Section 2.2.3.

2.2.2 HPGe detectors

The HPGe detectors form the core of LEGEND-200 experiment. They are semiconductor diodes sensitive to ionizing radiation and γ rays, with an excellent energy resolution and a high detection efficiency.

The HPGe detectors work with a reverse bias voltage, such that almost the entire volume is depleted of free charge carriers [72]. The high voltage (up to 5 kV) is applied to n^+ electrode, a Li-diffused relatively thick (~ 0.7 mm) dead layer, while the signal is readout on the very thin (~ 0.3 μm) p^+ electrode, obtained via Boron implantation.

LEGEND-200 is using p-type germanium detectors used in previous experiments: Broad Energy Germanium (BEGe) and semi-Coaxial (Coax) detectors from GERDA [73], and P-type Point Contact (PPC) detectors from MAJORANA [74]. In order to reach the 200 kg array, newly developed detectors are incorporated, namely the Inverted Coaxial Point Contact (ICPC) detectors [75], which form more than 60 % of total mass. This detector type has been already tested in the last phase of GERDA experiment [76]. All of them are made from isotopically enriched material in ^{76}Ge at 86 - 91%. Few details on the germanium detector types used in LEGEND-200 are listed below:

- **Coax detectors** (Figure 2.3 left) typically have a mass around 2-3 kg and they have a "wrap-around" n^+ conductive Li layer and a B implanted p^+ contact in the central hole, separated by a groove which is covered by an insulating silicon monoxide layer (passivation layer). This configuration leads to a strong field across the detector volume, enabling the fabrication of large detectors (8-10 cm). However, a disadvantage of this layout is the dependence of the pulse shape on the location where the charge is created within the detector volume.
- **PPC and BEGe detectors** (two central images of Figure 2.3) have an average mass of about 700 g and, unlike in the Coax, the p^+ contact is very small (especially for

⁶<https://www.caen.it/products/a1560h/>

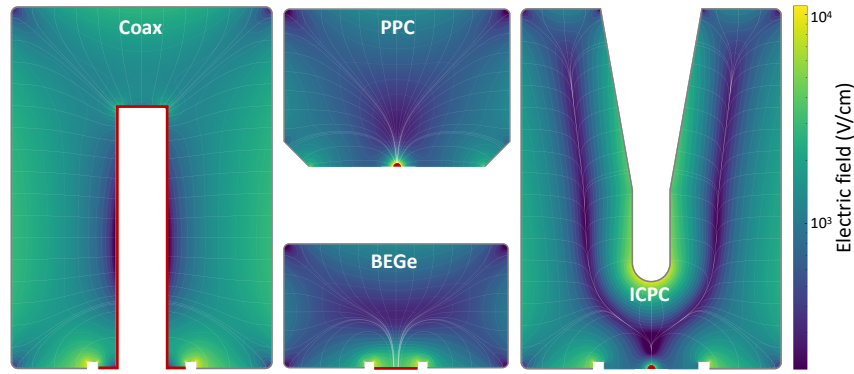


Figure 2.3: Electric fields of the HPGe detector types used in LEGEND-200. The red color indicates the p^+ electrode, where the signals are readout. Credit to D. Hervas Aguilar.

PPC detectors), called the point contact readout electrode. The small p^+ contact is located in the middle of the bottom side while the Li-diffused n^+ contact covers the whole outer surface. The special geometry of BEGe and PPC allows enhanced signal discrimination against background events and register also an excellent energy resolution in a broad energy range.

- **ICPC detectors** (Figure 2.3 right) have similar characteristics of BEGe and PPC detectors in terms of energy resolution and pulse shape discrimination. Moreover, they provide more active volume per readout channel with a larger mass (1.5-4 kg) and lower surface-to-volume ratio. The increased detector mass allows the overall number of detectors operated in LEGEND-200 to be reduced, also reducing the number of cables, readout channels, and detector support materials that are all sources of background. The reduction of the surface-to-volume ratio also helps in mitigating the background due to radioactive decays on the detector surfaces.

Readout electronics

The signal produced by the HPGe detectors are read-out by a resistive-feedback Charge-Sensitive Amplifier (CSA), operating in LAr [77]. The CSA is designed with low electronic noise (< 1 keV FWHM) and to guarantee an energy resolution of about 2.5 keV at $Q_{\beta\beta}$. It features a fast rise time (< 100 ns) which allows for pulse shape discrimination, high linearity and dynamic range up to 10 MeV for detecting high energy α decays.

The CSA is separated into two stages in order to meet stringent radiopurity constraints and to improve the over-all performance: the first stage is based on the MAJORANA Low-Mass Front-End (LMFE) [78], placed in the proximity of the HPGe detector and has a total activity lower than $1 \mu\text{Bq}$ of radioactivity; the main amplifier stage (called CC4), based on the GERDA design [79], is placed 30-150 cm above the HPGe detector (the distance depends on the detector location in the array) and has a total activity budget of about $50 \mu\text{Bq}$ per channel. The connection between the first and second stages involves four low-mass AXON pico-coaxial cables, which are custom made using carefully selected and tested copper wires and dielectric material.

A dynamic receiver positioned at the cryostat flange, called Head Electronics, is designed to serve as termination for signals originating from the CC4 and to drive them to the Data AcQuisition (DAQ) system. The incorporation of an active termination holds the potential to significantly reduce the power dissipated by the CSA within the liquid

argon. The system facilitates also the monitoring of the HPGe detector leakage current for LEGEND slow-control system. Furthermore, it provide the supply voltages for the pre-amplifier while also monitoring voltage and current levels.

Energy calibration and resolution

The energy calibration and the estimation of the energy resolution of each detector are performed by irradiating with ^{228}Th sources, with low neutron emission. The sources are inserted in the LAr cryostat through four funnels [52]. Each funnel contains four ^{228}Th sources of about 5 kBq activity per source, situated at different heights for homogeneous event distribution [80]. The calibration process is conducted on a weekly basis with a duration of few hours between physics runs.

The energy calibration relies on the seven primary γ lines originating from the ^{228}Th decay chain. These include the full energy peaks at 583.2, 860.6, and 2614.5 keV, the double escape peak at 1592.5 keV, and the single escape peak at 2103.5 keV from ^{208}Tl , along with the full energy peaks at 727.3 and 1620.7 keV from ^{212}Bi .

A dedicated software (see sub-Section 2.2.5) identifies the 7 gamma lines described above and perform a series of unbinned fits to extract the peak positions. The model used for the fits include a low-energy tail that accounts for possible energy underestimation. The peak positions are used to determine the calibration curve.

2.2.3 Data acquisition system

The signals from the detector systems, including HPGe, SiPMs, and PMTs, are recorded through a Flash Analog-to-Digital Converter (FADC) and subsequently processed digitally offline. The DAQ system employed in LEGEND-200 utilizes the modular FlashCam system, known for its scalability and readout capabilities through Gigabit Ethernet cables [81]. This system comprises four independent data streams, allocated to each crate of digitizer cards: two crates for HPGe detectors, one for SiPM readout, and one for PMTs. SiPM and HPGe crates accommodate 12 ADC cards, containing 6 channels each, for a total of 144 ADC channels for HPGe detectors and 72 for SiPMs. For PMTs, 3 cards of 24 ADC channels each are adopted, with total of 72 ADC channels. To maintain a suitable energy resolution while ensuring a single-channel readout across the desired dynamic range, the ADC resolution for HPGe and SiPM detectors is set at 16 bits at 62.5 MHz sampling rate, recording traces of about 8000 samples. While 12 bits at 250 MHz are implemented for PMTs.

The DAQ is configured to combine the readout of multiple crates into a single data stream, such as combining the readout from the two HPGe detector crates and one SiPM crate. The data written to each data stream is organized into periods, runs and cycles. A cycle contains a block of contiguous data synchronously initiated and terminated by the DAQ, and marked by the GPS timestamp of the second within which they are initiated. Moreover, the cycles can be characterized by physics data used for the primary physics analysis; calibration data when calibration source deployments for calibrating the HPGe detectors; LAr data containing only data for SiPMs of the LAr instrumentation; and test data used for other special test. A run is a series of DAQ cycles taken with a consistent detector configuration representing an analyzable block of stably collected data. A run lasts no longer than a week, typically starts with a calibration, then physics data taking. A period is a collection of runs with similar operating conditions, i.e. same hardware and DAQ configurations.

Trigger schemes

An event is characterized by the traces recorded in all operational HPGe detectors, PMT from muon veto system, and SiPM from the LAr instrumentation. The primary triggering condition relies on the HPGe detectors: if a signal surpasses a threshold of about 100 keV in any of the HPGe detectors⁷, it initiates data acquisition, and the corresponding event is saved to disk. The DAQ system may run either in global trigger mode, in which all channels are readout when any one channel triggers, or local trigger mode, where data is readout only for those channels which self-trigger. For physics runs, the global trigger mode is adopted, while for calibration runs the local trigger mode is used. For tracking each individual detector stability, test pulses are injected into each HPGe channel pre-amplifier at a constant rate of 50 mHz and 500 mHz, during physics and calibration data takings, respectively.

The SiPM trigger is also an integral part of the LEGEND-200 data taking. This trigger condition enables the identification and differentiation of correlated backgrounds, which may exhibit energy depositions in the LAr before or after deposition in the HPGe detectors, without any coincident energy deposition inside them. Thus, the events observed in the SiPM detectors are triggered independently of HPGe events: when a signal surpassing an energy threshold of 0.5 photoelectron per channel is detected on 16 SiPM channels in coincidence, the data are also written to the disk. The validation of the SiPM trigger has been established through a dedicated study on the triggered event rate per SiPM channel (see Section 3.9).

The DAQ of the muon veto is separate, it runs with an independent trigger condition, only sharing the timestamp of the arriving muons with the main DAQ. For all HPGe and SiPM triggers the muon veto is readout. The muon veto implements a coincidence trigger, i.e. it triggers independently of the HPGe and SiPM readout when: 6 out of 10 PMTs from the FlashCam card-0 (pillbox PMTs, i.e below the LAr cryostat), 4 out of 20 PMTs from the FlashCam card-1 (floor PMTs), and 4 out of 23 PMTs from the FlashCam card-2 (wall PMTs) record a signal within 60 ns time window [82]. If any of the three cards is triggered, the signal is sent to the master card, and the muon event is recorded.

Regardless of the triggering scheme, event reconstruction requires that all subsystems share a common clock and that data taking from all subsystems are started and stopped synchronously by the DAQ software.

Clock Distribution

The clock system for LEGEND-200 is based on a 10 MHz GPS clock with a PPS⁸ signal provided by a GPS unit [83]. For the FlashCam system, a master card provides clock distribution for the individual digitizer cards. The new system to assign accurate timestamps is based on a Master unit installed on surface (LNGS) and receiving time information from a GPS receiver, and Slave units placed underground which get data packet from the Master and assign the timestamps. The system is able to provide a time accuracy of 15 ns and precise reference frequencies to the experiment. The link between the Master and the Slave is performed via about 8 km single-mode optical fiber.

⁷The threshold is set in ADC, corresponding to about 100 keV. Below 100 keV the energy spectrum is dominated by ³⁹Ar β decay.

⁸Pulse per second.

2.2.4 Active background reduction techniques

LEGEND-200 incorporates a robust shielding system and utilizes radio-pure materials. However, despite these precautions, some radioactive isotopes stemming from natural, cosmogenic and anthropogenic radioactivity persist unavoidably. These isotopes constitute a substantial contributor to background radiation. α and β particles, due to their limited penetration depth, only contribute to this background when they are generated on or in close proximity to the detector surface.

Typical α -sources come from ^{226}Ra and ^{210}Po and they are peaked at high energies (around 5.3 MeV) in the energy spectrum. α particles experience rapid energy loss within a very short range. Consequently, upon entering the p^+ contact, or even before, a portion of their energy is dissipated. The fraction of detected energy results in prolonged low-energy tails that extend into the region of interest, potentially contributing to the background at $Q_{\beta\beta}$.

γ lines and β decays are distributed along the entire spectrum and they are mostly originating from ^{238}U and ^{232}Th chains (see Appendix A) and from ^{40}K , ^{42}K and ^{60}Co . The most intense γ lines from the ^{238}U and ^{232}Th chains are resulting from the decays of ^{214}Bi and ^{208}Tl , respectively. The sources could be located at different positions inside the experiment, like cables or holder structures. Especially, ^{40}K isotope was found in all screened materials while ^{42}K comes from ^{42}Ar , a cosmogenically-produced isotope in LAr (see Section 3.1).

In order to fulfill the LEGEND-200 background goal, the experiment relies on different types of pulse selection criteria and on a set of improved techniques for active background reduction. They are schematized in Figure 2.4 and described in details below.

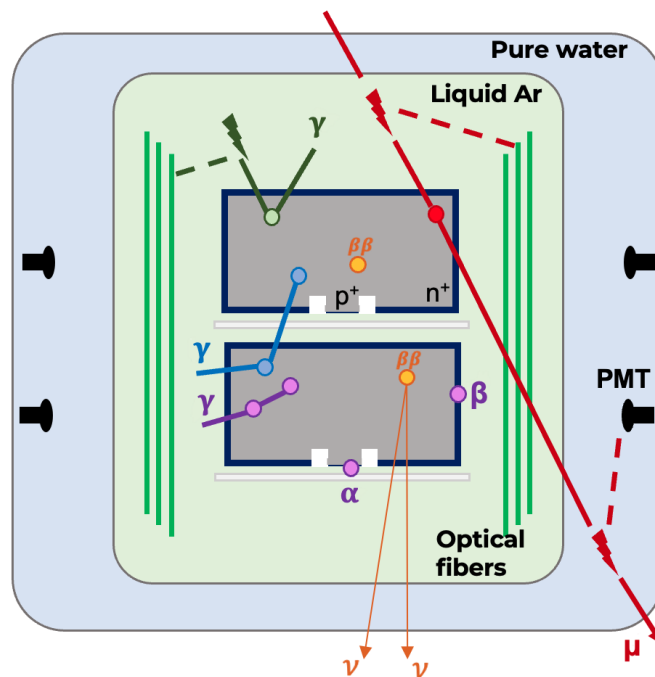


Figure 2.4: Active background reduction techniques for double beta decay events (orange): muon veto (red), detector anti-coincidence (blue), LAr veto (green) and PSD (violet).

Muon veto

Muons, upon entering the PMT detector, undergo energy loss through both electromagnetic interactions and inelastic reactions with nuclei. These interactions can give rise to high-energy neutrons, which subsequently trigger further inelastic reactions, resulting in the production of additional isotopes and more neutrons. Consequently, muons are a dual-source of background, both directly and indirectly. To efficiently identify muons, the instrumentation located within the water tank detect Cherenkov light with PMTs [84].

Liquid argon veto

The LAr instrumentation rejects background events characterized by simultaneous energy deposition in both the LAr and the HPGe detectors. LAr scintillates upon interaction with ionizing radiation or particles depositing energy. For each MeV of energy deposited, up to 40000 photons are emitted at a wavelength peaked at 128 nm [85]. The LAr scintillation light is used in LEGEND-200 to veto α and β decays near or on the HPGe detector surface (e.g. ^{226}Ra or ^{42}K) and γ background from natural decay chains (e.g. ^{228}Th or ^{226}Ra). They must be discriminated from the double beta decay signals, which have energy deposition inside the germanium detector and no energy deposition in the liquid argon. Information on LAr veto condition can be found in Section 4.4, where also the application on LEGEND-200 physics data will be shown.

Pulse shape discrimination

The drift of charges created by an ionizing particle in a HPGe detector depends on the electric field in the diode. A potential signal arising from $0\nu\beta\beta$ decay releases an energy of $Q_{\beta\beta} = 2039$ keV (for ^{76}Ge), typically contained within a small volume of the detector (~ 1 mm³). For this reason, it is categorized as a Single-Site Event (SSE). This type of event have to be distinguished from other events that can occur within the detector and/or on its surface.

Using the Pulse Shape Discrimination (PSD) techniques, the following events can be rejected:

- γ 's undergoing Compton scattering or pair production are mostly Multi-Site Events (MSE) and hence may lead to multiple energy depositions in HPGe detectors;
- energetic β rays (e.g. from ^{42}K) created at the n^+ electrode surface can penetrate the dead layer and deposit energy in the active volume; they can generate slow pulses with incomplete charge collection because of the low electric field in the lithium-diffused region;
- α events are mainly produced by ^{210}Po accumulated on the surface of the p^+ electrode and generate pulses with short rise times and high currents; α particles can trespass the HPGe detector only through the p^+ electrode and the insulating groove due to their thickness and the absence of the dead layer in the groove.

Due to the different geometries of the detectors and the varying electric field configurations inside them (Figure 2.3), different PSD techniques are used for the LEGEND-200 detectors [86]. For Coax detectors an Artificial Neural Network (ANN) was used in GERDA to discriminate between SSE and MSE events, and a signal risetime cutoff was applied to distinguish surface events. A novel technique is under investigation for LEGEND-200 Coax

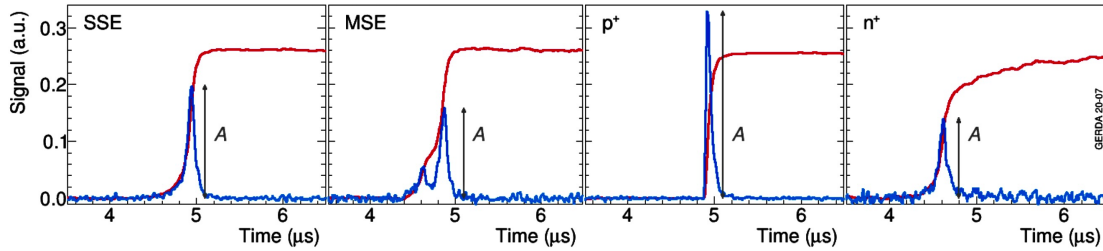


Figure 2.5: Illustrations of various normalized charge pulses (in red) and their associated derived current pulses (in blue): a single-site event (SSE), a multi-site event (MSE), an event occurring in close proximity to the p^+ contact, and an event occurring near the n^+ contact. Adapted from [86].

detectors to improve the PSD performance. In case of BEGe, PPC, and ICPC detectors, to distinguish between MSE and surface events, the A/E parameter is employed, where A represents the maximum current amplitude, and E stands for energy. MSE and surface events on the n^+ electrode feature a lower A/E value compared to SSE since they are characterized by wider current pulses. On the contrary, surface events at the very thin p^+ electrode show a higher A/E value (attributed to the strong electric field). The Figure 2.5 illustrates normalized sample pulses, highlighting four different scenarios: a SSE, a MSE, an event occurring in close proximity to the p^+ contact, and an event near the dead layer of the n^+ contact with incomplete charge collection.

^{228}Th calibration spectrum is used to understand and validate the discrimination power of SSE from MSE events: the Double Escape Peak (DEP) of the ^{208}Tl line (2614.5 keV), that shows up at 1592.5 keV, is mostly populated by SSE, like the $0\nu\beta\beta$ decays; on the other hand, Full Energy Peak (FEP), Single Escape Peak (SEP) and Compton continua events are mostly MSE. To remove MSE and events due to β decays on the n^+ electrode, a cutoff is chosen requiring the survival fraction of DEP events to be 90%, then the survival fractions of the FEP, SEP and Compton events are studied. To reject surface events occurring close to the p^+ electrode, a high side A/E cut is employed.

Detector anti-coincidence

Since the $\beta\beta$ signal is an SSE in one detector, all events in which some energy is simultaneously deposited in more than one detector are tagged and rejected as background. In the offline analysis of a physical event, a trigger algorithm is applied over each germanium trace from all detectors to determine the event multiplicity by checking the presence of other signals above the threshold.

2.2.5 Data processing

Pulses recorded with the FADC system are fully analyzed off-line and contain all information that can be extracted from the traces. The digital signal processing is performed within a dedicated python-based software⁹ developed by the LEGEND collaboration. The output data of the various stages of data processing are organized into a multi-tier structure based on five levels:

- DAQ data are binary data as output by the DAQ systems;

⁹<https://github.com/legend-exp/pygama/>

- Raw data are DAQ data converted into Igdo¹⁰ format, which contain same information as DAQ (e.g. traces, timestamp) but different encoding and layout optimized for analysis software;
- DSP (Digital Signal Processed) data contain parameters extracted by the analysis of each trace, such as information on baselines (e.g. mean value and standard deviation), trigger position of signals, event energy evaluated with different approaches. Different routines are employed for HPGe, SiPM and PMT detectors;
- HIT (High level Tier) data contain calibrated energy parameters, application of the quality cuts and extraction of other analysis parameters;
- EVT (EVENt level) data contain HIT data joined across subsystems and built into coincidence event structures, including high level flags (e.g PSD, muon veto, LAr veto) and other apparatus-wide event-level information.

2.3 LEGEND-200 status

The stand-alone commissioning of the LEGEND-200 LAr instrumentation has been successfully finalized in April 2022 (in Chapter 3 performance results will be shown). In May 2022 the first four strings of HPGe detectors (~ 60 kg) have been installed along with the full LAr instrumentation, marking the first LEGEND-200 integrated commissioning phase. In October 2022 started the assembly of ten strings of HPGe detectors (~ 140 kg), that has been successfully completed in Dec 2022. Various hardware activities have been carried out for electronic enhancements, HV filters and noise optimization. The commissioning activities involved also DAQ, calibration and trigger optimizations. Extensive HV scans and measurements with calibration sources have been performed to optimize the detectors performance. The beginning of the first physics runs officially took place in March 2023.

The current configuration of the LEGEND-200 setup comprises 101 HPGe detectors organized into 10 strings, all enclosed within the LAr instrumentation, as shown in the images of Figure 2.6. The arrangement of LEGEND-200 HPGe detectors in strings is detailed in the map provided in Appendix B. Out of the total 142 kg of HPGe detectors, about 120 kg are suitable for analysis. This configuration allows for an approximate weekly exposure of 2 kg·yr, with the aim of reaching about 100 kg·yr before the next maintenance operations and additional detector deployment scheduled for fall 2024.

2.3.1 Performance

The HPGe detector performances have been assessed using the first LEGEND-200 data release, collected from March to May 2023. The dataset corresponds to an exposure of 10.1 kg·yr and includes BEGe (2.1 kg·yr) and ICPC (8 kg·yr) detectors for which the PSD has been validated.

The energy resolution of HPGe detectors at $Q_{\beta\beta}$ is extracted from calibration spectra for each detector, then compared with the average resolutions of the γ -lines from ⁴⁰K (at 1461 keV) and ⁴⁰K (at 1525 keV) in physics spectrum. Figure 2.7 illustrates the calculated resolution for each detector type, computed as a weighted average across the HPGe

¹⁰<https://github.com/legend-exp/legend-pydataobj>

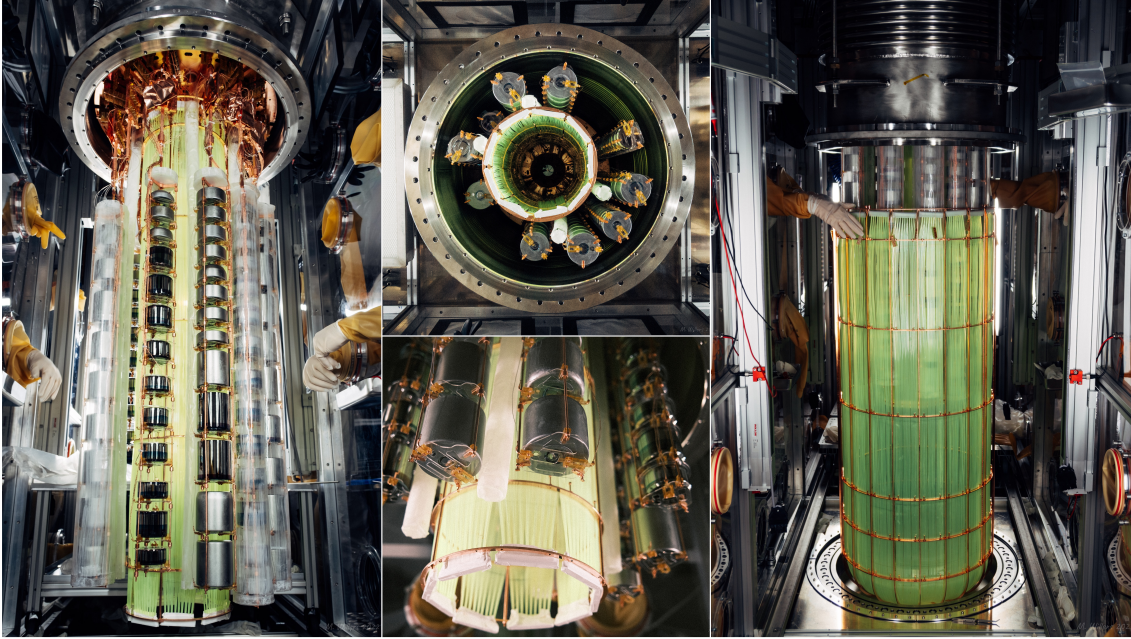


Figure 2.6: The current LEGEND-200 setup at LNGS: the first image provides a view of the inner WLS fiber shroud, with five out of the ten HPGe detector strings visible; notably, the two of these, centrally positioned, are without NMS, while the remaining three, positioned externally, are within the NMS; the central images offer a bottom view of all ten detector strings, and provide a closer look at the PEN plates used as detector supports; the four thin white funnels for the calibration sources insertion are also visible; the right picture showcases the insertion process of the inner shroud and the HPGe detectors string within the outer WLS fiber shroud. Credit to M. Willers.

detectors. The results are presented alongside resolution curves, showcasing the FWHM acquired at calibration peaks, as well as the FWHM observed in the physics data for the ^{42}K line (1525 keV) and at $Q_{\beta\beta}$. The resolution achieved with the HPGe detectors in LEGEND-200 surpasses that obtained in both GERDA and MAJORANA experiments. In Figure 2.8 the FWHM of each detector type as function of detector mass is shown.

The energy spectrum obtained from 10.1 kg·yr of exposure reveals no unexpected background components. Figure 2.9 shows a preliminary background decomposition before quality cuts, as determined by fitting a mixture of PDFs¹¹ to the BEGe (top panel) and ICPC (bottom panel) detectors data with the Bayesian Analysis Toolkit (BAT) [89] between 565 keV and 3 MeV.

The performance of the LAr veto application on physics data will be shown in Section 4.4, and the achieved BI after LAr veto and PSD will be presented in Section 4.5.

¹¹Probability Density Functions.

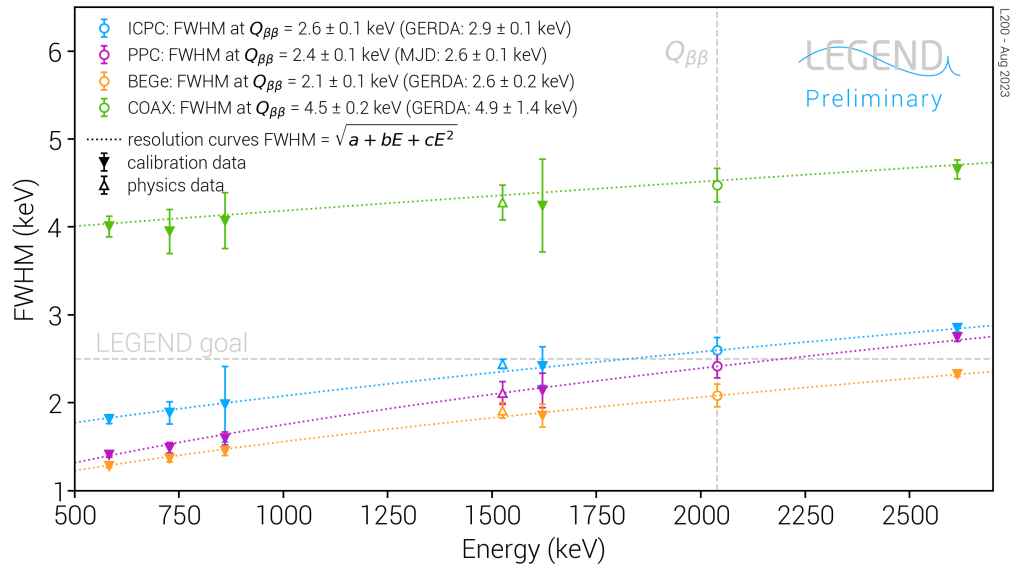


Figure 2.7: Resolution per detector type together with resolution curves. The FWHM is obtained for calibration peaks and for ^{42}K line (1525 keV) and $Q_{\beta\beta}$ from physics data. The comparison with the HPGe detector resolution obtained in previous GERDA and MAJORANA experiments is indicated in the legend. Plot from [87].

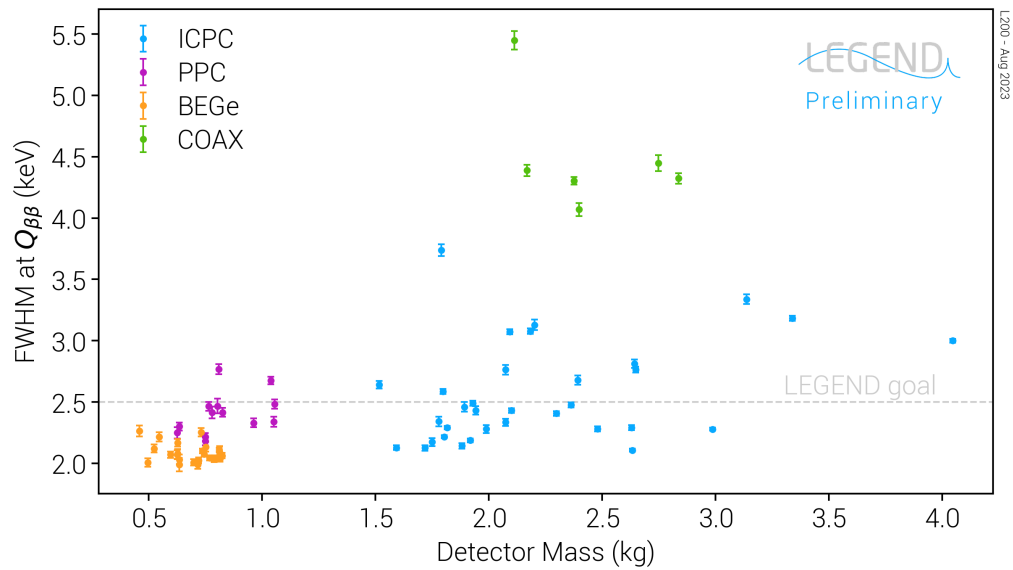


Figure 2.8: FWHM at $Q_{\beta\beta}$ as function of the HPGe detector mass. Plot from [87].

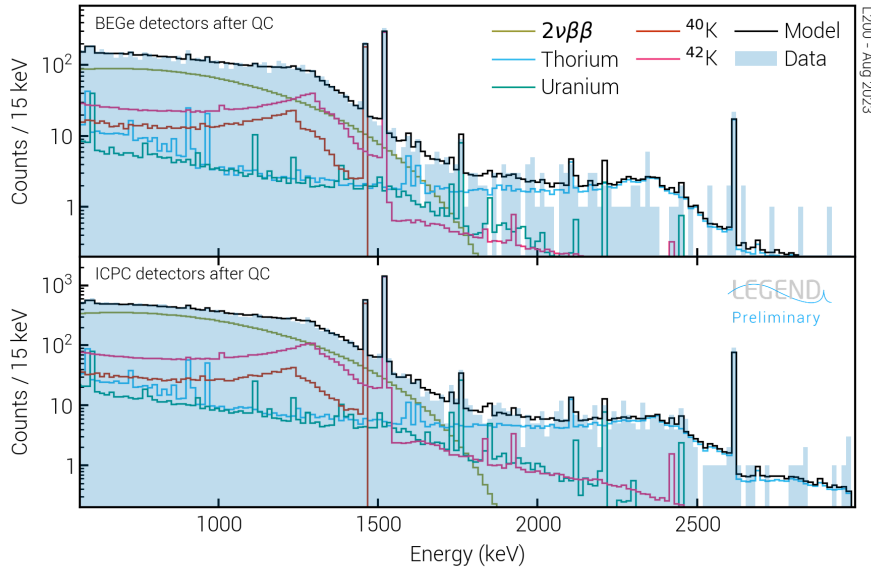


Figure 2.9: LEGEND-200 preliminary background decomposition spectrum before analysis cuts, for BEGe (top panel) and ICPC (bottom panel) detectors. Plot from [88].

2.4 Towards LEGEND-1000 experiment

The LEGEND-1000 technical design is currently prepared for an experimental site at LNGS and SNOLAB¹². The space that can be allocated to the detector dictates the design, while the site depth determines the cosmic ray rate and, therefore, the overall background index. As of the current writing, LNGS stands as the baseline choice to host LEGEND-1000. This section will provide an overview of the current design of LEGEND-1000, more details can be found in [53].

The technical design is centered around the demonstrated low background and excellent energy performance of p-type point-contact HPGe semiconductor detectors, enriched in ⁷⁶Ge more than 90% and operated bare in LAr. The innovative ICPC detector geometry has been developed to boost the experimental sensitivity and maximize synergy with the LAr scintillation light detection. Combined with the LEGEND-200 ICPC detectors, approximately 340 individual ICPC detectors with an average mass of 3 kg will be instrumented for a total detector mass of 1000 kg. The planned enrichment level in ⁷⁶Ge is 92%.

Figure 2.10 illustrates one of the baseline design proposal for LEGEND-1000 experiment. This configuration comprises about 48 single detector strings, each surrounded by a WLS fiber shroud coupled to SiPMs, for detection of LAr scintillation light. Each string is equipped with its own flange, facilitating access and retrieval through a single, movable lock pipe. This design enables a highly modular operation of LEGEND-1000. This will allow to operate LEGEND-1000 in a staged approach, whereby a first batch of HPGe detectors will be deployed and will collect data as subsequent batches are still in production.

The HPGe detector strings are immersed in about 15 m³ radiopure UnderGround-sourced Liquid Argon (UGLAr), reduced in the concentration of ⁴²Ar isotope. The UGLAr is enclosed within an electroformed copper cryostat, namely re-entrant tube, lined with WLSR material to increase LAr detection efficiency. The re-entrant tube is surrounded

¹²Sudbury Neutrino Observatory Laboratory.

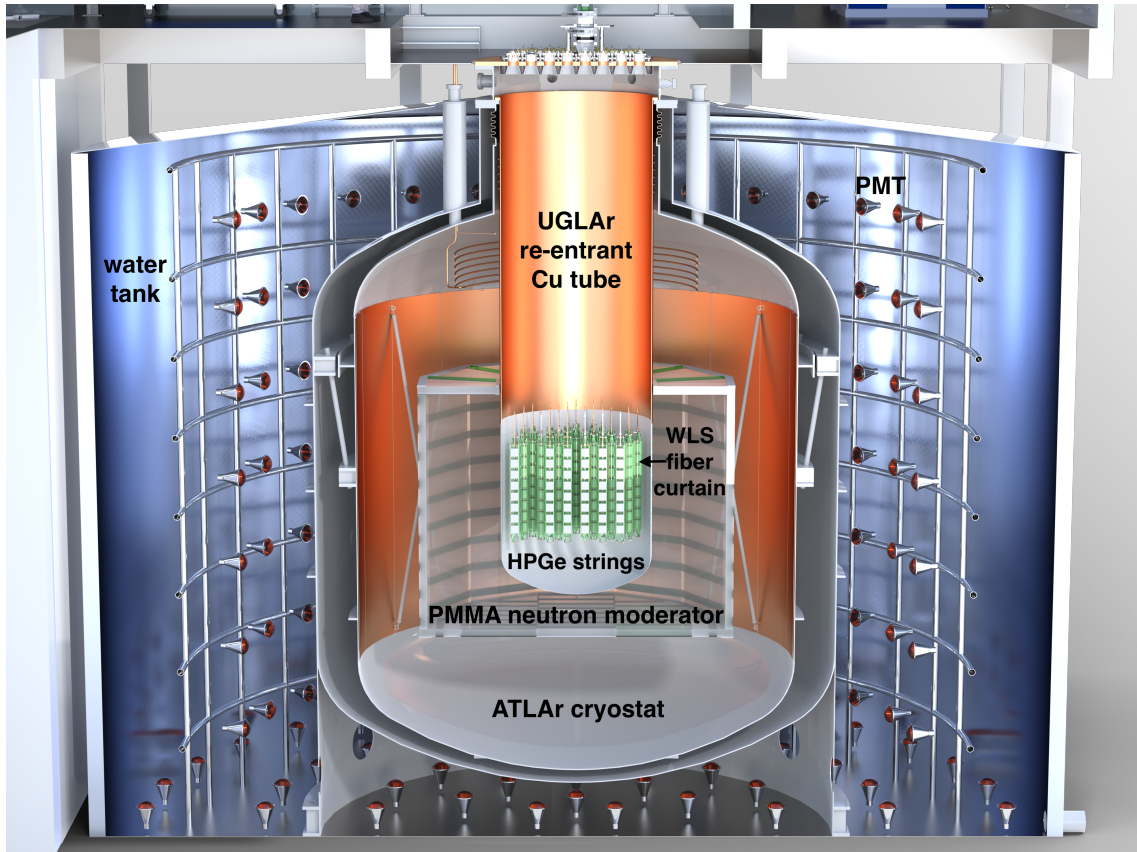


Figure 2.10: Artistic representation of LEGEND-1000 conceptual design. Main components are labeled. Reference design accommodates siting in LNGS Hall C or the SNOLAB Crypt. Credit to P. Krause.

by about 125 m^3 LAr produced from ATmospheric Liquid Argon (ATLAr), contained within a vacuum-insulated cryostat. It is planned that the LAr volumes are instrumented with a neutron moderator. In the current design the neutron absorber consists of twelve 3 m high, 1 m wide, and 10 cm thick Poly-Methyl MethAcrylate (PMMA) panels. Each panel includes WLS material coupled to SiPMs. These panels moderate passively muon-induced neutrons [90] and actively readout scintillation light produced by interactions in the ATLAr volume and the moderator panels.

The external volume of the LEGEND-1000 design consists of a 865 m^3 water tank instrumented with PMTs for additional γ and muon screening through the Cherenkov light detection. On top of the water tank, the clean-room will be situated, accommodating the movable single-string lock, the string assembly glove-box, and the racks for the DAQ systems.

CHAPTER 3

LEGEND-200 LAr Instrumentation

In LEGEND-200, the HPGe detectors are deployed bare in LAr. This noble liquid proves to be a highly effective scintillator, exhibiting scintillation when ionizing radiation interacts with it. By combining the detection of this scintillation light with signals from HPGe detectors, a robust method is established to distinguish background events, which may involve multiple interactions, from potential signals originating from double-beta decays. The LAr instrumentation was designed to capture the scintillation light within the LAr volume surrounding HPGe detectors. The system is built on its precursor operated in the completed GERDA experiment. Thanks to its efficient background recognition capabilities, it was pivotal to search for $0\nu\beta\beta$ decay of ^{76}Ge quasi-free of background events. An improved version of the LAr instrumentation has been developed and is currently operational in the LEGEND-200 experiment. It aims to enhance background rejection through an improved geometrical fiber coverage, an increase of the photoelectron (PE) yield together with an improved LAr quality to maximize light collection, and improved front-end electronics to discard background events at the single PE level.

In this chapter, a comprehensive overview of the LAr instrumentation is presented. Section 3.1 provides a summary of argon isotopic composition, focusing in particular on two Ar isotopes of interest. Section 3.2 describes the LAr scintillation mechanism, offering an overview of the processes that can contribute to the degradation of LAr scintillation light yield. In Section 3.3, the purification process employed during the filling of the LEGEND-200 cryostat is summarized. Section 3.4 illustrates the LAr instrumentation configuration and provides a description of its integration into the LEGEND-200 setup. Section 3.5 offers details on the front-end electronics of the LEGEND-200 LAr instrumentation; main components and integration within the LEGEND-200 setup will be described. In Section 3.6 the pulse shapes generated by the LAr instrumentation are presented. The study of LAr scintillation profile is described in Section 3.7. Pulse coincidence rates of the LAr instrumentation are described in Section 3.8. Finally, Section 3.9 presents the current status of the LAr instrumentation within the LEGEND-200 data taking.

3.1 Argon isotopic composition

Argon, with an atomic number $Z = 18$, is the third most abundant gas in the atmosphere, after nitrogen and oxygen. It can be easily purified and has a relatively high stopping power for ionizing radiation, making it suitable as a detection and/or shielding medium.

Isotope	Production process	Abundance (Bq/kg)	$T_{1/2}$ (yr)	Q_{β} (keV)
^{39}Ar	$^{40}\text{Ar}(n, 2n)^{39}\text{Ar}$ [93]	1.00 [94, 95, 96]	268 (8) [97]	565 (5) [97]
^{42}Ar	$^{40}\text{Ar}(\alpha, 2p)^{42}\text{Ar}$ [98]	40.4×10^{-6} [99]	32.9 (11) [100]	599 (6) [100]

Table 3.1: Properties of the primary radioactive isotopes of Ar relevant to the LEGEND-200 experiment.

Commercial argon is typically obtained through the separation of atmospheric air. There are three known stable isotopes of argon, ^{36}Ar , ^{38}Ar and ^{40}Ar as well as various unstable ones [91]. ^{40}Ar is the most abundant isotope of argon, making up about 99.6% of naturally occurring argon. The production of argon from air is cost efficient¹ and feasible on large industrial scales, but atmospheric argon is exposed to cosmic radiation, producing the radioactive isotopes such as ^{39}Ar and ^{42}Ar [92]. Their key characteristics are outlined below and summarized in Table 3.1.

^{39}Ar isotope

In the Earth atmosphere, ^{39}Ar is mainly produced by the $^{40}\text{Ar}(n,2n)^{39}\text{Ar}$ reaction, involving cosmogenic neutrons [93]. In the subsurface environment, it is also produced through neutron capture by ^{39}K through $^{39}\text{K}(n,p)^{39}\text{Ar}$ process [101] or α emission by ^{42}Ca , $^{42}\text{Ca}(n,\alpha)^{39}\text{Ar}$ [102]. The content of ^{39}Ar in natural argon is measured to be of 1.00 Bq/kg [94, 95, 96]. The β emitter ^{39}Ar (Figure 3.1 Left) is characterized by a half-life of 268 years and a β -endpoint energy of 565 keV [97]. By itself, ^{39}Ar is not of big concern for the $0\nu\beta\beta$ decay search in LEGEND-200, because its Q-value is below the Q-value of ^{76}Ge (2039 keV) and thus its decays do not fall within the region of interest for the experiment. However, ^{39}Ar constitutes the dominant background source for the LAr instrumentation of LEGEND-200 experiment, resulting in an expected rate of about 6 kBq of ^{39}Ar decays for 6 t of LAr inside the WLSR volume (Section 2.2.1). One challenge in background identification using LAr scintillation light is to discriminate uncorrelated (random) coincidences from ^{39}Ar β particles from real coincidences of background-like events.

^{42}Ar isotope

^{42}Ar originates predominantly in the atmosphere through the cosmogenic activation of ^{40}Ar . The dominant mechanism involves the interaction of energetic α particles with ^{40}Ar , resulting in the reaction $^{40}\text{Ar}(\alpha, 2p)^{42}\text{Ar}$ [98]. This reaction mainly occurs in the upper atmosphere, where cosmic-ray interactions generate a substantial flux of energetic α particles. An alternative pathway for ^{42}Ar production involves a two-step neutron capture process on ^{40}Ar : $^{40}\text{Ar} + n \rightarrow ^{41}\text{Ar} + n \rightarrow ^{42}\text{Ar}$ [92]. Nevertheless, this process is subdominant due to the short half-life of the intermediate ^{41}Ar (109 min). Significant production requires an exceptionally high neutron flux, such as that generated in nuclear tests and explosions [103]. The ^{42}Ar abundance from naturally occurring neutrons corresponds to about 100 $\mu\text{Bq/kg}$, taking into account the relative abundance of $^{42}\text{Ar}/^{40}\text{Ar} \sim 10^{-20}$ [98]. However, experimental measurements have reported a lower abundance, with the most recent result from the DEAP-3600 collaboration indicating 40.4 $\mu\text{Bq/kg}$ [99]. Other measurements are reported in Section 5.1. ^{42}Ar with its half-life of 32.9 years and β -endpoint of 599 keV [100], is not of big concern to LEGEND-200 experiment because of its low

¹The procurement cost of LAr is roughly 1 €/kg.

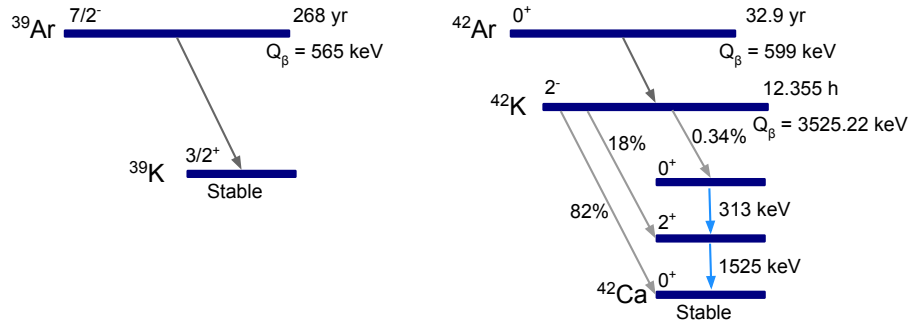


Figure 3.1: Left: decay scheme of ^{39}Ar . Right: decay scheme of $^{42}\text{Ar}/^{42}\text{K}$.

Q-value. However, ^{42}Ar decays via β decay to ^{42}K which further decays to ^{42}Ca via β decay (Figure 3.1 Right) with an endpoint of 3525.45 keV and a half-life of 12.355 h [100]. As the energy spectrum of electrons from a β decay is continuous, the ^{42}K constitutes a critical background for LEGEND-200 experiment. This leads the collaboration to an extensive ^{42}K background measurement and mitigation campaign. Further details will be discussed in Chapter 5, where a newly developed analysis will be presented to estimate the ^{42}Ar specific activity based on ^{42}K activity using the LAr instrumentation of LEGEND-200.

To reduce the backgrounds from ^{39}Ar and ^{42}Ar decays, the argon can be extracted from deep underground [104, 105]. The DarkSide-50 collaboration has demonstrated that the underground argon they used as their dark matter target has an ^{39}Ar rate of 7.3×10^{-4} Bq/kg [106], a factor ~ 1400 below atmospheric levels. An analogous reduced rate is expected for the contamination of ^{42}Ar [105].

3.2 Argon scintillation mechanism

Like other noble gases, Ar scintillates when exposed to ionizing radiation [107, 108, 109]. Typical particles inducing scintillation in argon are α and β particles as well as γ rays and neutrons. Also muons, fission fragments or heavy ions deposit energy in argon.

The passage of ionizing radiation through argon ionizes (Ar^+) and excites (Ar^*) argon atoms, as shown in Figure 3.2. The ratio of excitation to ionization depends strongly on the temperature and density of argon, as well as on the nature of the incident particle. For gaseous argon excitation is the dominant process, while for liquid argon ionization predominates [110].

These ionized or excited atoms form strong bonds with neutral argon atoms, resulting in ionized dimers Ar_2^+ or excited dimers Ar_2^* (so-called excimers). Due to momentum conservation the formation of ionized argon dimer occurs in three body processes referred to as self-trapping:



Ionized dimers recombine with a free electron, producing a highly excited argon atom (Ar^{**}), which then undergoes a non-radiative transition to the lowest excited argon atom (Ar^*).

The excited dimer Ar_2^* is formed through self-trapping of the Ar^* :



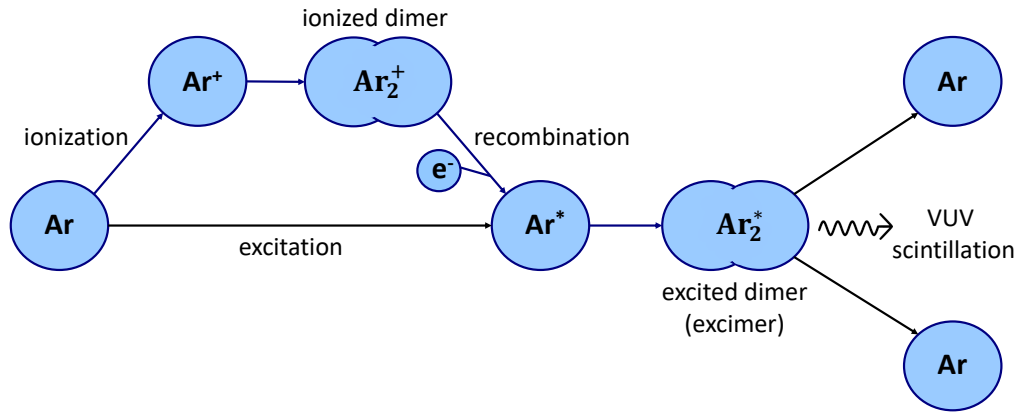


Figure 3.2: Argon scintillation mechanism via two different excimer formation processes and subsequent decay in two neutral argon atoms and emission of VUV scintillation light.

The formed Ar_2^* state is a Rydberg state, meaning it consists of an Ar_2^+ core with a bound electron and occurs in two different configurations, depending on the alignment of the spins of the electron and the core. The two configurations are the so-called singlet and triplet states². The decay of these two states into the repulsive ground state is the primary source of argon Vacuum-UltraViolet (VUV) scintillation light.

Due to overlapping rotational energy levels, the emission peaks of the singlet and triplet excimer decay are not resolved and only one broad peak with about 10 nm FWHM is observed at 126.8 nm [108]. The decay of the singlet state is allowed, while the decay of the triplet state is forbidden due to conservation of angular momentum. This is manifested in the characteristic lifetimes of the decay [111]:

- the decay of the singlet state with $\tau_s = (6 \pm 2)$ ns called the fast component;
- the decay of the triplet state with $\tau_t = (1590 \pm 100)$ ns called the slow component.

While the lifetimes of the excimers are independent of the exciting radiation, the population ratio R of excimer in singlet N_s and triplet N_t states ($R = N_s/N_t$) depends on the linear energy transfer (LET) dE/dx of the incident radiation, allowing particle identification through the pulse shape discrimination. The more energy is dissipated per unit track length, the more excimers are produced in the singlet state and the larger R becomes. R has been measured to be 0.3, 1.3, and 3.0 for photons, alpha particles, and fission fragments, respectively [111].

Effect of impurities on triplet lifetime

In ultra-pure liquid argon, the combined scintillation light yield (LY) of both components is 40 photons per keV of energy deposition [85]. However, various processes that reduce photon emission can occur in liquid argon, leading to a degradation of the scintillation LY. These processes include biexcitonic quenching, electron escape, charge carrier trapping, alpha quenching, and transfer of electronic energy to impurity atoms [85, 112].

Among these processes, electronic energy transfer to impurity atoms, such as nitrogen, water, or oxygen, has a noteworthy impact. This transfer predominantly depopulates

²The lowest excited states are obtained by lifting an electron from the 3p shell up to the 4s shell, where its spin can be parallel or anti-parallel to the resulting spin of the rest of the atom. In the case of anti-parallel spins, the atom is in a singlet state, while in the case of parallel spins, a triplet state arises.

the triplet state through collisional excitation energy transfers to impurity atoms. Subsequently, these impurity atoms relax via non-radiative pathways, leading to both scintillation light quenching and a reduction in the triplet lifetime. The relationship between triplet lifetime and nitrogen/oxygen contamination has been investigated and documented in previous research [113, 114]. From the findings presented in these studies, it can be inferred that the triplet lifetime serves as a reliable indicator of impurity concentration within LAr, regardless of the incident radiation conditions.

3.3 LEGEND-200 LAr purification

For the LEGEND-200 experiment, LAr with a purity of 5.0³ was acquired from Linde, the vendor contracted by LNGS. To optimize the performance of the LAr instrumentation, it was decided to purify the argon obtained from the vendor during the cryostat filling process. The goal for achieving the highest efficiency of the LAr instrumentation in LEGEND-200 was set with a purity requirement of $\tau_t \geq 1.2 \mu\text{s}$. It is expected that maintaining an impurity concentration below 0.1 ppm will be enough to meet this goal [113, 114].

The purification procedure took place during the filling of the LEGEND-200 cryostat in the summer 2021. Throughout this period, continuous monitoring of the purification system was essential. To ensure vigilant observation, a schedule of three shifts per day, each staffed by two individuals, has been established. These shifts have been set up and distributed among LEGEND members of different institutions, primarily from Jagiellonian University (Krakow), Roma Tre University, Technical University of Munich (TUM) and LNGS.

Purification system

LEGEND Liquid Argon purification System (LLArS) has been designed and tested by Jagiellonian and TUM groups. The system has been integrated with the argon filling line and placed between the LAr storage tank and the cryostat, as shown in Figure 3.3. The argon is processed by two units, each consist of two traps placed in vacuum insulation and equipped with heaters and temperature sensors. The LLArS goal is to remove O₂, H₂O and N₂ impurities from LAr. The comprehensive setup and operational specifics of LLArS can be found in [115, 116]. A brief summary is provided below, while the LLArS scheme is presented in Appendix C.

The oxygen removal module employs two traps, each containing 5 kg of copper catalyst⁴. In this process, oxygen is extracted from the LAr stream through a chemical reaction with copper: $\text{O}_2 + 2\text{Cu} \rightarrow 2\text{CuO}$. To facilitate this reaction, the catalyst must be activated, meaning it needs to be reduced to copper. This reduction is accomplished by flushing the cartridge with hydrogen gas: $\text{CuO} + \text{H}_2 \rightarrow \text{H}_2\text{O} + \text{Cu}$. This reaction is endothermic, whereas the oxidation shown before is exothermic, thus heat is applied during activation.

The water and nitrogen removal module utilizes two traps, each filled with 4 kg of 4 Å molecular sieve. These molecular sieves, highly porous synthetic materials derived from various chemical substances, possess pores similar in size to typical atomic and molecular dimensions. As they do not form a chemical bond with copper, the elimination of water and

³LAr 5.0 corresponds to 99.999% purity.

⁴A catalyst is a substance that speeds up chemical reactions by providing an alternative pathway with lower activation energy, participating in the reaction without being consumed.



Figure 3.3: LLArS situated underground at LNGS, in close proximity to the LAr cryogenic storage tank, from where the LEGEND-200 cryostat is filled. The first two pictures show the front and back side of the purification system, while the last picture shows the station of the scintillation analyzer.

nitrogen impurities from LAr relies on physical adsorption. In this process, the impurities attach to the surface of the molecular sieve through Van-der-Waals forces, a phenomenon distinct from absorption. Unlike absorption, where attachment occurs not only on the surface but also involves the diffusion of foreign molecules into the bulk of the material, adsorption specifically involves surface attachment.

Results of purification process

The purity of the LAr during the filling of the LEGEND-200 cryostat has been continuously monitored in real-time using two devices that measured the argon triplet lifetime. During the initial filling phase the argon triplet lifetime measurement has been performed with a dedicated scintillation analyzer: the LAr sample has been analyzed by two TPB⁵-coated PMTs arranged face-to-face and placed inside a 70 l dewar, registering the scintillation light and determining the triplet lifetime with a dedicated python-based software (Figure 3.3 Right). Simultaneous direct measurements of the concentrations of impurities (O₂, H₂O and N₂) with a sensitivity of 0.1 ppm have been realized with an impurity gas analyzer. Once the LAr level inside the LEGEND-200 cryostat reached the LLAMA system, it was possible to monitor the LAr quality directly inside the cryostat.

In total LLArS processed about 130 t of LAr in order to fill the 90 t LEGEND-200 cryostat (about 20 t of LAr were needed to cool down the cryostat). The results of the impurities concentration before and after the purification are summarized in Table 3.2.

The LAr purification system will also be used later to purify the LAr filled into the cryostat in the loop mode. A dedicated cryogenic pump has been installed at the bottom of the LEGEND-200 cryostat to circulate LAr between the purification system and the cryostat.

⁵Tetraphenyl butadiene (TPB).

Sample	O ₂ [ppm]	N ₂ [ppm]	H ₂ O [ppm]	τ_3 [μ s]
Unpurified LAr	0.3 - 0.7	0.3 - 0.5	0.3 - 0.9	~ 0.85
Purified LAr	< 0.1	< 0.1	< 0.1	~ 1.15

Table 3.2: Impurities concentration before and after the LAr purification process [117].

3.4 LAr instrumentation

The LAr instrumentation is a detector system designed to detect the LAr scintillation light near the HPGe detector array. The LAr scintillation light is created by energy deposition by ionizing radiation, arising from e.g. muons, radioactive isotopes in argon (e.g. ³⁹Ar and ⁴²Ar), cosmogenically produced radioactive isotopes in germanium detectors and radio-impurities in solids near detectors. Detecting this scintillation light in coincidence with germanium detector signals allows to discriminate between $0\nu\beta\beta$ decay signal events and background events.

The LEGEND-200 LAr instrumentation builds on the successful approach of the previous GERDA LAr system [118], which effectively minimized background levels. Several improvements have been implemented to enhance the collection of LAr scintillation light, including the integration of a wavelength-shifting reflector and an improved LAr instrumentation geometry: a design of two concentric optical fiber shrouds has been adopted instead of one used in GERDA [119]. Simultaneously, the system design minimizes the contribution to the total background budget.

Figure 3.4 illustrates a schematic view (horizontal cross-section) of the LAr instrumentation alongside the HPGe detectors. The instrumentation can be divided into two primary components: two concentric arrays of optical fibers (referred to as the inner and outer fiber shroud or Inner and Outer Barrel (IB and OB)) connected to Silicon PhotoMultipliers (SiPMs), and a WaveLength Shifting Reflector (WLSR) encompassing the fiber curtains. The WLSR reflects and shifts the VUV scintillation photons towards the optical fibers, where they undergo additional wavelength shifting and are subsequently detected by SiPMs.

Wavelength shifting reflector

The WLSR [68] is designed to fulfill two primary objectives. Firstly, it captures scintillation light that escapes initial detection by diffusely reflecting and spectrally shifting it, increasing the chance of detection by the optical fibers. The WLSR, coated internally with TPB shifts the VUV scintillation light towards the blue spectrum, extending thus the light attenuation length to several meters. Secondly, the WLSR shields the LAr instrumentation from scintillation light outside its boundaries, reducing random coincidences with HPGe detectors caused e.g. by ³⁹Ar β decays or other radioactive emissions from the cryostat walls. An upper limit on the efficiency of the WLSR in terms of absorbing, shifting, re-emitting and reflecting VUV photons was derived from a dedicated measurement during commissioning of the LAr instrumentation. This was found to be of $(64 \pm 1)\%$ [120].

3.4.1 WLS fiber shroud and SiPMs

To optimize the effective coverage of WLS fibers surrounding the circular arrangement of HPGe detector strings, a system incorporating two concentric cylindrical fiber shrouds is employed. These fiber shrouds are depicted in Figure 3.5. The IB, with a diameter

of 270 mm and a length of 1400 mm, allows the assembly of 9 fiber modules. The OB, measuring 580 mm in diameter and 1500 mm in height (with a fiber length of 1800 mm), accommodates 20 fiber modules. To ensure optical coverage beneath the HPGe detector strings, the OB modules are curved inward at the bottom. Each fiber module is equipped with a SiPM array at both ends, resulting in a total of 18 readout channels for the IB and 40 for the OB, summing up to 58 readout channels in total.

SiPM array

The SiPM array comprises nine Ketek PM33100T SiPMs, each measuring $3 \times 3 \text{ mm}^2$. Individual array corresponds to a single readout channel, significantly reducing the number of required readout cables, a critical factor in the background budget. The SiPMs are housed in pockets within a fused silica (artificial quartz) holder, known for its intrinsic radio purity. Two aluminum layers are sputtered onto this holder, serving as electrical traces. Six $\sim 15 \text{ }\mu\text{m}$ thin gold wires establish the electrical connection between the SiPMs and the aluminum traces. Two AXON pico-coaxial cables are connected to each array, one to the cathode and one to the anode, as shown in Figure 3.6. During data acquisition, the two signals are subtracted from each other, effectively eliminating the noise that equally couples into both differential lines, thereby isolating the SiPM signal.

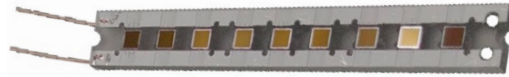


Figure 3.6: SiPM array composed of nine SiPMs in a fused silica holder connected to two AXON pico-coaxial cables for a differential readout.

WLS fiber module

The WLS fibers increase significantly the optically active area of the SiPMs and shift the VUV photons towards the optical range allowing the use of optical SiPMs. They are Saint Gobain fibers (BCF-91A) [121], which feature a core made of WLS polys-tyrene, accompanied by two cladding layers that enhance photon trapping efficiency. These fibers exhibit a square cross-section with a length of 1 mm, facilitating optimal coupling to square-shaped SiPMs. Considering the SiPMs active area of $3 \times 3 \text{ mm}^2$, the desired coverage is achieved by employing nine 1 mm^2 fibers. Since a SiPM array comprises 9 SiPMs, 9 fibers measuring $3 \times 3 \text{ mm}^2$ are organized by an acrylic optical coupling piece at both fiber ends. The collective set of 81 fibers constitutes what is called a *fiber module*.

Light collection

The LAr instrumentation SiPMs, optimized for a spectral response peaking around a wavelength of 440 nm [53, 122], necessitate a wavelength shift because of their insensitivity to VUV light. Thus, the 128 nm VUV photons from LAr scintillation are initially collected on the WLS fiber surface, where they are absorbed and shifted in the blue spectrum with a peak emission at 420 nm [123], thanks to TPB coating (by evaporation, reaching $1 \text{ }\mu\text{m}$ thickness [124]). Subsequently, blue photons enter the WLS fibers where they undergo an additional shift to green spectrum with a peak emission at 494 nm [121]. Guided through a sequence of total internal reflections, the light is directed to the SiPMs, ensuring minimal loss due to attenuation and facilitating the efficient detection of scintillation events. Figure

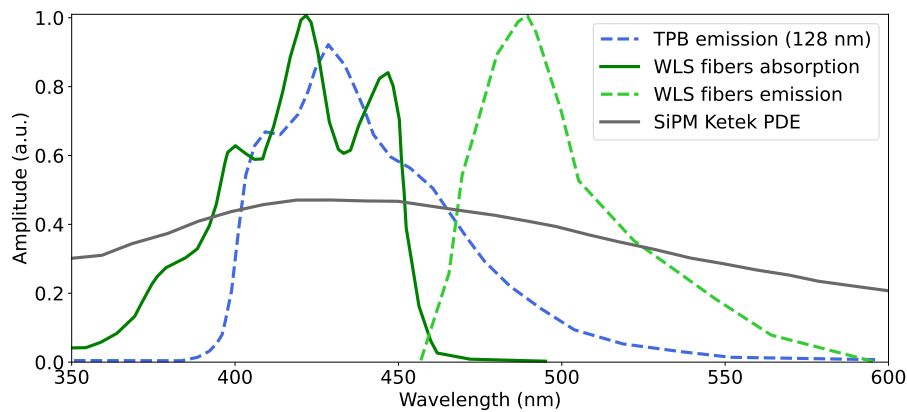


Figure 3.7: Absorption (full lines) and emission (dashed lines) spectra for different components of LAr instrumentation [123, 121]. The PDE of Ketek SiPMs is also illustrated [122].

3.7 provides the emission spectrum of TPB, the absorption and emission spectra of WLS fibers and the Photon Detection Efficiency (PDE) of SiPMs.

It is important to consider that a primary VUV photon travels a certain distance through the LAr to reach the WLS fibers, depending on the production point. Throughout this passage, it may be absorbed in interactions with residual LAr impurities. The attenuation length in LAr is significantly influenced by these impurities (Section 3.2) but generally falls within the range of tens of centimeters at a wavelength of 128 nm [125, 126]. Once it reaches the detection system, the VUV photon undergoes various steps, each contributing to losses before its ultimate detection. The cumulative effect of these steps has been observed in GERDA, yielding an overall scintillation photon detection probability of not more than 0.2% [125]. Consequently, the SiPM arrays mounted on the fiber modules are only able to detect a few single photo-electrons out of every 100 LAr scintillation events. A slightly higher detection probability is expected in LEGEND-200 due to increased LAr purity and greater LAr instrumentation coverage.

3.4.2 LAr instrumentation installation

The assembly of the LAr instrumentation took place in the clean room of the LEGEND-200 experiment. The distinct stages, including the coupling of SiPMs to the fiber modules and the subsequent assembly of the fibers onto the copper frames, are illustrated in Figure 3.8 and detailed below.

Firstly, the copper rings and rods underwent thorough cleaning to ensure effective decontamination. Subsequently, the copper support frames for the inner and outer barrels were assembled. Following this, the fiber modules were prepared: SiPM arrays were optically coupled onto the acrylic coupling piece, and they were secured using four copper pins bent at the back of the coupling piece to apply slight pressure and hold the SiPM arrays in place. In a subsequent step, it was decided to enhance insulation by wrapping the SiPM arrays in PolyTetraFluoroEthylene (PTFE) thin foils.

Given that two SiPM arrays are installed per fiber module (top and bottom), the cables of both arrays are connected to a single plug. The cable length for the top array is 20 cm, while the bottom array has a cable length of 150 cm for IB and 190 cm for OB. To manage the cables effectively, those from the bottom side are guided along the fiber module, passing through dedicated cuts in the copper pieces designed to secure the fiber arrangement.

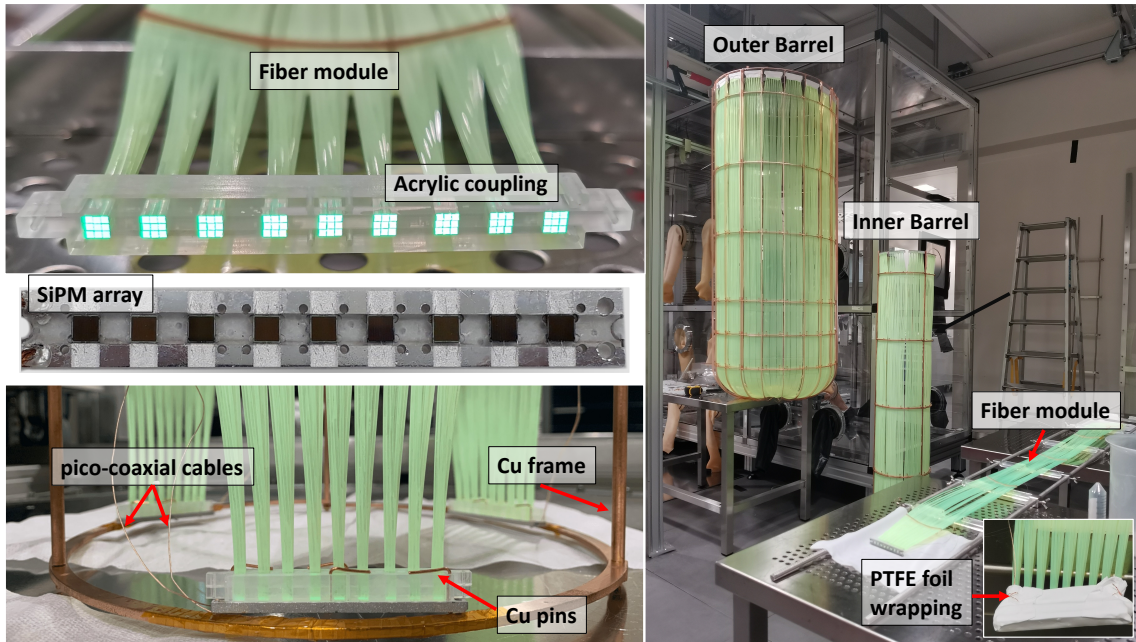


Figure 3.8: Assembly process of the LAr instrumentation: SiPM arrays are mounted on acrylic coupling of fiber modules on both ends and fixed with copper pins; then the fiber modules coupled to SiPM arrays are fixed to the copper frames of inner and outer barrel.

Both before and after mounting a pair of SiPM arrays, the resistances and diode voltage of the top and bottom SiPM arrays were examined at the plug. A properly functioning array typically exhibits a resistance of about $300\text{ k}\Omega$ and about 0.6 V of diode voltage in the forward direction and around $10\text{ M}\Omega$ in the reverse direction. Additionally, the resistances to ground and diode currents were measured. If the checks were successful, the array was deemed suitable for mounting; otherwise, necessary repairs were undertaken.

Afterward, the fiber modules, inclusive of the SiPM arrays, were attached to the copper frames. This process entailed securing the copper pieces on the fiber modules to the rings of the frame through the use of copper screws. Subsequent to the fixation process, an additional set of resistance checks were conducted on the SiPM arrays to verify that no damage had occurred throughout the mounting procedure.

The fiber modules, complete with SiPM arrays, were prepared and secured during the assembly of the inner barrel and outer barrel, incorporating nine and twenty fiber modules, respectively. Subsequently, these setups were installed into the lock system of the LAr cryostat. Following mechanical fixation, the plugs of individual fiber modules were connected to cables running through the top of the lock to an external flange. During this stage, the connections were meticulously verified by measuring resistances and diode voltages once again. Extending from the top flange, 6 m long shielded cables run to the crate housing the SiPM front-end electronics (see Section 3.5).

Following the closure of the lock, it was pumped to a pressure below 0.01 mbar and left to outgas at least 12 hours. The instrumentation then underwent cycles of pumping and flushing with argon to eliminate contaminants, primarily water from atmospheric humidity. After several iterations, the lock was flushed with argon, and once the pressures of the lock and the cryostat had equalized, the shutter to the cryostat was opened, and the setup was gradually lowered.

Upon immersion in LAr, the bias voltages for the SiPM arrays were set based on the breakdown voltages determined in the dedicated measurements (Section 3.4.3). The SiPM

signals traces were checked using an oscilloscope, and online measurements of energy spectra were conducted using the LEGEND-200 DAQ system.

3.4.3 SiPM voltage determination

A dedicated measurement was carried out at the underground laboratory of the TUM in Garching to establish the crucial parameters defining each SiPM array, such as breakdown and bias voltages, dark count rate, crosstalk and afterpulsing probabilities. The identified breakdown voltages spanned from 21 to 24 V and based on these values, the SiPM arrays operational (bias) voltages ranging from 24 to 26 V, i.e. 2-3 V higher than the determined breakdown voltages. The crosstalk probabilities were determined to be below 40%, with afterpulsing probabilities below 30% for the majority of SiPM arrays. The dark count rates were found to be less than 100 Hz, rendering this noise negligible compared to the approximately 6 kHz of ^{39}Ar activity in the WLSR argon volume. Further details on the SiPM characterization can be found in [127].

LNGS in-situ characterization

To determine the optimal bias voltage for the SiPM detectors, further measurements have been carried out underground at LNGS. The goal of these measurements was to identify, through the I-V response curve, a working point considered optimal channel-by-channel. Here optimal means that a uniform gain is achieved across all channels, rather than the maximum gain for each of them separately.

The voltage and current values were set and acquired using a picoammeter⁶ (Keithley 6487), connected at the flange level of the SiPM line and managed by a dedicated software. The setup is shown in Figure 3.9 Left. The I-V curves for each SiPM channel, immersed in LAr, were produced by incrementing the voltage from 0 V to 30 V in 0.25 V steps. To

⁶A picoammeter is a highly sensitive instrument designed to measure extremely low electrical currents, typically in the picoampere (pA) range.

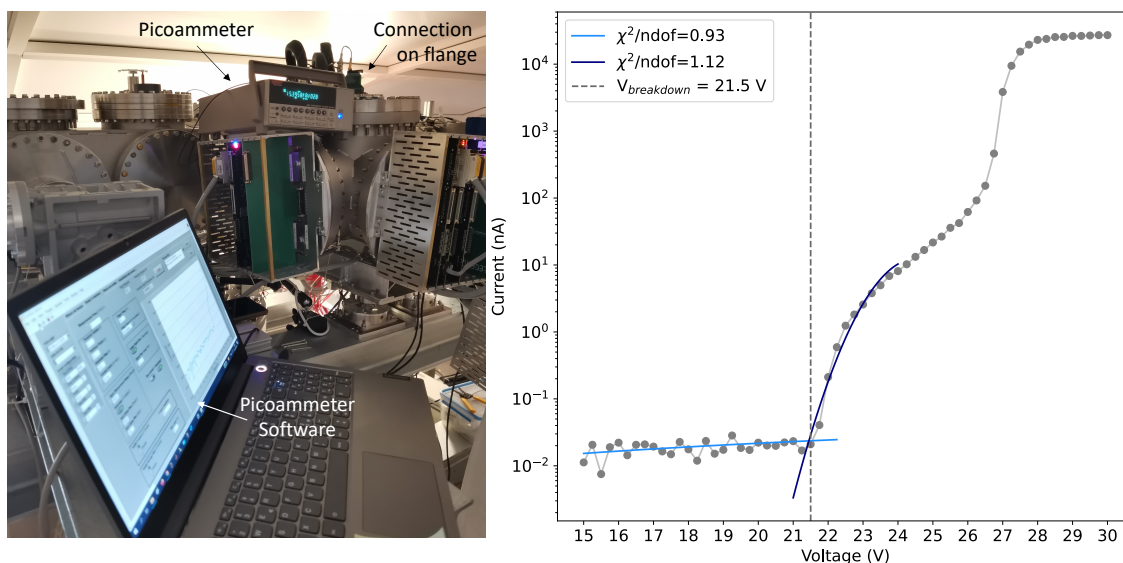


Figure 3.9: Left: setup at LNGS to acquire the I-V curves for each SiPM detectors immersed in LAr. Right: typical I-V curve acquired with the picoammeter. The plot starts from 15 V and the obtained breakdown voltage is highlighted.

ensure SiPM protection without causing damage, a threshold current of $30 \mu\text{A}$ was set, beyond which the SiPMs would enter a protective mode. A Python-based software was developed for the analysis of the obtained SiPMs I-V curves [128].

An example of acquired I-V curve is presented in Figure 3.9 Right. The breakdown voltage was determined by identifying the point at which the SiPM transitions into Geiger mode (see Appendix F), estimated as the intersection between the linear and "parabolic" behavior of the I-V curve. Breakdown voltage values for each SiPM channel were determined and fall within a range of 21-24 V, consistent with those observed in the TUM characterization.

For this analysis the gain is calculated as the ratio between bias and breakdown current, exploring values from 10^2 to 10^4 . Through comprehensive analysis, it was observed that not all SiPM channels reached the established gain. The percentage of SiPM channels achieving the specified gain was determined for four different values, as detailed in Table 3.3.

Gain	100	1000	5000	10 000
N° SiPMs (%)	93.9	91.8	79.6	75.5

Table 3.3: Percentage of SiPM channels capable of attaining a predetermined gain [128].

When the gain values exceed 100, 50% of SiPM channels experience bias voltages that exceed the recommended values established at TUM ($> 26 \text{ V}$). Consequently, the bias voltages associated with a gain of 100 have been compared with the bias values obtained during the characterization. The majority of SiPMs operated optimally with the established bias voltage, similar to the values achieved by fixing the gain at 100. However, for few SiPM channels, it was found advantageous to adopt the in-situ obtained values.

In summary, the SiPM arrays operate with a bias voltages of 2 to 3 V higher with respect to the obtained breakdown voltages. However, before each data-taking session, pulses from all SiPM arrays are scrutinized and bias voltages are adjusted taking into account the performed studies.

3.5 Front-end electronics

The anodes and cathodes of the SiPM arrays are connected to two AXON pico-coaxial cables, one for each electrode. These cables incorporate a grounded shroud, providing shielding against noise and eliminating the need for additional shielding. The adoption of a differential scheme offers a distinct advantage, particularly in its effectiveness at suppressing any noise interference that may be introduced along the entire signal propagation path.

At a distance ranging between 20 and 200 cm, depending on the array location, the coaxial cables are connected to a 10 m long Kapton flat-band cable, which carries the signals out of the cryostat. From the cryostat flanges, 6 m long CAT6 Ethernet cables extend to the Front-End (FE) electronics, where SiPM signals are readout and amplified. The FE boards are strategically positioned outside the cryostat, at room temperature, and at a considerable distance from the SiPM detectors. This placement minimizes the presence of radio-impurities in the liquid argon near the HPGe detectors but represents a significant challenge in maintaining a high signal-to-noise ratio.

Each FE board is equipped with a voltage operational amplifier set at a high-gain value, meticulously optimized to ensure sufficient resolution at a charge equivalent to a single PE above the white noise of the lines. To manage the signals from the 58 SiPM channels, five FE boards were created using the NIM⁷ standard, along with two spares.

3.5.1 FE design

The design of the LEGEND-200 SiPM FE electronics is driven by the necessity to precisely capture the SiPMs response to LAr scintillation light at the single PE level. Equally important is the requirement for seamless integration within the LEGEND-200 data acquisition framework. The developed FE chain consists of two sections, illustrated in Figure 3.10 and summarized below. Detailed characteristics can be found in [129].

Front-end boards

Each FE board is designed to accommodate 12 PCB-mounted circuits and incorporates all the essential components for reading, amplifying and controlling the SiPM detectors. Figure 3.11 provides a schematic view of one FE channel. The board is configured to connect to power supplies following the NIM standard, featuring dedicated linear adjustment sections to create a +5 V at 3 A clean power supply for the analog section and +3.3 V at 1 A for the digital slow-control section. Additionally, a primary voltage of 32 V at 20 mA and a digital communication protocol known as I²C is employed, generated and managed by a controller board.

Ensuring the correct operation of a SiPM array necessitates providing a suitable, stable, and precise diode voltage. To guarantee the detector safety, it is imperative to limit the current, protecting it from potential damage due to high light exposure or mishandling. Consequently, the power supply has been designed to generate an adjustable bias voltage between 15 and 31.5 V in increments of 0.05 V, ensuring optimal functionality and protection of the SiPMs.

The selected amplifier for adapting and amplifying signals is the ADA4930-1YCPZ-R7⁸, offering a total gain of 40. This amplifier falls within the category of very low noise (RMS of 53.8 μ V), low distortion (1.2 nV/ $\sqrt{\text{Hz}}$), and high-speed (3.4 kV/ μ s) differential amplifiers. Moreover a full bandwidth of 117 MHz is achieved, which allows to match in frequency the fast rise time and the slow decay time of SiPMs (see Section 3.6). These characteristics make it also an optimal choice, particularly for driving high-performance 0.9 V ADCs, as requested by LEGEND-200 experiment.

The amplifier output is configured with four parallel differential channels, accessible via RJ45 connectors, aligning with the specifications outlined by the LEGEND-200 DAQ system (FlashCam). This strategic configuration ensures efficient signal processing and compatibility with the experimental setup data acquisition requirements.

Controller Board

The processing core within the controller board is managed by a beaglebone black Microfluidic Processing Unit (MPU)⁹. This MPU efficiently oversees the comprehensive slow

⁷Nuclear Instrument Module.

⁸https://www.analog.com/media/en/technical-documentation/data-sheets/ADA4930-1_4930-2.pdf

⁹<https://www.beagleboard.org/boards/beaglebone-black>

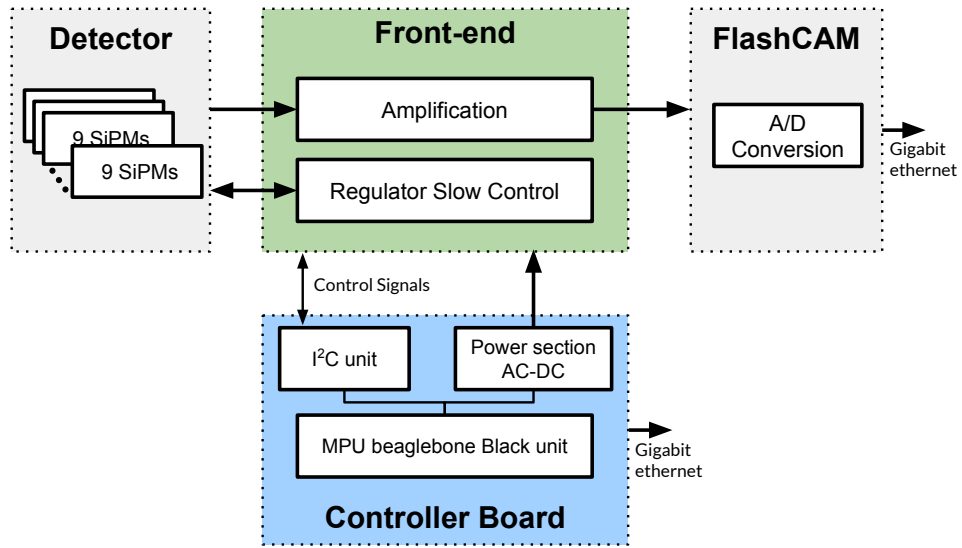


Figure 3.10: Schematics of the full electronic system chain of the LEGEND-200 LAr instrumentation. Credit to I. Abritta Costa.

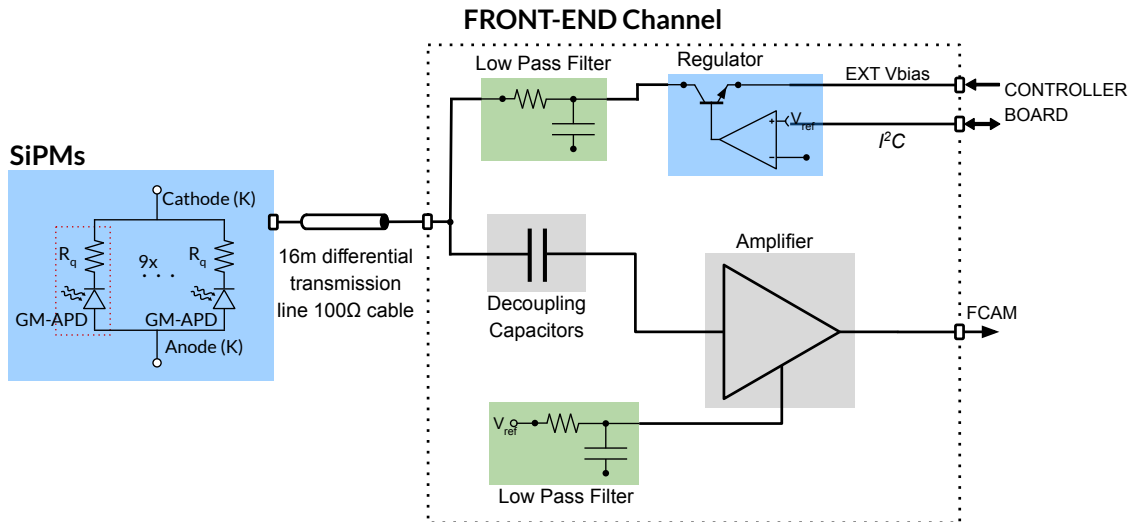


Figure 3.11: Illustrative schematic of one channel of the FE board. Credit to I. Abritta Costa.

control chain for all acquisition SiPM channels, alongside managing the primary voltage generation section. The coordination of FE board control is facilitated by components communicating seamlessly through the bidirectional I²C protocol. The software packages governing I²C communication are developed using Python and the SMBus library¹⁰. This software framework empowers the controller to enable and disable channels, configure individual channel voltage and current limits, and retrieve readings of all relevant parameters, as well as the status of each channel. The use of I²C communication in this manner ensures robust and versatile control over the entire experimental setup.

The controller board is responsible for providing power to ensure the proper functioning of the MPU. Voltage regulation and filtering are achieved through DC +12 V and +6 V power supplies conforming to the NIM standard. The primary voltage is generated by the control board via an AC-DC linear power supply. This board takes charge of overseeing the configuration and retrieval of crucial SiPM parameters, including the voltage bias and the current drawn. Temperature monitoring is also within its purview. The latter aspect is intended for integration with the LEGEND-200 slow control system, facilitating the real-time monitoring and archival of such information.

3.5.2 Integration in LEGEND-200

The FE electronics chain is structured to receive, filter, amplify the analogue signals from the SiPM detectors and pass them for acquisition by the DAQ FlashCam. It also serves the purpose of remotely controlling the detectors via the central slow-control of the LEGEND-200 experiment. Cables extend from four DSUB37 connectors on the cryostat flange to the NIM FE boards on the rack (Appendix D), featuring RJ45 back-connectors linking to the FlashCam. The cryostat flange incorporates 4 DSUB connectors, accommodating 15 SiPM channels, while each FE board is designed for a 12-fold multiplicity. To streamline the flange-to-FE interface, a patch panel was designed and installed between the flange and the FE boards, regrouping channels for clearer mapping and for a more functional implementation of the majority logics of nearby channels on the same board. Figure 3.12 shows a pictures of the FE boards, controller board, and the patch panel configuration installed in the clean room of LEGEND-200 experiment.

The initial step involved installing the NIM boards on the rack, followed by the insertion of cables between the controller and FE boards. Subsequently, 6 m CAT6 Ethernet cables from the cryostat flange to the FE boards were accommodated and plugged in. Finally, the 4 m RJ45 cables to FlashCam were incorporated into the setup. Following the installation, a series of tests were conducted to verify the integrity of the complete cabling lines and to ensure seamless communication between the FE and controller boards.

The traces were examined along the cabling lines leading to the FlashCam DAQ, to ensure their visibility and propagation from one end to another. The assessment included checking for any residual electromagnetic pick-up on the cables, both from the bird nest to the flange (Kapton band) and outside the cryostat, following the differential cancellation at the receivers. This channel-by-channel test was performed for each FE board. To perform this test, a programmable pulser was configured to simulate an expected SiPM signal with an amplitude of 770 μ V corresponding to ~ 1 PE, and a decay tail of 3 μ s. The pulses were sequentially input to each of the FE channels. Given that the pulser electrical output is singular while the FE employs a differential receiver, a transformer was employed to replicate the pulser signal.

¹⁰<https://github.com/kplindegaard/smbus2>

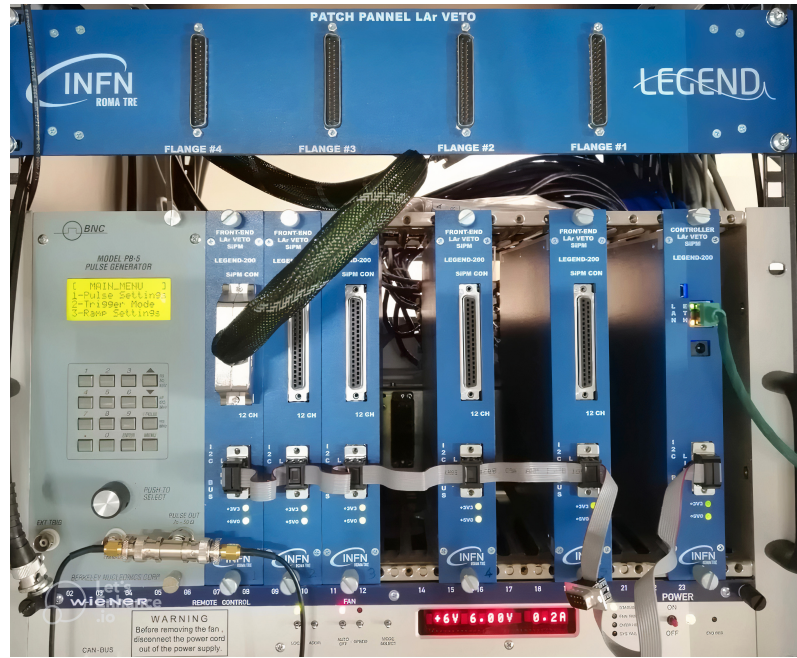


Figure 3.12: Photo of the crate with 5 FE boards and the controller board, on the right; on top the Patch panel is also visible.

The DAQ system was utilized to individually examine the output traces for each FE channel after traversing the entire chain, assessing both amplitude and time profile. The noise, assessed using a pulser exclusively to probe the FE board effect, was measured to be of 0.15 mV (peak-to-peak). This value was determined through trace examination with both an oscilloscope and the DAQ system. The gain was evaluated and found to be in accordance with the design specifications (40 per differential line).

Overall noise level

In summer 2021, the FE system was installed and commissioned successfully, alongside the LAr instrumentation. Initially, a significant noise level of approximately 2.5 mV was observed using an unshielded preliminary twisted cable band between cryostat flange and FE boards. The observed noise was influenced by this cable band, which picked up ambient noise and displayed floating grounds due to the insecure fixation of the Kapton band.

Upon addressing these issues by securing the Kapton ground to the FE crate and implementing single shielded cables with twisted pairs at 100 Ω impedance, the noise was reduced to 0.65 mV, although with some residual wiggles. Further improvements were achieved by refining the grounding connections, bringing the noise down to approximately 0.4 mV.

The finalized cabling and grounding scheme utilizes CAT6 Ethernet cables installed between DSUBs of the flange and the FE boards. The shield of each cable is grounded to the flange. Additionally, few internal cables are employed to connect the Kapton ground to the FE rack, ensuring a robust and noise-resistant configuration.

Figure 3.13 Left provides an example of a baseline from a SiPM connected to the FE electronics. The two blue dashed-lines denote the Root Mean Square (RMS), while the light-blue band represents the overall noise level (SiPM + cables + FE + ADC) of the baseline, corresponding to 250 μ V (peak-to-peak). Additionally, the Right side of Figure 3.13 depicts the mean RMS level of 12 channels from the same FE board. For

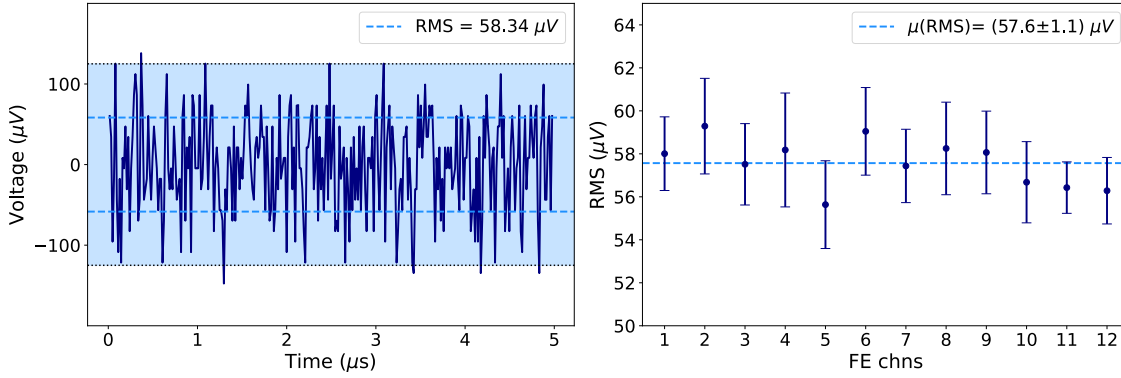


Figure 3.13: **Left:** example of a baseline trace of $5 \mu\text{s}$ length: the dark-grey dashed horizontal lines represent the level of RMS for this specific trace ($58.34 \mu\text{V}$); while the light-grey band represent the noise level of the baseline ($250 \mu\text{V}$, peak-to-peak). **Right:** RMS mean values of about 3000 baselines for each 12 channels of a FE board. The grey dashed line represents the RMS mean value between all channels.

each channel, the mean value was calculated based on 3000 selected baselines. The blue dashed line indicates the average RMS value across all channels. Notably, all RMS values are compatible within one standard deviation.

In conclusion, the FE electronics exhibits an exceptionally low level of electrical noise, with an RMS of $(57.6 \pm 1.1) \mu\text{V}$ and a peak-to-peak excursion of $250 \mu\text{V}$. This low noise level was achieved even with considerable distances between the detectors and the FE boards. The numerical values align with the outputs from the circuit simulation and demonstrate excellent stability over time (see Appendix E). The temporal stability was further validated during the physics runs as an integral component of the LEGEND-200 data acquisition process.

3.6 SiPM pulses

The operational principles of SiPM are detailed in Appendix F, showcasing expected output pulses in Figure F.1. A crucial aspect in evaluating the performance of the SiPM array is the analysis of their pulses recorded by the DAQ system. A python-based software has been developed for this purpose. The main features have been derived from the shape of SiPM pulses using test data collected in October 2021. This dataset is collected by a global trigger of the DAQ with a majority of 1, i.e. a single SiPM ADC channel triggers the DAQ readout of all active SiPM channels. The trace length was set to $250 \mu\text{s}$ (sampled at 16 ns) and the leading edge of the triggered pulses are positioned at around $5.5 \mu\text{s}$.

Pulse shapes for each SiPM array were examined generating super-pulses, i.e. averaged single-peak pulses. To build super-pulses, the initial $30 \mu\text{s}$ of the trace window was chosen, a duration deemed sufficient for analyzing pulse decay times. First of all, single-peak traces were identified for each SiPM channel by counting the number of peaks in each trace to eliminate pile-up pulses. From these single-peak traces, only those that triggered the DAQ readout and whose maximum value is located around $5.5 \mu\text{s}$ are selected. The distribution of the peak positions from single-peak traces is presented in Figure 3.14 Left on a logarithmic scale, for one SiPM channel. The majority of pulses cluster around the main trigger position. In order to have a clean sample of traces, a Gaussian fit has been performed and only traces with single-peak pulses within a range of two standard

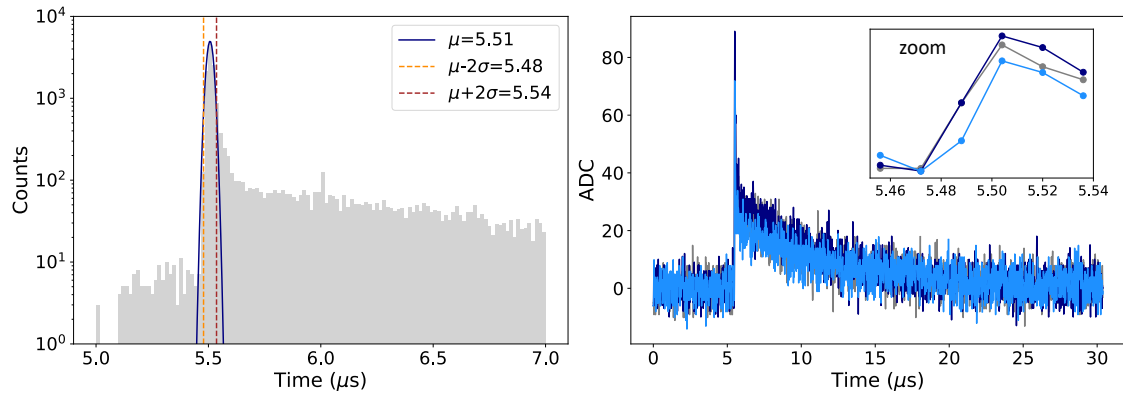


Figure 3.14: **Left:** typical peak position distribution of a SiPM channel. Using a Gaussian fit, only traces that have a single peak around the mean value of the distribution ($\pm 2\sigma$) are selected to build super-pulses. **Right:** example of single-peak baseline-subtracted traces used to construct super-pulses. A zoom into the leading edge region is also illustrated.

deviations (2σ) from the mean trigger position are retained. With these criteria, about 10^4 traces are selected for each SiPM channel. The mean baseline value, extracted for each particular channel within the first $4 \mu\text{s}$ of the trace, is then subtracted from each traces.

Some of these selected baseline-subtracted traces are displayed in Figure 3.14 Right. In this figure also a zoom into the leading edge region (rise-time of about 2 samples, corresponding to 32 ns) is visible. No cut was applied to the pulse height. Following traces selection and baseline subtraction, the average of these traces was computed to generate super-pulses for each SiPM array.

The construction of super-pulses reveals the existence of three distinct categories of traces, contingent upon the specific SiPM array [130]. An example for each category is reported in Figure 3.15, while the super-pulses for all working SiPM of the current setup (Section 3.9) can be found in Appendix G.

- The first category pertains to a SiPM array exhibiting traces with the expected shape (see Appendix F), featuring a rapid component of approximately 30 ns and a slower component lasting around $8 \mu\text{s}$, as shown in the left-most plot of Figure 3.15.
- The second category encompasses traces characterized by only one decay component lasting approximately $3 \mu\text{s}$ (second plot of Figure 3.15).

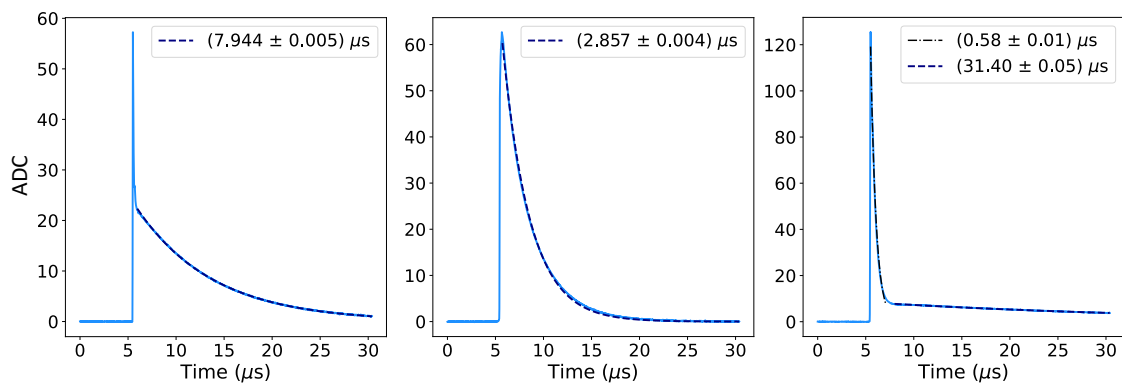


Figure 3.15: Super-pulses found for the three pulse shape categories. The exponential fit (dashed line) is performed to evaluate the decay time for each category.

- The third category includes traces with a fast component of about $0.5 \mu\text{s}$ and a more prolonged component lasting $30 \mu\text{s}$ (last plot of Figure 3.15).

The decay time of the first component is attributed to the fast charge supply from the parasitic capacitance, while the second decay time represents the recovery time of the microcell (refer to Appendix F).

Following discussions with the manufacturer (Ketek) these variations are attributed to differences in SiPM production, primarily stemming from variations in the quenching resistor. Although the quenching resistor geometry remains consistent across all cases, it was manufactured at two different sites, influencing the temperature sensitivity of the quenching resistance. Additionally, the trenches were filled with materials of varying resistivities, impacting the traces as the trench is integrated into the signal readout chain. Further insights into SiPM production can be found in [127].

Within a SiPM array, most traces share the same category, as the SiPMs employed in a given array are neighboring SiPMs from the same wafer. This minimizes the differences, such as gain, among the SiPMs. It is observed that the pulse category of a SiPM array is closely related to on the wafer from which the SiPMs were sourced [127].

3.6.1 Decay time distributions

The super-pulses exclusively display the average decay time of the SiPM arrays. To better investigate the SiPM pulse properties, the exponential decay time has been extracted from each single-peak baseline-subtracted pulse, following the previously established criteria for trace selection.

The decay time distributions for the three categories are presented in Figure 3.16 and Figure 3.17. Gaussian fits have been employed to derive the mean values (μ) and standard deviations (σ) of the distributions.

- The distribution of the first category has $\mu = 7.8 \mu\text{s}$ and $\sigma = 1.6 \mu\text{s}$ (Figure 3.16 left).
- The second category distribution has $\mu = 2.8 \mu\text{s}$ and $\sigma = 0.36 \mu\text{s}$ (Figure 3.16 right).
- The distribution of the first component of the third category has $\mu = 0.56 \mu\text{s}$ and $\sigma = 0.05 \mu\text{s}$ (Figure 3.17 left), while the second component of the third category exhibits $\mu = 29 \mu\text{s}$ with variations exceeding $13.5 \mu\text{s}$ (Figure 3.17 right).

The decay time distributions for all working SiPM of the current setup are reported in Appendix G. The comparison between the decay times of super-pulses and the mean values of decay time distributions are summarized in Table 3.4. The obtained mean values for most SiPM array align within one standard deviation with the decay times identified through super-pulses. The deviation for some SiPM channels can be explained by the presence of a slight tail on the right side of the decay time distribution (see Appendix G).

Non-Gaussian decay time distributions

Some SiPM array of the second category exhibit a non-Gaussian behavior in their decay time distributions, as illustrated in Figure 3.18. These SiPM arrays feature pulses corresponding to smaller and shorter decay times, as can be observed in Figure 3.19: the pulse with longer decay time include a small component of a rapidly decaying signal, similar to

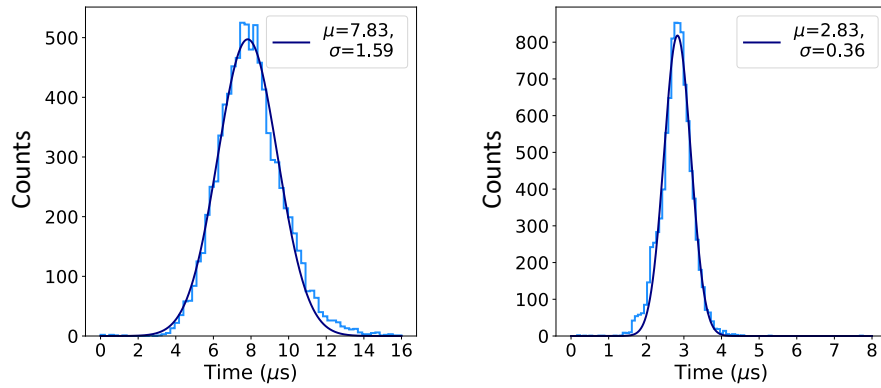


Figure 3.16: Decay time distributions for SiPM array of the first (left plot) and second (right plot) pulse category. Gaussian fits are applied to the distributions to quantify the spread.

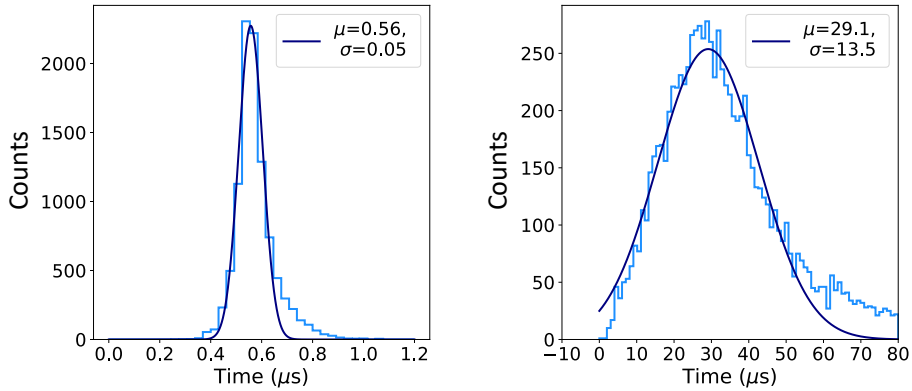


Figure 3.17: Decay time distributions for SiPM array of the third pulse category with two components, fast decay (left plot) and slow decay (right plot). Gaussian fits are applied to the distributions to quantify the spread.

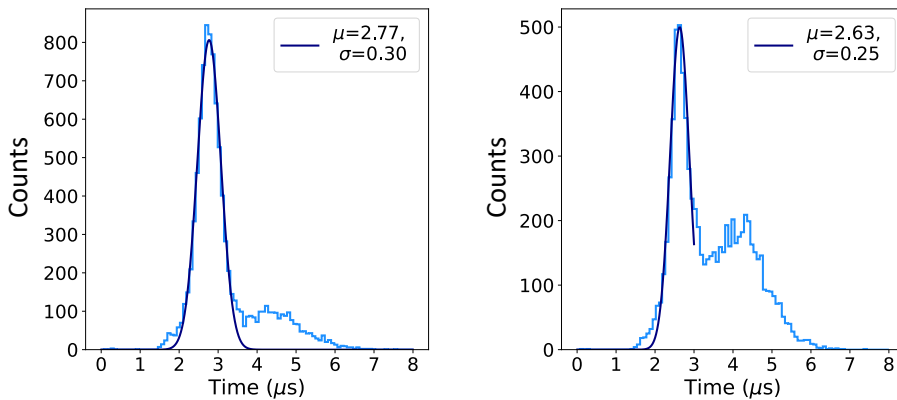


Figure 3.18: Two examples of double-peaked decay time distributions for the second pulse category. Gaussian fits are applied to the first part of the distributions to quantify the spread.

SiPM	Category	τ_{SP} (μs)	μ_{hist} (μs)	Agree in 1σ
S060	1st	6.965 ± 0.010	6.2 ± 0.5	no
S061	1st	7.416 ± 0.016	6.6 ± 0.7	no
S055	2nd	3.077 ± 0.005	2.9 ± 0.2	yes
S054	2nd	3.412 ± 0.007	3.1 ± 0.3	yes
S017	2nd	3.043 ± 0.006	2.9 ± 0.4	yes
S074	1st	7.722 ± 0.018	7.0 ± 2.0	yes
S073	1st	6.445 ± 0.007	6.2 ± 0.6	yes
S071	1st	7.878 ± 0.011	7.6 ± 0.9	yes
S070	1st	7.461 ± 0.011	6.5 ± 1.4	yes
S067	1st	7.588 ± 0.012	7.4 ± 1.2	yes
S068	3rd	28.736 ± 0.085	35.2 ± 15.3	yes
S029	3rd	27.223 ± 0.067	28.7 ± 12.7	yes
S042	1st	6.736 ± 0.007	6.8 ± 1.0	yes
S041	1st	7.156 ± 0.008	7.2 ± 1.0	yes
S024	2nd	2.981 ± 0.004	2.9 ± 0.3	yes
S023	2nd	2.873 ± 0.008	2.6 ± 0.3	yes
S030	3rd	32.780 ± 0.085	35.8 ± 18.3	yes
S031	3rd	20.167 ± 0.135	24.9 ± 16.9	yes
S002	2nd	2.785 ± 0.005	2.7 ± 0.3	yes
S003	2nd	2.656 ± 0.004	2.6 ± 0.3	yes
S032	1st	7.196 ± 0.010	6.7 ± 0.7	yes
S036	1st	6.381 ± 0.005	6.2 ± 0.5	yes
S058	1st	6.568 ± 0.007	6.2 ± 0.6	yes
S057	1st	6.411 ± 0.007	6.1 ± 0.7	yes
S065	1st	6.793 ± 0.012	6.3 ± 0.8	yes
S046	1st	8.996 ± 0.023	7.3 ± 0.8	no
S047	3rd	22.896 ± 0.099	34.6 ± 7.4	no
S012	1st	8.596 ± 0.018	7.5 ± 0.8	no
S020	2nd	2.825 ± 0.006	2.6 ± 0.2	no
S026	2nd	3.333 ± 0.010	3.2 ± 0.5	yes
S025	2nd	2.956 ± 0.005	2.8 ± 0.4	yes
S015	2nd	3.052 ± 0.006	2.7 ± 0.3	no
S043	1st	8.713 ± 0.019	7.4 ± 1.0	no
S048	3rd	28.723 ± 0.064	31.5 ± 15.4	yes
S049	3rd	22.168 ± 0.049	27.5 ± 12.3	yes
S053	3rd	26.384 ± 0.060	35.4 ± 16.7	yes
S052	3rd	33.690 ± 0.076	34.2 ± 16.7	yes
S050	2nd	3.472 ± 0.009	2.8 ± 0.2	no
S051	2nd	3.299 ± 0.007	2.9 ± 0.4	yes
S044	3rd	17.978 ± 0.034	16.6 ± 8.3	yes
S037	3rd	30.144 ± 0.066	34.3 ± 16.9	yes
S035	3rd	30.955 ± 0.078	33.7 ± 18.9	yes

Table 3.4: Comparison between the decay times of super-pulses (SP) and the mean values (μ) of decay time distributions. The agreement within one standard deviation is indicated.

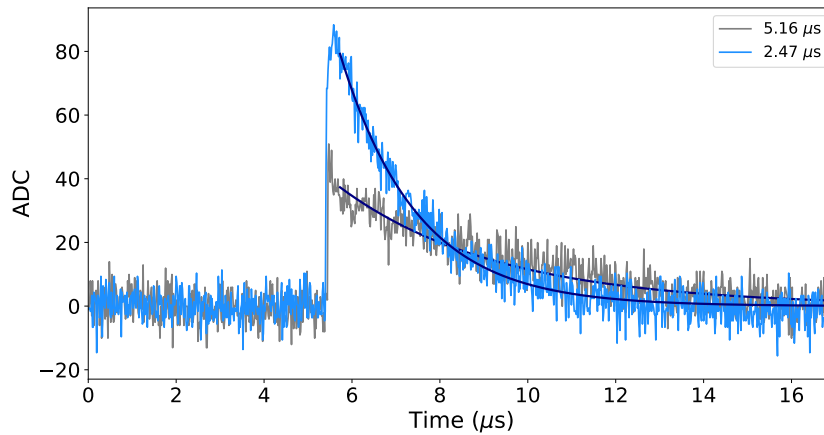


Figure 3.19: Example of two traces with distinct decay times from the same SiPM array.

the first category, although with a lower amplitude; in contrast, the pulse with shorter decay times lack this characteristic. This observation suggests potential differences between the SiPM cells in the SiPM arrays.

During the SiPM array production, SiPMs were taken from neighboring positions on a wafer and should therefore have the same characteristics within a SiPM array. However, during repair works, some SiPMs had to be replaced and if no SiPMs were available on the original wafer of the array, SiPMs had to be taken from other wafers. For this reason, some arrays have SiPMs with different decay times or even with different pulse categories.

In total within the LAr instrumentation there are 30 SiPM arrays of first category, 16 of the second category and 12 of the third category. Non-Gaussian decay time distributions are found in one SiPM of first category (SiPM 70), three SiPM channels of second category (SiPM 15, 33, 50) and one SiPM of the third category (SiPM 31).

Building upon the obtained pulse shapes and decay time distributions of the LEGEND-200 SiPM arrays, specific energy reconstruction methods have been developed, the details of which will be discussed in Chapter 4.

3.6.2 LAr instrumentation dynamic range

To evaluate the dynamic range of the LAr instrumentation, a dataset containing high-energy events (up to GeV energies) generated by muons has been acquired during the commissioning of the instrumentation. To accomplish this, a configuration of 12 SiPM channels was set up in coincidence, with an energy threshold set above 20 PE.

Figure 3.20 illustrates a representative baseline-subtracted SiPM trace attributed to a muon event. In the presence of an ultra high-energy event, a significant amount of energy is deposited in the LAr, leading in a substantial scintillation light emission that saturates the LAr instrumentation (SiPMs and FE electronics). The saturation amplitude is observed at around 30 000 ADC, corresponding to about 500 PE. This value exceeds the average single PE amplitude by over three orders of magnitude, showcasing a dynamic range exceeding three orders of magnitude for the LEGEND-200 LAr instrumentation. Due to this saturation effect, the next signal extraction is possible after more than 10 μ s, depending on the amount of energy deposited.

In addition to assessing the dynamic range of the LAr instrumentation, investigating muon events offers valuable insights into muon-induced isotopes, such as $^{77(m)}\text{Ge}$, within

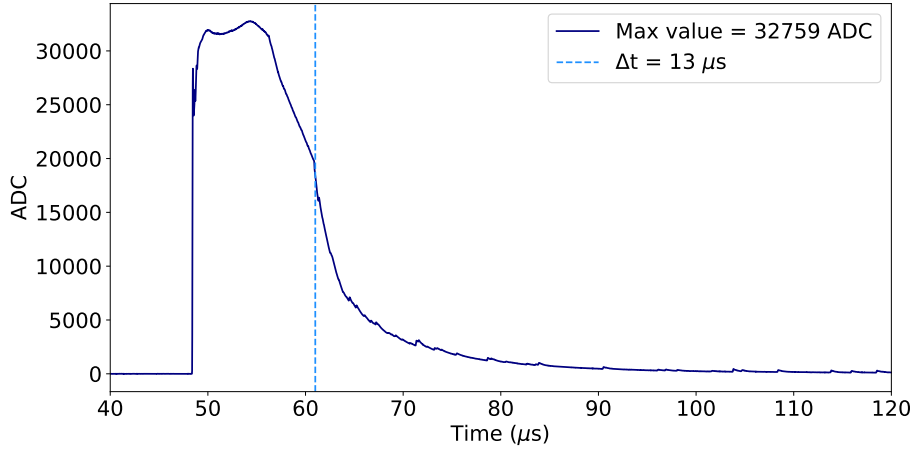


Figure 3.20: Typical muon event in one SiPM channel. The event saturates the LAr instrumentation at around 30 000 ADC. A new signal extraction is possible after 13 μs .

the experiment. A preliminary analysis of the muon-induced neutron rate, based on this data set, can be found in [120].

3.7 LAr scintillation profile

A comprehensive understanding of the light detection efficiency and rejection capability of the LAr instrumentation is essential for LEGEND-200 experiment. To gain insights into the response of the LAr detector, a dedicated measurement has been conducted during the commissioning of the LAr instrumentation. Using two ^{241}Am sources, one directed towards the fiber modules and another towards the WLSR, the goal was to determine the fraction of detected scintillation events compared to the actual number of scintillation events. The triplet lifetime and the singlet-to-triplet ratio have been calculated by fitting a model describing the photon emission time profile to the measured photon arrival time spectrum. This setup allowed for the estimation of the photo detection efficiencies of the fiber modules, indicating how likely scintillation light emitted by the two sources is detected by the fiber modules. By directing the source away from the fiber modules, it became possible to estimate the additional scintillation light detected due to reflections at the WLSR and measure its efficiency. Detailed analysis and results can be found in [120, 127]. This section will outline the analysis used to estimate the triplet lifetime and the singlet-to-triplet ratio.

3.7.1 LAr instrumentation and source setup

The measurement setup includes three fiber modules arranged in a row on the provisional aluminum outer barrel frame, as depicted in the left image of Figure 3.21. Additionally, two triggered scintillation light sources are fixed to the central rod, suspended from the mounting plate of the lock system, as shown in the central picture of Figure 3.21. One source is directed towards the fiber modules, while the other is positioned diametrically and directed towards the WLSR.

The two sources comprise a copper vessel and a central cavity of triangular shape. The cavity of each copper vessel contains an enclosed ^{241}Am source, which emits radiation outward. Due to the encapsulation capturing α particles, scintillation light is generated solely

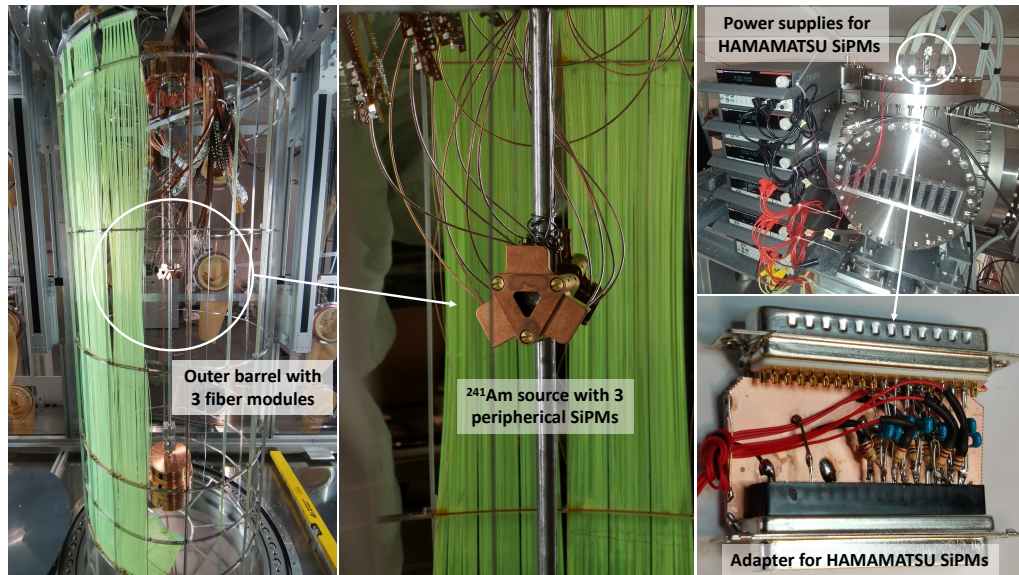


Figure 3.21: Setup of the LAr instrumentation with two ^{241}Am sources containing three peripherals VUV sensitive SiPMs. The power supplies for HAMAMATSU SiPMs are visible in the top-right pictures, while the bottom-right picture shows the custom-made adapter.

through the subsequent emission of 59.5 keV photons in the cavity. Three HAMAMATSU VUV4¹¹ sensitive SiPMs are situated in the side walls of the cavity, for each source, detecting the scintillation light produced during ^{241}Am decays. The open section of the vessel enables the escape of 128 nm scintillation photons, which then travel towards the fiber modules or the WLSR, depending on the source direction.

As the HAMAMATSU VUV4 SiPMs operate with a bias voltage of about 50 V [131], and considering that the maximum voltage that the FE electronics can generate is 31.5 V, six external power supplies were employed (Figure 3.21 top-right). Additionally, an adapter was custom-made to supply the bias voltage and read the signals from the six HAMAMATSU SiPMs. Specially crafted at the LNGS electronics workshop for this particular measurement, the adapter is made to accommodate the DB37 connection (Appendix D) on the flange level. It includes 1 k Ω resistors for voltage and ground connections, as well as 1 μF capacitors to decouple the signals from potential voltage fluctuations and noise (bottom-right picture of Figure 3.21). Subsequently, CAT 6 cables were connected to the adapter, passing through a deactivated FE board, and then routed to the FlashCam DAQ. The FlashCam has been configured to record data only when all three SiPMs within one of two source cavity detect scintillation light. The acquisition window was configured to be 6000 samples (96 μs), with trigger position at 1300 samples (20.8 μs).

3.7.2 Time profile analysis

The investigation of the photon emission time profile in LAr has been performed using one top SiPM from the central fiber module and the ^{241}Am source directed towards the fiber modules. This was conducted to assess the feasibility of independently monitoring triplet lifetime, distinct from LLAMA (Section 2.2.1). This investigation also aimed to assess the quality of liquid argon on the upper part of the cryostat after multiple deployments.

The time differences between the detected scintillation photons by the LAr instrumen-

¹¹[https://hamamatsu.su/files/uploads/pdf/3_mppc/s13370_vuv4-mppc_b_\(1\).pdf](https://hamamatsu.su/files/uploads/pdf/3_mppc/s13370_vuv4-mppc_b_(1).pdf)

tation SiPM array and detected scintillation light by SiPMs on ^{241}Am source are computed by subtracting the time of a SiPM array pulse that arrive within $10\ \mu\text{s}$ after a reference pulse. The reference pulse is defined as the coincidence of the three pulses of SiPMs from the ^{241}Am source.

The photon emission time profile of LAr can be described by a double-exponential model [132] with one component corresponding to the decay of singlet excimers (τ_s) and the other to the decay of triplet excimers (τ_t) (Section 3.2). Furthermore, an intermediate component is included in the model which has a time component $\tau_{rec} \sim 20\text{-}100\ \text{ns}$ [133]. This component takes into account light emission from neutral excimer molecules formed in recombination processes of ions (or ionic excimer molecules) with electrons. The complete model is as follows [133]:

$$f(t) = a_s \cdot \exp\left\{-\frac{t}{\tau_s}\right\} + a_t \cdot \exp\left\{-\frac{t}{\tau_t}\right\} + a_{rec} \cdot \left(1 + \frac{t}{\tau_{rec}}\right)^{-2} + c \quad (3.3)$$

where a_s , a_t and a_{rec} represent the intensities of the singlet, triplet and intermediate components, respectively; the constant c is added to account for accidental uncorrelated events.

A binned extended log-likelihood fitting procedure has been performed for the complete model using a histogram with 16 ns bins (DAQ time resolution). The outcomes, along with the individual components of the model, are presented in Figure 3.22. All parameters are free in the fit and the fit range is from 0 to $10\ \mu\text{s}$. The goodness-of-fit parameter is $\chi^2/\text{ndof} = 1.2$, and the residuals, shown in units of sigma in the lower panel, indicate that the fit model describes the data within 2σ deviation.

Despite the flexibility in parameterization, the used model fails to accurately describe the singlet component within the distribution of photon emission time profile. This discrepancy can be attributed to inadequate time resolution, as the expected singlet lifetime of 6 ns (Section 3.2) falls below the sample width of 16 ns. Consequently, the determined singlet lifetime of $(18.5 \pm 0.5)\ \text{ns}$ is prone to overestimation, as it attempts to compensate for the limitations in time resolution.

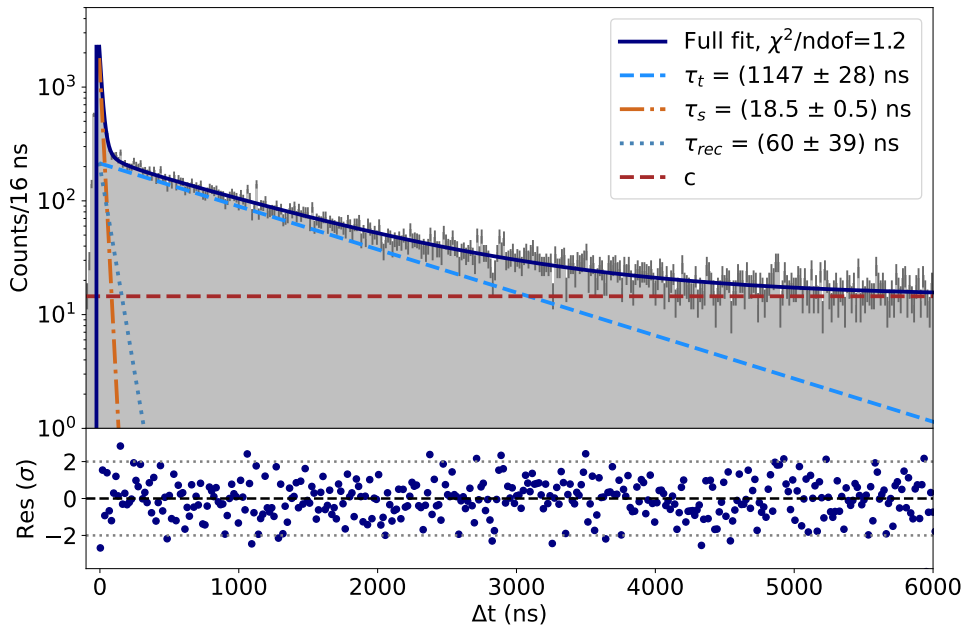


Figure 3.22: Photon emission time profile of LAr scintillation. The individual components of the model are displayed. The lower panel illustrates the residuals in terms of number of sigma.

The fitting parameter for the intermediate time component is $\tau_{rec} = (60 \pm 39)$ ns. The extracted triplet lifetime of (1.147 ± 0.028) μ s is well aligned with the 1.15 μ s value measured by LLAMA [134].

As discussed in Section 3.2, the intensity ratio of light stemming from singlet and triplet decays depends on the type and energy of an incident particle. This singlet-to-triplet ratio is computed as [133]:

$$\frac{I_s}{I_t} = \frac{\int_0^\infty a_s \cdot \exp\left\{-\frac{t}{\tau_s}\right\} \cdot dt}{\int_0^\infty a_t \cdot \exp\left\{-\frac{t}{\tau_t}\right\} \cdot dt}. \quad (3.4)$$

The predominant scintillation events in the enclosed LAr volume of the WLSR are generated by the β decays of ^{39}Ar , and consequently, the majority of the exciting particles are electrons. The singlet-to-triplet ratio for electrons as exciting particles is approximately 0.3 [111]. Using the final fitting results from the model (3.3) in the expression (3.4), a singlet-to-triplet ratio of 0.2 is determined for the photon emission time profile. This calculation does not account for light from recombination processes. The ratio exhibits slight variations, depending on whether the light at intermediate times is considered part of the fast or slow component of light emission, but the variations are of the order of 1%. The lower value extracted from the fit can be related to an underestimation of the singlet component by the fitting model, possibly due to the relatively low time resolution of the LAr instrumentation.

3.8 LAr instrumentation response studies

During the commissioning of the LAr instrumentation, the signal rates of each SiPM array has been examined to investigate the homogeneity of light production inside the LAr volume enclosed by the WLSR and to identify a possible trigger configuration for the LEGEND-200 physics data acquisition. Coincidence rates among the full inner and outer barrel have been compared and majority rates were determined and compared to the rates obtained by FlashCam ADC.

Majority definition

The LEGEND-200 ADC, FlashCam, allows to set different majority logics for data taking, such as two-fold coincidences (majority 2) where at least two channels have a coincident signal within a certain time. Higher majority settings can be also applied to reduce the amount of data. Choosing an appropriate majority setting is crucial in LEGEND-200 to reduce the rate of low energy events, e.g. triggered by ^{39}Ar , and to allow the study of high energy events, such as those from ^{42}K (Chapter 5).

As discussed in Section 2.2.3, the readout of SiPM arrays is divided into cards whereas each card can host six readout channels. Hence, two majorities can be set:

- ADC majority (amaj) - majority within an ADC card;
- Master majority (mmaj) - majority among ADC cards.

The total majority configuration is denoted as amajN-mmajM, where N represents the number of ADC channels, and M represents the number of ADC cards. For instance, amaj2-mmaj3 indicates events where a coincident signal is detected in at least 2 ADC

channels across a minimum of 3 cards, equivalent to a total of at least 6 SiPM channels. For master majority of 1, the mmajM can be omitted and the ADC majority is simply denoted as amajN.

3.8.1 Majority trigger schemes

In October 2021, test data has been collected with the complete IB with the purpose of studying the majority rates estimated online by FlashCam and compare them with majority rates calculated offline. On one hand this represented a preliminary assessment of the amount of light per unit time seen as a function of the number of SiPMs in time coincidence and the consequent load on the DAQ. On the other hand it provided a rough idea of the optical response of the overall LAr instrumentation taking ^{39}Ar decays as a benchmark.

Out of the 9 fiber modules comprising the IB, 6 modules were identified as fully operational, i.e. with both top and bottom working SiPM, as shown in Figure 3.23. One top SiPM and one bottom SiPM from two different fiber modules were turned off due to operational issues, and one top SiPM from a fiber module was excluded due to high rate of events. With the final selection of 6 fiber modules, it was decided to distribute the 12 corresponding SiPM channels across 2 ADC cards, with the top channels assigned to the first card and the bottom channels to the second ADC card. Figure 3.23 shows the scheme of the IB fiber modules with corresponding SiPM channels connected to ADC cards.

Data in several majority conditions have been taken for an online investigation of rates. A first rate calculation, with different majority configurations, has been performed online by the FlashCam with a threshold in ADC corresponding to about 0.1 PE (estimated by FlashCam ADC) using $3\ \mu\text{s}$ -length traces. In Figure 3.24 the rate values obtained from the online analysis are shown for 12 channel and for 12 majority schemes. The mean value over 12 SiPM channels for each majority setting is reported with a dashed line. The rates are consistent among the 12 SiPM channels, demonstrating a uniformity of light detection. The lower SiPM arrays seem to receive a slightly higher amount of light compared to the upper SiPM arrays. This observation can be attributed to the exposure of the lower SiPM arrays to a larger volume of liquid argon. The presence of conditions between ADC cards amplifies the event rate for the same number of coinciding channels, as can be observed from the rate values of amaj2 and amaj1-mmaj2, amaj4 and amaj2-mmaj2, as well as amaj6 and amaj3-mmaj2.

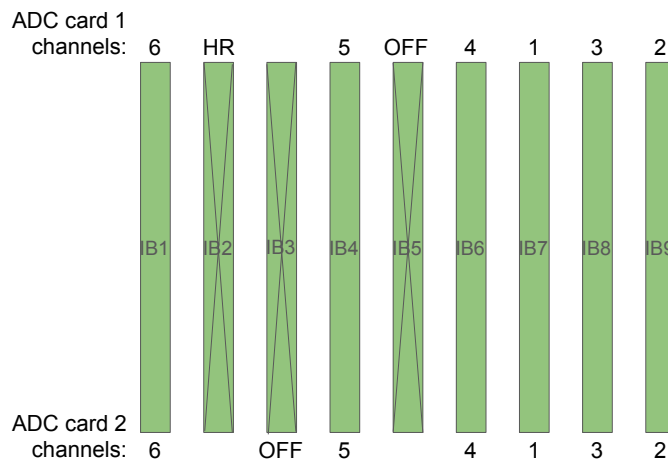


Figure 3.23: Scheme of the IB fiber modules with corresponding SiPM channels connected to ADC cards. Three fiber out of nine have been excluded from the analysis.

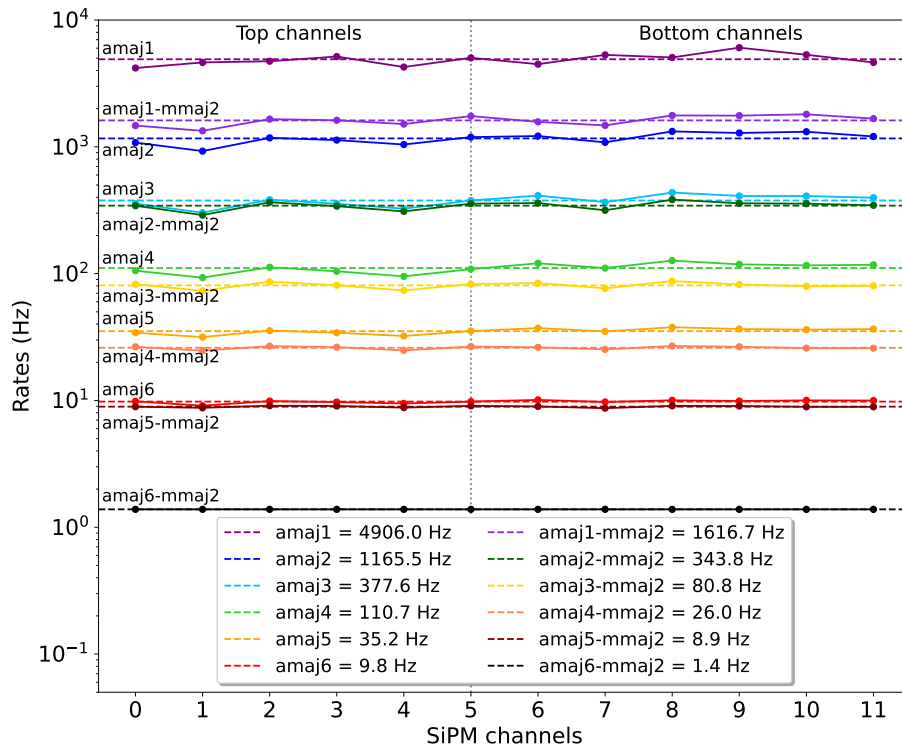


Figure 3.24: FlashCam ADC rates for 12 SiPM channels and 12 majority trigger schemes. The mean value for each majority logic is indicated by a dashed line.

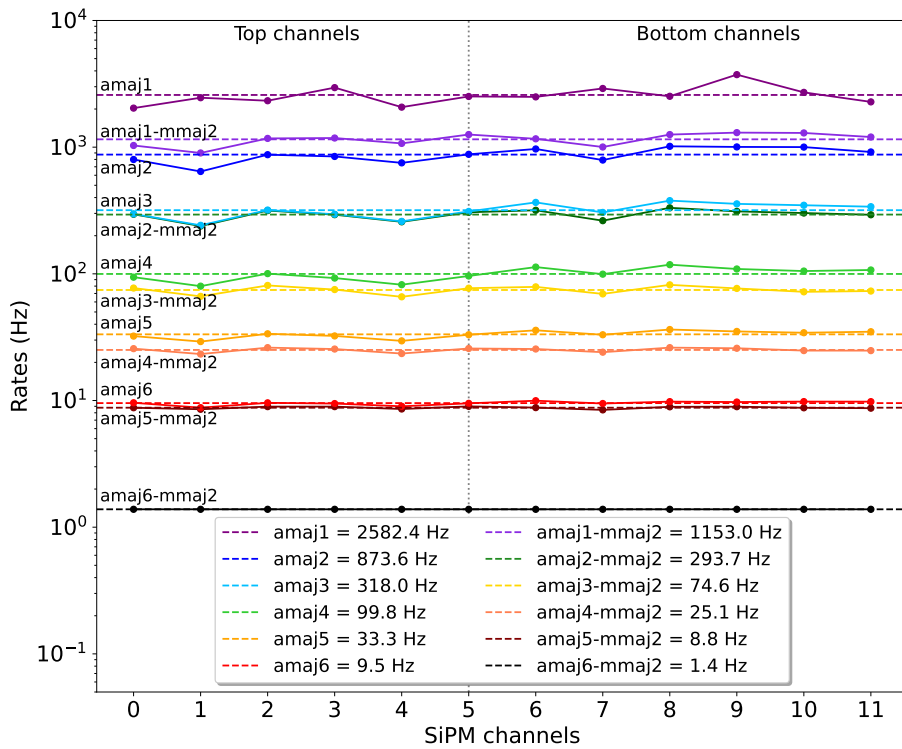


Figure 3.25: Rate values derived from offline trace selection for 12 SiPM channels and 12 majority trigger schemes. The mean value for each majority logic is indicated by a dashed line.

A more refined analysis has been performed offline, considering traces with a signal surpassing 0.3 PE in the $3 \mu\text{s}$ acquisition window. The PE values were estimated from the PE spectra, using as energy estimator the maximum pulse values and the PE calibration has been performed using the position of the first PE peak. Compared to the online rate calculation, events without pulses (noise traces) are excluded more efficiently thanks to the more refined PE calibration procedure and the higher threshold. The outcomes are presented in Figure 3.25.

When comparing the absolute rate values obtained in the online analysis, an overestimation is evident for low triggering schemes. For example, FlashCam measures an amaj1 rate of nearly 5 kHz, while the offline analysis yields 2.6 kHz. FlashCam amaj2 rate is 1.2 kHz, whereas it is 0.85 kHz in this analysis. Similarly, FlashCam amaj1-mmaj2 rate is 1.6 kHz, and here it is 1.2 kHz. This discrepancy can be attributed to the different selection criteria. However, for coincidences involving more than 4 channels, the rates converge. This can be attributed to the selection of high-energy events, making the application of a different threshold inconsequential.

Similar analysis has been carried out for the commissioning of the OB. The rate observed in single channels is of about 3 kHz for top SiPM channels and about 5 kHz for bottom SiPM channels. The higher rate of OB SiPM bottom channels can be attributed to more LAr volume visible and to the fact that they are bent towards the center.

An examination of various triggering configurations and event rates has been performed for the complete LAr instrumentation layout to identify the most effective setup to ensure the efficiency of data collection for the entire LEGEND-200 experiment. The final majority configuration for the LAr instrumentation is chosen upon a rate scan with FlashCam for the fully assembled LAr instrumentation which will be presented in Section 3.9.

3.8.2 Two-fold coincidence

An analysis of coincidence signals in top and bottom SiPM channels of the same fiber module has been performed to ensure a uniform distribution of light production from ^{39}Ar . The coincidence between SiPM channels of the same fiber modules allows to exclude noise and dark counts, leaving predominantly true physics events. For this analysis a wide range of time windows has been considered, starting from 16 ns (the time resolution of the ADC) up to $3 \mu\text{s}$, using the six fiber modules from IB commissioning. Figure 3.26 left shows an example of top-bottom coincidence with 144 ns time difference.

The top-bottom coincidence rates for these modules are reported in Table 3.5 for different time windows and Figure 3.26 right shows the behavior of the rate averaged across the six fiber modules. The coincidence rates increase with increasing time windows according to a two-component exponential. Within the first three data points from a window length of 0 to 30 ns the exponential increase is fast, while a smaller increase is visible for longer times. This behavior is related to the emission of scintillation light from the singlet and triplet components. Using a window of $3 \mu\text{s}$ around a pulse in one SiPM channel, coincidences signals in top and bottom channels of the same fiber module happen in about 40% of the total two-fold coincidence events (amaj1-mmaj2 from Figure 3.25).

In general, two-fold coincidence rates exhibit notable consistency across different fiber modules, also the ones from OB. No modules stand out for detecting significantly greater amounts of light than others, excluding SiPM channels with high rate of events. This observation suggests a uniform distribution of light production within the LAr volume enclosed by the WLSR.

	Fiber 1	Fiber 4	Fiber 6	Fiber 7	Fiber 8	Fiber 9	Mean values
dt < 3.0 μ s	676	394	494	392	497	436	481
dt < 2.5 μ s	674	393	493	391	496	436	481
dt < 2.0 μ s	673	392	491	390	495	435	479
dt < 1.5 μ s	656	383	480	382	488	430	470
dt < 1.0 μ s	603	353	446	355	456	405	436
dt < 800 ns	573	335	425	340	437	390	417
dt < 600 ns	526	309	391	313	405	365	384
dt < 400 ns	468	275	350	280	366	336	346
dt < 200 ns	383	230	293	234	302	293	291
dt < 100 ns	328	206	260	208	278	269	258
dt < 50 ns	288	190	234	191	257	253	235
dt < 40 ns	256	180	196	173	240	205	208
dt < 30 ns	154	121	100	101	163	75	120
dt < 16 ns	39	33	17	20	33	11	26

Table 3.5: Top-bottom coincidence rates (Hz) for the 6 IB fiber modules at different time windows. The mean rate values for each time window are reported in the last column.

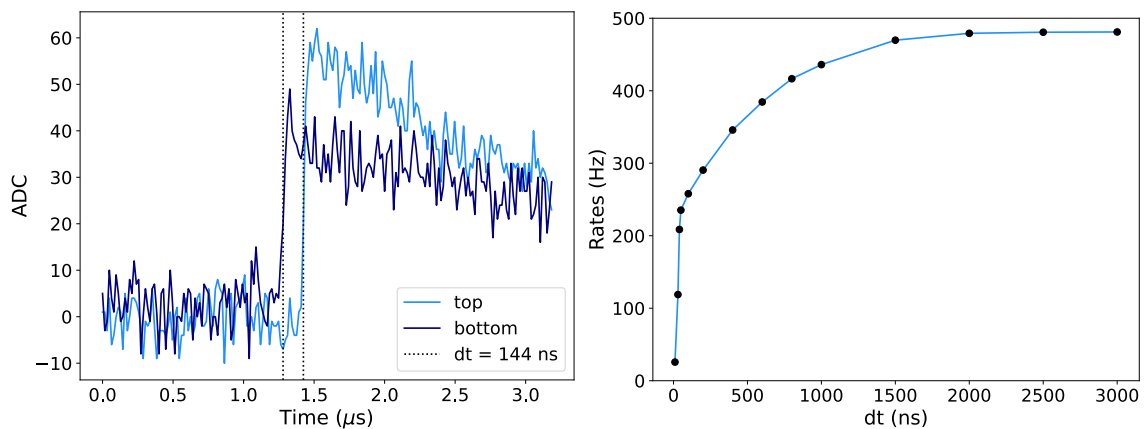


Figure 3.26: Left: example of top-bottom coincidence. Right: top-bottom coincidence mean rate values for different time windows (Table 3.5).

3.9 Current status of LAr instrumentation

Figure 3.27 shows the distribution of top (left plot) and bottom (right plot) SiPM channels of the two barrels in the final configuration of the LAr instrumentation. Eleven out of 58 SiPM arrays were lost after the immersion in LAr, mostly due to cable issues producing an infinite resistance between the differential traces. The single rates of all remaining channels were determined and five channels were found to exceed 10 kHz. Those channels are not included in physics analysis, leaving 42 SiPM working channels.

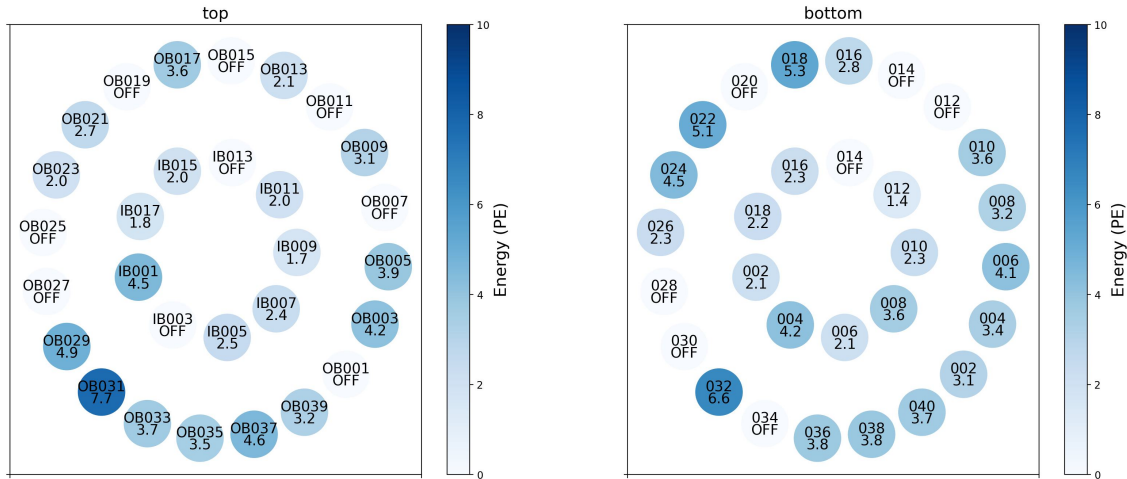


Figure 3.27: Schematic representation of the current status of each SiPM arrays mounted on IB (internal configuration) and OB (external configuration) fiber modules. The left plot illustrates the top SiPMs, while the right plot showcases the bottom SiPMs. The color bar indicates the detected energy in PE by individual SiPM channels during a triggered event.

LAr instrumentation majority trigger

Following the preliminary rate studies described in the previous section, in the LEGEND-200 final configuration, during physics data taking, in addition to the trigger on the HPGe detectors, a trigger on SiPM channels, referred to as LAr trigger, has been implemented. The LAr trigger events allow to identify and discriminate correlated backgrounds independently of the trigger on the HPGe detectors. For the fully assembled LAr instrumentation, together with the HPGe detectors, a study has been performed over various majority configuration with FlashCam to select an appropriate majority scheme for the LAr trigger.

Rate scans were performed using FlashCam as follows: when a signal exceeds 0.5 PE threshold, a $1.6 \mu\text{s}$ long window is opened to search for other signals that must also exceed the specified threshold. The obtained majority rates are shown in Figure 3.28.

Possible majority configurations for the LAr trigger can be derived from this measurement. In order to have a manageable amount of LAr triggered data during LEGEND-200 data taking, not exceeding the rate of the HPGe triggered events, it was decided to choose a majority setting of the LAr trigger rate < 1 Hz. Possible majority scenarios for 0.5 PE threshold are amaj1-mmaj10, amaj2-mmaj7 or amaj3-mmaj4, or higher majorities. Generally, majority settings with a distribution over several cards, such as amaj2-mmaj7, are preferred over settings that require many channels to trigger in only a few cards, like amaj6-mmaj2. This applies because in several cards, not all six channels can be considered, as shown in Figure 3.29.

In the end, amaj2-mmaj8 with 0.5 PE threshold has been selected for the entire LEGEND-200 data taking, resulting in a LAr trigger rate of about 0.2 Hz. This configuration ensures a sufficiently low rate while still enabling the study of high-energy background events as will be reported in Chapter 5.

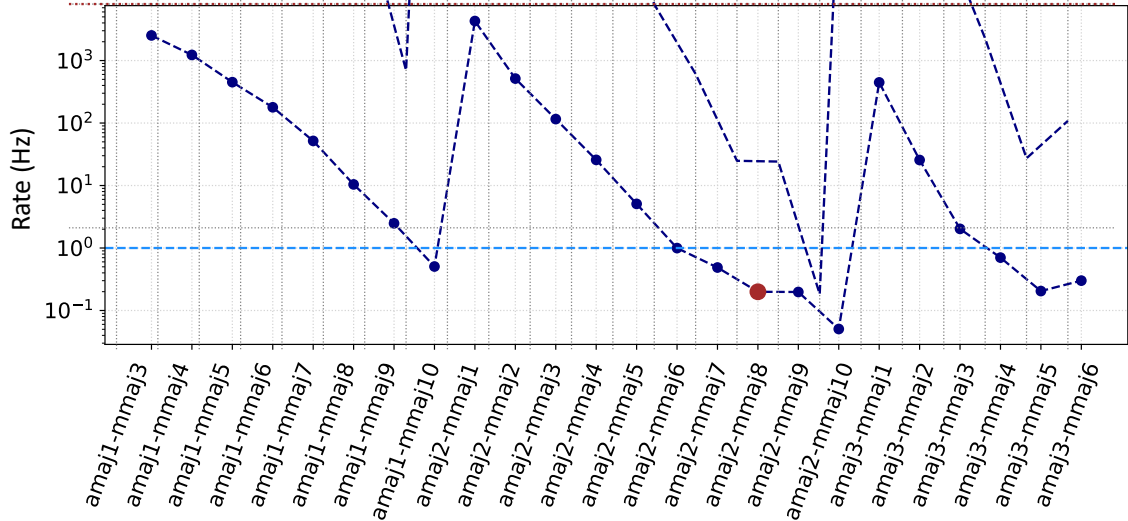


Figure 3.28: Majority trigger settings (see definition in Section 3.8) with 0.5 PE thresholds. The blue horizontal dashed line indicates a rate of 1 Hz. Majority combinations with values below this line can be accepted for LEGEND-200 data taking. Adapted from [135].

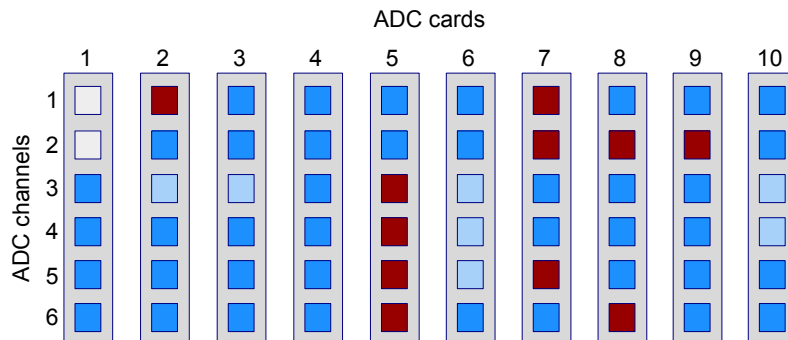


Figure 3.29: FlashCam SiPM channel mapping: grey slots are not connected; blue slots are operational SiPMs and included in the LAr trigger; light-blue slots are operational SiPMs but excluded from the trigger due to a high trigger rate; red slots are not operational SiPM channels.

CHAPTER 4

Optimum Filter Synthesis for SiPM Charge Estimation

The goal of the LAr instrumentation is to identify background events that lead to simultaneous energy deposition in LAr and in HPGe detectors. Specifically, the focus is on detecting energy depositions in LAr corresponding to backgrounds in the region of interest for $0\nu\beta\beta$ decay in HPGe detectors, i.e. around 2 MeV for ^{76}Ge isotope. For instance, background generated by 2.2 MeV gammas emitted subsequent to β decays of ^{214}Bi [136]. This is feasible when ^{214}Bi initially undergoes decay to a more energetic state, emitting gammas of up to 100 keV before the 2.2 MeV gamma. Detecting small energy depositions in the LAr provides a chance to reject this type of background. This relies on the efficient identification of single-photoelectron (SPE) events, requiring a good separation of SPE signals from electronic noise. To achieve this, an optimum filter based on Digital Penalized Least Mean Squares (DPLMS) method has been developed within the framework of this thesis.

The chapter is structured as follows. Section 4.1 illustrates the requirements for the SiPM charge estimator in LEGEND-200. In Section 4.2, a novel signal processing algorithm for SiPM using an optimum filter synthesis based on DPLMS method is described. Section 4.3 demonstrates the algorithm effectiveness in charge reconstruction on simulated SiPM traces. Section 4.4 outlines the efficiency of the LAr instrumentation background suppression when in coincidence with HPGe detectors. In Section 4.5 the first physics results from LEGEND-200 are presented.

4.1 SiPM charge estimators

The SiPM event charge is generally reconstructed through the integration of the signal trace. For SiPM signals exhibiting decay times exceeding $3\ \mu\text{s}$, as observed in the SiPMs employed in LEGEND-200 (see Section 3.6), a wide integration window is necessary for precise charge reconstruction. However, this results in heightened uncertainty due to the integration of noise. Alternatively, one can consider the amplitude of the pulse maximum, which have worse resolution due to varying decay times. For both estimators, accurately reconstructing the baseline becomes challenging when an entire event occurs on the decay tail of a previous energetic event, making charge estimation difficult.

Furthermore, the time emission profile of the LAr scintillation mechanism, featuring its triplet component, can give rise to event topologies where multiple PE are detected within a few microseconds in a single SiPM channel. The probability density function (PDF) for

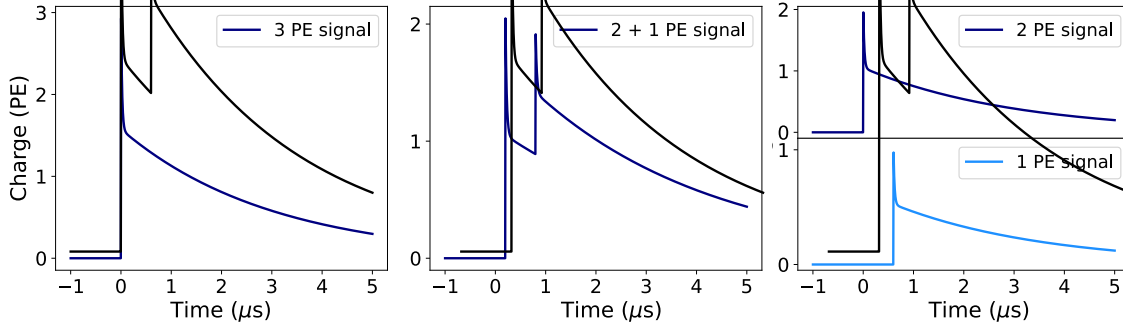


Figure 4.1: Illustration of three event topologies: **Left** - 3 PE signal recorded simultaneously by a SiPM array; **Center** - delayed signals (2 PE + 1 PE) recorded by a SiPM array; **Right** - two signals registered by two distinct SiPM arrays (2 PE + 1 PE). All these types, and any other possible combination, should yield 3 PE in the charge reconstruction of the event.

the emission of scintillation light from the triplet time component of the LAr scintillation mechanism is an exponential function with a decay time of $1.15 \mu\text{s}$ (in LEGEND-200 LAr, see Section 3.7). Hence, if N photons are produced following an energy deposition in LAr, they are emitted according to the triplet PDF. Only a fraction of these scintillation photons is detected by the LAr instrumentation, Section 3.4. Assuming M detected photons, different event topologies can occur as illustrated in Figure 4.1:

- M photons simultaneously detected and recorded by a single SiPM channel, generating a pulse with an amplitude corresponding to M PE; in the Left-most plot of Figure 4.1 for illustrative purpose a case of $M = 3$ is presented;
- M photons detected sequentially with a time delay and a single SiPM channel records multiple photons with distinct time delays; the Central plot of Figure 4.1 illustrates a primary 2 PE signal with 1 PE delay signal on the tail of the primary event;
- M photons are detected with a time delay and each photon is registered by a distinct SiPM channel, as shown in the Right plot of Figure 4.1.

All these event topologies and any other combination, also considering many SiPM channels, should result in M PE during the charge reconstruction of the event.

As the recovery time of the SiPM arrays is of several microseconds (Section 3.6), the topology described in the second point produces pulses that start on the slope of another pulse. This creates a maximum amplitude of the delayed signal that is higher than its actual amplitude (considering the baseline level of the main pulse). The area is also overestimated for the delayed pulse due to its offset, and for the prompt pulse, the integration time window also includes the delayed pulse. Consequently, it is difficult to estimate the charge using the area or the amplitude of the pulses as a PE estimator.

Another PE estimator that can be adopted is the amplitude of the pulse derivative. The derivative of SiPM pulses returns signals that are proportional to their rise and solves two main problems. The baseline does not need to be reconstructed, as it can be assumed zero after the derivative. Delayed pulses sitting on the decay tails of earlier arriving pulse get well reconstructed since the slope of the long decay tail is negligible compared to the fast risetime of the new pulse, as shown in the top plot of Figure 4.2. Furthermore, the time position of a pulse is easily obtained by using a simple above-threshold peak-search algorithm. The Figure 4.2 shows the raw traces and their derivative for the three category of SiPM pulses (see Section 3.6).

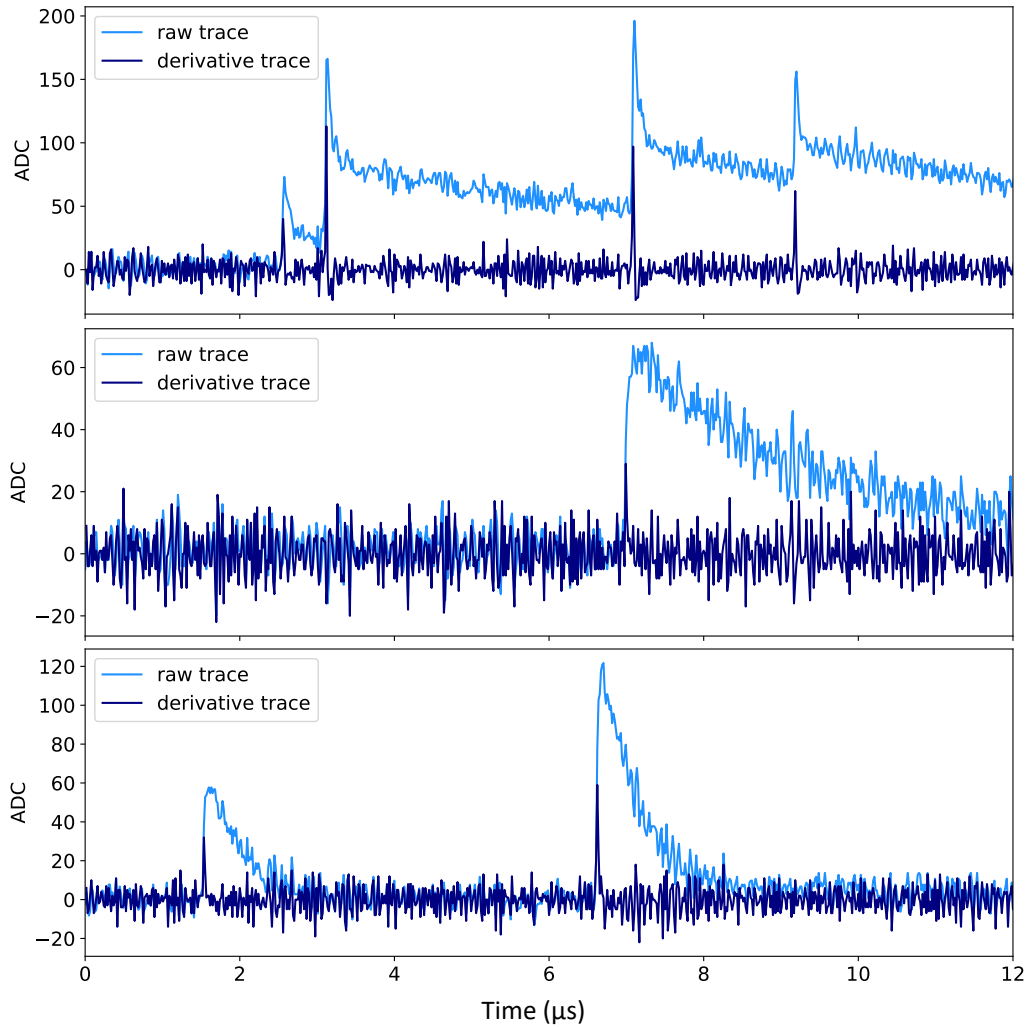


Figure 4.2: Raw traces (as registered by the DAQ) of an event and its derivative with one or multiple detected peaks for the three category of SiPM pulses (see Section 3.6).

Since the PE estimator utilizes the steepness of the derivative of the current pulse, it is called Hypercurrent estimator. The Hypercurrent is the default charge reconstruction method of the SiPM signals in LEGEND-200 and has been developed in [127].

During the first operation of the LAr instrumentation together with the HPGe detectors, an unexpected coupling of electromagnetic noise into the SiPM traces has been observed. This includes SiPM channels with large noise bursts, with a typical signal frequency of 25 kHz, as well as a large SiPM channels with sinusoidal disturbances with a typical oscillation frequency of 3 MHz [137]. Both disturbances are challenging as they also occur in coincidence with signals from HPGe detectors. An example of SiPM traces for these types of disturbances are shown in Figure 4.3 for two different SiPM channels.

Standard filters, e.g. Gaussian [138] and trapezoidal [139] filters, cannot completely eliminate the sinusoidal noise and bursts. These disturbances affect the PE resolution of SiPM energy distribution (see Appendix F) and especially result in a worse SPE separation from electronic noise. As a good SPE reconstruction is crucial to detect low energy depositions in the LAr, hardware and software efforts have been made to mitigate this noise. By meticulously investigating a possible noise source on hardware side and improving the connection schemes of the overall detector systems (including LAr instrumentation and HPGe detectors), a substantial reduction in noise has been achieved. In particular, the

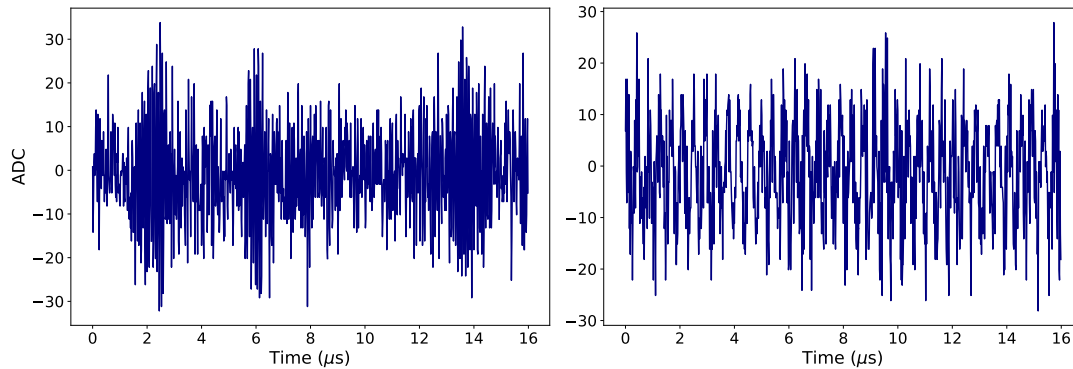


Figure 4.3: Example of SiPM trace with burst noise (left) and with sinusoidal noise (right).

bursts have been nearly entirely eliminated, but some residual sinusoidal disturbances still persist. To further improve the signal-to-noise ratio and achieve a better SPE separation, a digital optimum filter has been developed in the frame of this thesis work. Built on the DPLMS method, this approach has proven effective in efficiently eliminating sinusoidal disturbances, as demonstrated in [140]. Furthermore, since it relies on experimental acquired traces, it takes into account the various noise scenarios across different SiPM channels. The filter synthesis and its application on SiPM signals has been implemented in the LEGEND-200 analysis routines and is described below.

4.2 DPLMS optimum filter

The DPLMS method is especially effective among the synthesis algorithms since it derives the optimum filters directly from the experimentally acquired signal and noise traces. Originally it was proposed for HPGe detectors [140] and is currently undergoing integration into the processing chain of the LEGEND-200 HPGe detectors. For SiPM of the LAr instrumentation, a simplified version of this filter is employed, incorporating only noise information from data. The goal is to design a filter that minimally alters the input signal while effectively removing superimposed sinusoidal disturbances. This approach is similar to the one developed in [141].

4.2.1 Overview on DPLMS method

The DPLMS method for synthesizing optimal Finite Impulse Response (FIR) filters is very effective. This effectiveness stems from the fact that all optimally synthesized filters, in addition to meet any specific requirements delineated in the time or frequency domain, inherently fulfill the fundamental requirement of minimizing the impact of noise and environmental disturbances present in the relevant measurements. A concise overview of how the DPLMS method operates is presented below. Additional details can be explored in [140, 142].

The DPLMS method is based on minimizing a figure of merit composed of the sum of the variance of the experimental noise at the filter output and additional terms related to the satisfaction of any constraints imposing deterministic requirements in the time or frequency domain, as required in specific applications.

The synthesis procedure of filters with the DPLMS method consists of three main steps:

- the output noise variance of the filter is expressed in terms of the input noise and the filter itself; in this way, the method precisely accounts for the actual experimental noise;
- a series of experimental acquisitions of the signals of interest is averaged to obtain a deterministic and non-noisy reference signal; alternatively, a synthetic reference signal can be employed; in both cases any constraints on the output signal from the filter, i.e. on the convolution between the reference signal and the optimal filter, can be specified in the time or frequency domain;
- the output noise variance is added to the quadratic expressions of the previously obtained constraints, and the resulting functional is minimized with respect to the unknown coefficients of the digital filter.

As the output signal from the amplifier can be likened to a stochastic process due to the presence of electronic noise and disturbances, the most convenient way to impose constraints on the overall weight function is to derive a digital filter that determines the desired mean output value while simultaneously minimizing the variance of the noise superimposed on the output signal. This approach is highly general and allows for imposing fundamental constraints in both the time and frequency domains.

Since the desired digital filter belongs to the class of FIR filters, the output signal from it can be simply expressed as the weighted sum (x_i) of the input signal samples (ψ_{in}). Denoting ψ_{out} as a generic output sample from the digital filter, it can be expressed as follows:

$$\psi_{out} = \sum_i x_i(\psi_{in})_i. \quad (4.1)$$

The variance of the output signal from the filter is defined as:

$$Var[\psi_{out}] = E[(\psi_{out} - E[\psi_{out}])^2]. \quad (4.2)$$

Since it is generally necessary to impose constraints both on the deterministic value of the output signal from the filter and on the minimization of its variance, and these conditions must be satisfied simultaneously, it is possible to define a single functional to minimize. This functional is expressed as a sum of quadratic forms with respect to the parameters of the unknown filter:

$$\Phi(\psi_{out}, \psi_0, a_1, a_2) = a_1 Var[\psi_{out}] + a_2 (E[\psi_{out}] - \psi_0)^2 \quad (4.3)$$

The minimum value of this functional, which depends on the choice of the two weights, favoring either of the two requirements to be simultaneously satisfied, can be determined by imposing that all its derivatives with respect to each unknown coefficient of the FIR filter, x_i , are set to zero. This results in a linear system of equations with x_i as the unknown variables. The system can also be expressed in matrix form as:

$$A \cdot x = B \quad (4.4)$$

where A is a square matrix, B is the known term, and x is the filter. The filter is then obtainable as the solution of the corresponding linear system, since, by construction, the number of independent equations is always equal to the number of filter coefficients.

Therefore, the DPLMS method, which is based on minimizing a suitable figure of merit, translates into the straightforward resolution of a linear system once the elements A and B are obtained. The solution of this system coincides with the desired optimum filter.

4.2.2 DPLMS filter synthesis

The DPLMS method considered for the synthesis of a digital filter for SiPM detectors imposes constraints in the time domain. The matrix A is formed by summing two contributions, appropriately weighted, one constructed from information about the experimental noise and the other one from information about the reference signal:

$$A = a_1 \cdot NoiseMatrix + a_2 \cdot RefMatrix. \quad (4.5)$$

The known term is given by the weighted reference signal vector:

$$B = a_2 \cdot RefV. \quad (4.6)$$

The two weighted coefficients can be adjusted based on the experimental situation, ranging from the maximally effective value ($a_i = \infty$) to the completely ineffective value ($a_i = 0$). The specifics of each contribution, along with the respective values of their weighted coefficients, are outlined below.

Noise matrix

The *NoiseMatrix* of the expression (4.5) is calculated as the average of the matrix products obtained from 10^4 experimental acquired baselines (derivative), i.e. traces without pulses (Figure 4.4 Left), similar to matrices of pseudo auto-correlation:

$$NoiseMatrix = Baseline^T \cdot Baseline, \quad (4.7)$$

where T is the transposition operator.

The noise matrix correspond to a quadratic form and thus is symmetric, positive definite and exhibit higher values on the main diagonal, as shown in Figure 4.4 Right, where the auto-correlation of each trace of the baseline is maximal. The baseline dimension is fixed to 1000 samples ($16 \mu s$), and the *NoiseMatrix* is reduced to the filter length via a 2D convolution operation with a unitary matrix. This ensures the preservation of noise information.

It is worth noting that correlation noise matrices serve not only as a valuable tool for creating optimal filters from experimental signals but also as an effective method for investigating noise and monitoring its consistency over time.

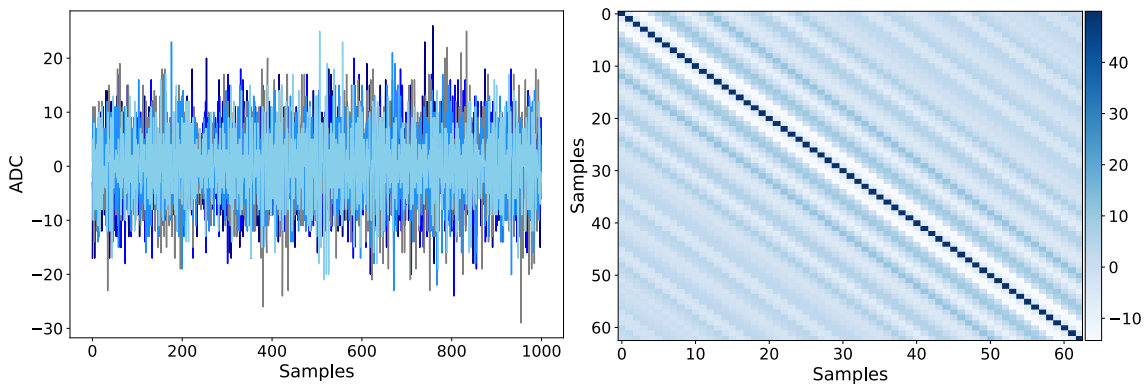


Figure 4.4: Left: few derivative baseline traces used for *NoiseMatrix* calculation. Right: visual representation of *NoiseMatrix* calculated from the derivative baseline traces. A zoom-in of up to 60 samples is reported to better observe the matrix layout.

Reference signal matrix and flat-top constraint

A straightforward approach to ensure minimal alteration of the input signal at the output is to introduce a simple synthetic reference signal, like a Dirac delta. By requiring that the output should be similar to the Dirac delta, this specific signal can be used as the basis for constructing the *RefMatrix* of expression (4.5) and the known term of expression (4.6):

$$RefMatrix = RefSignal^T \cdot RefSignal \quad (4.8)$$

$$RefV = RefSignal^T. \quad (4.9)$$

The reference matrix takes into account also the addition of a flat-top. The optimum filter flat-top feature is essential for reducing the ballistic deficit effect [143] and obtaining a proper energy estimation of experimental signals. Thus, the flat-top is used on the calculation of the *RefMatrix*, as it is necessary for SiPM channels which features a signal risetime exceeding 1 sample, i.e. > 16 ns.

Filter synthesis

Filter are synthesized with dual objectives: minimizing noise at the filter output while preserving the input signal as much as possible. For these reasons the values of a_1 and a_2 weighted coefficients have been set at one ensuring equal importance.. The value of flat-top length, as well as the filter length, are optimized channel by channel in terms of charge reconstruction efficiency (see Section 4.3).

The length of the flat-top has been varied with values of 0, 1 and 2, corresponding to 1, 3 or 5 points on top of the output reference signal ([0], [-1 ,0, 1], [-2, -1, 0, 1, 2]), in order to take into account the risetime of all SiPM channels. The filter length has been initially varied in increments of 10 samples, ranging from 10 to 40 samples. Nevertheless, for the physics analysis discussed in Chapter 5, the decision has been made to fine-tune the filter length within the range of 10 to 20 samples (in 5 samples step), ensuring a higher time resolution for the detection of incoming pulses.

After identifying all contributions, the filter is determined by solving the linear system of Equation (4.4). Figure 4.5 shows three examples of synthesized optimal filter shapes corresponding to the three flat-top values. In the first plot of Figure 4.5, a filter of 20 samples length is depicted with a single point on top of the output reference signal; the middle plot illustrates a filter with three points on top; the third plot of Figure 4.5 presents an example of a filter with five points on top.

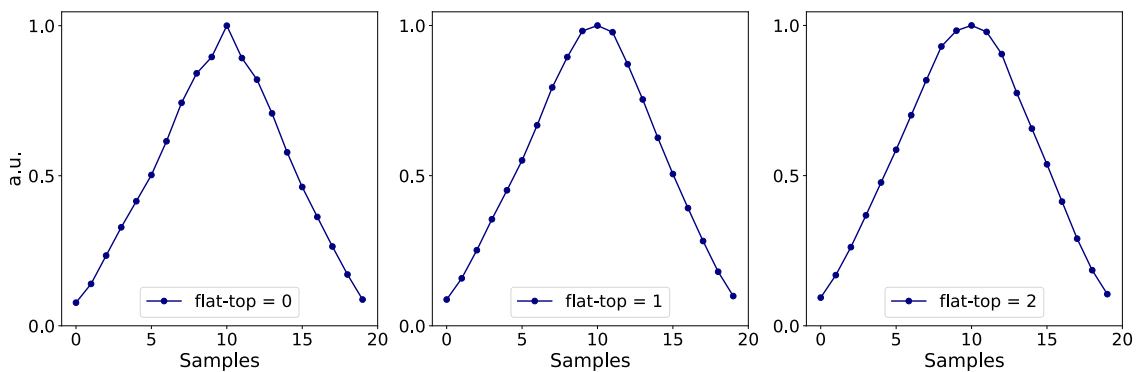


Figure 4.5: Example of digital optimum filters with a length of 20 samples, synthesized using the DPLMS method, incorporating various flat-top values.

4.2.3 SiPM processing chain

The hypercurrent and DPLMS streams employ the same processing chain, differing in the signal filtering step, as shown in the block scheme of Figure 4.6. In case of hypercurrent, a Gaussian filter is applied to smooth the electronic noise, follows the applications of the average derivative filter to the traces. For DPLMS stream, since the filter is constructed on the derivative signals, the SiPM traces undergo a sequence where the derivative is applied first, followed by the filter application. The subsequent steps remain unchanged.

After the filtering and derivative of the traces, a series of processors are employed to search for SiPM pulses. The first step involves the projection of the derivative and filtered traces on the y-axis. This allows the estimation of the mean and FWHM of the baseline. After the FWHM of the baseline is determined, a multi-local-extrema finder is used to find each peak in the derivative traces. The baseline FWHM value is then used to set an absolute threshold that the derivative amplitude has to overpass to be recognized as a valid pulse candidate. If a peak fulfills this condition, the prominence¹ of the peak is evaluated. If the prominence is larger than the given value, depending on SiPM gain², the amplitude of the valid peak is saved. In addition, the time of every valid peak in a trace is extracted. Due to the fast risetime of the pulses, a precise determination of the onset time is possible.

The Hypercurrent and DPLMS DSP chain (see Section 2.2.5 for LEGEND-200 data processing chain) outputs consist of two arrays each. The first array contains amplitudes corresponding to individual valid peaks, representing the estimated uncalibrated charge of each delayed scintillation pulse in an event. The second array contains onset times for all valid peaks in the trace.

After the DSP tier is built, the processing moves on to build the HIT tier. Here the energy values obtained in the DSP tier are calibrated in units of PE. The energy of a scintillation event is reconstructed by summing up all derivative amplitudes. Filling this values into a histogram, a PE spectrum is obtained (see Appendix F). The first two PE peaks of the SPE spectrum are fitted with a Gaussian function. A linear fit is performed to extract the calibration curve. The slope and the constant are saved to a configuration file for each channel and read in by the HIT tier processing. Each value of the DSP array of energies is then converted to PE and saved to disk together with the unchanged time array.

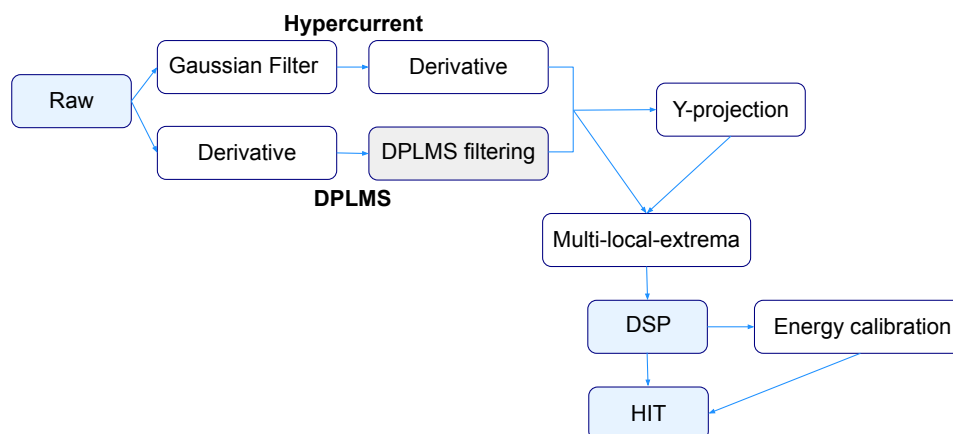


Figure 4.6: Schematic diagram of the SiPM processing chain from the Raw-tier to the HIT-tier.

¹The prominence of a peak quantifies how much a peak stands out from the surrounding baseline of the signal. It is defined as the vertical distance between the peak and its lowest contour line.

²The threshold, set as factor of FWHM from baseline standard deviation, is optimized channel-by-channel, as the SiPM gain varies.

4.3 Charge reconstruction efficiency and SPE resolution

The processing of SiPM traces, i.e. filtering and pulse search, depends on few parameters, such as the penalized coefficients and the absolute and prominence thresholds to accept a valid SiPM pulse. To extract a proper set of parameters for each SiPM channel the charge reconstruction efficiency is calculated as the difference between reconstructed charge from the filter and expected charge from simulation. For this purpose, a Monte-Carlo simulation has been performed in [127] to produce a dataset of SiPM traces with realistic conditions as extracted from LEGEND-200. The traces are simulated separately for each active SiPM channel of the LAr instrumentation. They undergo the same SiPM processing chain as the real-life pulses.

The difference between reconstructed and expected charge is calculated for each event and filled into a histogram, as shown in Figure 4.7 Left (for one SiPM channel). This process is reiterated for every set of parameters. Negative values correspond to events in which the reconstructed energy is underestimated, e.g. due to missed peak detection. Positive values represent events in which the reconstructed energy is overestimated. In an ideal scenario, a Gaussian distribution is expected to be centered at zero with a FWHM equal to the PE resolution of the SiPM array.

The reconstruction efficiency (ϵ) is determined by the count of events deviating no more than a certain tolerance from the expected energy, divided by the overall number of simulated events. To account for the variation due to SPE resolution, a tolerance value of 0.3 PE has been used for all SiPM channels. The reconstruction efficiency is illustrated in the right side plot of Figure 4.7. Two SiPM channels have been omitted due to inadequate performance attributed to low gain. On average, an efficiency of $(92.4 \pm 0.5)\%$ is achieved. With a tolerance of 0.5 PE, the average reconstruction efficiency is $(95.8 \pm 0.2)\%$.

Parameter optimization

Figure 4.8 shows an example of the optimization of digital filter parameters. In the first plot, the values of the filter length are displayed, indicating that the maximum reconstruction efficiency is obtained for a filter length of 10 samples. For most of SiPM channels, the optimal filter length is 10 samples, corresponding to 160 ns. This allows to separate pulses which distant at least 10 samples. The right plot of Figure 4.8 displays the optimal parameter for the flat-top length, which is 2, i.e. 5 points on top of the output reference signal.

In Figure 4.9 an example of the absolute and prominence thresholds to accept a valid SiPM pulse is illustrated. In the left plot, the values of absolute threshold are displayed, indicating that for this channel the maximum reconstruction efficiency is achieved for a threshold of 5 ADC. For the prominence threshold low values are preferred and the maximum efficiency is obtained also for 5 ADC, as shown in the right plot of Figure 4.9.

PE peaks reconstruction

To investigate the performance of the implemented method, the reconstruction efficiency has been calculated at various PE values using the optimized parameters. The results are reported in Figure 4.10 for 1 PE, 2 PE and 3 PE pulses. The average efficiency for 1 PE peaks is of $(99.7 \pm 0.1)\%$, for 2 PE pulses is $(95.6 \pm 0.3)\%$ and for 3 PE pulses is $(90.1 \pm 0.9)\%$. These results suggest that the reconstruction method, based on the optimum DPLMS filter and utilizing parameters that maximize the overall efficiency, can

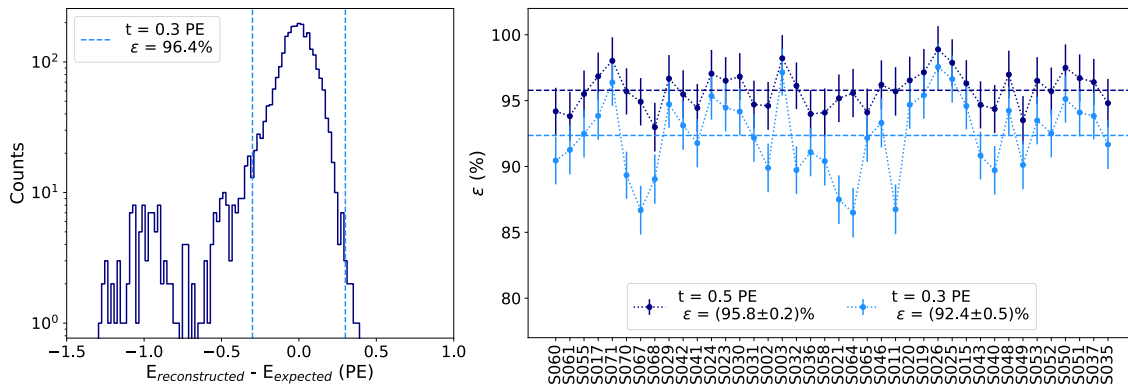


Figure 4.7: Left: example of difference between the reconstructed PE from the DSP chain and the expected PE as simulated for SiPM S071. The tolerance at 0.3 PE and the corresponding efficiency is indicated. Right: SiPM reconstruction efficiency for tolerance 0.3 and 0.5 PE.

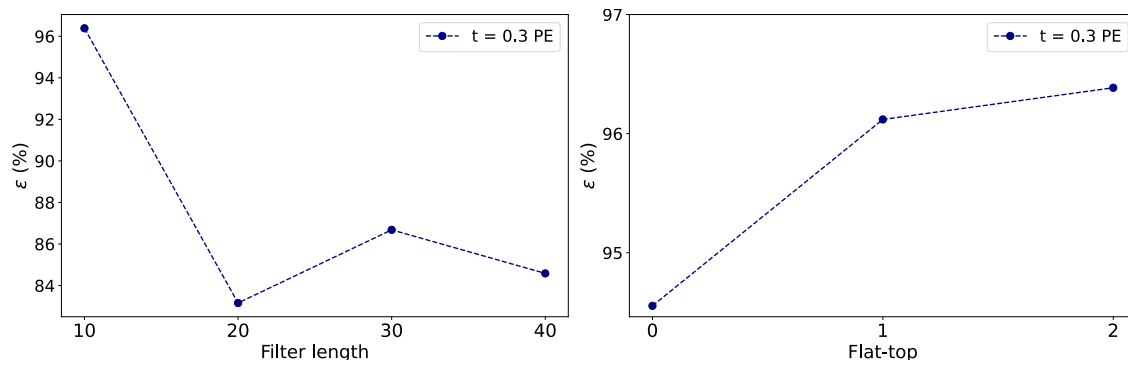


Figure 4.8: SiPM S071 optimization in terms of reconstruction efficiency (ϵ) for filter length and flat-top values.

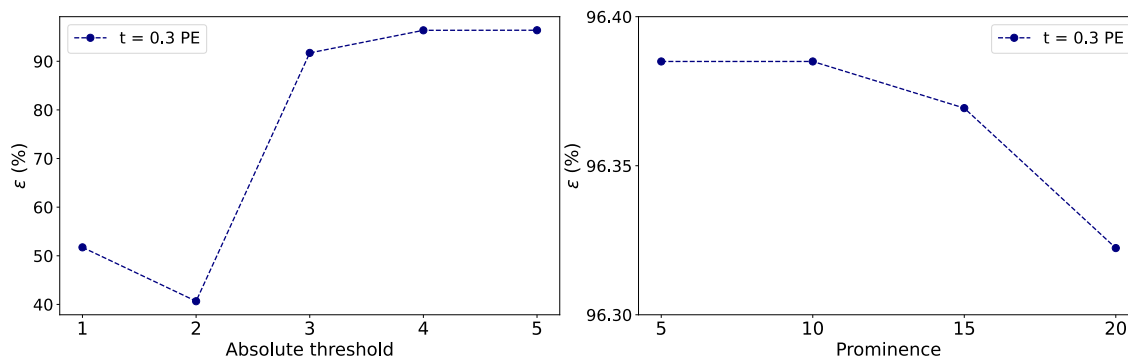


Figure 4.9: SiPM S071 optimization in terms of reconstruction efficiency (ϵ) for absolute threshold and prominence threshold.

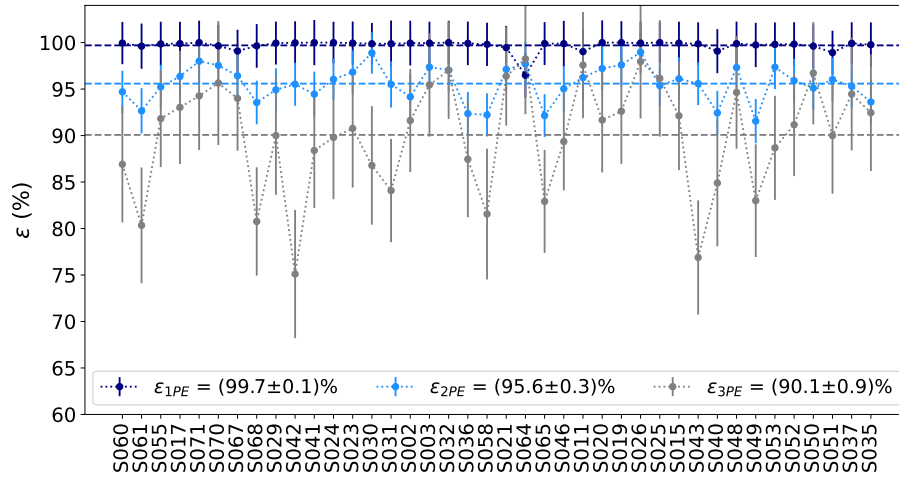


Figure 4.10: Peak reconstruction efficiency for 1, 2 and 3 PE peaks.

efficiently reconstruct the 1 PE peaks with almost 100% efficiency, while experiencing a decrease in efficiency for higher PE pulses. This ensures an excellent performance of the LAr instrumentation when employed as a veto for background events in the search for $0\nu\beta\beta$ decay, as will be illustrated in the next section.

SPE resolution

Figure 4.11 shows the FWHM values of the first PE peak of the energy spectrum. The left plot provides an example of the PE spectrum for SiPM S071. On the right, the FWHM values for all SiPMs are displayed, excluding the two channels mentioned earlier. The average FWHM is observed at (0.25 ± 0.01) PE, with the maximum value being 0.36 PE. This indicates an outstanding resolution of the first PE peak, ensuring a considerable separation from noise peak and consequently resulting in excellent single PE peak reconstruction.

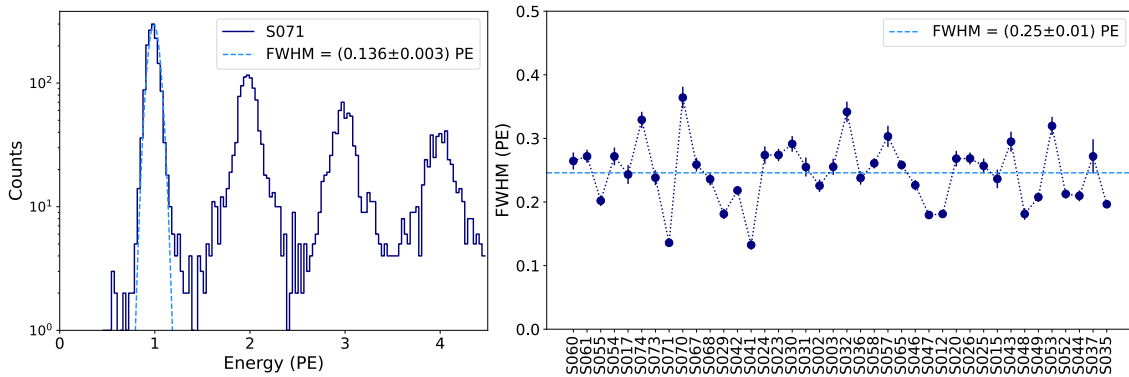


Figure 4.11: Left: SiPM S071 PE spectrum with the gaussian fit on 1 PE peak. Right: SiPM FWHM values at 1 PE peak of spectrum.

4.4 LAr instrumentation performance

The excellent resolution achieved through the use of the optimum DPLMS filter enables an efficient rejection of background events that deposit energy in LAr coinciding with HPGe detectors. The rejection criteria for the LAr instrumentation, designed to enhance the rejection of correlated and coincident signals from HPGe detectors while minimizing the rejection of accidental coincidences, have been investigated in [127] and are summarized below.

Various criteria have been examined to establish a veto cut for identifying HPGe events as background. The first criterion involves defining a time window around the trigger of HPGe detectors within which light signals are accepted to form the veto cut. Considering the LAr scintillation mechanism (Section 3.2), an exponential time delay is expected, determined by the decay time of the triplet state (Section 3.7). Therefore, it has been decided to include pulses with a delay of up to $5 \mu\text{s}$ based on a straightforward estimate using the PDF of the triplet state:

$$\int_0^{5\mu\text{s}} \frac{1}{\tau_t} \exp(-t/\tau_t) dt \simeq 0.987, \text{ with } \tau_t = 1.15 \mu\text{s}. \quad (4.10)$$

As a result, nearly 99% of the light from the triplet state is expected to be captured within a $5 \mu\text{s}$ time window. To accommodate the drift time of charges in the HPGe detector [144], light signals arriving up to $1 \mu\text{s}$ before the HPGe detector trigger are also considered. This leads to a total analysis window width of $6 \mu\text{s}$ for the LAr instrumentation data.

Another crucial parameter is the acceptance of random coincidences, i.e. events where no coincident light is produced. An effective approach for this is the use of events triggered by the pulser, which is injected into the HPGe detector readout system with a rate of 50 mHz. The acceptance of random coincidences characterizes the discriminatory capability of the LAr instrumentation between signal-like events (with no energy deposition in the LAr) and background-like events (with energy deposition in the LAr). A higher random coincidences acceptance indicates a reduced probability of the LAr instrumentation misclassifying signal-like events as background-like events (false coincidences). The primary contributor to false coincidences stems from random coincidences originating from ^{39}Ar intrinsic to the instrumented LAr volume, as anticipated in Section 3.1.

Currently, the LAr veto cut is tuned to attain a random coincidences acceptance similar to that of GERDA experiment (97% [46]). GERDA accomplished this without any tuning, solely relying on a light-or-no-light condition³. However, due to the enhanced light yield and the much larger optical active volume⁴ in LEGEND-200, adopting the GERDA LAr veto approach would reduce the random coincidence acceptance to 60% [127]. Thus two parameters have been varied to achieve a random coincidence acceptance similar to GERDA. These are the total number of detected PE per event (NPE) and the number of SiPM channels triggered per event, leading to the following veto cut:

$$\text{NPE} \geq 4 \ \& \ \text{N}(\text{SiPM}) \geq 4. \quad (4.11)$$

In this way the achieved random coincidence acceptance is of 95% [127].

The energy distribution spectrum, before and after the application of the LAr veto cut, is illustrated in Figure 4.12. These spectrum has been derived from the first LEGEND-200 data release, corresponding to an exposure of 10.1 kg·yr [88].

³Events that present at least 1 PE of energy in the LAr instrumentation was tagged as background.

⁴6 t in LEGEND-200 v.s. less than 2 t in GERDA.

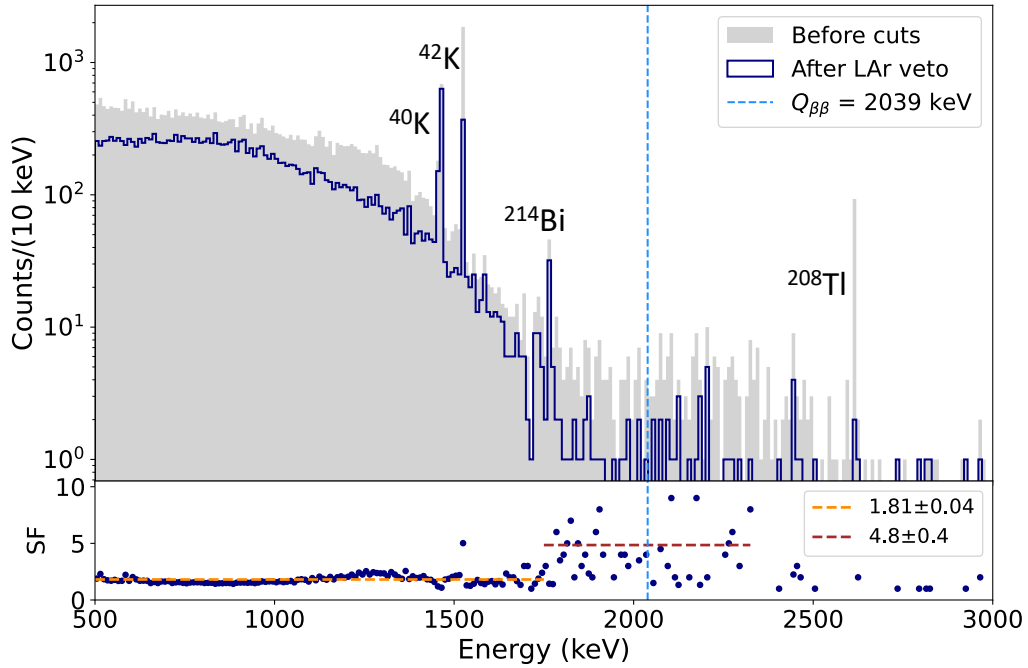


Figure 4.12: LEGEND-200 energy distribution (10.1 kg-yr of exposure) before and after the application of LAr veto cut. The Suppression Factor (SF) after the LAr veto is shown in the lower panel.

The Compton continuum below the gamma lines of ^{40}K and ^{42}K is efficiently suppressed by a Suppression Factor (SF) of (1.81 ± 0.04) for energies below 1700 keV, leaving an almost pure $2\nu\beta\beta$ spectrum. The events around $Q_{\beta\beta}$ (2039 keV) are suppressed by a factor of (4.8 ± 0.4) , while the suppression factor of K lines are discussed below.

Potassium suppression

Using the characteristics of ^{40}K and ^{42}K decays provides a natural test for assessing the background suppression capability of the LAr instrumentation. ^{40}K can be found in various materials within the LEGEND-200 setup and undergoes decay via β and electron capture (EC), as illustrated in Figure 4.13 Left. Gamma radiation only occurs in the EC branch, and none of the decay pathways produce coincident β or γ radiation that could trigger the LAr instrumentation. Consequently, the ^{40}K peak should not be suppressed by the LAr instrumentation.

^{42}K originates as a radioactive progeny of ^{42}Ar (Figure 4.13 Right), as discussed in Section 3.1. As ^{42}K originates from the LAr itself, a simultaneous energy deposition from the initial β -decay in the LAr to the predominant line at 1525 keV is probable. The coincident energy deposition suggests effective suppression of the 1525 keV line.

Figure 4.14 displays the energy region containing the gamma lines of ^{40}K and ^{42}K before and after the application of the LAr veto cut. As expected, the ^{40}K line persists with a survival fraction of $(92.2 \pm 5.1)\%$, as fine-tuned through the random coincidence acceptance discussed previously. In contrast, the ^{42}K line experiences substantial suppression, with only $(19.9 \pm 5.7)\%$ of the original counts in the peak surviving the LAr discrimination. The corresponding suppression factor is 5.

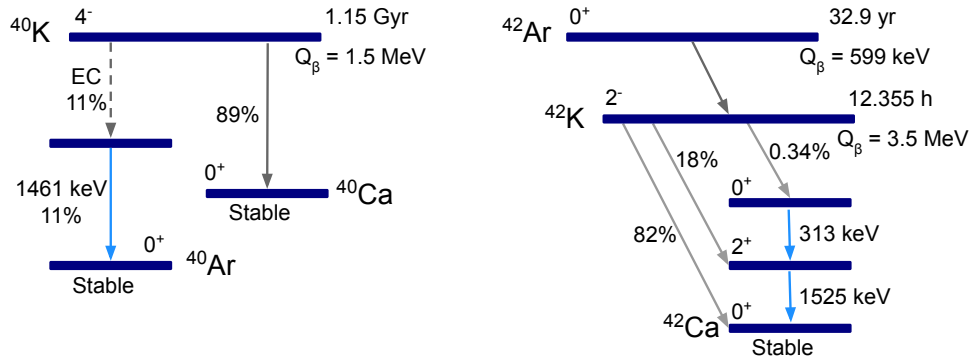


Figure 4.13: Decay schemes of ^{40}K and ^{42}K .

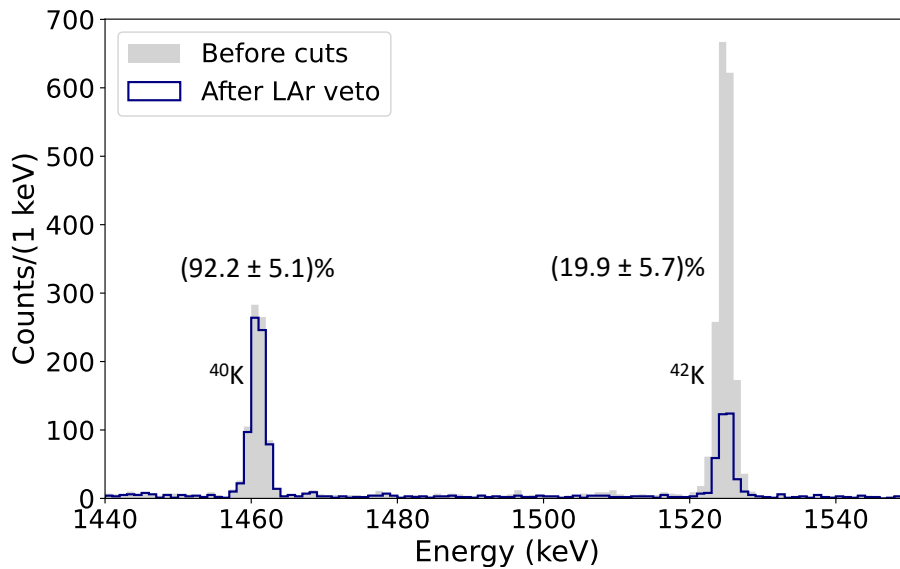


Figure 4.14: Suppression of ^{40}K (1461 keV) and ^{42}K (1525 keV) gamma lines.

4.5 LEGEND-200 background index

For the $0\nu\beta\beta$ decay analysis an energy window from 1930 keV to 2190 keV is considered, excluding the intervals corresponding to ^{208}Tl (2104 keV) and ^{214}Bi (2119 keV), within a ± 5 keV window, as shown in Figure 4.15. No other γ -lines are expected in this energy region.

The Figure 4.15 depicts the energy distribution after LAr veto and PSD cuts. After the application of LAr veto cut 20 events are found in the analysis energy window for 10.1 kg·yr of exposure, corresponding to a suppression factor of (4.8 ± 0.4) . This leads to a BI of 8.25×10^{-3} cts/(keV·kg·yr). Applying also the PSD cut, 1 event is found in the analysis window. Thus the obtained LEGEND-200 background index at the 68% CL is:

$$\text{BI} = \frac{\text{counts}(\Delta E)}{\varepsilon \cdot \Delta E} = 4.1_{-2.6}^{+7.3} \times 10^{-4} \text{ cts}/(\text{keV}\cdot\text{kg}\cdot\text{yr}) \quad (4.12)$$

with $\Delta E = 240$ keV being the net width of the analysis window and ε the exposure. This result is compatible with the LEGEND-200 project goal of 2×10^{-4} cts/(keV·kg·yr).

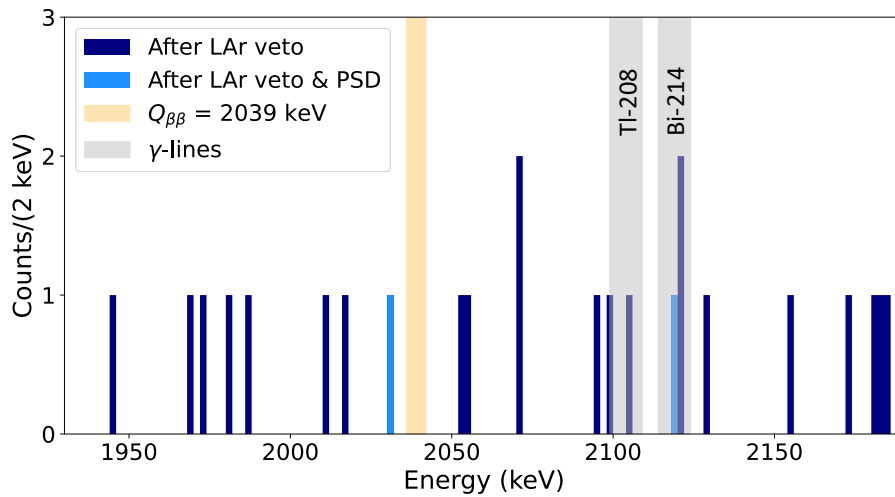


Figure 4.15: Energy of the observed events in the analysis window after LAr veto cut and PSD cut.

CHAPTER 5

LAr Instrumentation for $^{39}\text{Ar}/^{42}\text{Ar}$ Activity Estimation

A preliminary analysis has been conducted to characterize the LAr instrumentation response as an independent detector system, using relevant background decay processes from ^{39}Ar , ^{40}K and $^{42}\text{Ar}/^{42}\text{K}$. Maintaining effective background control is critical for low background experiments, such as LEGEND-200. It is crucial to comprehend all contributions to minimize and accurately estimate their impact. A noteworthy background element within the LEGEND-200 experiment is the β continuum of ^{42}K , a daughter isotope of ^{42}Ar , naturally occurring in the LAr used in the LEGEND-200 setup. Decaying through a β decay its end point is above the $Q_{\beta\beta}$ of the $0\nu\beta\beta$ decay. Understanding and addressing this particular background component is essential for the overall success and reliability of the experimental results. In the context of this thesis, a preliminary investigation has been conducted to evaluate the specific activity of ^{42}K within the LEGEND-200 LAr cryostat. The study employs the LAr instrumentation as a standalone detector system. Further future analysis are required to comprehend and validate the obtained results.

The chapter is organized as follows. Section 5.1 provides a summary of previous measurements pertaining to the ^{42}Ar specific activity. Section 5.2 details the efforts undertaken by the LEGEND-200 collaboration to mitigate the background from ^{42}K . The proposal for measuring the ^{42}Ar specific activity using the LAr instrumentation and the associated dataset is outlined in Section 5.3. In Section 5.4, the study of the LAr energy distribution, primarily influenced by the decays of ^{39}Ar , is presented, including the estimation of the light yield and resolution of the LAr instrumentation. Additionally, the ^{39}Ar specific activity is estimated by employing a simplified fitting model. Section 5.5 discusses the selection of β events from ^{42}K decays, incorporating a PSD parameter. Lastly, Section 5.6 presents and discusses the obtained results for the ^{42}Ar specific activity using a streamlined fitting approach.

5.1 Previous measurements of ^{42}Ar specific activity

Due to its long half-life of 32.9 years [100], ^{42}Ar is thoroughly mixed in the atmosphere, maintaining a constant specific activity over time. The short half-life of its daughter, ^{42}K (12.4 hours [100]), ensures that the isotopes are in secular equilibrium. Consequently, the β decays of ^{42}K , with an endpoint of 3.5 MeV [100], are more readily measurable than the β decays of ^{42}Ar , which have a lower endpoint at 599 keV [100]. Previous investigations have focused on scrutinizing the concentration of ^{42}Ar in atmospheric argon. The different

Reference	Year	Technique	Specific activity ($\mu\text{Bq}/\text{kg}$)
Ashitkov et al. [145]	1998	LAr ion. det.	< 61.4 (90% CL)
Ashitkov et al. [146]	2003	LAr ion. det.	< 43.0 (90% CL)
Barabash et al. [147]	2016	LAr ion. det.	92_{-46}^{+22}
GERDA Collaboration [148, 149]	2019	HPGe γ -spec.	$91_{-20}^{+8} - (186 \pm 39)$
DEAP Collaboration [99]	2019	Scintillation	40.4 ± 5.9

Table 5.1: Previous results on ^{42}Ar specific activities in atmospheric Ar. The different detection techniques are also indicated. Adapted from [99].

measurements of $^{42}\text{Ar}/^{42}\text{K}$ activity, as summarized in Table 5.1, reveal discrepancies and tensions among the reported results.

Ashitkov et al. conducted studies on ^{42}K decays using a LAr ionization detector [145, 146]. Subsequently, Barabash et al. reanalyzed the data [147]. In the LAr ionization detector, events in the energy range of 3.1 to 3.6 MeV are considered, capturing β emissions at the tail end of the ^{42}K spectrum. This involves subtracting expected background events. The reported central value activity is $92 \mu\text{Bq}/\text{kg}$, with the primary sources of systematic uncertainties stemming from background subtraction and energy calibration in this specific energy region.

Using a LAr scintillation detector, the DEAP-3600 Collaboration determined the specific activity of ^{42}Ar through a comprehensive fit of the electronic recoil (ER) background model. This approach, particularly sensitive in the energy region above 2.8 MeV, involved analyzing events associated with ER after applying a pulse shape discrimination. The process also incorporated a sophisticated background model to differentiate and quantify the contribution from ^{42}Ar . The resulting central value of specific activity is $40.4 \mu\text{Bq}/\text{kg}$, with a set of systematic uncertainties primarily linked to the topology corrections [99].

In the GERDA experiment the determination of ^{42}K activity involves extracting data from a comprehensive background model fit, primarily tuned to the 1524.6 keV peak counts from the ^{42}K excited state transition. Different model assumptions, varying in complexity, have led to results spanning from 91 to $186 \mu\text{Bq}/\text{kg}$ [148, 149]. Given the substantial increase in background events introduced by ^{42}K decays for $0\nu\beta\beta$ decay searches, the GERDA collaboration conducted an extensive background measurement and mitigation campaign. These efforts are detailed in the next section, as the findings are crucial and have been taken into account for the ongoing LEGEND-200 experiment.

5.2 LEGEND-200 ^{42}K background mitigation

The LEGEND-200 ^{42}K background mitigation strategy builds upon the insights gained from extensive studies conducted during the GERDA experiment. These studies serve as a foundational framework for addressing and minimizing the impact of ^{42}K background in the context of the LEGEND-200 experiment.

During the commissioning runs of GERDA Phase I (2010-2011), the intensity of the 1525 keV gamma line, stemming from ^{42}K , was found to surpass the expected levels. This observation was based on the assumption of a homogeneous distribution of ^{42}Ar , considering a natural abundance of $< 43 \mu\text{Bq}/\text{kg}$. A similar discrepancy was observed in the measurements conducted in the LArGe test facility [150], operating within the context of GERDA. The studies presented in [148] indicate that the increased ^{42}K background could be attributed to an accumulation effect: a fraction of ^{42}K daughters became charged

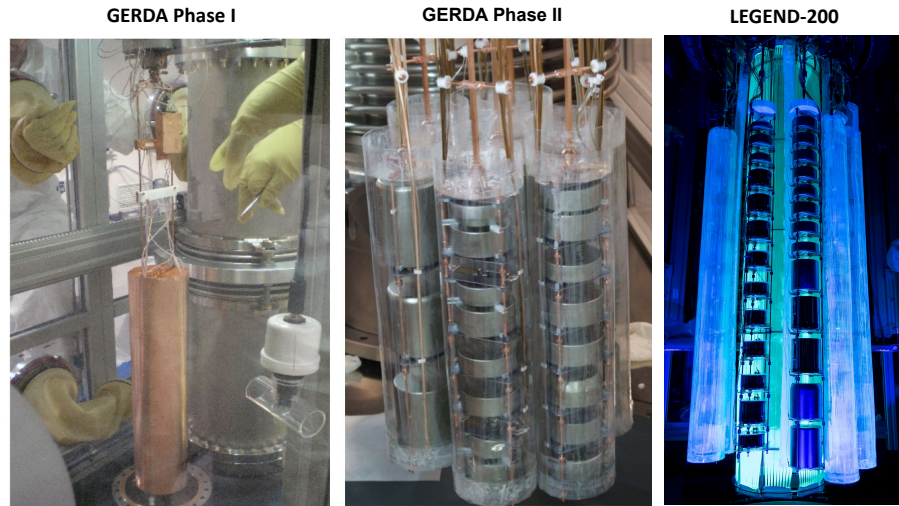


Figure 5.1: Mechanical barrier for ^{42}K background mitigation in GERDA Phase I (copper MS), GERDA Phase II (NMS) and LEGEND-200 (NMS). Images from [64, 151].

following the initial ^{42}Ar decay, and the resulting ^{42}K ions retained their positive charge long enough to move within the electric field generated in LAr by the high voltages (up to 5 kV) of the HPGe detectors. This attraction of ^{42}K ions towards the n^+ surface of the detectors creates a non-uniform distribution of ^{42}K events in LAr and thus an increase of ^{42}Ar activity measured by HPGe detectors.

A significant reduction in the background contribution from the ^{42}K decay was achieved by enclosing the HPGe detector strings with a cylinder made of thin copper foil, referred to as the mini-shroud (MS) [64], as depicted in Figure 5.1 left picture. The MS effectively screens the electric field of the HPGe detectors and serves as a mechanical barrier against a convective drift of the ions in the LAr. This prevents the accumulation of ^{42}K ions on detector surfaces, thereby reducing the background level of ^{42}K . This approach hasn't been used in the GERDA Phase II for two main reasons. Firstly, the LAr scintillation light generated inside the copper MS would be blocked from detection by the LAr instrumentation, significantly compromising the veto efficiency. Secondly, the radiopurity of the copper MS used in GERDA Phase I did not meet the more stringent radiopurity requirements imposed in Phase II.

The solution chosen was the nylon mini-shroud (NMS), made of a thin nylon film [71, 151], as shown in the central picture of Figure 5.1. It was selected as the construction material due to its robustness, durability, flexibility, good transparency for visible light and very low intrinsic radioactivity [152, 153]. The NMS did not screen the electric field of the HPGe detectors; instead, it works as a mechanical barrier to prevent the drift of ^{42}K ions towards the n^+ electrodes of the HPGe detectors. The NMS enveloped the detector but is not tight to prevent liquid argon from pouring inside during the immersion. In this configuration, the collected ^{42}K atoms undergoes decay on the surface of the nylon foil, positioned several millimeters away from the detector. This setup ensures that β particles are attenuated by the surrounding LAr¹.

Since the nylon is opaque for deep ultraviolet radiation (below 300 nm), to allow light to pass through the NMS it was covered with a wavelength shifter [71]. The coating has been applied by brushing both sides of nylon foils with TPB, which allows to shift the LAr

¹The path length of ^{42}K β particles in LAr is less than 1.6 cm, but the generated Bremsstrahlung photons can travel up to 10 cm.

scintillation light inside and outside the NMS to be detectable by the LAr instrumentation. This strategic use of a wavelength shifter enhances the overall sensitivity and functionality of the NMS within the experimental setup.

The same NMS are adopted for LEGEND-200 experiment to provide a mechanical barrier towards the collection of ^{42}K ions by the HPGe detectors. The right-most picture of Figure 5.1 shows the LEGEND-200 HPGe detector strings, few of them inside NMS, under UV light exposure. To completely prevent ions from drifting towards the HPGe detectors, the complete encapsulation can be employed. The ongoing investigation involves encapsulating HPGe detectors using 3D-printed technologies with low-background material, such as PEN² [154].

5.3 LAr instrumentation data for ^{42}K activity estimation

To counter the potential inaccuracies in event counting arising from the high bias voltage of the HPGe detector, which tends to attract ^{42}K ions, it has been decided to use the LAr instrumentation. The estimation of the specific activity of ^{42}Ar is thus derived by extrapolating the activity of ^{42}K , based on a specific set of LEGEND-200 data, containing LAr triggered events.

To carry out this estimation, a modeling of the LAr energy spectrum observed by the LAr instrumentation has been performed. A PSD method has been developed to extract the β/γ events and a model based on the theoretical β distribution linked to the decay of ^{42}K has been used. Following this, the estimated specific activity of ^{42}K is corrected for the half-life of ^{42}Ar . As the theoretical model offers only a preliminary estimate, future simulation will be required to study the LAr detection efficiency and validate the obtained result.

LAr instrumentation data selection

For the analysis of ^{42}K specific activity, a released dataset collected between April 15 and May 3 (2023), corresponding to a runs-time of about 388 hours, has been selected. This dataset is the only one (from released data) which includes events triggered by both HPGe detectors and LAr instrumentation (see Section 2.2.3). The dataset includes a total of 1.2 million events across the runs.

Due to the significant crosstalk observed between the pulser signals and the LAr instrumentation [137, 155] (Appendix H, Figure H.1), events in coincidence with the pulser injection has been excluded. Moreover, muon events detected by the PMT Cherenkov detectors have been also excluded (Appendix H, Figure H.2). In total, $8 \cdot 10^4$ events were rejected, constituting 6.7% of the total number of events.

Upon identifying pulser and muon traces, it is also essential for the analysis to differentiate between HPGe and LAr triggered events. To achieve this distinction, an energy threshold of 50 keV has been applied on HPGe traces to tag them as Ge triggered events and separate them from LAr triggered events.

5.3.1 Event trigger evaluation

For a more precise estimation of event energy, it is essential to accurately determine the trigger position for each event. To accomplish this, it has been decided to avoid relying on

²Polyethylene 2,6-naphthalate.

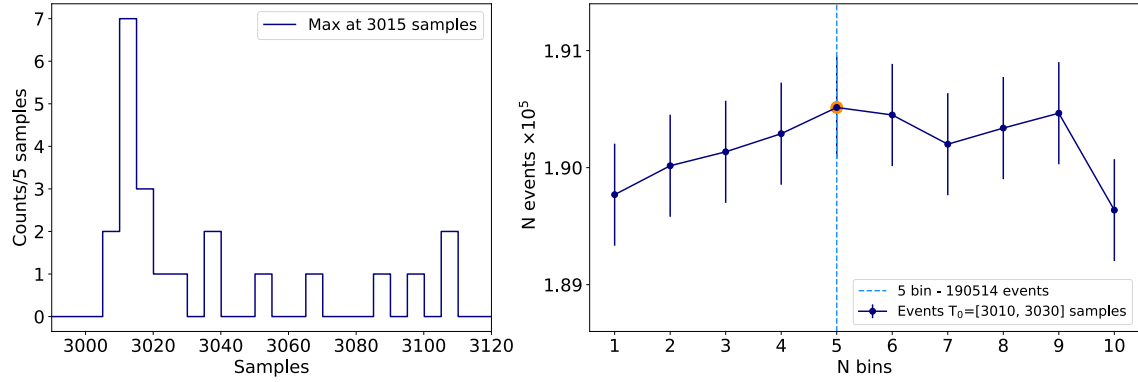


Figure 5.2: **Left:** example of the t_0 distribution of the most energetic pulse for all SiPM channels; the position of the maximum defines the T_0 of an event. **Right:** optimization of number of bins employed for t_0 distribution, using LAr triggered events.

the trigger from the DAQ and, instead, to calculate it through offline analysis.

To obtain the trigger position for an event, first the time position (t_0) for each SiPM pulse has been estimated from the timing of the most energetic pulse within the $130 \mu\text{s}$ acquisition window. An example of t_0 distribution for one event is presented in Figure 5.2 Left. The trigger of the event (T_0) is then defined as the most frequently occurring t_0 within a window of 5 samples (80 ns), requiring a minimum coincidence of 2 SiPM channels. The number of samples has been optimized by maximizing the number of events in the time window of the LAr T_0 distribution corresponding to the trigger position set by the DAQ, (3020 ± 10) samples (Figure 5.2 Right). Whereas, the traces which do not meet the requirement of 2 SiPM channels in coincidence, are tagged as no-coincidence and are excluded from the analysis.

The distribution of T_0 within the acquisition window of $130 \mu\text{s}$ is provided in Figure 5.3, distinguishing between Ge and LAr triggered events. The dataset comprises approximately $1.5 \cdot 10^5$ Ge triggered events and $6.6 \cdot 10^5$ events triggered by LAr. In Table 5.2 the number of events of each type are reported. As evident, no-coincidence events make up 25.5% of the overall events. This includes events arising from HPGe detector discharges and events triggered by the Ge detectors that fail to meet the condition of having 2 SiPM channels in coincidence. Both of these categories should be excluded, as our focus is on the LAr triggered events.

Total	1 202 660	
Pulser	75 122	6.2 %
Muons	5 118	0.4 %
Ge	150 937	12.6 %
LAr	664 623	55.3 %
No-coincidence	306 860	25.5 %

Table 5.2: Number of total events for each category.

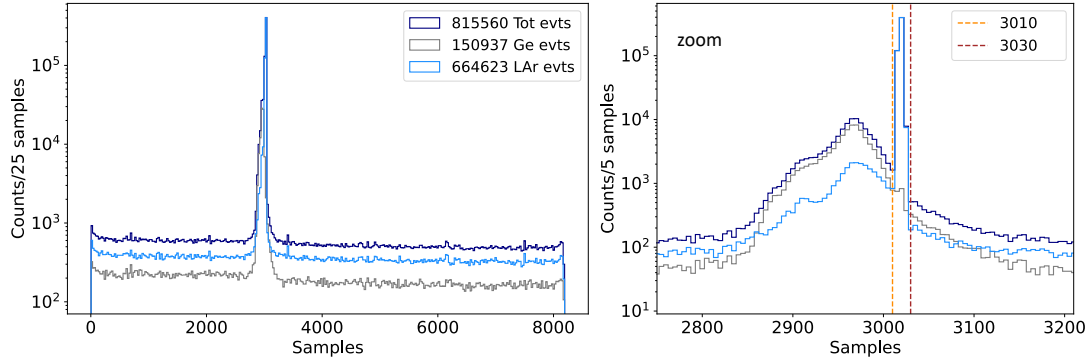


Figure 5.3: Left: T_0 distribution of the LAr events; the contribution of Ge and LAr triggered events are distinguished; the total number corresponds to the sum of the two contributions. Right: zoom from 2700 to 3200 samples of the T_0 distribution; the cuts to optimize the number of bins used for T_0 evaluation are highlighted by two vertical dashed lines.

5.3.2 LAr energy distribution

The LAr energy distribution is determined using the energies values estimated by the DPLMS optimum filter detailed in Section 4.2. The events energies are summed within a $6 \mu\text{s}$ time window, as explained in Section 4.4, across all operational SiPM channels. The resulting LAr energy distribution is illustrated in Figure 5.4, with separate contributions for Ge trigger events and LAr trigger events. The comparison between the LAr energy distribution estimated using the DPLMS method and the Hypercurrent estimator is provided in Appendix I, showing a good agreement between the two methods.

The events triggered by HPGe detectors exhibit a substantial contribution within a relatively low energy range, primarily up to 500 PE. In contrast, events triggered by the LAr instrumentation dominate the high energy spectrum. The lower energy spectrum is predominantly influenced by ^{39}Ar β decays. To comprehend the origin of the two distributions at higher energies, one ranging from 100 to 500 PE and the other from 500 to 1300 PE, pulse shape discrimination is required. This topic will be explored and discussed in details in Section 5.5.

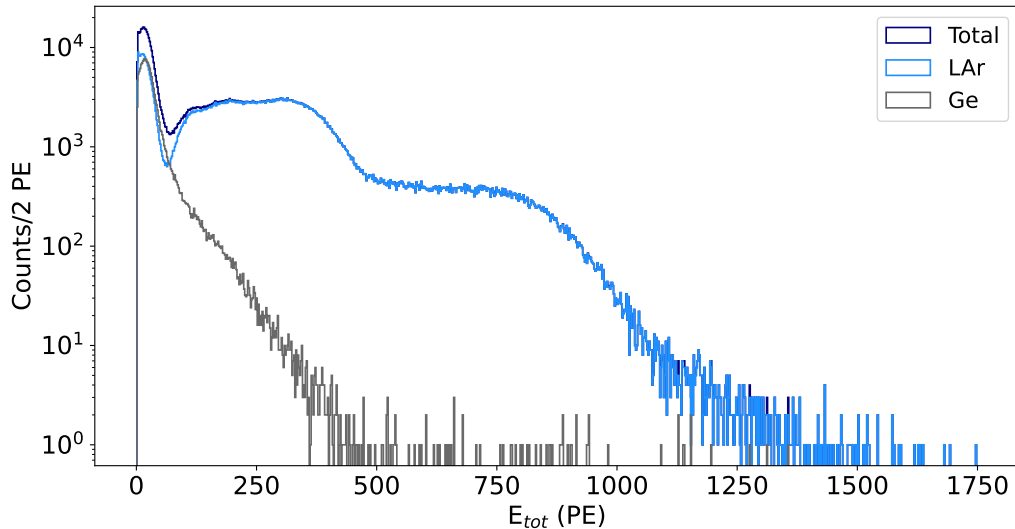


Figure 5.4: LAr instrumentation energy distribution summed in $6 \mu\text{s}$ time window among all working SiPM channels. The contribution of Ge and LAr triggered events are separated.

5.4 ^{39}Ar energy distribution study

^{39}Ar , a naturally occurring β -emitter, is present in the atmospheric argon used in LEGEND-200, as discussed in Section 3.1. The β decays of ^{39}Ar offer a high-statistics sample of LAr scintillation in response to electrons with energies falling between the trigger threshold of the HPGe detectors and the ^{39}Ar endpoint at 565 keV [97]. Consequently, the LAr energy distribution up to 100 PE, involving Ge triggered events, can be used for the estimation of the Light Yield (LY) and the resolution of the LAr instrumentation.

Accidental coincidence event selection

It is important to note that HPGe detectors can be triggered by background processes unrelated to ^{39}Ar , such as radioactive decays of ^{208}Tl and ^{214}Bi , which deposit only a fraction of the energy in LAr. To ensure a reliable sample of ^{39}Ar , random coincidence events have been selected as follows. In the T_0 distribution, a constant contribution is evident across the entire time range, as visible in Figure 5.5, which can be attributed to accidental coincidence events. Since the T_0 distribution within the time window [2750, 3200] samples does not exhibit a Gaussian behavior, as illustrated in Figure 5.3 (Right), it is not feasible to apply a Gaussian fit to select cuts based on standard deviation. Consequently, the cuts have been determined by considering the boundaries of the constant T_0 region: events with T_0 occurring before 2750 samples and after 3200 samples from Ge triggered events have been taken into account.

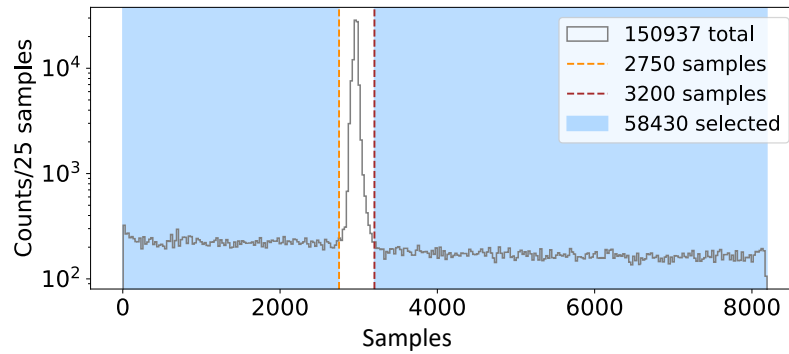


Figure 5.5: T_0 distribution of Ge triggered events. The LAr accidental coincidences region is highlighted.

^{39}Ar fitting model

To model the ^{39}Ar spectrum, a theoretical beta spectrum is employed from [156], as illustrated in Figure 5.6 Left. To account for the energy resolution of the LAr instrumentation, this theoretical spectrum is convoluted with a Gaussian function centered at zero, as depicted in Figure 5.6 Right. Additionally, a linear function is assumed to represent the background component.

The simplified model for fitting the ^{39}Ar β spectrum can be expressed as follows:

$$\left\{ [N(^{39}\text{Ar}) \cdot \beta(^{39}\text{Ar}) \cdot LY] * \left[\frac{1}{\sqrt{2\pi\sigma^2(x)}} \exp\left(\frac{-x^2}{2\sigma^2(x)}\right) \right] \right\} + p \cdot x + q. \quad (5.1)$$

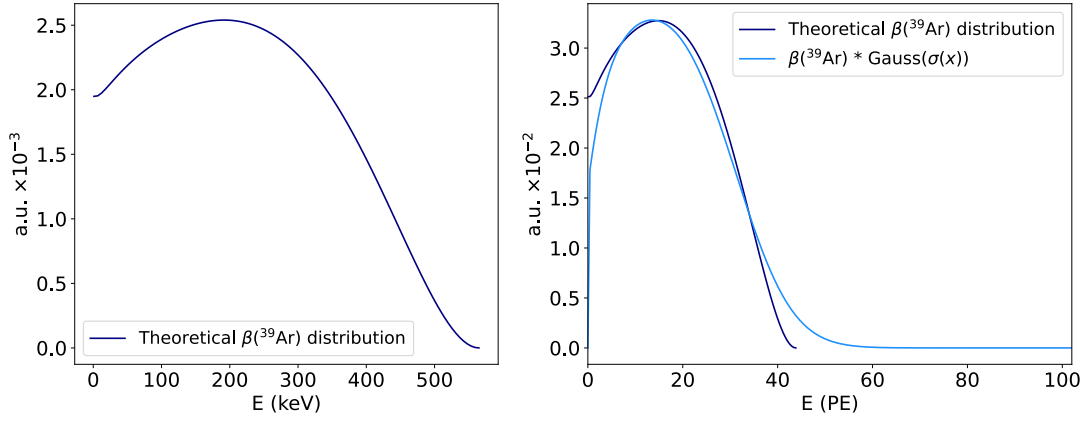


Figure 5.6: Left: normalized ^{39}Ar theoretical β distribution from [156]. Right: normalized theoretical β distribution of ^{39}Ar compared to its convolution with a Gaussian function using the resolution defined in expression (5.2).

The energy resolution of the LAr instrumentation is empirically described by the following function [157]:

$$\sigma^2(x) = a + b \cdot x + c \cdot x^2. \quad (5.2)$$

The three terms accounts from non-uniform light collection (a), statistical fluctuations in the light production (b) and electronic noise (c). Consequently, the free parameters of this model are: the number of ^{39}Ar events, $N(^{39}\text{Ar})$, the LY , the three parameters of the energy resolution (a, b, c) and the two parameters of the linear background component (p and q).

A binned extended likelihood fitting procedure has been adopted to the complete model using a histogram with 0.5 PE bins in the interval from 10 PE to 100 PE. The fit range starts at 10 PE since the very low energy events deviate from the expected values. This deviation is attributed to the loss of photons from various regions, which needs an accurate modeling at lower energies.

The outcomes of the fit are illustrated in Figure 5.7. The chosen goodness of fit figure of merit is the χ^2 normalized to the number of degrees of freedom (ndof). The figure of merit for this fit is $\chi^2/\text{ndof} = 1.44$ and the residuals, presented in units of sigma in the lower panel of Figure 5.7, indicate that the fit model describes the data within a 2.5σ deviation, with larger deviation observed at energies up to 25 PE and higher than 60 PE where the statistics is lower.

The systematic uncertainties for $N(^{39}\text{Ar})$, LY and $\sigma(x)$ have been determined by varying the fit range, the histogram binning and by employing an alternative background component. A constant background component has been used instead of the linear function assumed in Equation (5.1). Two scenarios have been considered for the fit range: one starting from 5 PE and the other from 15 PE. The histogram binning has been changed to 1 PE. It has been verified that varying one parameter (LY or $\sigma(x)$) while estimating the other does not affect the evaluation of the relative uncertainty. The obtained results are discussed in the following sub-sections.

5.4.1 LAr instrumentation LY and resolution

The fit model is sensitive to the LY parameter, which is defined as the ratio of the number of scintillation photons to the deposited energy. This sensitivity arises from the definite

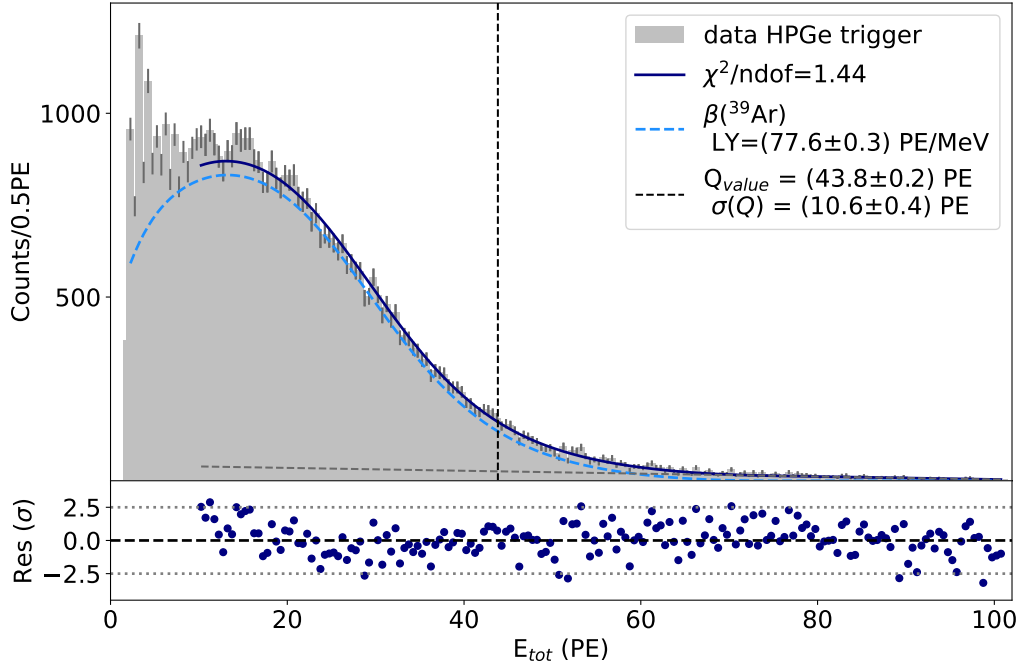


Figure 5.7: Fit of the data in the low energy range derived from the Ge triggered events and using the fitting model of Equation (5.1). The individual components of the model are displayed. The lower panel illustrates the residuals in terms of the number of sigma.

value of the end point of the ³⁹Ar β spectrum (565 keV). Consequently, the LY has been extracted from the fit, and it acts as an indicator of the scintillation efficiency within the LAr instrumentation. The resulting LY value is:

$$\text{LY}({}^{39}\text{Ar}) = (77.6 \pm 0.3_{\text{stat}} \pm 5.2_{\text{syst}}) \text{ PE/MeV}. \quad (5.3)$$

The systematic uncertainties are outlined in Table 5.3, revealing a significant source of uncertainty arising from the choice of the energy range and the histogram binning employed in the fitting process.

Item	absolute uncertainty (PE/MeV)	relative error (%)
Hist bins	2.5	3.2
Fit range	2.6	3.35
Background model	0.1	0.13
Total	5.2	6.7

Table 5.3: Systematic uncertainties for the LY estimation.

The determined LY value is consistent within 1σ with the LY value of (80.1 ± 0.5) PE/MeV obtained in [127], where the measurement utilized the Compton continuum from a ¹³⁷Cs source. Notably, the experimental setup for that measurement comprised 60 kg of HPGe detectors organized in 4 strings. In the present configuration with 10 strings, one has to also take into account the shadowing effect of additional HPGe detector strings, i.e. the additional light absorption from the extra detector mass. This is expected to reduce the LY extracted from the data used here. A precise calibration for LY estimation is planned also for the current setup. The accurate determination of LY is important to understand the response of the detector to incident radiation and is particularly relevant in the context of assessing detector performance and calibrating energy measurements.

LAr instrumentation resolution

The resolution of the LAr instrumentation at the Q-value of ^{39}Ar β spectrum of 565 keV obtained from the fit with the assumed model is:

$$\frac{\sigma(Q(^{39}\text{Ar}))}{Q(^{39}\text{Ar})} = (24 \pm 1_{stat} \pm 8_{syst})\%. \quad (5.4)$$

Table 5.4 provides an overview of systematic uncertainties, highlighting a significant source of uncertainty originating from the chosen background model for the simplified fitting model of Equation (5.1). The resolution curve, generated using the parameters a, b, c from the fit, is presented in Figure 5.8.

Item	absolute uncertainty (%)	relative error (%)
Hist bins	2	8
Fit range	2	8
Background model	4	17
Total	8	33

Table 5.4: Systematic uncertainties for the LAr instrumentation resolution estimation.

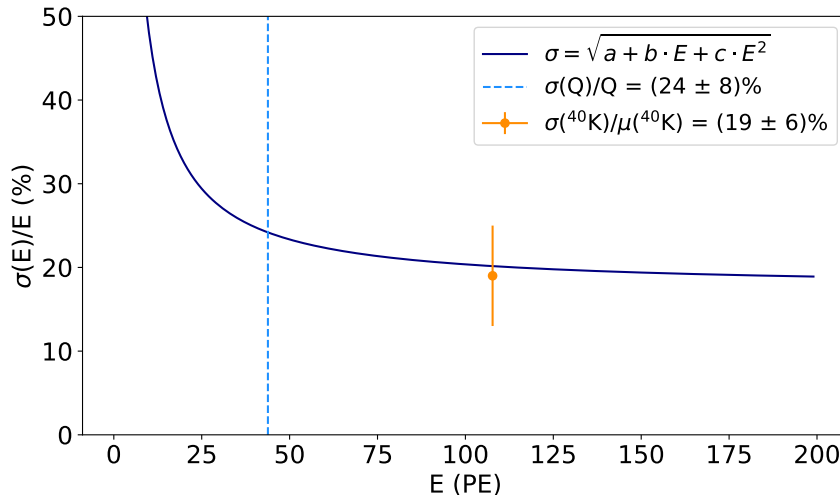


Figure 5.8: Energy resolution of the LAr instrumentation from Equation (5.2) with a, b, c parameters obtained from the fit of ^{39}Ar β spectrum. The resolution value of the ^{40}K gamma line is reported and will be discussed in Section 5.6.

5.4.2 ^{39}Ar activity estimation

The number of ^{39}Ar events extracted from the fit has been used to evaluate a preliminary ^{39}Ar specific activity within the WLSR volume. The specific activity of ^{39}Ar can be estimated by considering the ratio between the measured event rate and the LAr mass:

$$A(^{39}\text{Ar}) = \frac{R(^{39}\text{Ar})}{M(\text{LAr})}. \quad (5.5)$$

The ^{39}Ar event rate can be determined by taking into account the extracted number of ^{39}Ar from the fit:

$$N(^{39}\text{Ar}) = 51615 \pm 338, \quad (5.6)$$

divided by the acquisition time, that can be calculated as the total event number multiplied by the acquisition window. The obtained rate of ³⁹Ar event is:

$$R(^{39}\text{Ar}) = \frac{N(^{39}\text{Ar})}{T} = \frac{N(^{39}\text{Ar})}{N(\text{HPGe}) \cdot 130 \mu\text{s}} = (6740 \pm 45) \text{ Hz} \quad (5.7)$$

The mass of LAr within the WLSR can be calculated by considering the volume of the WLSR and the density of LAr:

$$M(\text{LAr})_{\text{WLSR}} = \rho_{\text{LAr}} \cdot V_{\text{WLSR}} = 6160 \text{ kg.} \quad (5.8)$$

The LAr density (ρ_{LAr}) of 1384.9 kg/m³ at a temperature of 89 K and a pressure of 1.2 bar has been considered³, which are the working condition of LEGEND-200 LAr cryostat. For the volume calculation the following WLSR dimensions have been considered: a height of 3 m and a diameter of 1.374 m.

LAr mass consideration

The LAr mass obtained in Equation (5.8) is also incorporating the mass in the WLSR volume occupied by HPGe detectors and the fiber shrouds mounted on copper frames. The total mass of the HPGe detectors is 142 kg, corresponding to a LAr mass of about 37 kg ($\rho_{\text{Ge}} = 5.32 \text{ g/cm}^3$). The copper components, forming both the outer and inner barrel, amount to about 10 kg in total and additional copper components such as the copper plate, source vessels, and HPGe mounting structure contribute another 10 kg, resulting in a total LAr mass of 3 kg ($\rho_{\text{Cu}} = 8.96 \text{ g/cm}^3$). The fiber modules collectively weigh about 4 kg, equivalent to a LAr mass of 5.5 kg ($\rho_{\text{fibers}} = 1.05 \text{ g/cm}^3$). Therefore, a total of about 50 kg of LAr mass is attributed to these primary components.

Subtracting the total LAr mass associated with these main components from the calculation of the LAr mass inside the WLSR volume yields a LAr mass of:

$$M(\text{LAr}) = (6110 \pm 150) \text{ kg.} \quad (5.9)$$

The uncertainty of 2.5% takes into account the contributions from other components within the detector systems and the volumes both below and above the detector systems, where the probability of scintillation light reaching the detector systems is reduced.

Correction of ³⁹Ar lifetime

A correction is necessary for the measured specific activity determined from the exponential fit to account for the age of the argon, as the specific activity is exponentially decaying with the lifetime of ³⁹Ar: $T_{1/2} = (268 \pm 8) \text{ y}$ [97]. The correction factor is calculated as:

$$\eta_t = 2^{\frac{t_{\text{LAr}}}{T_{1/2}}}, \quad (5.10)$$

where t_{LAr} represents the average time between the atmospheric extraction of argon and the beginning of the data considered for this analysis. The time from atmospheric extraction by the vendor to the start of data taking is estimated as 2 yr but has a large uncertainty. The cosmogenic activation of ³⁹Ar during the time after the argon was extracted from the atmosphere is considered negligible.

³<http://webbook.nist.gov/chemistry/fluid/>

The average age during the dataset of (2.0 ± 0.3) yr corrects for 0.52% the ^{39}Ar activity:

$$\eta_t = (1.0052 \pm 0.0015). \quad (5.11)$$

The large uncertainty is due to the uncertainty in the ^{39}Ar lifetime.

^{39}Ar specific activity estimation

The specific activity, derived from the rate of events obtained in Equation (5.7) and the estimated LAr mass in Equation (5.9), is given by:

$$A(^{39}\text{Ar}) = \frac{R(^{39}\text{Ar})}{M(\text{LAr})} = (1.103 \pm 0.034_{stat}) \text{ Bq/kg} \quad (5.12)$$

Correcting the obtained value with the η_t factor of Equation (5.11), the corrected specific activity of ^{39}Ar is:

$$A(^{39}\text{Ar})_{corr} = (1.109 \pm 0.034_{stat} \pm 0.106_{syst}) \text{ Bq/kg} \quad (5.13)$$

Table 5.5 presents an overview of systematic uncertainties, emphasizing a significant source of uncertainty arising from the chosen background component in the simplified fitting model of Equation (5.1). To mitigate these uncertainties, future simulations are essential for accurately modeling the background. Another significant contributor to uncertainty is the mass of LAr.

It is crucial to note that despite these challenges, the result obtained from the simplified fitting model aligns within a 1σ range with independent measurements, as outlined in Table 5.6. This agreement underscores the reliability and consistency of the obtained result in the broader context of existing measurements.

Item	absolute uncertainty (PE/keV)	relative error (%)
Hist bins	0.005	0.45
Fit range	0.0045	0.4
Background model	0.07	6
LAr mass	0.026	2
Total	0.106	9

Table 5.5: Systematic uncertainties of the ^{39}Ar specific activity estimation.

Reference	Year	Specific activity (Bq/kg)
WARP Collaboration [95]	2006	$(1.01 \pm 0.02_{stat} \pm 0.08_{syst})$
ArDM Collaboration [158]	2017	(0.95 ± 0.05)
DEAP Collaboration [96]	2023	$(0.964 \pm 0.001_{stat} \pm 0.024_{syst})$
This work	2023	$(1.109 \pm 0.034_{stat} \pm 0.106_{syst})$

Table 5.6: Previous results on ^{39}Ar specific activities in atmospheric Ar.

5.5 Pulse shape discrimination in LAr

The good LY of the LAr instrumentation and its capability to detect time-resolved scintillation pulses within a scintillation event allow for the application of a PSD parameter. This parameter facilitates the discrimination of various background types in the LAr energy spectrum.

To distinguish between different types of radiation losing energy in the LAr, a PSD parameter, called F_{prompt} [159], has been employed. As elaborated in Section 3.2, the scintillation event is distinctly characterized by two excimer states: the singlet state and the triplet state. The population ratio of excimers in the singlet (N_s) and triplet states (N_t) plays a pivotal role in discriminating backgrounds in LAr detectors. This discrimination is achieved as the ratio depends on the linear energy transfer dE/dx of the radiation deposited in LAr and the nature of the primary radiation responsible for the scintillation event.

The F_{prompt} parameter is defined as the ratio of the light emitted in the singlet component (N_s), or prompt light, to the total light intensity of an event ($N = N_s + N_t$):

$$F_{prompt} = \frac{N_s}{N}. \quad (5.14)$$

In the LEGEND-200 data processing of SiPM from the LAr instrumentation (see Section 4.2.3) for each scintillation event is extracted the time t_i and the energy $E_i(t_i)$ of each pulse. Thus, to calculate the energy of an event, the sum of the energies over the pulses in a trace for each SiPM has to be performed:

$$E_j = \sum_{t_i=T_0-1\mu s}^{T_0+5\mu s} E_{i,j}(t_i), \quad (5.15)$$

where i indicates the time in which a pulse is present in the $6 \mu s$ reconstruction range [$T_0 - 1 \mu s, T_0 + 5 \mu s$] (as described in Section 4.4), while j indicates the SiPM channels. The total light intensity of an event is then evaluated as the sum over the energies of all SiPM channels:

$$E_{evt} = \sum_{j=1}^{N_{SiPM}} E_j. \quad (5.16)$$

The the prompt light N_s is defined as:

$$N_s = \sum_{j=1}^{N_{SiPM}} \sum_{t_i=T_0}^{T_0+\Delta t} E_{i,j}(t_i), \quad (5.17)$$

where Δt , called prompt window, is the time window in which pulses pertain to the singlet component. The selection of the Δt is essential to achieve a proper separation of the population that can be attributed to β/α events in the F_{prompt} vs energy space. For this purpose the Δt has been tuned by maximizing the following figure-of-merit (FOM):

$$FOM = \frac{(\mu_\alpha - \mu_{\beta/\gamma})}{\sqrt{(\sigma_\alpha^2 + \sigma_{\beta/\gamma}^2)}}. \quad (5.18)$$

where μ_α and σ_α are the mean value and the standard deviation of the α distribution, while $\mu_{\beta/\gamma}$ and $\sigma_{\beta/\gamma}$ are the mean value and the standard deviation of β/γ distribution. These

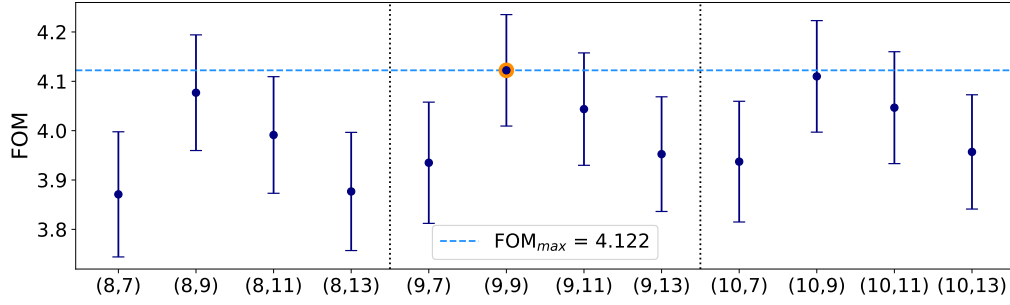


Figure 5.9: Combinations of number of samples before and after T_0 for FOM values exceeding 3.7. The maximum FOM value is achieved by the combination (9, 9) and is indicated by the horizontal dashed line.

values have been extracted by performing a double Gaussian fit to the two distributions in the energy range from 60 PE to 300 PE. The study involves varying the number of samples before T_0 from 2 to 10 (with a step of 1) and the number of samples after T_0 from 5 to 15 (with a step of 2). The double Gaussian fit has been systematically performed for all possible combinations.

In Figure 5.9, the FOM values are presented for combinations surpassing a value of 3.7. Among these combinations, the optimal configuration is identified as (9, 9), meaning that 9 samples are included for the F_{prompt} calculation, both before and after the T_0 for each event. This time interval corresponds to 288 ns. The selection driven by maximizing the FOM, guarantees an efficient discrimination between α and β/γ events.

5.5.1 Event PSD distribution

Using the PSD parameter F_{prompt} , defined in expression (5.14), and the optimized prompt window for singlet component of the SiPM pulses, the plot of F_{prompt} versus the LAr total energy is presented in Figure 5.10. For this plot both Ge and LAr trigger events are considered. Five distinct components can be identified:

- The high F_{prompt} band is likely associated with the fast scintillation light produced by the PEN holders of the HPGe detectors or from the TPB-coated NMS. By building F_{prompt} on the LAr instrumentation commissioning data, where such detector elements had not been assembled yet, one verifies that this band is indeed absent. Thus this represents an artificial band, not associated with LAr scintillation.
- The band with a mean value of (0.83 ± 0.05) is associated with events originated from α particles [159]. The significant number of events clustered within this band raises the possibility of a contribution from a contamination with an α -emitter. An analysis for possible contaminations from ^{22}Ra daughters has been conducted, looking for time coincident energy releases in LAr compatible with the rapidly subsequent decay of ^{214}Bi (β particles) and then ^{214}Po (α particles). This is known as the Bi-Po method. The Bi-Po analysis has been conducted in [127], yielding an activity of $(32 \pm 6) \mu\text{Bq}$. This does not explain the high number of α particles observed. Furthermore, the PSD parameter has been independently applied to both the inner and outer barrel, as well as to the top and bottom SiPM channels. The results reveal a significant contribution to the α band seen by the outer barrel and the bottom SiPM channels (see Appendix J). Ongoing investigations are being conducted to identify the source of α contamination.

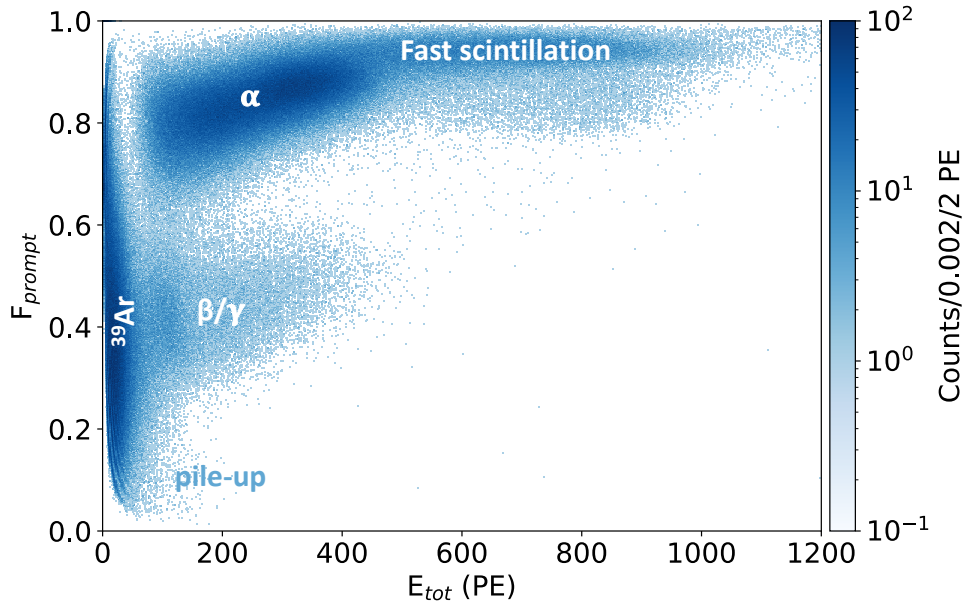


Figure 5.10: PSD distribution of Ge and LAr trigger events. Five distinct components are indicated.

- The band with a mean value of (0.41 ± 0.01) is linked to β/γ particles. It appears higher than the expected value of 0.3 [159], possibly attributable to the large prompt integration window.
- The vertical F_{prompt} band observed for energies below 100 PE is attributed to accidental coincidences, mainly due to ^{39}Ar decays. This distribution spreads in F_{prompt} due to the random occurrence of the trigger position for an ^{39}Ar pulse in relation to the main event trigger.
- The low F_{prompt} band, below 0.2, is primarily attributed to pile-up events.

5.6 $^{42}\text{Ar}/^{42}\text{K}$ activity estimation

For the analysis of the ^{42}K specific activity, only events triggered by the LAr instrumentation within the time window of 2800 to 3100 samples in the T_0 distribution are considered, as illustrated in Figure 5.11. As the T_0 distribution within the time window [2800, 3100] samples does not exhibit a Gaussian behavior, it is not appropriate to apply a Gaussian fit to select cuts based on standard deviation. As a result, the cuts have been established by taking into account the boundaries of the peaked T_0 region. These cuts ensure an efficiency of 99% in selecting events within the β/γ band above an energy of 100 PE and the F_{prompt} cuts calculated below.

The β/γ events are selected by considering a specific F_{prompt} range. This is extracted by performing a Gaussian fit in the F_{prompt} range from 0 to 1, and for energies ranging from 60 to 300 PE. An asymmetrical cut to separate the β/γ band from pile-up and α events has been chosen to ensure that 99% of events fall within the β/γ band. A left cut of 3σ from the mean value of β/γ distribution and a right cut of 2.4σ are employed, as shown in Figure 5.12.

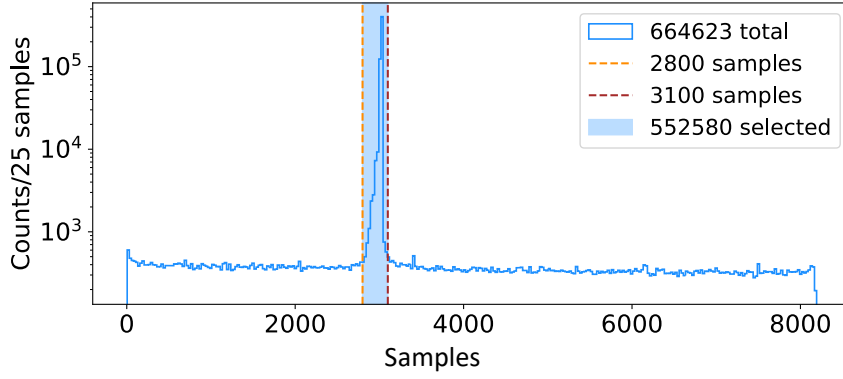


Figure 5.11: Left: T_0 distribution of the LAr triggered events. The T_0 region used for the analysis is highlighted.

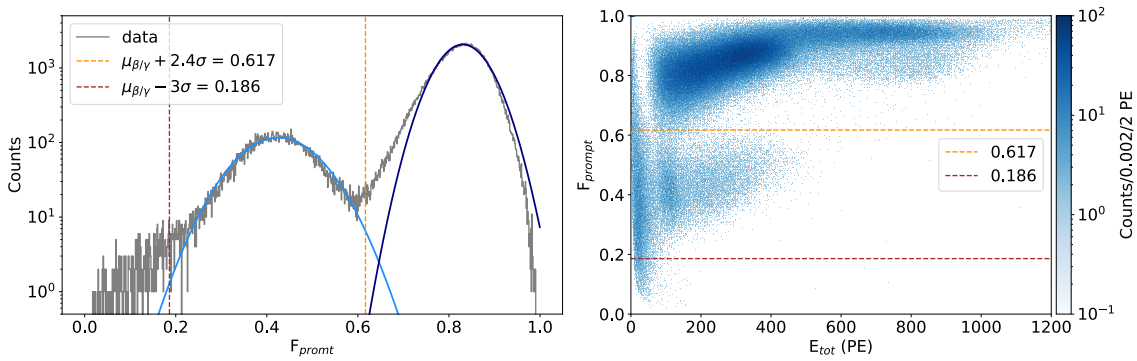


Figure 5.12: Left: double Gaussian fit applied to the α and β/γ distributions within the energy range from 60 PE to 300 PE. The two cuts which allow to select 99% of events in the β/γ band are indicated by two vertical dashed lines. **Right:** PSD distribution of LAr triggered events with T_0 in [2800, 3100] samples time window. The two cuts to select the β/γ band are indicated by two horizontal dashed lines.

The resulting cut values are:

$$\text{Pile-up cut} = \mu_{\beta/\gamma} - 3\sigma = 0.186, \quad (5.19)$$

$$\alpha\text{-cut} = \mu_{\beta/\gamma} + 2.4\sigma = 0.617. \quad (5.20)$$

Therefore, events falling within the F_{prompt} window of [0.186, 0.617] are considered for the determination of ^{42}K specific activity. The resulting β/γ band is then projected onto the x-axis, showing the energy spectrum of Figure 5.13 Left. In this plot, a distribution peaking at around 100 PE, can be observed. Considering the LY estimated in sub-Section 5.4.1, this distribution can be attributed to the ^{40}K gamma line at 1460.8 keV (see decay scheme in Figure 4.13).

5.6.1 Light yield and resolution cross-check from ^{40}K gamma line

Assuming that the distribution around 100 PE corresponds to the ^{40}K gamma line, a Gaussian function has been employed to model the energy spectrum within the range of 60 to 150 PE. A fit has been then performed to extract the LY and the resolution. This serves as a cross-check with the results obtained in Section 5.4.1 based on the ^{39}Ar β spectrum fit. Additionally, to enhance the selection of ^{40}K events and reduce accidental coincidence

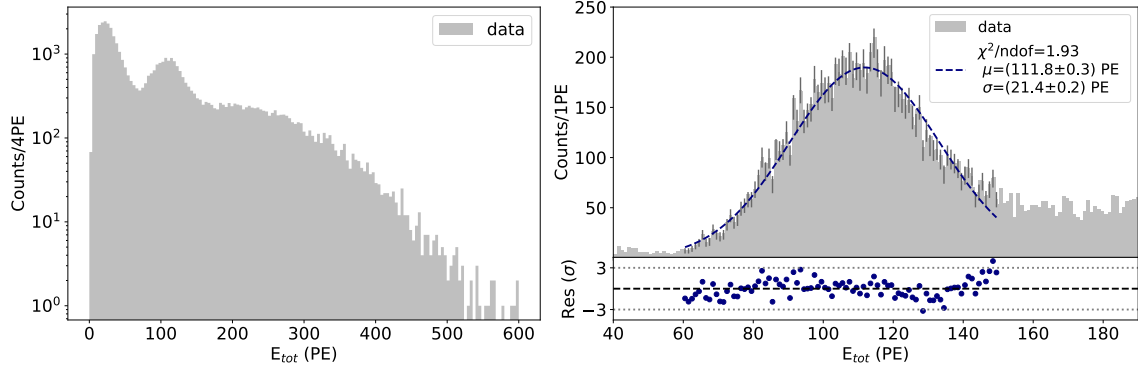


Figure 5.13: **Left:** energy spectrum of LAr triggered events, after the selection of β/γ events **Right:** fit of the ^{40}K distribution in the energy range from 60 to 150 PE. The lower panel illustrates the residuals in terms of number of sigma.

contributions below 50 PE, only events within the T_0 range of 3010 to 3030 samples are considered.

The results of the fit are displayed in Figure 5.13 Right. The goodness-of-fit parameter is $\chi^2/\text{ndof} = 1.93$, and the residuals, expressed in units of sigma in the lower panel, indicate that the fit describes the data within a 3σ deviation. A greater deviation is observed for energies beyond 140 PE, which can be attributed to the presence of an additional component not considered in the current model.

The systematic uncertainties have been evaluated by considering different fit ranges and binning, with the primary source of uncertainty arising from the range chosen for the fit. The obtained LY value and its associated uncertainties are:

$$LY(^{40}\text{K}) = (76.5 \pm 0.2_{\text{stat}} \pm 2_{\text{syst}}) \text{ PE/MeV}. \quad (5.21)$$

This value aligns within one standard deviation with the previously obtained LY value from the Q-value of the ^{39}Ar β spectrum fit (sub-Section 5.4.1).

The mean value between the LY value extracted from the study of the ^{39}Ar β spectrum (Equation (5.3)) and the LY value extracted from the fit of the γ line from ^{40}K is:

$$LY = (77 \pm 2) \text{ PE/MeV} \quad (5.22)$$

This value is employed for the analysis of the ^{42}Ar specific activity.

The resolution of the ^{40}K gamma line, as determined from the fit, is given by:

$$\frac{\sigma(^{40}\text{K})}{\mu(^{40}\text{K})} = (19 \pm 0.2_{\text{stat}} \pm 6_{\text{syst}})\%. \quad (5.23)$$

This result is consistent within one standard deviation with the resolution value extracted from the resolution curve of Figure 5.8, obtained from ^{39}Ar β spectrum fit. It is important to note that the peak shape and thus the resolution may be influenced on the left side by the DAQ majority condition, which potentially can lead to a larger effective resolution.

5.6.2 β/γ spectrum fit

For the fitting of the ^{42}K spectrum, a theoretical beta spectrum is employed from [156]. Considering the decaying scheme of the ^{42}K (see Figure 4.13 right) the spectrum has to take into account different contributions. First of all the β spectrum of ^{42}K decaying to the ground state of ^{42}Ca with branching ratio of 82%. In 18% of the cases, ^{42}K decays to an excited level of ^{42}Ca , which subsequently de-excites, emitting a 1525 keV photon. Although this line is observed in the LEGEND-200 background spectrum (see Section 4.4), for this analysis, with energy release in LAr, the energy of the photon is always detected together with the β emission, resulting in a continuous spectrum from 1525 keV to the Q-value of ^{42}K . Combining these contributions, the resulting energy spectrum extends from 0 to the Q-value of ^{42}K , as shown in Figure 5.14, with the distinctive "dolphin fin" shape at 1525 keV.

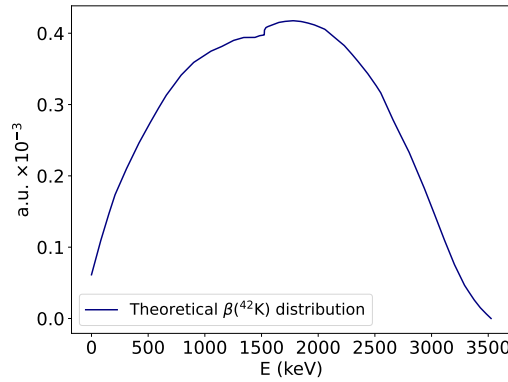


Figure 5.14: Normalized ^{42}K theoretical β distribution from [156].

The theoretical energy distribution spectrum is convoluted with a Gaussian function to consider the energy resolution of the LAr instrumentation, as performed for the ^{39}Ar analysis. Including also the Gaussian function for the fit of the ^{40}K gamma line, the assumed simplified model for fitting the β/γ spectrum can be expressed as:

$$[N(^{42}\text{K}) \cdot \beta(^{42}\text{K}) \cdot LY] * \left[\frac{1}{\sqrt{2\pi\sigma^2(x)}} \exp\left(\frac{-x^2}{2\sigma^2(x)}\right) \right] + \frac{N(^{40}\text{K})}{\sqrt{2\pi\sigma^2}} \exp\left(\frac{-(x - \mu_{40\text{K}})^2}{2\sigma_{40\text{K}}^2}\right). \quad (5.24)$$

The LY value is fixed to the mean value determined in expression (5.22). The energy resolution $\sigma^2(x)$ is expressed by the relation (5.2); $\mu_{40\text{K}}$ and $\sigma_{40\text{K}}$ are the mean value and the standard deviation of the ^{40}K gamma line. The central values of $\mu_{40\text{K}}$ and $\sigma_{40\text{K}}$ are taken from the ^{40}K Gaussian fit, allowing for potential variations within one standard deviation. Therefore, the free parameters of the fit are: the number of ^{42}K decays ($N(^{42}\text{K})$), the a, b, c parameters of the resolution and the number of ^{40}K decays ($N(^{40}\text{K})$).

A binned extended likelihood fit has been performed using a histogram with 1 PE bins. The fitting procedure has been executed in the energy range from 60 to 450 PE. Low energies have been excluded since are dominated by accidental coincidences mainly from ^{39}Ar . Furthermore, the fit was implemented under the assumption that the energy spectrum from 200 PE is entirely dominated by ^{42}K decays, aligning its end-point with

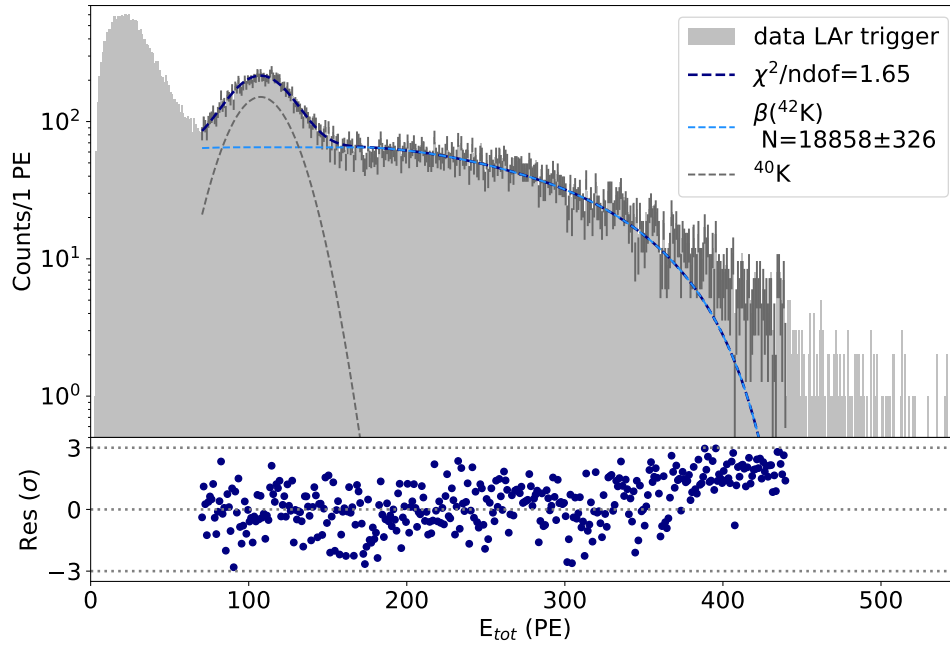


Figure 5.15: Fit of the β/γ events derived from LAr triggered events within $T_0 = [2800, 3100]$ samples, using the fit model of expression (5.24). The two contribution from the fit are show separately for the ^{40}K gamma line and for ^{42}K beta spectrum. The residuals in terms of sigma are show in the lower panel.

that of the ^{42}K β decay. For this purpose the resolution is not constrained to be compatible with the resolution curve obtained in Section 5.4.1.

The fit outcomes are presented in Figure 5.15. The goodness-of-fit parameter is $\chi^2/\text{ndof} = 1.65$, and the residuals, shown in units of σ in the lower panel, indicate that the fit model describes the data within 3σ deviation. The results suggest that the employed model is not describing correctly the spectrum, in particular for energies exceeding 300 PE, where an underestimation is observed. This suggests the presence of an additional component not considered in the study of this energy spectrum. The fit converges, but the obtained resolution is significantly large, about 50% of the Q-value of ^{42}K β decays.

^{42}K activity

By utilizing the number of ^{42}K events obtained from the fit, a counting analysis allows to obtain a preliminary indication of the ^{42}K specific activity within the WLSR volume. The number of ^{42}K events from the fit is equal to:

$$N(^{42}\text{K})_{\text{fit}} = 18\,858 \pm 326. \quad (5.25)$$

This count needs to be corrected for the efficiency of both the PSD cut (99%) and the T_0 cut (99%):

$$N(^{42}\text{K}) = \frac{N(^{42}\text{K})_{\text{fit}}}{\epsilon_{\text{PSD}} \cdot \epsilon_{T_0}} = 19\,240 \pm 333. \quad (5.26)$$

To estimate the specific activity of ^{42}K , the corrected extracted number of ^{42}K events from the fit, the LAr mass estimated in expression (5.9) and the acquisition time have been considered. The precise acquisition time can be derived by accounting for the number of pulser signals (from Table 5.2) that are injected in the system every 20 s. Consequently,

the specific activity is given by:

$$A(^{42}\text{K}) = \frac{N(^{42}\text{K})}{T \cdot M(\text{LAr})} = \frac{N(^{39}\text{Ar})}{N(\text{Pulser}) \cdot 20 \text{ s} \cdot M(\text{LAr})} = (2.096 \pm 0.088) \mu\text{Bq/kg} \quad (5.27)$$

The correction factor for the specific activity, needed to compensate for the exponential decay of ^{42}Ar with a half-life of $T_{1/2} = (32.9 \pm 1.1) \text{ yr}$ [100], is:

$$\eta_t = 1.043 \pm 0.008. \quad (5.28)$$

This correction accounts for a $(4.3 \pm 0.8)\%$ modification of the ^{42}K specific activity. The resulting corrected ^{42}K specific activity is:

$$A(^{42}\text{K})_{\text{corr}} = (2.186 \pm 0.088_{\text{stat}} \pm 0.154_{\text{syst}}) \mu\text{Bq/kg} \quad (5.29)$$

Table 5.7 provides a comprehensive overview of systematic uncertainties, with a significant emphasis on uncertainties stemming from the fitting procedure. Additionally, the mass of the LAr inside the WLSR volume emerges as a significant contributor to the overall uncertainty.

Item	absolute uncertainty ($\mu\text{Bq/kg}$)	relative error (%)
Hist bins	0.055	2.5
Fit range	0.032	1.5
LAr mass	0.05	2.3
LAr age	0.017	0.8
Total	0.154	7

Table 5.7: Systematic uncertainties for the $^{42}\text{Ar}/^{42}\text{K}$ specific activity estimation.

5.6.3 Discussion

The ^{42}Ar specific activity determined in this analysis is considerably lower compared to independent estimations. The final result (Equation (5.29)) is more than a factor 10 below the lowest value reported in Table 5.1. This suggests that the analysis presented here is not conclusive and additional efforts are necessary to accurately measure the ^{42}Ar activity.

To comprehensively understand and validate these results, it is essential to model the detector response through a simulation campaign. Unfortunately, as of the completion of this thesis work, the modeling of the optical response of the LEGEND-200 LAr instrumentation is still in progress. This ongoing effort aims to elucidate and validate all components of the detector setup.

A first factor that has not been considered in the ^{42}Ar activity estimation presented in this work, is the detection efficiency of the LAr instrumentation. This is expected to vary depending on both the energy released in LAr and the event position within the WLSR volume. While the processing chain of SiPM channels has been tuned to ensure high efficiency in detecting single photoelectrons, primarily for vetoing background events in the search for $0\nu\beta\beta$ decay using HPGe detectors, the efficiency for detecting events with larger numbers of photoelectrons is not known at the moment. This is expected to affect both the total number of events detected and the observed spectral shape. Additionally, geometrical effects, which could lead to variations in detection efficiency based on the event spatial

distribution, have not been included. Therefore, the complete simulation of the LEGEND-200 setup is indispensable to understand the response of the LAr instrumentation and its implications on the experimental outcomes.

Another potential contributing factor could be the majority condition of the DAQ. Only a fraction of ^{42}K β decays may be detectable far from LAr instrumentation, and this fraction is constrained by the DAQ majority settings. An acquisition with a lower majority scheme could provide valuable insights into the ^{42}K β distribution. This is currently under consideration for one of the upcoming data taking periods of LEGEND-200.

An additional consideration involves the assumption made regarding the distribution of ^{42}K decays inside the LAr volume enclosed by the WLSR. Due to the HV applied to the HPGe detectors, the attracted ^{42}K ions tend to move towards the electric field created by HV cables, resulting in a non-homogeneous distribution. Although this phenomenon is more pronounced inside the NMS, outside it is expected that attracted ^{42}K ions decay on the surface of the NMS, making them detectable by LAr instrumentation. Simulations are crucial to comprehend the behavior of ^{42}K ions induced by the electric fields created by the HV of HPGe detectors.

A last consideration involves the adopted fitting model of Equation (5.24). The simplified fitting model does not account for potential contributions from other background sources, such as ^{214}Bi and ^{208}Tl gamma lines. While the contribution from ^{214}Bi can be assumed negligible (due to its activity of $(32 \pm 6) \mu\text{Bq}$ [127]), the ^{208}Tl contribution may be significant in the energy region around 200 PE, potentially leading to a reduction in the obtained value of ^{42}Ar specific activity.

Conclusions

This thesis work has been conducted in the framework of the LEGEND-200 LAr instrumentation, encompassing activities from its assembly and installation to the commissioning phase and its subsequent integration with LEGEND-200 HPGe detectors. The analysis of the first LEGEND-200 physics data has been performed to explore the search for neutrinoless double beta decay, with a particular emphasis on optimizing the efficiency of the LAr instrumentation. Furthermore, the ability of the LAr instrumentation to operate independently as a detector system for background studies has been evaluated.

The assembly and commissioning of the LAr instrumentation, along with the integration of the new front-end electronics for SiPM of the LAr instrumentation, have been performed. Analysis of test data has been studied to improve the overall system efficiency, aiming for a single photoelectron sensitivity. Enhancements in the differential lines between the LAr instrumentation and the front-end electronics have been implemented, achieving an exceptionally low level of electrical noise, with an RMS of $(57.6 \pm 1.1) \mu\text{V}$ and a peak-to-peak excursion of $250 \mu\text{V}$.

An examination of SiPM signals has revealed three distinct categories of pulse shapes, associated with variations in SiPM production at the manufacturer. This consideration has been incorporated into the development of an efficient photoelectron reconstruction method.

The time profile of the LAr scintillation has been examined by employing ^{241}Am sources emitting 60 keV gammas. These sources provide the timing of scintillation light emission, enabling the generation of a time profile spectrum. This spectrum has been used for fitting purposes, extracting key components such as the triplet lifetime, determined to be $(1.147 \pm 0.028) \mu\text{s}$. This outcome aligns with the value measured by the LEGEND Liquid Argon Monitoring Apparatus (LLAMA), which continuously monitors the optical properties of LAr in the LEGEND-200 cryostat.

In addition to the trigger on the HPGe detectors, LEGEND-200 incorporates a trigger on the LAr instrumentation to autonomously identify correlated backgrounds. Rates under different majority configurations of the data acquisition have been explored as input to determine a suitable majority setting for the data acquisition with the LAr trigger.

To explore the signal rates of the LAr instrumentation, single rates and coincidence rates between the SiPM channels have been examined, with the dominance of the scintillation light signals originating from β decays of ^{39}Ar . It has been observed that twofold coincidence rates for an arbitrary channel pair are similar among the SiPM channels of the LAr instrumentation. This indicates a homogeneous scintillation light production in the LAr volume surrounding the detector systems.

Detecting small energy depositions in the LAr provides a chance to efficiently reject background events. This requires a good separation of single photoelectron signals from electronic noise. To achieve this, an optimum filter, based on Digital Penalized Least Mean Square (DPLMS) method, has been developed. It effectively addresses the noise levels of the experiment and has been integrated into the LEGEND-200 analysis framework. The optimum filter achieves a high $(95.8 \pm 0.2)\%$ accuracy in energy reconstruction and an efficiency for single photoelectron peak reconstruction of $(99.7 \pm 0.1)\%$. This significant improvement in noise separation from SiPM signals has contributed to enhancing the performance of the LAr instrumentation.

The efficacy of LAr instrumentation to veto background events in HPGe detectors has been evaluated. The ^{42}K gamma line is efficiently suppressed by $(19.9 \pm 5.7)\%$ while maintaining a 95 % signal acceptance. By utilizing the first LEGEND-200 dataset, corresponding to an exposure of 10.1 kg·yr, only one background event remains after applying all cuts, including the LAr veto. This results in a background index of 4.1×10^{-4} cts/(keV·kg·yr), aligning with the goal of the LEGEND-200 project.

Furthermore, the present work introduces an innovative algorithm for particle and background tagging using LAr instrumentation signals. This aims to demonstrate the capability of LAr instrumentation to work as independent detector, beyond its original veto purpose. The LAr energy distribution has been used to provide an estimation of the LAr instrumentation light yield and resolution. A pulse shape discrimination technique has been developed and applied to select a sample of events from ^{39}Ar and ^{42}Ar β decays, two naturally occurring radioactive isotopes present in the LAr. A preliminary analysis has been conducted to determine the specific activity of ^{39}Ar using a simplified model, resulting in (1.109 ± 0.106) Bq/kg, and to establish a framework for studying the activity of ^{42}Ar , a critical background component in the LEGEND-200 experiment.

The estimation of the specific activity of ^{42}Ar presented in this study remains not conclusive and future efforts are required to accurately evaluate the ^{42}Ar activity. The optimization of the SiPM processing chain has been fine-tuned to ensure high efficiency in detecting single photoelectrons, primarily for the purpose of vetoing background events in the search for $0\nu\beta\beta$ decay using HPGe detectors. The efficiency for detecting events with larger numbers of photoelectrons is currently unknown. This efficiency is expected to have an impact on both the overall number of detected events and the observed spectral shape. Therefore, the complete simulation of the LEGEND-200 setup is indispensable to understand the response of the LAr instrumentation and its implications on the experimental outcomes.

In summary, this thesis documents the successful commissioning of the LAr instrumentation in LEGEND-200 setup. The work has encompassed both hardware and software aspects, utilizing the system to fulfill its crucial role in characterizing environmental and cosmogenic backgrounds in LEGEND-200.

APPENDIX A

Thorium and Uranium Chain

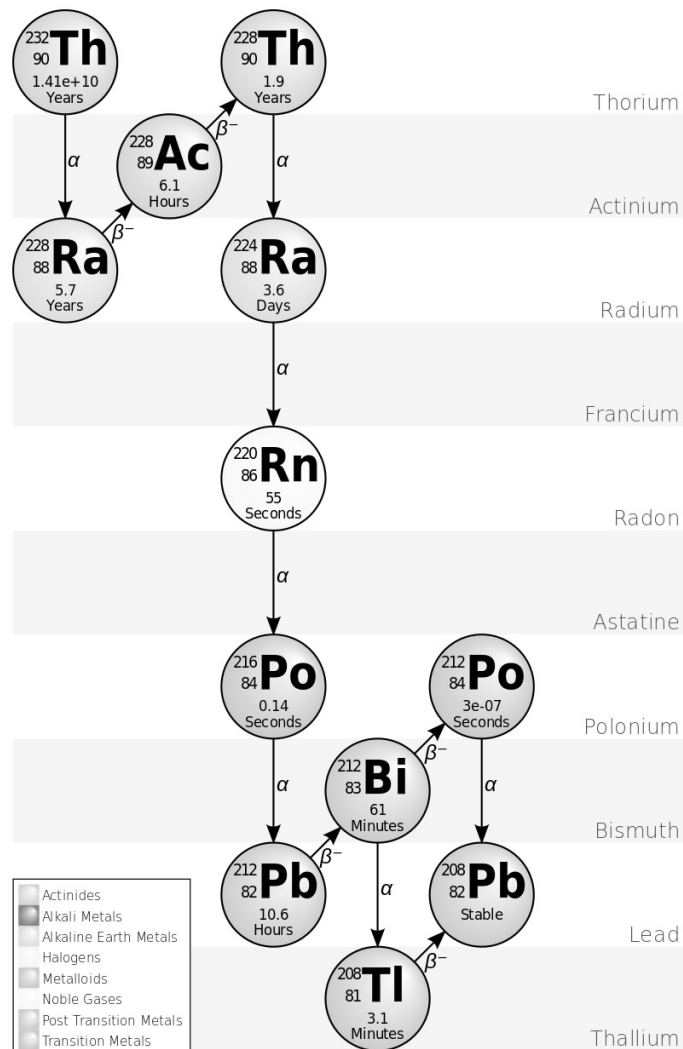


Figure A.1: ^{232}Th is the main naturally occurring isotope of thorium, with a relative abundance of 99.98%. It has a half life of 14 billion years, which makes it the longest-lived isotope of thorium.

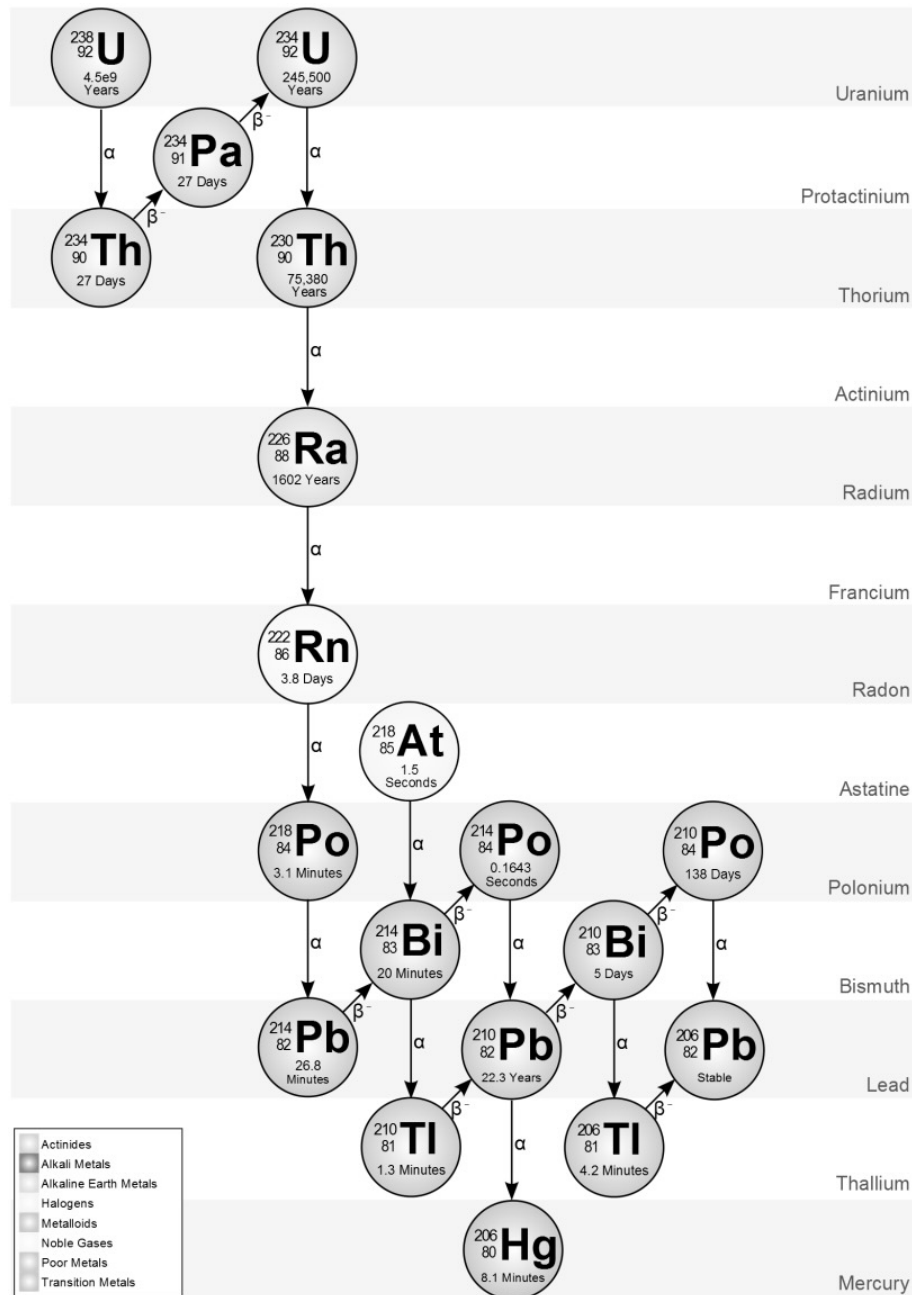


Figure A.2: ^{238}U is the most common isotope of uranium found in nature, with a relative abundance of 99%.

APPENDIX B

HPGe Detector Configuration

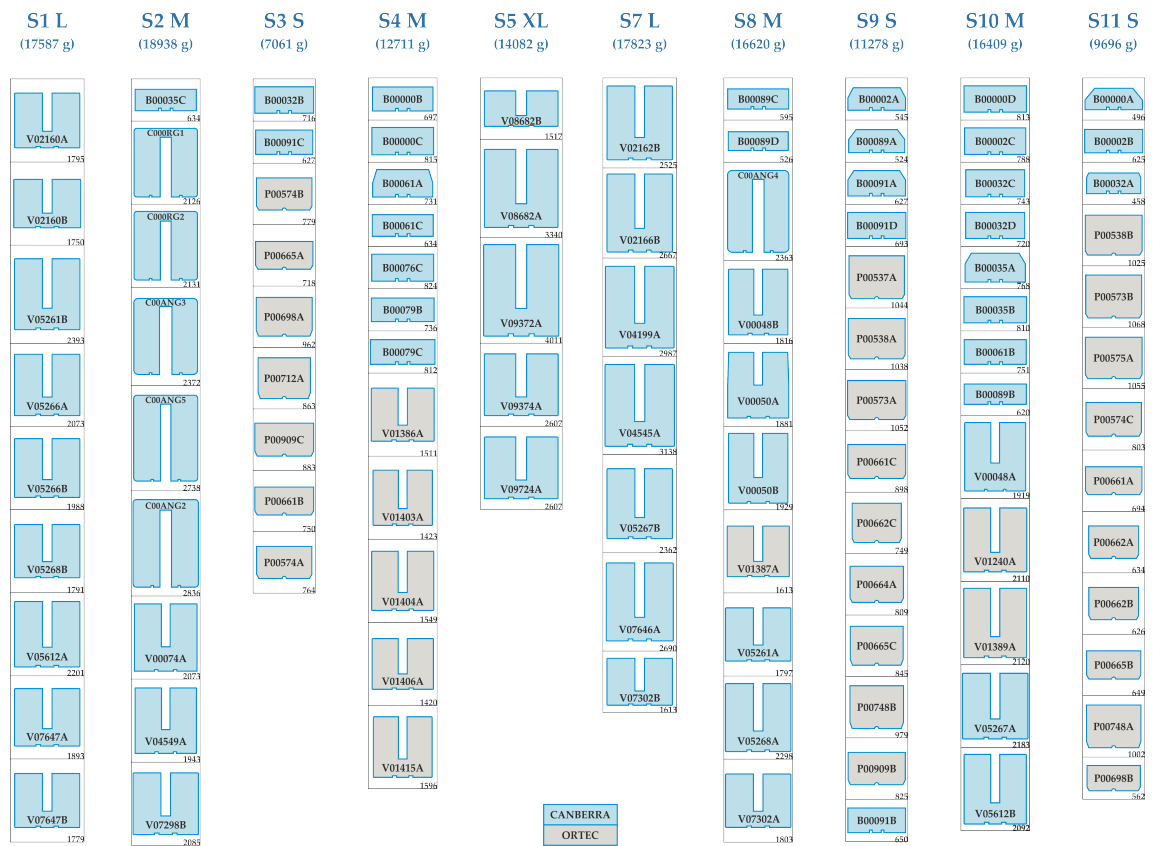


Figure B.1: The map displays the arrangement of LEGEND-200 HPGe detectors in 10 strings (142 kg), each with distinct characteristics denoted by their shape and nomenclature. Coaxial detectors can be identified by names beginning with "C00...", BEGe detectors with "B00...", PPC detectors with "P00...", and ICPC detectors are labeled as "V0...". The top of each string specifies its mass, and the color differentiation indicates whether the detectors are from Canberra or Ortec.

APPENDIX C

LEGEND Liquid Argon Purification System

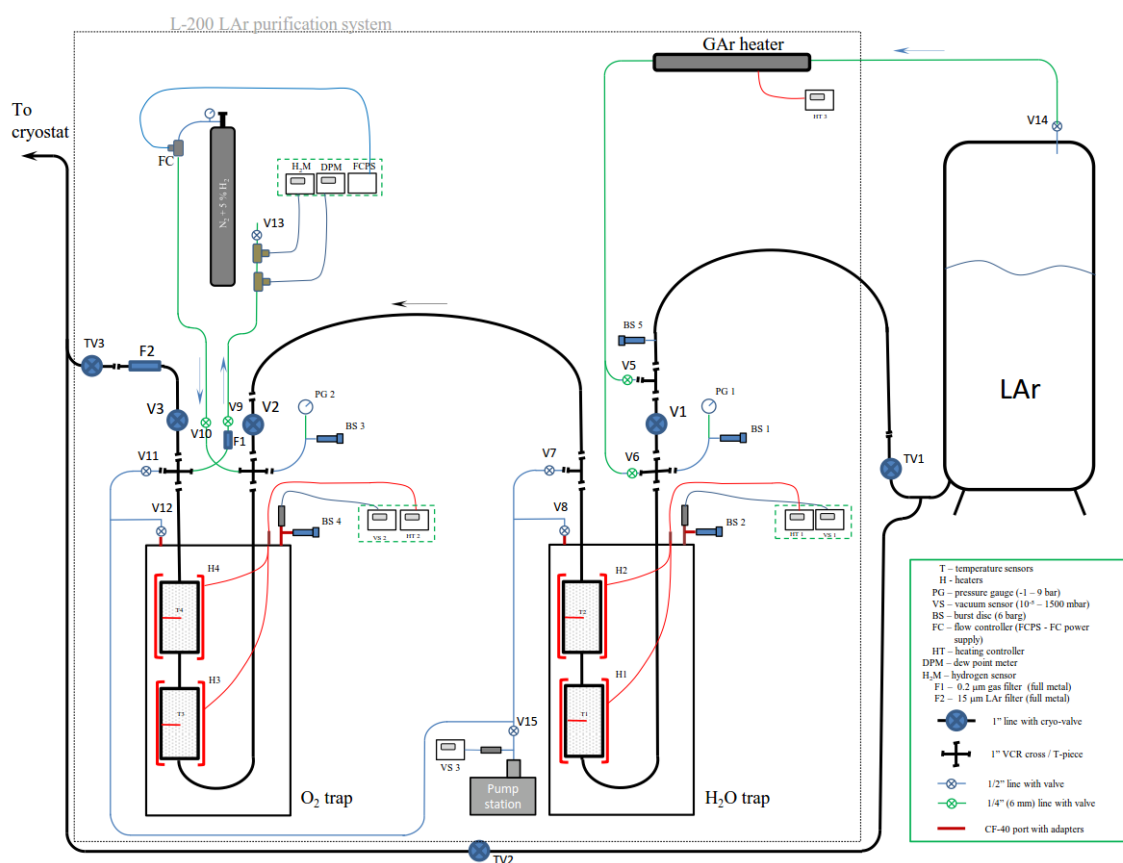


Figure C.1: Piping and instrumentation diagram of the LEGEND LAr purification system. Figure from [116].

APPENDIX D

Connections of Front-End Electronics

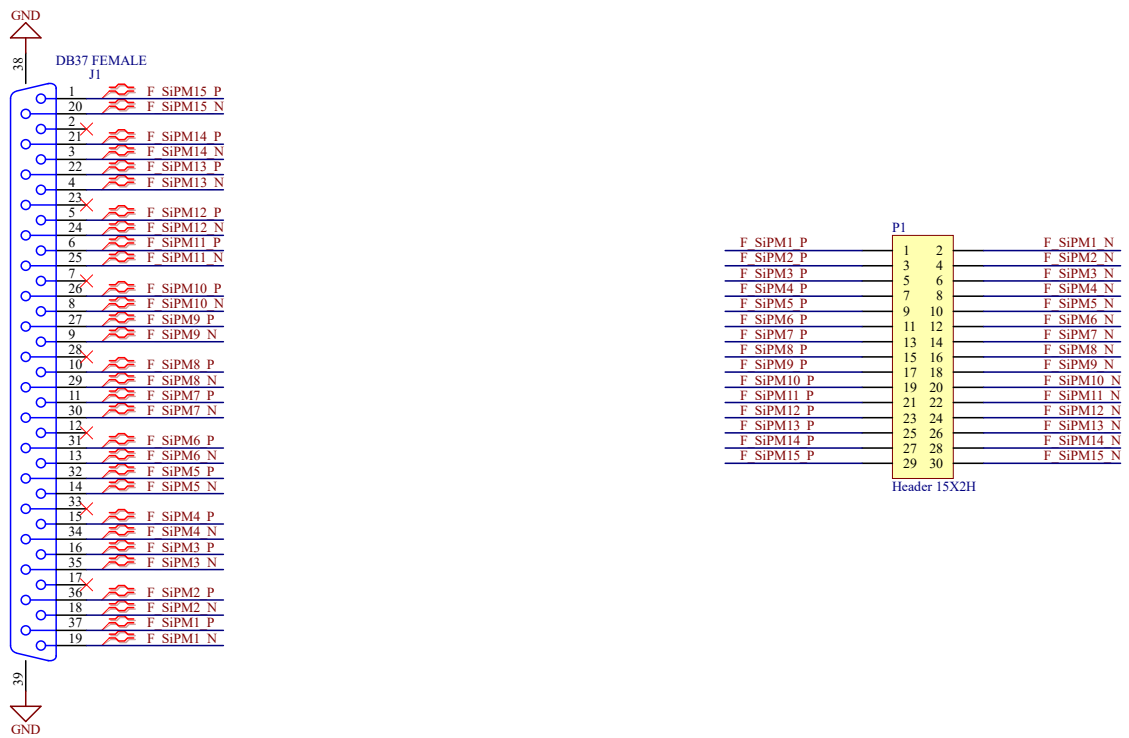


Figure D.1: Scheme of one DB37 connection on flange side, which accommodates 15 SiPM channels.

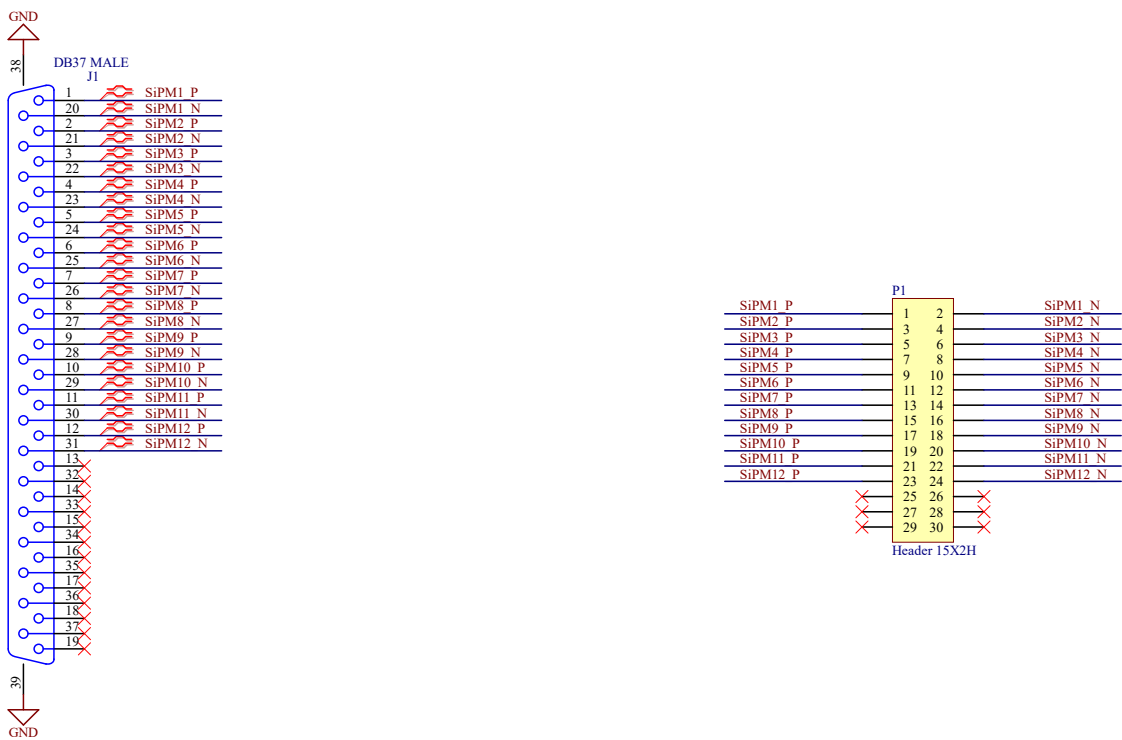


Figure D.2: Scheme of one DB37 connection on front-end side, which accommodates 12 SiPM channels.

APPENDIX E

LAr Instrumentation Front-End Stability Tests

The Front-End (FE) electronics has been tested at the electronics workshop at Roma Tre University. Electrical tests were conducted for all channels of the FE boards, ensuring compliance with the specified common mode voltage of 0.9 V required as input to Flash-Cam DAQ. The firmware for communication between the controller and FE boards, based on the I²C protocol, was developed to enable the configuration and retrieval of key SiPM parameters, such as drawn current and bias voltage.

Validation of the bias voltage set by the controller board was rigorously performed using a digital Keithley multimeter (Model 2001¹). This involved extended runs, including over-weekend testing. To assess stability and accuracy, a Ketek SiPM was enclosed in a black box at room temperature. Since the workshop temperature was not consistent, it experienced fluctuations attributable to the temperature variation between day and night. These temperature fluctuations affected not only the electronics card but, more significantly, the SiPM detector itself. This led to alterations in its characteristics, causing variations in both current and voltage, especially the one recorded with the multimeter. The voltage set by the controller remained constant, as predetermined, given the relatively low internal read-back sensitivity of the ADC of 14 mV. Consequently, it did not capture voltage fluctuations with the same precision as the multimeter, which boasts a sensitivity of 0.1 mV.

The values of SiPM current, voltage, and room temperature over the four-day testing period are illustrated in Figure E.1. Notably, this testing underscored the stability of the drawn current and, significantly, demonstrated that the accuracy of the bias voltage set by the controller, relative to an independent reference, such as a multimeter, remained stable at 0.8% [160]. Figure E.2 shows a zoom into two-day period (Saturday and Sunday) in which the temperature was stable.

A stability test, similar to the one conducted at the Roma Tre workshop, has been also carried out at LNGS. In this scenario, the SiPM detectors are immersed in LAr, eliminating thermal fluctuations on the SiPM itself. Thus, environmental thermal fluctuations exclusively impact the FE boards. Nevertheless, the FE electronics is situated in a controlled clean room, where temperature is consistently monitored and maintained stable, ensuring a precise and stable measurement of detectors current and voltage. The values of SiPM current, voltage, and room temperature over a two-day testing period are illustrated in Figure E.3.

¹https://download.tek.com/manual/2001_903_01B.pdf

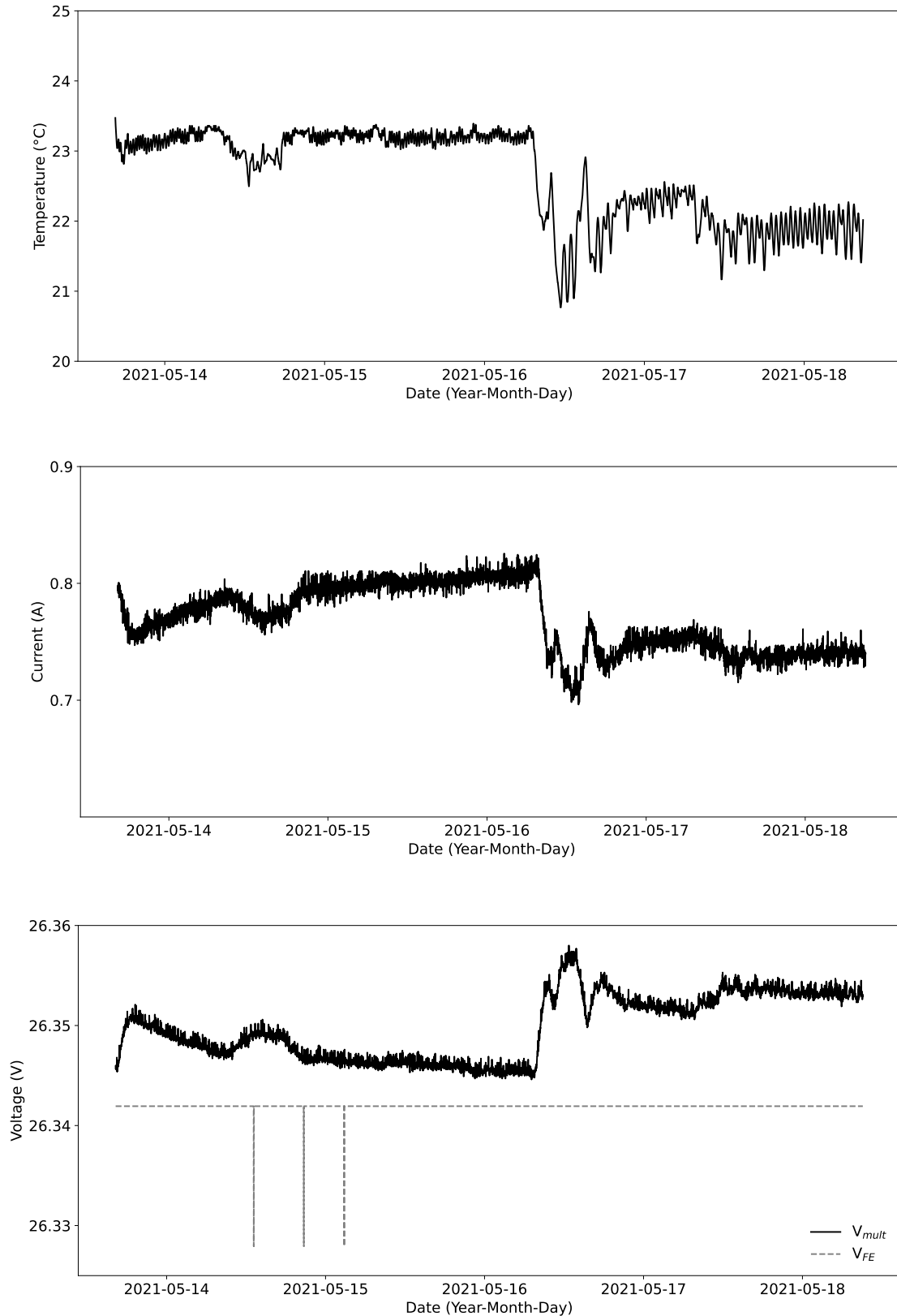


Figure E.1: Four-day testing period performed at Roma Tre electronic workshop. The temperature and current values read by the controller board are shown in the first two plots. Voltage values measured by the controller board (dashed line) and by a multimeter (black) are illustrated in the bottom plot, in which also the read-back sensitivity of the ADC is clearly visible by the three vertical segments.

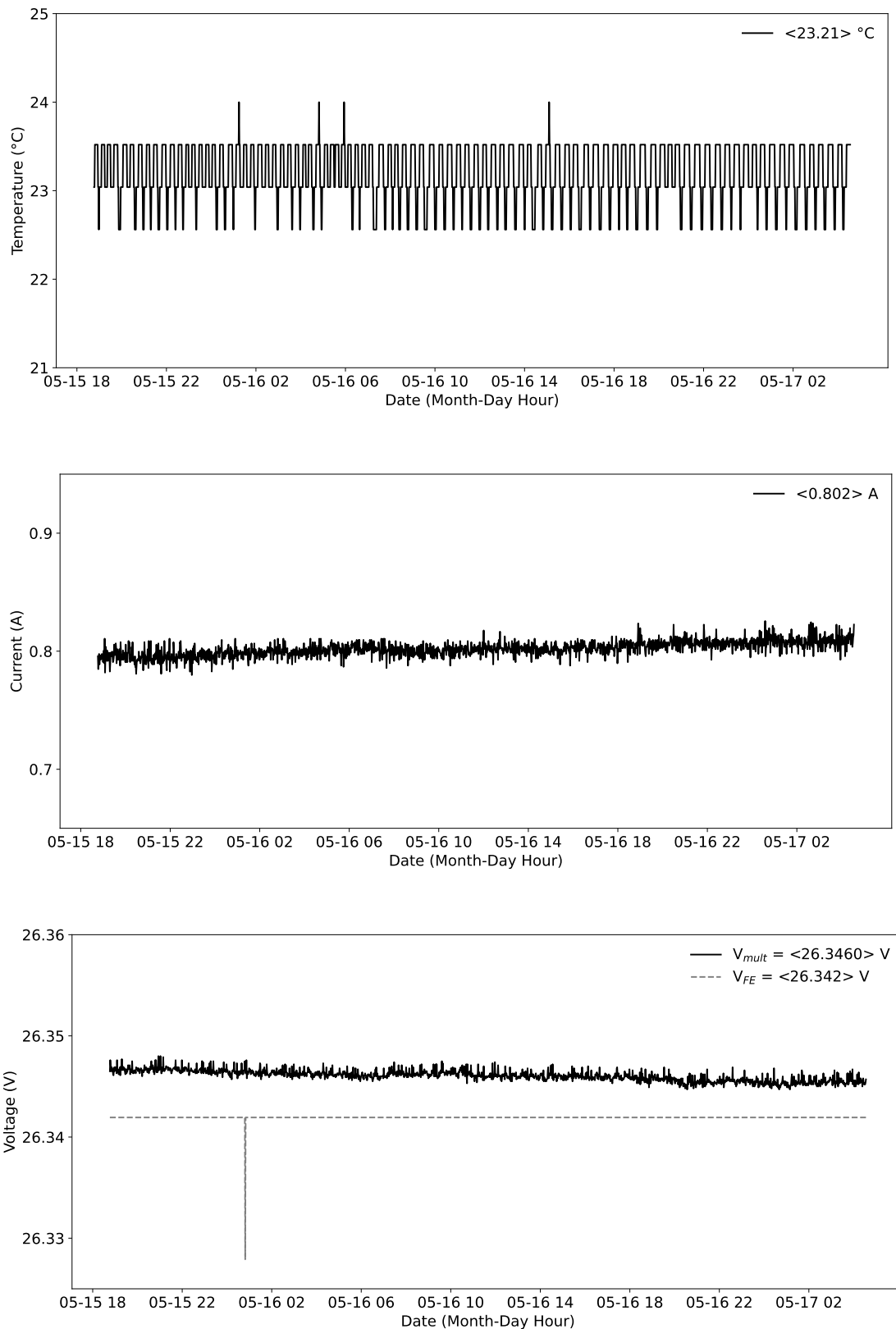


Figure E.2: Zoom on the two-day test period with stable temperature performed at Roma Tre electronic workshop. The temperature and current values read by the controller board are shown in the first two plots. Voltage values measured by the controller board (dashed line) and by a multimeter (black) are illustrated in the bottom plot.

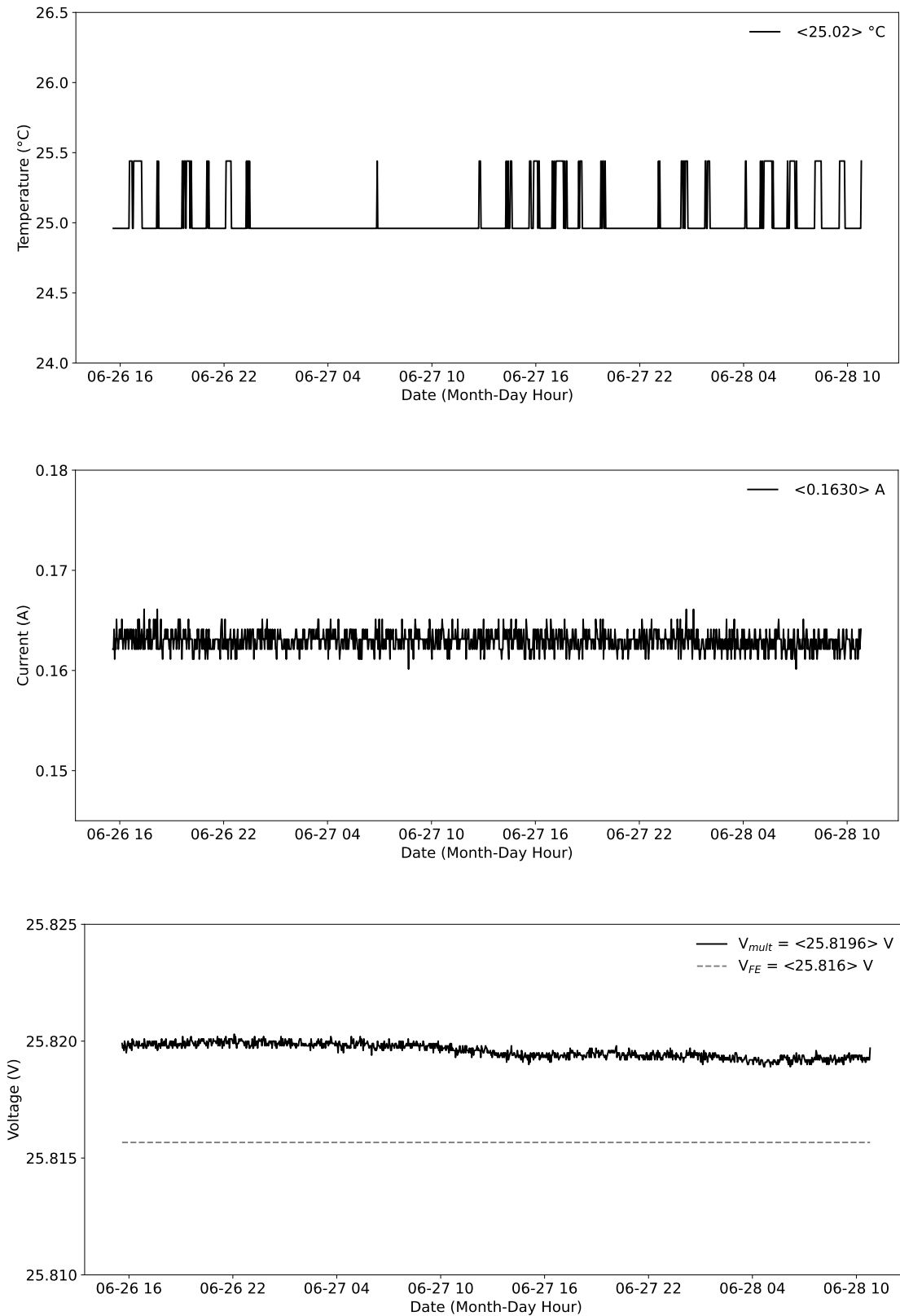


Figure E.3: Stability test performed at LNGS in 2022 with SiPM in LAr. The temperature and current values read by the controller board are shown in the first two plots. Voltage values measured by the controller board (dashed line) and by a multimeter (black) are illustrated in the bottom plot.

APPENDIX F

SiPMs Working Principle

Silicon PhotoMultipliers (SiPMs) are highly sensitive light sensors based on silicon technology. Functionally, a SiPM is a multi-pixel avalanche photodiode that operates in Geiger mode, enabling it to offer single-photon resolution with remarkable detection efficiency [161]. These distinctive characteristics, coupled with their advantages, such as requiring low bias voltage and having minimal mass, resulting in a low contribution to radioactive background, establish SiPMs as an optimal choice for light detection in low-background experiments.

Avalanche photodiode

An Avalanche PhotoDiode (APD) is a type of semiconductor photodetector device designed for detecting light primarily in the form of photons. The key principle behind their operation is the avalanche multiplication process, which allows them to amplify the signal generated by incoming photons.

In the initial phase of operation, when a photon with sufficient energy strikes the APD photosensitive material, it generates an electron-hole pair. What sets APDs apart is their ability to trigger the avalanche effect. To achieve this, APDs are typically operated under reverse bias conditions. Under reverse bias, the electrons and holes generated by the absorbed photons gain enough energy to initiate a process called impact ionization. When an electron acquires sufficient energy from the electric field, it can collide with other electrons, leading to the creation of additional electron-hole pairs. These newly generated carriers, in turn, can undergo further impact ionization, resulting in a cascading effect known as an avalanche or Geiger mode. This effect leads to a substantial multiplication of charge carriers for each absorbed photon, resulting in a significant increase in the electric current flowing through the diode. This amplified electrical signal is directly proportional to the number of incident photons.

To prevent excessive multiplication and avoid potential damage to the device, APDs often incorporate a quenching mechanism, such as a resistive element, which reduce the bias voltage to a level at or below the breakdown voltage, limiting the duration of the avalanche process. The bias voltage is subsequently restored to enable the detection of another photon. The combination of APDs and their associated quenching resistors is commonly referred to as "microcells" [162].

SiPM operation and output

A SiPM comprises an array of individual APD pixels, operating in parallel and within Geiger mode. Each pixel functions as a miniature APD, complete with its quenching resistor and a dedicated output. The SiPM signal results from the sum of all activated microcells coinciding in time. The operating voltage of a SiPM is typically 3 to 5 V higher than the breakdown voltage.

The components of a SiPM pulse, originating from the superposition of activated microcells, can be understood by examining the key elements of an equivalent electrical circuit for a single microcell (APD). The distinctions between an APD and a SiPM equivalent circuit encompass additional passive components representing non-activated microcells and a parasitic grid capacitance [162, 163].

An equivalent electrical circuit for an APD is depicted in Figure F.1 (left) and described below:

- each microcell is modeled as a parallel combination of the diode capacitance C_d , which models the depletion region of the p-n junction, and the internal diode resistance R_d ;
- the quenching segment of the circuit is described by a quenching resistor R_q , and a parallel quenching capacitance C_q , connected in series with the diode capacitance.

Before a microcell discharges, C_d is charged to the SiPM applied bias voltage, which is connected to the anode and cathode. An avalanche, triggered by incident photons or thermal excitation, is modeled by closing a switch, resulting in the discharge of capacitance C_d via resistance R_d . The voltage drop across C_d induces a corresponding voltage change at C_q , leading to a rapid increase in current and, consequently, a sharp rising component of the signal. During the discharge, the quenching mechanism engages, causing the voltage at the APD to decrease as the voltage drop across the quenching resistor rises. Once the voltage at the APD reaches the breakdown voltage, the impact ionization process stops, and the microcell is recharged to the operational voltage.

The pulse recovery consists of two components: the first is a fast decay (τ_{fast}) due to rapid charge supply from parasitic capacitance; the second component represents the

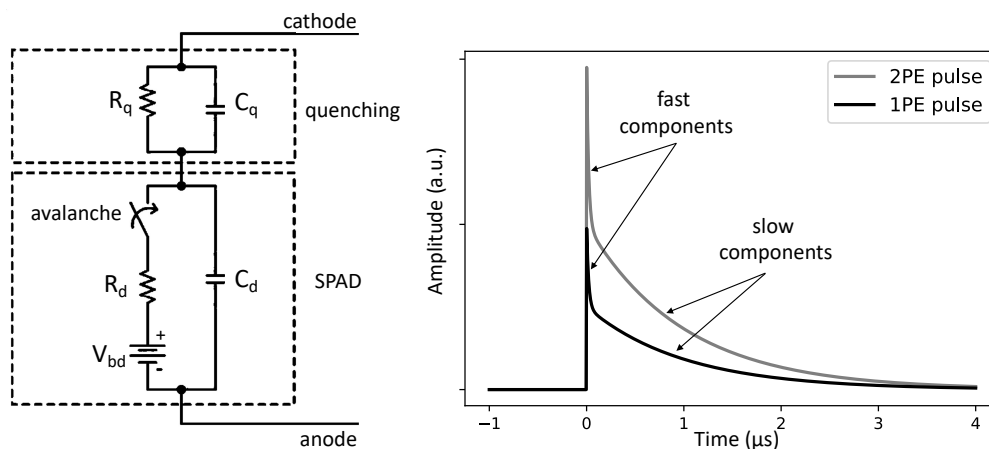


Figure F.1: Left: equivalent electrical circuit of a single photon avalanche diode (SPAD) with an integrated quenching resistor; adapted from [162]. Right: illustration of two SiPM pulses composed of a fast rise and two recovery components (fast of 20 ns and slow of 1 μs).

microcell recharge with a distinct time constant, $\tau_{\text{rec}} = R_q(C_q + C_d)$, which is significantly slower than the first component and is known as the recovery time.

An example of SiPM signal can be found in Figure F.1 (right), which displays 1 and 2 PE pulses characterized by a sharp rising component and the two recovery components (fast and slow). The pulse amplitude increases with the number of photoelectrons (PE), which is the number of activated cells in a SiPM, assuming that, due to their small area, a pixel is typically illuminated by a single photon at a time.

SiPM noise effect

While highly sensitive and versatile detectors, the SiPMs are susceptible to various sources of noise that can affect their performance. Understanding and mitigating these noise sources is essential when working with SiPMs. Figure F.2 illustrates the primary sources of noise in SiPMs which are described below:

Dark count noise

Dark count noise is caused by the spontaneous generation of electron-hole pairs in the absence of incident photons. These dark counts can produce false signals that mimic photon-induced signals. Dark count rates depend on the temperature, bias voltage, and the specific SiPM design. Cooling the SiPM and reducing the bias voltage can help reduce dark count noise.

Prompt crosstalk

Crosstalk is a phenomenon in which an avalanche event in one pixel of the SiPM triggers secondary avalanches in neighboring pixels. This can lead to false signals that are correlated with the primary photon-induced signal on a very short time scale, typically within a few ns. This phenomenon, known as "prompt" optical crosstalk, leads to pulses that cannot be distinguished from those generated by multiple incident photons. Such pulses may exhibit amplitudes that are two or even three times that of a single-cell signal, depending on the number of crosstalk events. Reducing cross-talk typically involves designing SiPMs with appropriate pixel isolation and geometry.

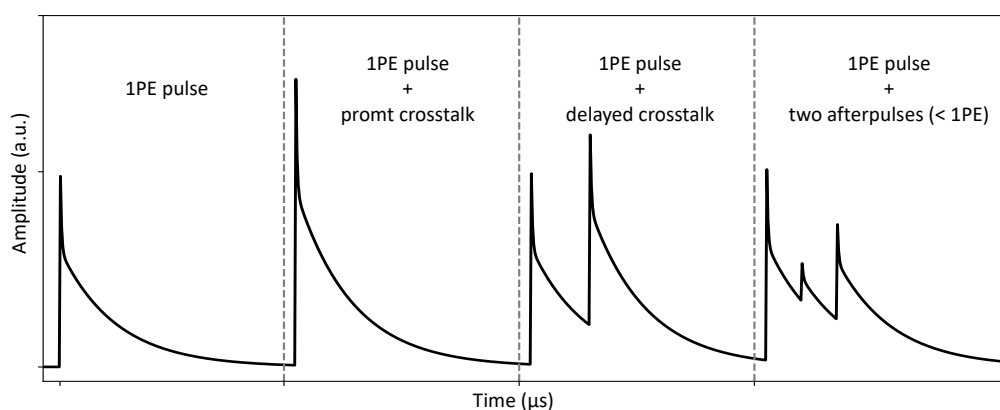


Figure F.2: Primary sources of noise in SiPMs.

Delayed crosstalk

Delayed optical crosstalk is caused by photons generated during an avalanche event in one pixel escaping and reaching neighboring pixels, leading to false counts in those neighboring pixels. It takes several nanoseconds up to microseconds for these charge carriers to diffuse into the active regions, where they subsequently trigger an avalanche. This results in "delayed" optical crosstalk. Unlike prompt optical crosstalk, the time difference between a prompt pulse and a crosstalk pulse can be resolved, as indicated in Figure F.2. Similar pulse shapes can be generated by two incident photon occurring within a short time frame. Minimizing optical crosstalk often involves the use of optical barriers or advanced pixel designs that reduce the probability of photons escaping.

Afterpulsing

Afterpulsing occurs when charge carriers generated during a previous detection event get trapped within the SiPM and are released after the quenching period. These delayed pulses can be mistaken for new photon detection. Given that this process occurs on a timescale during which the microcell is unlikely to be fully recovered, the amplitude of an after-pulse is typically a fraction of the usual single-cell signal amplitude, as shown in Figure F.2. This figure also illustrates the possibility of multiple afterpulses following a photon-induced prompt pulse. Minimizing afterpulsing often requires careful optimization of the quenching time and the use of specific SiPM designs that reduce this effect.

Readout electronics noise

Noise in the readout electronics can also contribute to the overall noise level in SiPM-based systems. High-quality readout electronics with low noise characteristics are essential to maximize the signal-to-noise ratio.

To mitigate these noise sources several techniques can be adopted, such as:

- reducing the operating temperature of the SiPM can decrease dark count rates and improve overall performance;
- careful tuning of the bias voltage and quenching parameters can help reduce afterpulsing;
- advanced SiPM designs with improved pixel isolation and reduced optical cross-talk can minimize these noise sources;
- digital signal processing techniques can be used to filter and remove the noise sources from SiPM signals.

Despite the presence of noise, SiPMs remain valuable detectors for applications requiring single-photon sensitivity due to their excellent time resolution and overall performance. Proper calibration, control of operating conditions, and noise mitigation strategies can help ensure accurate and reliable results in SiPM-based systems.

PE spectrum

The photoelectron (PE) spectrum of a SiPM refers to the distribution of detected signals corresponding to individual photons incident on the SiPM. This spectrum is used to characterize the SiPM response to single photons and is essential in understanding its performance. The PE spectrum typically provides information about the number of electrons or charge carriers generated for each detected photon.

An example of PE spectrum is presented in Figure F.3. The process of generating this spectrum involves plotting in a histogram the SiPM pulse parameter (e.g. amplitude or area) that is proportional to the charge. Subsequently, the spectrum is normalized with respect to the number of photoelectrons. In this normalized representation, the noise peak is centered at 0, while the photopeaks start at 1 PE. The PE spectrum of Figure F.3 exhibits variations due to inherent non-uniformities among microcells, which contribute to a spread in gain, and is influenced by the magnitude of external light, represented by the Poisson distribution. The illustrated PE spectrum does not include the noise effects due to e.g. optical crosstalk and afterpulses. When optical crosstalk is integrated, the events in the spectrum will be distributed towards higher numbers of photoelectrons. While incorporating afterpulsing will exhibit a greater concentration of events between the PE peaks, as afterpulses are subsequent pulses with amplitudes smaller than 1 PE.

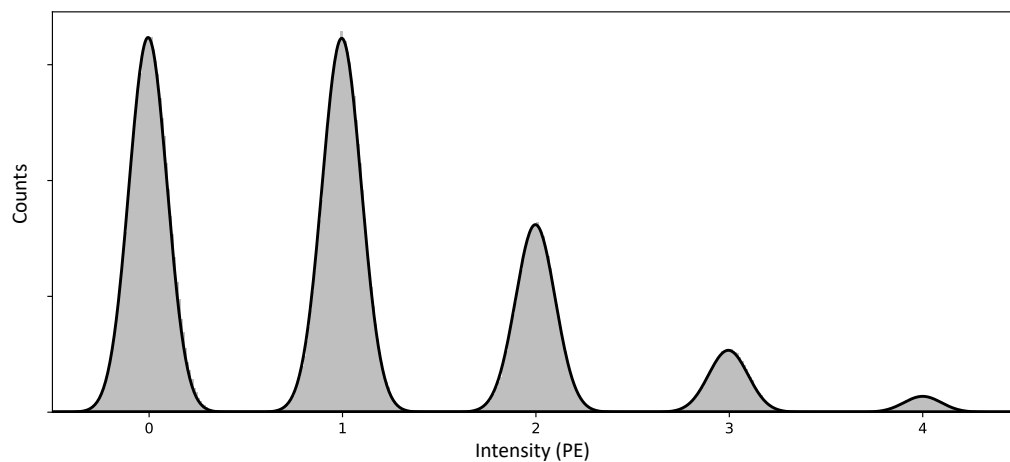
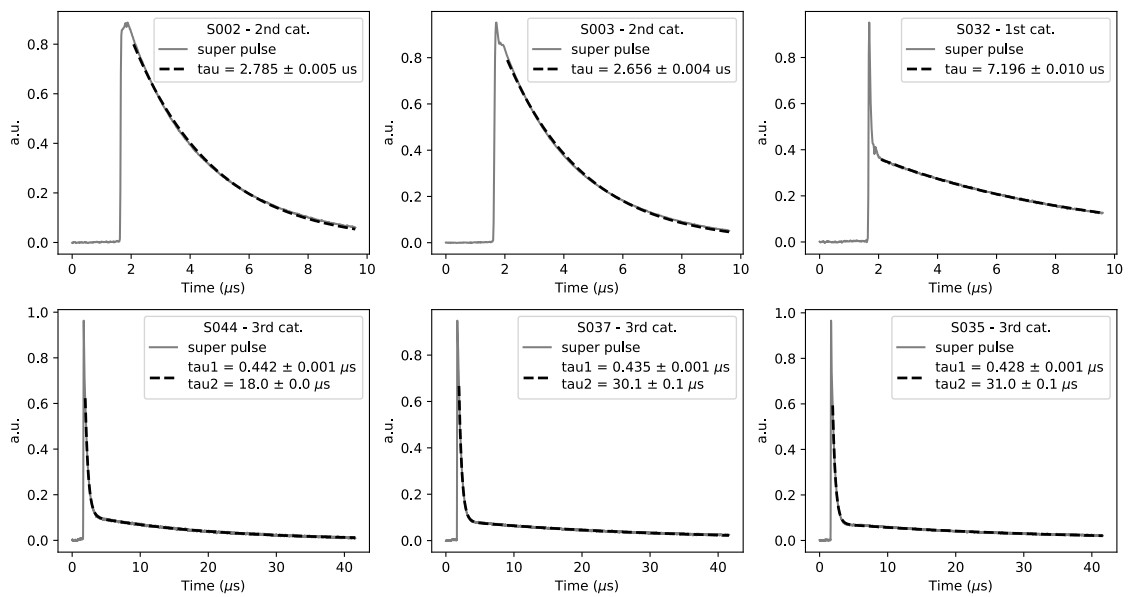


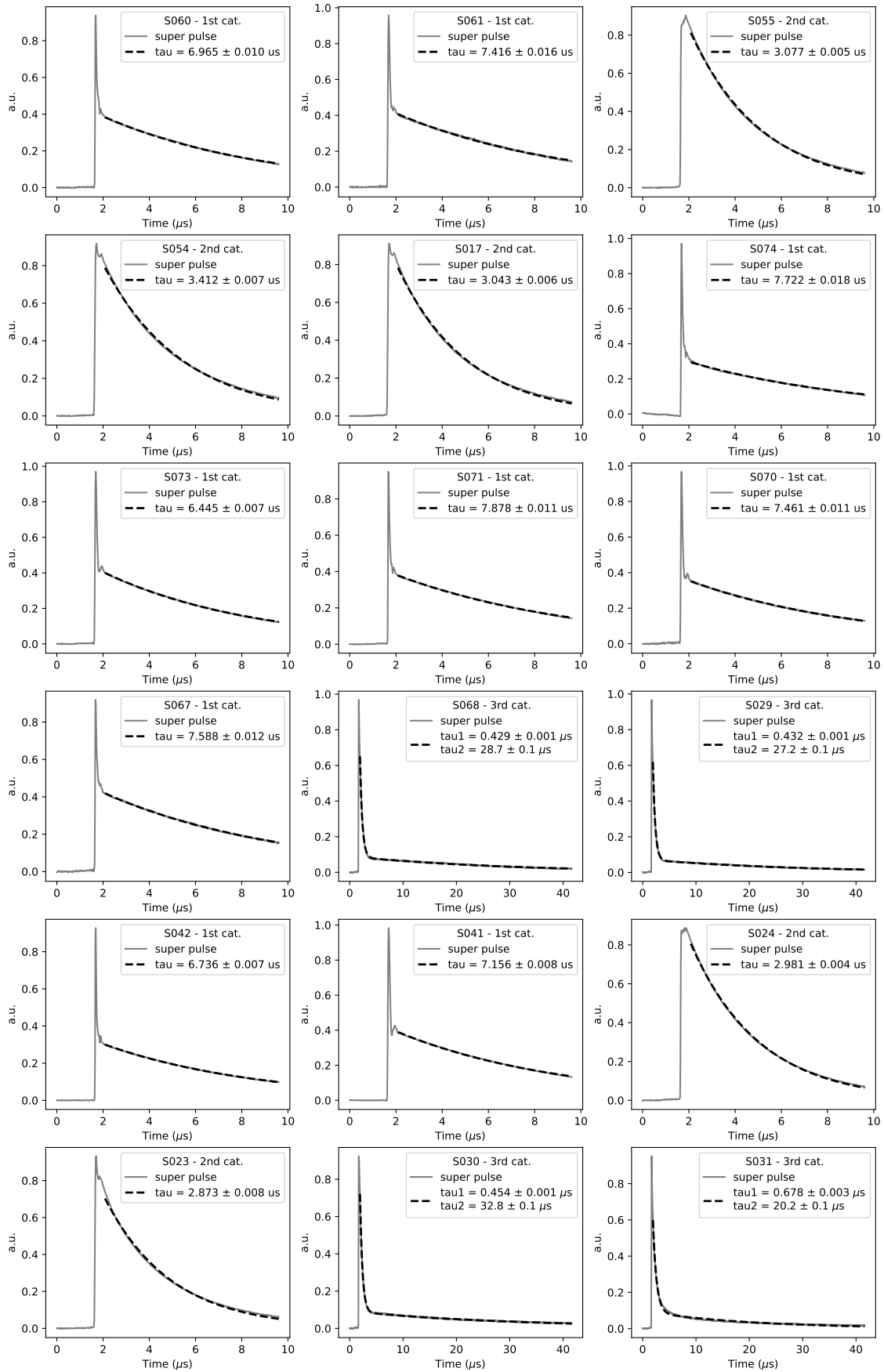
Figure F.3: Example of normalized PE spectrum using Poisson distributed PE events with $\lambda=1$ and a gaussian spread with $\sigma = 0.1$ PE.

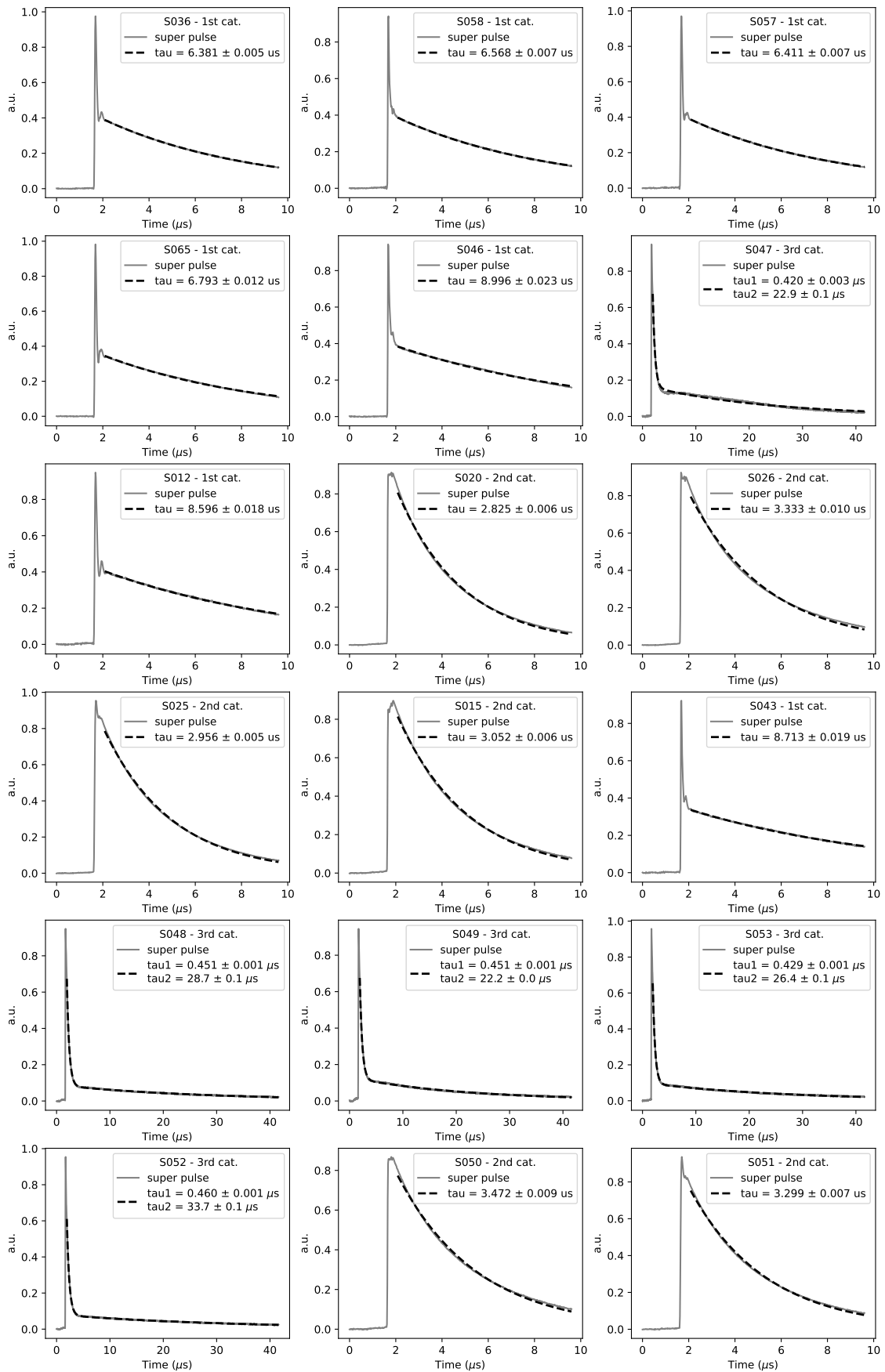
APPENDIX G

LAr Instrumentation SiPM Super-Pulses & Decay Times

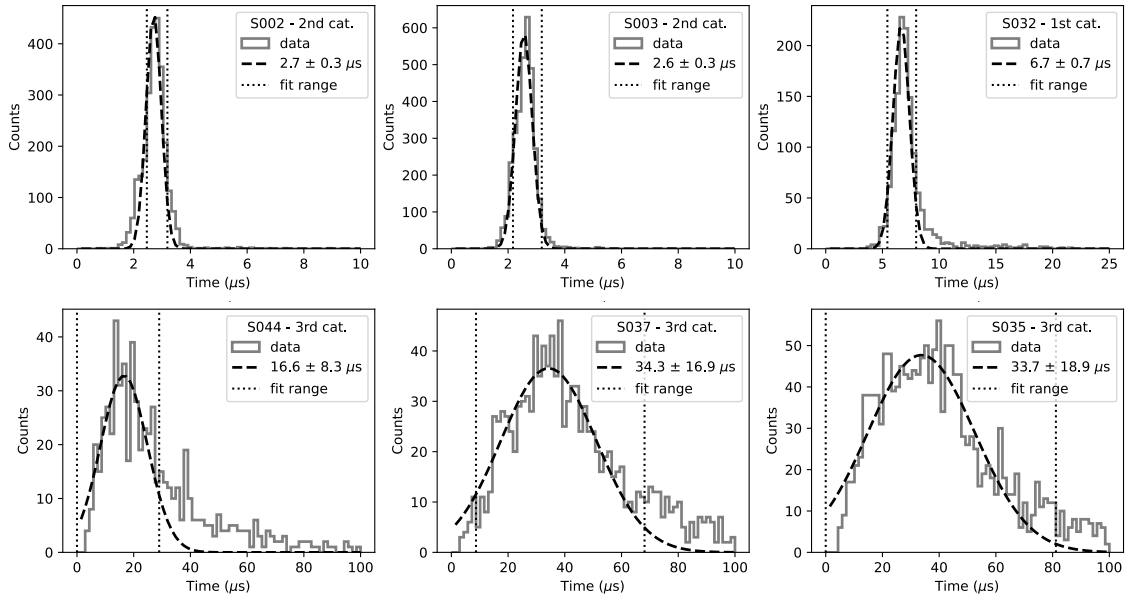
LAr instrumentation SiPM super-pulses

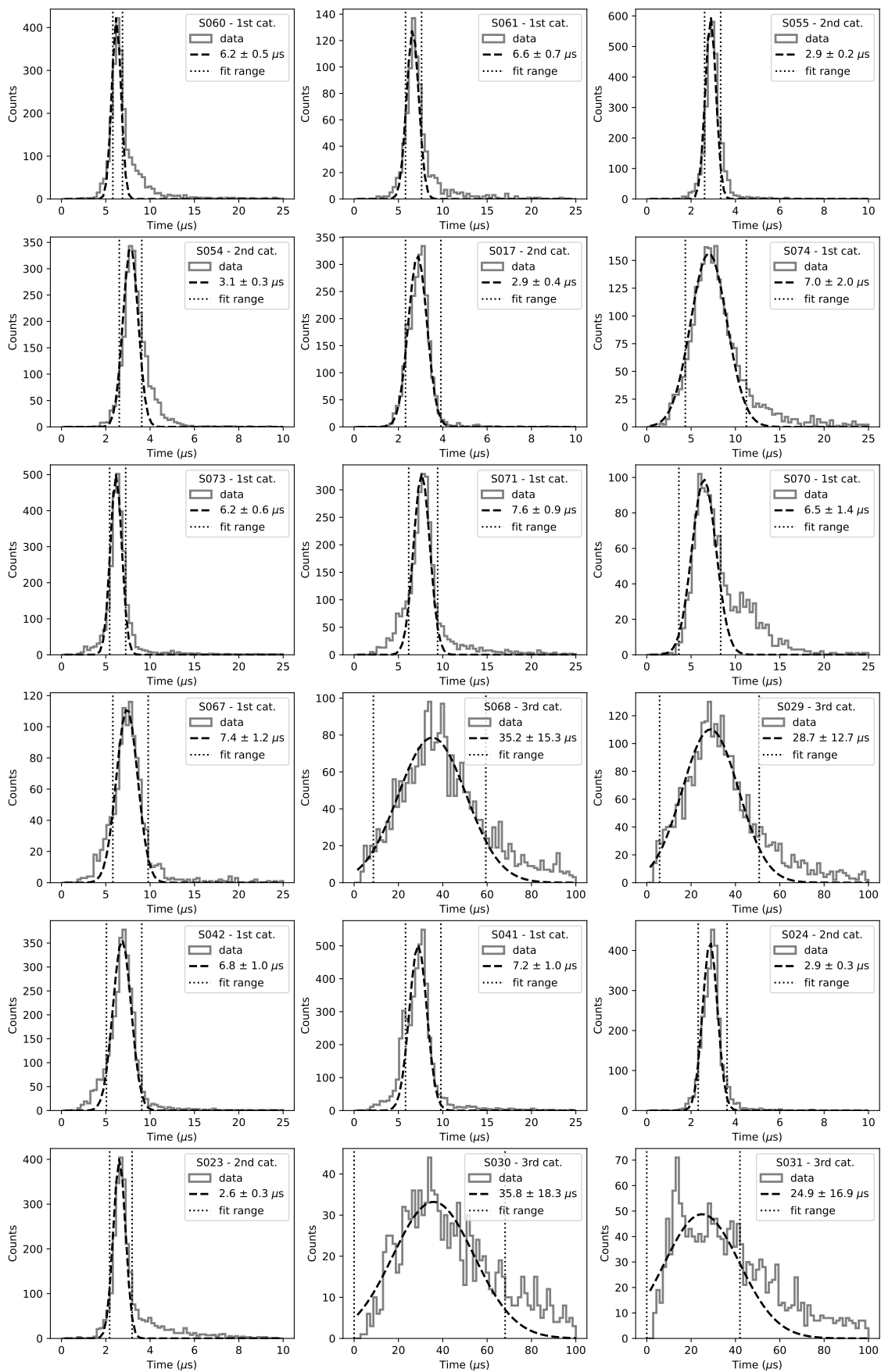


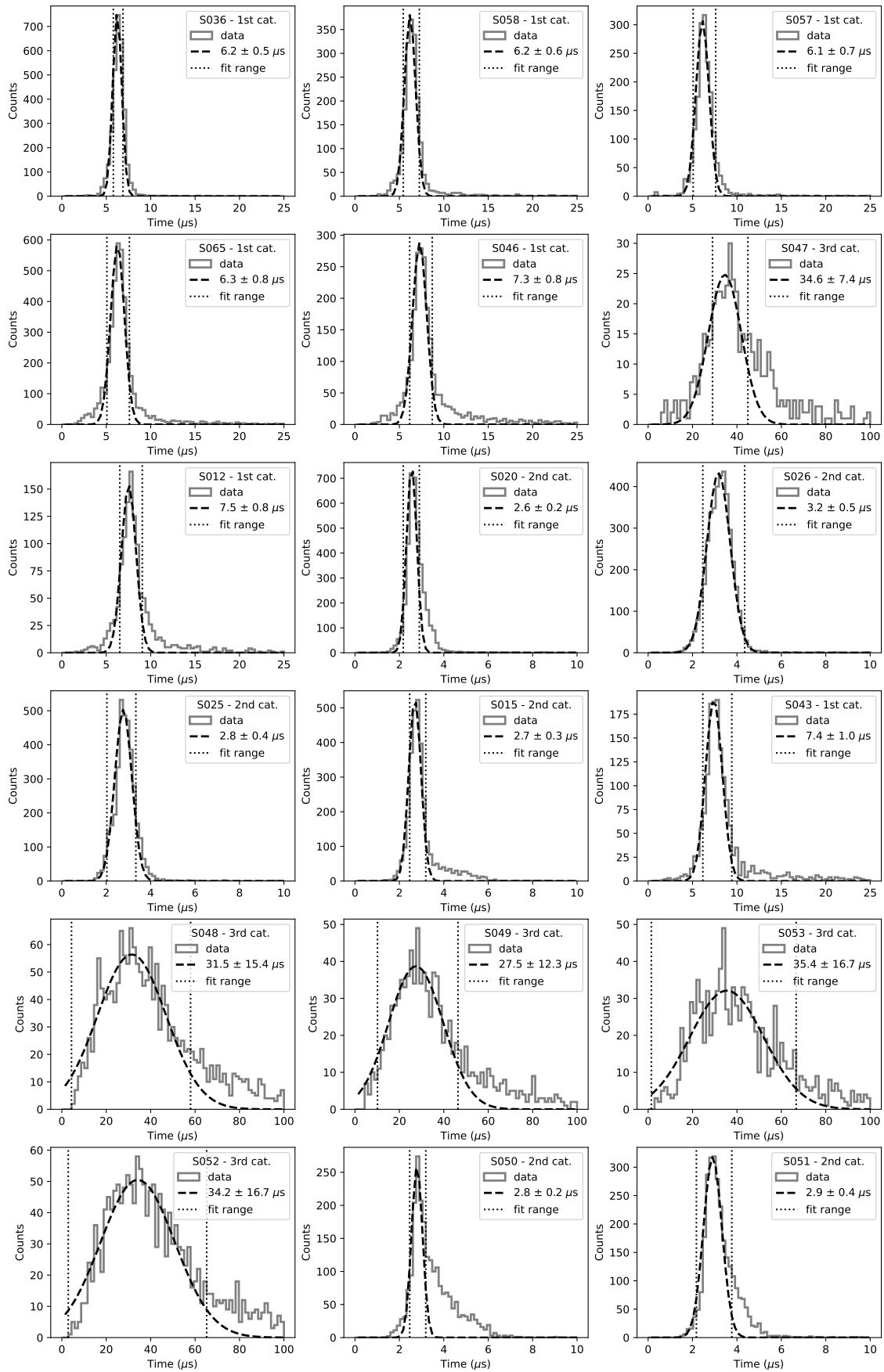




LAr instrumentation SiPM decay time distributions







APPENDIX H

Pulser Crosstalk and Muon Events from LAr Instrumentation

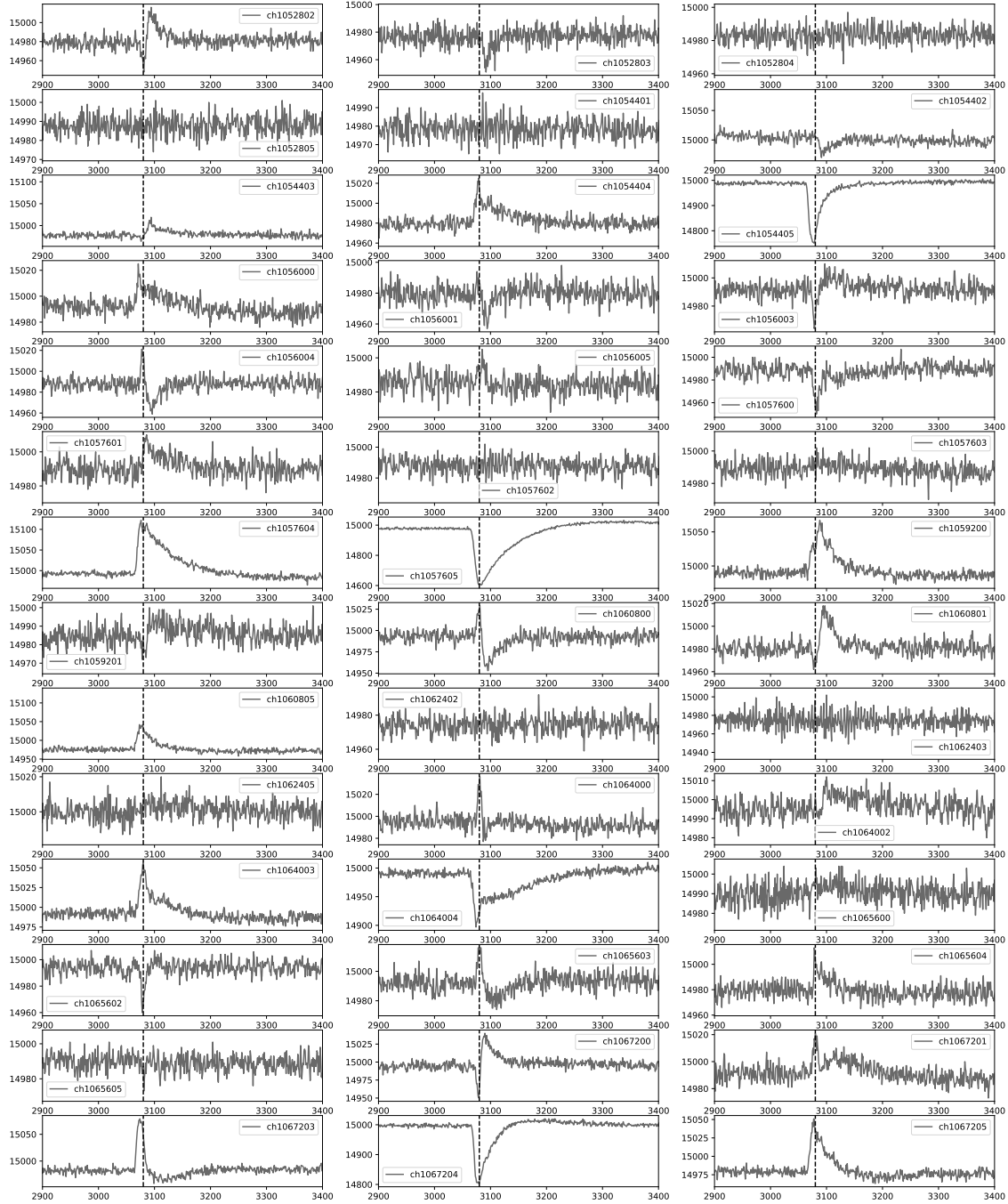


Figure H.1: Pulsar crosstalk on SiPMs of the LAr instrumentation.

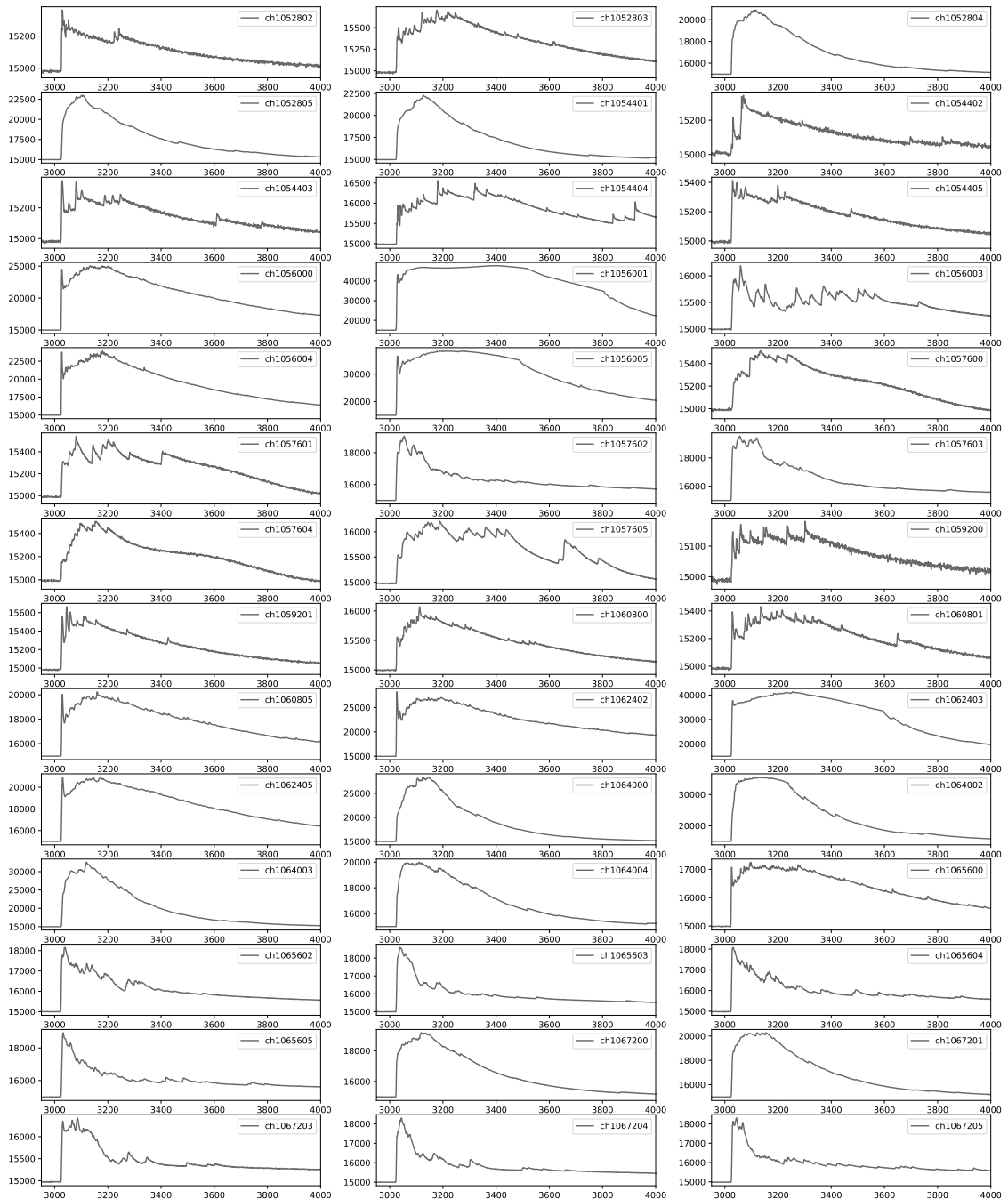


Figure H.2: Muon event measured by SiPMs of the LAr instrumentation.

APPENDIX I

LAr Energy Distribution: DPLMS vs Hypercurrent

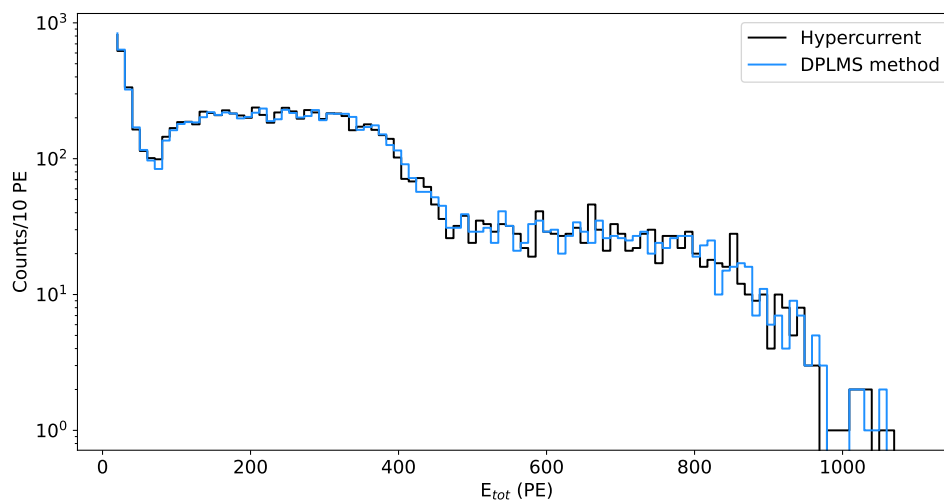


Figure I.1: Comparison between the LAr energy distribution estimated using the Hypercurrent estimator and the DPLMS method.

APPENDIX J

Alpha Contamination

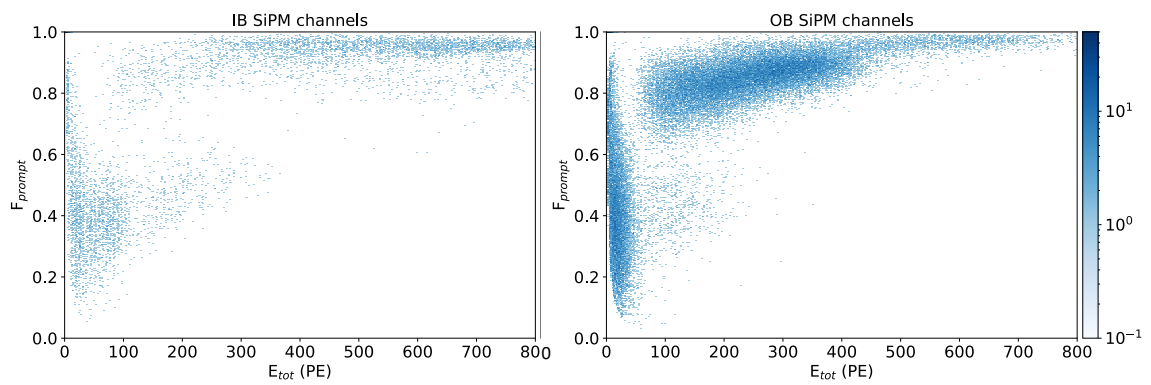


Figure J.1: PSD distributions performed separately for inner barrel (IB) SiPMs and outer barrel (OB) SiPMs. A significant contribution to the α band is seen by the OB channels.

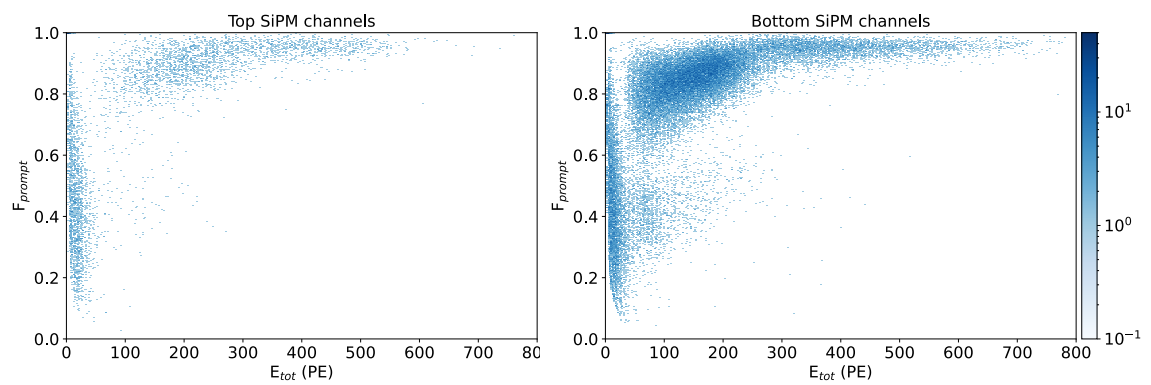


Figure J.2: PSD distributions performed separately for Top SiPMs and Bottom SiPMs. A significant contribution to the α band is seen by the Bottom channels.

$\beta\beta$ double beta

$0\nu\beta\beta$ neutrinoless double beta

$2\nu\beta\beta$ double beta with the emission of two neutrinos

ADC Analog to Digital Converter

APD Avalanche PhotoDiode

ATLAr Atmospheric Liquid Argon

BEGe Broad Energy Germanium

BI Background Index

CC4 Commercial CMOS, version 4

CKM Cabibbo-Kobayashi-Maskawa

C.L. Confidence Level

CMOS Complementary Metal-Oxide Semiconductor

CSA Charge Sensitive Amplifier

CP Charge-Parity

DAQ Data AcQuisition

DPLMS Digital Penalized Least Mean Square

DSP Digital Signal Processor

EVT EVenT level

FE Front-End

FOM Figure Of Merit

FWHM Full Width at Half Maximum

HIT High level Tier

HV High Voltage

HPGe High Purity Germanium

IB Inner Barrel

ICPC Inverted Coaxial Point Contact

INFN Istituto Nazionale di Fisica Nucleare

GERDA GERmanium Detector Array

LAr Liquid Argon

LEGEND Large Enriched Germanium Experiment
for Neutrinoless $\beta\beta$ Decay

LET Linear Energy Transfer

LLAMA LEGEND LAr Monitoring Apparatus

LLArS LEGEND Liquid Argon Purification System

LNGS Laboratori Nazionali del Gran Sasso

LY Light Yield

MS Mini Shroud

MSE Multi Site Event

MSW Mikheyev-Smirnov-Wolfenstein

NME Nuclear Matrix Element

NMS Nylon Mini Shroud

OB Outer Barrel

PDF Probability Density Function

PE PhotoElectron

PEN PolyEthylene Naphthalate

PMMA Poly-Methyl MethAcrylate

PMNS Pontecorvo-Maki-Nakagawa-Saka

PMT PhotoMultiplier Tube

PPC P-type Point Contact

PSD Pulse Shape Discrimination

PTFE PolyTetraFluoroEthylene

-
- RMS** Root Mean Square
- SF** Suppression Factor
- SiPM** Silicon PhotoMultiplier
- SM** Standard Model
- SPAD** Single Photon Avalanche Diode
- SPE** Single PhotoElectron
- SSE** Single Site Event
- TPB** TetraPhenyl Butadiene
- TUM** Technical University of Munich
- VUV** Vacuum-UltraViolet
- UGLAr** UnderGround Liquid Argon
- WLS** WaveLength-Shifting
- WLSR** WaveLength-Shifting Reflector

Ringraziamenti

Questa tesi di dottorato è il risultato di poco più di tre anni di impegno costante, durante i quali ho avuto il privilegio di contare sull'aiuto e il sostegno di diverse persone.

Prima di tutto, desidero esprimere la mia profonda gratitudine al Prof. Giuseppe Salamanna e al Dr. Valerio D'Andrea per la loro guida e il sostegno durante il percorso della mia ricerca di dottorato. Un sentito ringraziamento va anche all'Ing. Diego Tagnani, per aver condiviso con me la sua esperienza nel campo dell'elettronica, e al Prof. Stefano Riboldi, per i preziosi insegnamenti nel campo dei filtri digitali.

La dedizione e competenza di ciascuno di voi hanno giocato un ruolo fondamentale nel plasmare sia il contenuto che la direzione di questa tesi, contribuendo in modo significativo all'arricchimento del mio approccio alla ricerca.

I would like to express my sincere gratitude to all the members of the LEGEND collaboration I met during my PhD journey. I am especially grateful to Bernhard Schwingenheuer for his guidance and involvement during my time at Laboratori Nazionali del Gran Sasso, and to the TUM group for giving me the opportunity to work alongside them.

Un ringraziamento speciale va ai miei colleghi Igor e Patrizio per aver reso la mia permanenza a Roma piacevole, rendendo i giorni di lavoro più leggeri. Grazie per tutte le avventure, siete stati davvero la ciliegina sulla torta di questa esperienza romana.

Desidero ringraziare calorosamente anche i miei fantastici colleghi di ufficio, Matteo e Elisabetta. Le nostre discussioni e il nostro supporto reciproco sono stati un sostegno prezioso durante i momenti più difficili di questo percorso. Senza di voi, l'ufficio 105 sarebbe stato un luogo davvero molto triste e cupo.

E infine, ma non meno importante, un enorme grazie va alla mia famiglia e ai miei amici per avermi sempre sostenuto e incoraggiato in ogni fase del mio percorso accademico.

Grazie a tutti per non avermi lasciata naufragare nel mare della ricerca da sola!

Bibliography

- [1] J. Chadwick. “The intensity distribution in the magnetic spectrum of beta particles from radium (B + C)”. In: *Verh. Phys. Gesell.* 16 (1914), pp. 383–391.
- [2] Wolfgang Pauli. “Pauli letter collection: letter to Lise Meitner”. Wissenschaftlicher Briefwechsel mit Bohr, Einstein, Heisenberg, Letter 259. URL: <https://cds.cern.ch/record/83282>.
- [3] E Fermi. “Tentativo di una Teoria Dei Raggi β ”. In: *Nuovo Cim* 11.1-19 (1934), pp. 1–19. DOI: [10.1007/BF02959820](https://doi.org/10.1007/BF02959820).
- [4] Frederick Reines and Clyde L. Cowan. “The neutrino”. In: *Nature* 178 (1956), pp. 446–449. DOI: [10.1038/178446a0](https://doi.org/10.1038/178446a0).
- [5] Bruno Pontecorvo. “Small probability of the $\mu \rightarrow e + \gamma$ and $\mu \rightarrow e + e + e$ processes and neutral currents in weak interactions”. In: *Physics Letters* 1 (1962), pp. 287–288. URL: <https://api.semanticscholar.org/CorpusID:118343184>.
- [6] G. Danby et al. “Observation of High-Energy Neutrino Reactions and the Existence of Two Kinds of Neutrinos”. In: *Phys. Rev. Lett.* 9 (1962), pp. 36–44. DOI: [10.1103/PhysRevLett.9.36](https://doi.org/10.1103/PhysRevLett.9.36).
- [7] K. Kodama et al. “Observation of tau neutrino interactions”. In: *Phys. Lett. B* 504 (2001), pp. 218–224. DOI: [10.1016/S0370-2693\(01\)00307-0](https://doi.org/10.1016/S0370-2693(01)00307-0). arXiv: [hep-ex/0012035](https://arxiv.org/abs/hep-ex/0012035).
- [8] Y. Fukuda et al. “Evidence for oscillation of atmospheric neutrinos”. In: *Phys. Rev. Lett.* 81 (1998), pp. 1562–1567. DOI: [10.1103/PhysRevLett.81.1562](https://doi.org/10.1103/PhysRevLett.81.1562). arXiv: [hep-ex/9807003](https://arxiv.org/abs/hep-ex/9807003).
- [9] Q. R. Ahmad et al. “Measurement of the rate of $\nu_e + d \rightarrow p + p + e^-$ interactions produced by ^8B solar neutrinos at the Sudbury Neutrino Observatory”. In: *Phys. Rev. Lett.* 87 (2001), p. 071301. DOI: [10.1103/PhysRevLett.87.071301](https://doi.org/10.1103/PhysRevLett.87.071301). arXiv: [nucl-ex/0106015](https://arxiv.org/abs/nucl-ex/0106015).
- [10] Ziro Maki, Masami Nakagawa, and Shoichi Sakata. “Remarks on the unified model of elementary particles”. In: *Prog. Theor. Phys.* 28 (1962), pp. 870–880. DOI: [10.1143/PTP.28.870](https://doi.org/10.1143/PTP.28.870).
- [11] V. N. Gribov and B. Pontecorvo. “Neutrino astronomy and lepton charge”. In: *Phys. Lett. B* 28 (1969), p. 493. DOI: [10.1016/0370-2693\(69\)90525-5](https://doi.org/10.1016/0370-2693(69)90525-5).

- [12] Raymond Davis Jr., Don S. Harmer, and Kenneth C. Hoffman. “Search for neutrinos from the sun”. In: *Phys. Rev. Lett.* 20 (1968), pp. 1205–1209. DOI: [10.1103/PhysRevLett.20.1205](https://doi.org/10.1103/PhysRevLett.20.1205).
- [13] K. Abe et al. “Atmospheric neutrino oscillation analysis with external constraints in Super-Kamiokande I-IV”. In: *Phys. Rev. D* 97.7 (2018), p. 072001. DOI: [10.1103/PhysRevD.97.072001](https://doi.org/10.1103/PhysRevD.97.072001). arXiv: [1710.09126](https://arxiv.org/abs/1710.09126) [hep-ex].
- [14] K. Eguchi et al. “First results from KamLAND: Evidence for reactor anti-neutrino disappearance”. In: *Phys. Rev. Lett.* 90 (2003), p. 021802. DOI: [10.1103/PhysRevLett.90.021802](https://doi.org/10.1103/PhysRevLett.90.021802). arXiv: [hep-ex/0212021](https://arxiv.org/abs/hep-ex/0212021).
- [15] E. Radicioni. “Results from the CHORUS experiment at CERN”. In: *Nucl. Phys. B Proc. Suppl.* 85 (2000). Ed. by G. Bruni, F. L. Navarra, and P. G. Pelfer, pp. 95–100. DOI: [10.1016/S0920-5632\(00\)00489-8](https://doi.org/10.1016/S0920-5632(00)00489-8).
- [16] A. Yu. Smirnov. “The MSW effect and solar neutrinos”. In: *10th International Workshop on Neutrino Telescopes*. May 2003, pp. 23–43. arXiv: [hep-ph/0305106](https://arxiv.org/abs/hep-ph/0305106).
- [17] Ivan Esteban et al. “Global analysis of three-flavour neutrino oscillations: synergies and tensions in the determination of θ_{23} , δ_{CP} , and the mass ordering”. In: *JHEP* 01 (2019), p. 106. DOI: [10.1007/JHEP01\(2019\)106](https://doi.org/10.1007/JHEP01(2019)106). arXiv: [1811.05487](https://arxiv.org/abs/1811.05487) [hep-ph].
- [18] Babak Abi et al. “Deep Underground Neutrino Experiment (DUNE), Far Detector Technical Design Report, Volume III: DUNE Far Detector Technical Coordination”. In: *JINST* 15.08 (2020), T08009. DOI: [10.1088/1748-0221/15/08/T08009](https://doi.org/10.1088/1748-0221/15/08/T08009). arXiv: [2002.03008](https://arxiv.org/abs/2002.03008) [physics.ins-det].
- [19] K. Abe et al. “Physics potential of a long-baseline neutrino oscillation experiment using a J-PARC neutrino beam and Hyper-Kamiokande”. In: *PTEP* 2015 (2015), p. 053C02. DOI: [10.1093/ptep/ptv061](https://doi.org/10.1093/ptep/ptv061). arXiv: [1502.05199](https://arxiv.org/abs/1502.05199) [hep-ex].
- [20] Angel Abusleme et al. “JUNO physics and detector”. In: *Prog. Part. Nucl. Phys.* 123 (2022), p. 103927. DOI: [10.1016/j.pnpnp.2021.103927](https://doi.org/10.1016/j.pnpnp.2021.103927). arXiv: [2104.02565](https://arxiv.org/abs/2104.02565) [hep-ex].
- [21] Esteban Roulet and Francesco Vissani. *Neutrinos in Physics and Astrophysics*. World Scientific, 2023.
- [22] Ettore Majorana. “Teoria simmetrica dell’elettrone e del positrone”. In: *Nuovo Cim.* 14 (1937), pp. 171–184. DOI: [10.1007/BF02961314](https://doi.org/10.1007/BF02961314).
- [23] R. Primulando, J. Julio, and P. Uttayarat. “Zee model with quasidegenerate neutrino masses and where to find it”. In: *Eur. Phys. J. C* 82.3 (2022), p. 253. DOI: [10.1140/epjc/s10052-022-10189-0](https://doi.org/10.1140/epjc/s10052-022-10189-0). arXiv: [2201.01960](https://arxiv.org/abs/2201.01960) [hep-ph].
- [24] Pierre Fayet. “The Supersymmetric Standard Model”. In: *Adv. Ser. Direct. High Energy Phys.* 26 (2016), pp. 397–454. DOI: [10.1142/9789814733519_0020](https://doi.org/10.1142/9789814733519_0020). arXiv: [1506.08277](https://arxiv.org/abs/1506.08277) [hep-ph].
- [25] Evgeny K. Akhmedov, G. C. Branco, and M. N. Rebelo. “Seesaw mechanism and structure of neutrino mass matrix”. In: *Phys. Lett. B* 478 (2000), pp. 215–223. DOI: [10.1016/S0370-2693\(00\)00282-3](https://doi.org/10.1016/S0370-2693(00)00282-3). arXiv: [hep-ph/9911364](https://arxiv.org/abs/hep-ph/9911364).
- [26] Frank F Deppisch. *A Modern Introduction to Neutrino Physics*. 2053-2571. Morgan Claypool Publishers, 2019. ISBN: 978-1-64327-680-9. DOI: [10.1088/2053-2571/ab21c9](https://doi.org/10.1088/2053-2571/ab21c9).

- [27] N. Aghanim et al. “Planck 2018 results. VI. Cosmological parameters”. In: *Astron. Astrophys.* 641 (2020). [Erratum: *Astron. Astrophys.* 652, C4 (2021)], A6. DOI: [10.1051/0004-6361/201833910](https://doi.org/10.1051/0004-6361/201833910). arXiv: [1807.06209](https://arxiv.org/abs/1807.06209) [astro-ph.CO].
- [28] M. Aker et al. “Direct neutrino-mass measurement with sub-electronvolt sensitivity”. In: *Nature Phys.* 18.2 (2022), pp. 160–166. DOI: [10.1038/s41567-021-01463-1](https://doi.org/10.1038/s41567-021-01463-1). arXiv: [2105.08533](https://arxiv.org/abs/2105.08533) [hep-ex].
- [29] A. Gando et al. “Search for Majorana Neutrinos near the Inverted Mass Hierarchy Region with KamLAND-Zen”. In: *Phys. Rev. Lett.* 117.8 (2016). [Addendum: *Phys. Rev. Lett.* 117, 109903 (2016)], p. 082503. DOI: [10.1103/PhysRevLett.117.082503](https://doi.org/10.1103/PhysRevLett.117.082503). arXiv: [1605.02889](https://arxiv.org/abs/1605.02889) [hep-ex].
- [30] Matteo Agostini et al. “Toward the discovery of matter creation with neutrinoless $\beta\beta$ decay”. In: *Rev. Mod. Phys.* 95.2 (2023), p. 025002. DOI: [10.1103/RevModPhys.95.025002](https://doi.org/10.1103/RevModPhys.95.025002). arXiv: [2202.01787](https://arxiv.org/abs/2202.01787) [hep-ex].
- [31] M. Goeppert-Mayer. “Double beta-disintegration”. In: *Phys. Rev.* 48 (1935), pp. 512–516. DOI: [10.1103/PhysRev.48.512](https://doi.org/10.1103/PhysRev.48.512).
- [32] Alexander Barabash. “Double Beta Decay Experiments: Recent Achievements and Future Prospects”. In: *Universe* 9.6 (2023), p. 290. DOI: [10.3390/universe9060290](https://doi.org/10.3390/universe9060290).
- [33] W. H. Furry. “On Transition Probabilities in Double Beta-Disintegration”. In: *Phys. Rev.* 56 (12 Dec. 1939), pp. 1184–1193. DOI: [10.1103/PhysRev.56.1184](https://doi.org/10.1103/PhysRev.56.1184).
- [34] Michael Duerr, Manfred Lindner, and Alexander Merle. “On the Quantitative Impact of the Schechter-Valle Theorem”. In: *JHEP* 06 (2011), p. 091. DOI: [10.1007/JHEP06\(2011\)091](https://doi.org/10.1007/JHEP06(2011)091). arXiv: [1105.0901](https://arxiv.org/abs/1105.0901) [hep-ph].
- [35] Werner Rodejohann. “Neutrinoless double beta decay and neutrino physics”. In: *J. Phys. G* 39 (2012), p. 124008. DOI: [10.1088/0954-3889/39/12/124008](https://doi.org/10.1088/0954-3889/39/12/124008). arXiv: [1206.2560](https://arxiv.org/abs/1206.2560) [hep-ph].
- [36] M. Doi et al. “Neutrino Mass, the Right-handed Interaction and the Double Beta Decay. 1. Formalism”. In: *Prog. Theor. Phys.* 66 (1981). [Erratum: *Prog. Theor. Phys.* 68, 347 (1982)], p. 1739. DOI: [10.1143/PTP.66.1739](https://doi.org/10.1143/PTP.66.1739).
- [37] J. Kotila and F. Iachello. “Phase space factors for double- β decay”. In: *Phys. Rev. C* 85 (2012), p. 034316. DOI: [10.1103/PhysRevC.85.034316](https://doi.org/10.1103/PhysRevC.85.034316). arXiv: [1209.5722](https://arxiv.org/abs/1209.5722) [nucl-th].
- [38] Sabin Stoica and Mihail Mirea. “New calculations for phase space factors involved in double- β decay”. In: *Phys. Rev. C* 88.3 (2013), p. 037303. DOI: [10.1103/PhysRevC.88.037303](https://doi.org/10.1103/PhysRevC.88.037303). arXiv: [1307.0290](https://arxiv.org/abs/1307.0290) [nucl-th].
- [39] J. Barea, J. Kotila, and F. Iachello. “Nuclear matrix elements for double- β decay”. In: *Phys. Rev. C* 87.1 (2013), p. 014315. DOI: [10.1103/PhysRevC.87.014315](https://doi.org/10.1103/PhysRevC.87.014315). arXiv: [1301.4203](https://arxiv.org/abs/1301.4203) [nucl-th].
- [40] Jonathan Engel and Javier Menéndez. “Status and Future of Nuclear Matrix Elements for Neutrinoless Double-Beta Decay: A Review”. In: *Rept. Prog. Phys.* 80.4 (2017), p. 046301. DOI: [10.1088/1361-6633/aa5bc5](https://doi.org/10.1088/1361-6633/aa5bc5). arXiv: [1610.06548](https://arxiv.org/abs/1610.06548) [nucl-th].
- [41] Jouni Suhonen and Osvaldo Civitarese. “Probing the quenching of g_A by single and double beta decays”. In: *Physics Letters B* 725.1 (2013), pp. 153–157. ISSN: 0370-2693. DOI: <https://doi.org/10.1016/j.physletb.2013.06.042>.

- [42] R. G. H. Robertson. “Empirical Survey of Neutrinoless Double Beta Decay Matrix Elements”. In: *Mod. Phys. Lett. A* 28 (2013), p. 1350021. doi: [10.1142/S0217732313500211](https://doi.org/10.1142/S0217732313500211). arXiv: [1301.1323](https://arxiv.org/abs/1301.1323) [nucl-th].
- [43] Stefano Dell’Oro et al. “Neutrinoless double beta decay: 2015 review”. In: *Adv. High Energy Phys.* 2016 (2016), p. 2162659. doi: [10.1155/2016/2162659](https://doi.org/10.1155/2016/2162659). arXiv: [1601.07512](https://arxiv.org/abs/1601.07512) [hep-ph].
- [44] S. Abe et al. “Search for the Majorana Nature of Neutrinos in the Inverted Mass Ordering Region with KamLAND-Zen”. In: *Phys. Rev. Lett.* 130.5 (2023), p. 051801. doi: [10.1103/PhysRevLett.130.051801](https://doi.org/10.1103/PhysRevLett.130.051801). arXiv: [2203.02139](https://arxiv.org/abs/2203.02139) [hep-ex].
- [45] G. Anton et al. “Search for Neutrinoless Double- β Decay with the Complete EXO-200 Dataset”. In: *Phys. Rev. Lett.* 123.16 (2019), p. 161802. doi: [10.1103/PhysRevLett.123.161802](https://doi.org/10.1103/PhysRevLett.123.161802). arXiv: [1906.02723](https://arxiv.org/abs/1906.02723) [hep-ex].
- [46] M. Agostini et al. “Final Results of GERDA on the Search for Neutrinoless Double- β Decay”. In: *Phys. Rev. Lett.* 125.25 (2020), p. 252502. doi: [10.1103/PhysRevLett.125.252502](https://doi.org/10.1103/PhysRevLett.125.252502). arXiv: [2009.06079](https://arxiv.org/abs/2009.06079) [nucl-ex].
- [47] I. J. Arnquist et al. “Final Result of the Majorana Demonstrator’s Search for Neutrinoless Double- β Decay in Ge76”. In: *Phys. Rev. Lett.* 130.6 (2023), p. 062501. doi: [10.1103/PhysRevLett.130.062501](https://doi.org/10.1103/PhysRevLett.130.062501). arXiv: [2207.07638](https://arxiv.org/abs/2207.07638) [nucl-ex].
- [48] D. Q. Adams et al. “Search for Majorana neutrinos exploiting millikelvin cryogenics with CUORE”. In: *Nature* 604.7904 (2022), pp. 53–58. doi: [10.1038/s41586-022-04497-4](https://doi.org/10.1038/s41586-022-04497-4). arXiv: [2104.06906](https://arxiv.org/abs/2104.06906) [nucl-ex].
- [49] O. Azzolini et al. “Final Result on the Neutrinoless Double Beta Decay of ^{82}Se with CUPID-0”. In: *Phys. Rev. Lett.* 129.11 (2022), p. 111801. doi: [10.1103/PhysRevLett.129.111801](https://doi.org/10.1103/PhysRevLett.129.111801). arXiv: [2206.05130](https://arxiv.org/abs/2206.05130) [hep-ex].
- [50] C. Augier et al. “Final results on the $0\nu\beta\beta$ decay half-life limit of ^{100}Mo from the CUPID-Mo experiment”. In: *Eur. Phys. J. C* 82.11 (2022), p. 1033. doi: [10.1140/epjc/s10052-022-10942-5](https://doi.org/10.1140/epjc/s10052-022-10942-5). arXiv: [2202.08716](https://arxiv.org/abs/2202.08716) [nucl-ex].
- [51] V. Albanese et al. “The SNO+ experiment”. In: *JINST* 16.08 (2021), P08059. doi: [10.1088/1748-0221/16/08/P08059](https://doi.org/10.1088/1748-0221/16/08/P08059). arXiv: [2104.11687](https://arxiv.org/abs/2104.11687) [physics.ins-det].
- [52] N. Abgrall et al. “The Large Enriched Germanium Experiment for Neutrinoless Double Beta Decay (LEGEND)”. In: *AIP Conf. Proc.* 1894.1 (2017). Ed. by Osvaldo Civitarese, Ivan Stekl, and Jouni Suhonen, p. 020027. doi: [10.1063/1.5007652](https://doi.org/10.1063/1.5007652).
- [53] N. Abgrall et al. “The Large Enriched Germanium Experiment for Neutrinoless $\beta\beta$ Decay: LEGEND-1000 Preconceptual Design Report”. In: (July 2021). arXiv: [2107.11462](https://arxiv.org/abs/2107.11462) [physics.ins-det].
- [54] K. Alfonso et al. “CUPID: The Next-Generation Neutrinoless Double Beta Decay Experiment”. In: *J. Low Temp. Phys.* 211.5-6 (2023), pp. 375–383. doi: [10.1007/s10909-022-02909-3](https://doi.org/10.1007/s10909-022-02909-3).
- [55] G. Adhikari et al. “nEXO: neutrinoless double beta decay search beyond 10^{28} year half-life sensitivity”. In: *J. Phys. G* 49.1 (2022), p. 015104. doi: [10.1088/1361-6471/ac3631](https://doi.org/10.1088/1361-6471/ac3631). arXiv: [2106.16243](https://arxiv.org/abs/2106.16243) [nucl-ex].
- [56] J. J. Gomez-Cadenas. “Status and prospects of the NEXT experiment for neutrinoless double beta decay searches”. In: *54th Rencontres de Moriond on Electroweak Interactions and Unified Theories.* 2019, pp. 201–206. arXiv: [1906.01743](https://arxiv.org/abs/1906.01743) [hep-ex].

- [57] F. Agostini et al. “Sensitivity of the DARWIN observatory to the neutrinoless double beta decay of ^{136}Xe ”. In: *Eur. Phys. J. C* 80.9 (2020), p. 808. DOI: [10.1140/epjc/s10052-020-8196-z](https://doi.org/10.1140/epjc/s10052-020-8196-z). arXiv: [2003.13407](https://arxiv.org/abs/2003.13407) [physics.ins-det].
- [58] Nina Burlac and Giuseppe Salamanna. “Present and Future of $0\nu 2\beta$ Searches with Germanium”. In: *Universe* 7.10 (2021), p. 386. DOI: [10.3390/universe7100386](https://doi.org/10.3390/universe7100386).
- [59] Thibaud Le Noblet. “Latest results from NEMO-3 and commissioning status of the SuperNEMO demonstrator”. In: *J. Phys. Conf. Ser.* 1342.1 (2020). Ed. by Ken Clark et al., p. 012029. DOI: [10.1088/1742-6596/1342/1/012029](https://doi.org/10.1088/1742-6596/1342/1/012029).
- [60] R. Arnold et al. “Probing New Physics Models of Neutrinoless Double Beta Decay with SuperNEMO”. In: *Eur. Phys. J. C* 70 (2010), pp. 927–943. DOI: [10.1140/epjc/s10052-010-1481-5](https://doi.org/10.1140/epjc/s10052-010-1481-5). arXiv: [1005.1241](https://arxiv.org/abs/1005.1241) [hep-ex].
- [61] Valerio D’Andrea et al. “Neutrinoless Double Beta Decay with Germanium Detectors: 1026 yr and Beyond”. In: *Universe* 7.9 (2021), p. 341. DOI: [10.3390/universe7090341](https://doi.org/10.3390/universe7090341). arXiv: [2109.07575](https://arxiv.org/abs/2109.07575) [hep-ex].
- [62] J. Barea, J. Kotila, and F. Iachello. “Limits on Neutrino Masses from Neutrinoless Double-beta Decay”. In: *Phys. Rev. Lett.* 109 (2012), p. 042501. DOI: [10.1103/PhysRevLett.109.042501](https://doi.org/10.1103/PhysRevLett.109.042501). arXiv: [1506.08533](https://arxiv.org/abs/1506.08533) [nucl-th].
- [63] Christoph Wiesinger. “No neutrinos not found. First exploration of neutrinoless double beta decay half-lives beyond 10^{26} years”. PhD thesis. Munich, Tech. U., May 2020. URL: <https://d-nb.info/1223617025/34>.
- [64] K. H. Ackermann et al. “The GERDA experiment for the search of $0\nu\beta\beta$ decay in ^{76}Ge ”. In: *Eur. Phys. J. C* 73.3 (2013), p. 2330. DOI: [10.1140/epjc/s10052-013-2330-0](https://doi.org/10.1140/epjc/s10052-013-2330-0). arXiv: [1212.4067](https://arxiv.org/abs/1212.4067) [physics.ins-det].
- [65] M. Agostini et al. “Flux Modulations seen by the Muon Veto of the GERDA Experiment”. In: *Astropart. Phys.* 84 (2016), pp. 29–35. DOI: [10.1016/j.astropartphys.2016.08.002](https://doi.org/10.1016/j.astropartphys.2016.08.002). arXiv: [1601.06007](https://arxiv.org/abs/1601.06007) [physics.ins-det].
- [66] K. T. Knöpfle and B. Schwingenheuer. “Design and performance of the GERDA low-background cryostat for operation in water”. In: *JINST* 17.02 (2022), P02038. DOI: [10.1088/1748-0221/17/02/P02038](https://doi.org/10.1088/1748-0221/17/02/P02038). arXiv: [2202.03847](https://arxiv.org/abs/2202.03847) [physics.ins-det].
- [67] Mario Schwarz et al. “Liquid Argon Instrumentation and Monitoring in LEGEND-200”. In: *EPJ Web Conf.* 253 (2021), p. 11014. DOI: [10.1051/epjconf/202125311014](https://doi.org/10.1051/epjconf/202125311014).
- [68] G. R. Araujo et al. “R &D of wavelength-shifting reflectors and characterization of the quantum efficiency of tetraphenyl butadiene and polyethylene naphthalate in liquid argon”. In: *Eur. Phys. J. C* 82.5 (2022), p. 442. DOI: [10.1140/epjc/s10052-022-10383-0](https://doi.org/10.1140/epjc/s10052-022-10383-0). arXiv: [2112.06675](https://arxiv.org/abs/2112.06675) [physics.ins-det].
- [69] L. Manzanillas et al. “Optical properties of low background PEN structural components for the Legend-200 experiment”. In: *JINST* 17.09 (2022), P09007. DOI: [10.1088/1748-0221/17/09/P09007](https://doi.org/10.1088/1748-0221/17/09/P09007). arXiv: [2204.13747](https://arxiv.org/abs/2204.13747) [physics.ins-det].
- [70] N. Abgrall et al. “The Majorana Demonstrator radioassay program”. In: *Nucl. Instrum. Meth. A* 828 (2016), pp. 22–36. DOI: [10.1016/j.nima.2016.04.070](https://doi.org/10.1016/j.nima.2016.04.070). arXiv: [1601.03779](https://arxiv.org/abs/1601.03779) [physics.ins-det].
- [71] A. Lubashevskiy et al. “Mitigation of $^{42}\text{Ar}/^{42}\text{K}$ background for the GERDA Phase II experiment”. In: *Eur. Phys. J. C* 78.1 (2018), p. 15. DOI: [10.1140/epjc/s10052-017-5499-9](https://doi.org/10.1140/epjc/s10052-017-5499-9). arXiv: [1708.00226](https://arxiv.org/abs/1708.00226) [physics.ins-det].

- [72] J. Eberth and J. Simpson. “From Ge(Li) detectors to gamma-ray tracking arrays—50 years of gamma spectroscopy with germanium detectors”. In: *Progress in Particle and Nuclear Physics* 60.2 (2008), pp. 283–337. ISSN: 0146-6410. DOI: <https://doi.org/10.1016/j.pnpnp.2007.09.001>.
- [73] M. Agostini et al. “Characterization of ^{30}Ge enriched Broad Energy Ge detectors for GERDA Phase II”. In: *Eur. Phys. J. C* 79.11 (2019), p. 978. DOI: [10.1140/epjc/s10052-019-7353-8](https://doi.org/10.1140/epjc/s10052-019-7353-8). arXiv: [1901.06590](https://arxiv.org/abs/1901.06590) [physics.ins-det].
- [74] E. Aguayo et al. “Characteristics of Signals Originating Near the Lithium-Diffused N+ Contact of High Purity Germanium P-Type Point Contact Detectors”. In: *Nucl. Instrum. Meth. A* 701 (2013), pp. 176–185. DOI: [10.1016/j.nima.2012.11.004](https://doi.org/10.1016/j.nima.2012.11.004). arXiv: [1207.6716](https://arxiv.org/abs/1207.6716) [physics.ins-det].
- [75] R.J. Cooper et al. “A novel HPGe detector for gamma-ray tracking and imaging”. In: *Nuclear Instruments and Methods in Physics Research Section A: Accelerators, Spectrometers, Detectors and Associated Equipment* 665 (2011), pp. 25–32. ISSN: 0168-9002. DOI: <https://doi.org/10.1016/j.nima.2011.10.008>.
- [76] M. Agostini et al. “Characterization of inverted coaxial ^{76}Ge detectors in GERDA for future double- β decay experiments”. In: *Eur. Phys. J. C* 81.6 (2021), p. 505. DOI: [10.1140/epjc/s10052-021-09184-8](https://doi.org/10.1140/epjc/s10052-021-09184-8). arXiv: [2103.15111](https://arxiv.org/abs/2103.15111) [physics.ins-det].
- [77] Michael Willers. “Signal Readout Electronics for LEGEND-200”. In: *J. Phys. Conf. Ser.* 1468.1 (2020). Ed. by Masayuki Nakahata, p. 012113. DOI: [10.1088/1742-6596/1468/1/012113](https://doi.org/10.1088/1742-6596/1468/1/012113). arXiv: [1911.05847](https://arxiv.org/abs/1911.05847) [physics.ins-det].
- [78] Paul Barton et al. “Low-noise low-mass front end electronics for low-background physics experiments using germanium detectors”. In: *2011 IEEE Nuclear Science Symposium Conference Record*. 2011, pp. 1976–1979. DOI: [10.1109/NSSMIC.2011.6154397](https://doi.org/10.1109/NSSMIC.2011.6154397).
- [79] S. Riboldi et al. “Cryogenic readout techniques for Germanium detectors”. In: *2015 4th International Conference on Advancements in Nuclear Instrumentation Measurement Methods and their Applications (ANIMMA)*. 2015, pp. 1–6. DOI: [10.1109/ANIMMA.2015.7465549](https://doi.org/10.1109/ANIMMA.2015.7465549).
- [80] L. Baudis et al. “Calibration sources for the LEGEND-200 experiment”. In: *JINST* 18.02 (2023), P02001. DOI: [10.1088/1748-0221/18/02/P02001](https://doi.org/10.1088/1748-0221/18/02/P02001). arXiv: [2211.05026](https://arxiv.org/abs/2211.05026) [physics.ins-det].
- [81] A. Gadola et al. “FlashCam: a novel Cherenkov telescope camera with continuous signal digitization”. In: *JINST* 10.01 (2015), p. C01014. DOI: [10.1088/1748-0221/10/01/C01014](https://doi.org/10.1088/1748-0221/10/01/C01014).
- [82] G. Grunauer. “Muon Veto – Status Update”. In: *Talk at the LEGEND Collaboration Meeting* (Roma Tre University, May 2023.).
- [83] M. De Deo et al. “Accurate GPS-based timestamp facility for Gran Sasso National Laboratory”. In: *JINST* 14.04 (2019), P04001. DOI: [10.1088/1748-0221/14/04/P04001](https://doi.org/10.1088/1748-0221/14/04/P04001). arXiv: [1903.00233](https://arxiv.org/abs/1903.00233) [physics.ins-det].
- [84] K. Freund et al. “The Performance of the Muon Veto of the GERDA Experiment”. In: *Eur. Phys. J. C* 76.5 (2016), p. 298. DOI: [10.1140/epjc/s10052-016-4140-7](https://doi.org/10.1140/epjc/s10052-016-4140-7). arXiv: [1601.05935](https://arxiv.org/abs/1601.05935) [physics.ins-det].

- [85] Tadayoshi Doke et al. “Let dependence of scintillation yields in liquid argon”. In: *Nuclear Instruments and Methods in Physics Research Section A: Accelerators, Spectrometers, Detectors and Associated Equipment* 269.1 (1988), pp. 291–296. ISSN: 0168-9002. DOI: [https://doi.org/10.1016/0168-9002\(88\)90892-3](https://doi.org/10.1016/0168-9002(88)90892-3).
- [86] M. Agostini et al. “Pulse shape analysis in Gerda Phase II”. In: *Eur. Phys. J. C* 82.4 (2022), p. 284. DOI: [10.1140/epjc/s10052-022-10163-w](https://doi.org/10.1140/epjc/s10052-022-10163-w). arXiv: [2202.13355](https://arxiv.org/abs/2202.13355) [physics.ins-det].
- [87] M. Willers. “LEGEND-200: From Construction to Physics Data Taking”. In: *Talk at XVIII TAUP Conference* (Vienna, September 2023.).
- [88] K. von Sturm. “LEGEND-200: A first glance at the background in physics data”. In: *Talk at XVIII TAUP Conference* (Vienna, September 2023.).
- [89] Allen Caldwell, Daniel Kollár, and Kevin Kröninger. “BAT – The Bayesian analysis toolkit”. In: *Computer Physics Communications* 180.11 (2009), pp. 2197–2209. ISSN: 0010-4655. DOI: <https://doi.org/10.1016/j.cpc.2009.06.026>.
- [90] M Neuberger et al. “The cosmic muon-induced background for the LEGEND-1000 alternative site at LNGS”. In: *Journal of Physics: Conference Series* 2156.1 (Dec. 2021), p. 012216. DOI: [10.1088/1742-6596/2156/1/012216](https://doi.org/10.1088/1742-6596/2156/1/012216).
- [91] Philippe Sarda. “Argon Isotopes”. In: *Encyclopedia of Geochemistry: A Comprehensive Reference Source on the Chemistry of the Earth*. Ed. by William M. White. Cham: Springer International Publishing, 2018, pp. 56–58. ISBN: 978-3-319-39312-4. DOI: [10.1007/978-3-319-39312-4_206](https://doi.org/10.1007/978-3-319-39312-4_206).
- [92] P. Cennini et al. “On atmospheric Ar-39 and Ar-42 abundance”. In: *Nuclear Instruments and Methods in Physics Research Section A: Accelerators, Spectrometers, Detectors and Associated Equipment* 356.2 (1995), pp. 526–529. ISSN: 0168-9002. DOI: [https://doi.org/10.1016/0168-9002\(94\)01234-2](https://doi.org/10.1016/0168-9002(94)01234-2).
- [93] R. Saldanha et al. “Cosmogenic production of ^{39}Ar and ^{37}Ar in argon”. In: *Phys. Rev. C* 100.2 (2019), p. 024608. DOI: [10.1103/PhysRevC.100.024608](https://doi.org/10.1103/PhysRevC.100.024608). arXiv: [1902.09072](https://arxiv.org/abs/1902.09072) [nucl-ex].
- [94] H.H. Loosli and H. Oeschger. “Detection of ^{39}Ar in atmospheric argon”. In: *Earth and Planetary Science Letters* 5 (1968), pp. 191–198. ISSN: 0012-821X. DOI: [https://doi.org/10.1016/S0012-821X\(68\)80039-1](https://doi.org/10.1016/S0012-821X(68)80039-1).
- [95] P. Benetti et al. “Measurement of the specific activity of ar-39 in natural argon”. In: *Nucl. Instrum. Meth. A* 574 (2007), pp. 83–88. DOI: [10.1016/j.nima.2007.01.106](https://doi.org/10.1016/j.nima.2007.01.106). arXiv: [astro-ph/0603131](https://arxiv.org/abs/astro-ph/0603131).
- [96] P. Adhikari et al. “Precision measurement of the specific activity of ^{39}Ar in atmospheric argon with the DEAP-3600 detector”. In: *Eur. Phys. J. C* 83.7 (2023), p. 642. DOI: [10.1140/epjc/s10052-023-11678-6](https://doi.org/10.1140/epjc/s10052-023-11678-6). arXiv: [2302.14639](https://arxiv.org/abs/2302.14639) [physics.ins-det].
- [97] Jun Chen. “Nuclear Data Sheets for A=39”. In: *Nuclear Data Sheets* 149 (2018), pp. 1–251. ISSN: 0090-3752. DOI: <https://doi.org/10.1016/j.nds.2018.03.001>.

- [98] A.J Peurrung et al. “Expected atmospheric concentration of ^{42}Ar ”. In: *Nuclear Instruments and Methods in Physics Research Section A: Accelerators, Spectrometers, Detectors and Associated Equipment* 396.3 (1997), pp. 425–426. ISSN: 0168-9002. DOI: [https://doi.org/10.1016/S0168-9002\(97\)00819-X](https://doi.org/10.1016/S0168-9002(97)00819-X).
- [99] R. Ajaj et al. “Electromagnetic backgrounds and potassium-42 activity in the DEAP-3600 dark matter detector”. In: *Phys. Rev. D* 100.7 (2019), p. 072009. DOI: [10.1103/PhysRevD.100.072009](https://doi.org/10.1103/PhysRevD.100.072009). arXiv: [1905.05811](https://arxiv.org/abs/1905.05811) [nucl-ex].
- [100] Jun Chen and Balraj Singh. “Nuclear Data Sheets for $A = 42$ ”. In: *Nuclear Data Sheets* 135 (2016), pp. 1–192. ISSN: 0090-3752. DOI: <https://doi.org/10.1016/j.nds.2016.06.001>.
- [101] W. Kutschera et al. “Long-lived noble gas radionuclides”. In: *Nuclear Instruments and Methods in Physics Research Section B: Beam Interactions with Materials and Atoms* 92.1 (1994), pp. 241–248. ISSN: 0168-583X. DOI: [https://doi.org/10.1016/0168-583X\(94\)96013-5](https://doi.org/10.1016/0168-583X(94)96013-5).
- [102] Stephanie Musy and Roland Purtschert. “Reviewing ^{39}Ar and ^{37}Ar underground production in shallow depths with implications for groundwater dating”. In: *Science of The Total Environment* 884 (2023), p. 163868. ISSN: 0048-9697. DOI: <https://doi.org/10.1016/j.scitotenv.2023.163868>.
- [103] A.S Barabash, V.N Kornoukhov, and V.E Jants. “Estimate of the ^{42}Ar content in the Earth’s atmosphere”. In: *Nuclear Instruments and Methods in Physics Research Section A: Accelerators, Spectrometers, Detectors and Associated Equipment* 385.3 (1997), pp. 530–534. ISSN: 0168-9002. DOI: [https://doi.org/10.1016/S0168-9002\(96\)01074-1](https://doi.org/10.1016/S0168-9002(96)01074-1).
- [104] D. Acosta-Kane et al. “Discovery of underground argon with low level of radioactive ^{39}Ar and possible applications to WIMP dark matter detectors”. In: *Nuclear Instruments and Methods in Physics Research Section A: Accelerators, Spectrometers, Detectors and Associated Equipment* 587.1 (2008), pp. 46–51. ISSN: 0168-9002. DOI: <https://doi.org/10.1016/j.nima.2007.12.032>.
- [105] Sagar S. Poudel et al. “Subsurface cosmogenic and radiogenic production of ^{42}Ar ”. In: (Sept. 2023). arXiv: [2309.16169](https://arxiv.org/abs/2309.16169) [physics.ins-det].
- [106] P. Agnes et al. “Results From the First Use of Low Radioactivity Argon in a Dark Matter Search”. In: *Phys. Rev. D* 93.8 (2016). [Addendum: *Phys.Rev.D* 95, 069901 (2017)], p. 081101. DOI: [10.1103/PhysRevD.93.081101](https://doi.org/10.1103/PhysRevD.93.081101). arXiv: [1510.00702](https://arxiv.org/abs/1510.00702) [astro-ph.CO].
- [107] C Amsler et al. “Luminescence quenching of the triplet excimer state by air traces in gaseous argon”. In: *Journal of Instrumentation* 3.02 (Feb. 2008), P02001–P02001. DOI: [10.1088/1748-0221/3/02/p02001](https://doi.org/10.1088/1748-0221/3/02/p02001).
- [108] T. Heindl et al. “The scintillation of liquid argon”. In: *EPL (Europhysics Letters)* 91.6 (Sept. 2010), p. 62002. DOI: [10.1209/0295-5075/91/62002](https://doi.org/10.1209/0295-5075/91/62002).
- [109] G. S. Hurst, T. E. Stewart, and J. E. Parks. “Vacuum Ultraviolet Radiation and Jesse Effects in the Noble Gases”. In: *Phys. Rev. A* 2 (5 Nov. 1970), pp. 1717–1720. DOI: [10.1103/PhysRevA.2.1717](https://doi.org/10.1103/PhysRevA.2.1717).

- [110] M.J. Carvalho and G. Klein. “Alpha-particle induced scintillation in dense gaseous argon: emission spectra and temporal behaviour of its ionic component”. In: *Nuclear Instruments and Methods* 178.2 (1980), pp. 469–475. ISSN: 0029-554X. DOI: [https://doi.org/10.1016/0029-554X\(80\)90826-5](https://doi.org/10.1016/0029-554X(80)90826-5).
- [111] G Heusser. “Low-Radioactivity Background Techniques”. In: *Annual Review of Nuclear and Particle Science* 45.1 (1995), pp. 543–590. DOI: [10.1146/annurev.ns.45.120195.002551](https://doi.org/10.1146/annurev.ns.45.120195.002551). eprint: <https://doi.org/10.1146/annurev.ns.45.120195.002551>.
- [112] Tadayoshi Doke et al. “Absolute Scintillation Yields in Liquid Argon and Xenon for Various Particles”. In: *Japanese Journal of Applied Physics* 41.3R (Mar. 2002), p. 1538. DOI: [10.1143/JJAP.41.1538](https://doi.org/10.1143/JJAP.41.1538).
- [113] R. Acciarri et al. WArP Collaboration. “Effects of Nitrogen contamination in liquid Argon”. In: *Journal of Instrumentation* 5.06 (June 2010), P06003–P06003. DOI: [10.1088/1748-0221/5/06/p06003](https://doi.org/10.1088/1748-0221/5/06/p06003).
- [114] R. Acciarri et al. WArP Collaboration. “Oxygen contamination in liquid Argon: combined effects on ionization electron charge and scintillation light”. In: *Journal of Instrumentation* 5.05 (May 2010), P05003–P05003. DOI: [10.1088/1748-0221/5/05/p05003](https://doi.org/10.1088/1748-0221/5/05/p05003).
- [115] Christoph Vogl. “Liquid Argon: Purification and Xenon-Doping for LEGEND”. PhD thesis. Munich, Tech. U., Sept. 2021. DOI: <https://doi.org/10.13140/RG.2.2.23118.54084>.
- [116] Malgorzata Haranczyk et al. “Purification of large volume of liquid argon for LEGEND-200”. In: *PoS PANIC2021* (2022), p. 102. DOI: [10.22323/1.380.0102](https://doi.org/10.22323/1.380.0102).
- [117] G. Zuzel. “LAr purification and fill results”. In: *Talk at the LEGEND Collaboration Meeting* (Remote, October 2021.).
- [118] M. Agostini et al. “Liquid argon light collection and veto modeling in GERDA Phase II”. In: *Eur. Phys. J. C* 83.4 (2023), p. 319. DOI: [10.1140/epjc/s10052-023-11354-9](https://doi.org/10.1140/epjc/s10052-023-11354-9). arXiv: [2212.02856](https://arxiv.org/abs/2212.02856) [physics.ins-det].
- [119] Patrick Krause. *The Liquid Argon Instrumentation of GERDA and LEGEND200*. Oct. 2020. DOI: [10.5281/zenodo.4123760](https://doi.org/10.5281/zenodo.4123760).
- [120] Rosanna Deckert. *Master Thesis: First Light in LEGEND-200: Commissioning of the Liquid Argon Instrumentation*. Apr. 2023.
- [121] Saint-Gobain Crystals. “Organic Scintillation Materials and Assemblies”. In: *Technical report* (2016). URL: <https://docplayer.net/179263845-Organic-scintillation-materials-and-assemblies.html>.
- [122] KETEK GmbH. “SiPM”. In: *Product Data Sheet* (2021). URL: <https://www.ketek.net/wp-content/uploads/KETEK-PM33xx-WL-A0-Datasheet.pdf>.
- [123] V. M. Gehman et al. “Fluorescence Efficiency and Visible Re-emission Spectrum of Tetraphenyl Butadiene Films at Extreme Ultraviolet Wavelengths”. In: *Nucl. Instrum. Meth. A* 654 (2011), pp. 116–121. DOI: [10.1016/j.nima.2011.06.088](https://doi.org/10.1016/j.nima.2011.06.088). arXiv: [1104.3259](https://arxiv.org/abs/1104.3259) [astro-ph.IM].

- [124] Julian Kratz. “Investigation of tetraphenyl butadiene coatings for wavelength shifting fibers for the liquid argon veto in GERDA”. In: *Verhandlungen der Deutschen Physikalischen Gesellschaft* (2017). URL: https://inis.iaea.org/search/search.aspx?orig_q=RN:50000616.
- [125] M. Agostini et al. “Liquid argon light collection and veto modeling in GERDA Phase II”. In: *Eur. Phys. J. C* 83.4 (2023), p. 319. DOI: [10.1140/epjc/s10052-023-11354-9](https://doi.org/10.1140/epjc/s10052-023-11354-9). arXiv: [2212.02856](https://arxiv.org/abs/2212.02856) [[physics.ins-det](https://arxiv.org/abs/2212.02856)].
- [126] Mario Schwarz. “PhD thesis in preparation.” PhD thesis. Munich, Tech. U., 2024.
- [127] Patrick Krause. “Shining light on backgrounds”. PhD thesis. Munich, Tech. U., Nov. 2023.
- [128] Rita Feriozzi. “Bachelor Thesis: Studio della risposta dei fotomoltiplicatori al silicio dell’esperimento LEGEND-200”. In: (Sept. 2022).
- [129] I. Abritta Costa et al. “The Front-End electronics for the liquid Argon instrumentation of the LEGEND-200 experiment”. In: *JINST* 18.09 (2023), P09007. DOI: [10.1088/1748-0221/18/09/P09007](https://doi.org/10.1088/1748-0221/18/09/P09007). arXiv: [2211.03069](https://arxiv.org/abs/2211.03069) [[physics.ins-det](https://arxiv.org/abs/2211.03069)].
- [130] N. Burlac. “First LAr commissioning analysis”. In: *Talk at the LEGEND Collaboration Meeting* (Remote, October 2021.).
- [131] Teal Pershing et al. “Performance of Hamamatsu VUV4 SiPMs for detecting liquid argon scintillation”. In: *JINST* 17.04 (2022), P04017. DOI: [10.1088/1748-0221/17/04/P04017](https://doi.org/10.1088/1748-0221/17/04/P04017). arXiv: [2202.02977](https://arxiv.org/abs/2202.02977) [[physics.ins-det](https://arxiv.org/abs/2202.02977)].
- [132] P. Adhikari et al. “The liquid-argon scintillation pulseshape in DEAP-3600”. In: *Eur. Phys. J. C* 80.4 (2020), p. 303. DOI: [10.1140/epjc/s10052-020-7789-x](https://doi.org/10.1140/epjc/s10052-020-7789-x). arXiv: [2001.09855](https://arxiv.org/abs/2001.09855) [[physics.ins-det](https://arxiv.org/abs/2001.09855)].
- [133] M. Hofmann et al. “Ion-beam excitation of liquid argon”. In: *Eur. Phys. J. C* 73.10 (2013), p. 2618. DOI: [10.1140/epjc/s10052-013-2618-0](https://doi.org/10.1140/epjc/s10052-013-2618-0). arXiv: [1511.07721](https://arxiv.org/abs/1511.07721) [[physics.ins-det](https://arxiv.org/abs/1511.07721)].
- [134] M. Schwarz. “Liquid argon properties in LEGEND-200”. In: *Talk at the LEGEND Collaboration Meeting* (GSSI, October 2022.).
- [135] S. Schonert. “LAr trigger”. In: *Private communication and talk at the LEGEND Technical Council Call* (10 Jan 2023.).
- [136] Shaofei Zhu and E.A. McCutchan. “Nuclear Data Sheets for A=214”. In: *Nuclear Data Sheets* 175 (2021), pp. 1–149. ISSN: 0090-3752. DOI: <https://doi.org/10.1016/j.nds.2021.06.001>.
- [137] N. Burlac. “LAr instrumentation noise and mitigation”. In: *Talk at the LEGEND Collaboration Meeting* (GSSI, October 2022.).
- [138] “Gaussian Filter”. In: *Computational Surface and Roundness Metrology*. London: Springer London, 2009, pp. 33–38. ISBN: 978-1-84800-297-5. DOI: [10.1007/978-1-84800-297-5_5](https://doi.org/10.1007/978-1-84800-297-5_5).
- [139] Will Gersch. “A note on trapezoidal digital filter design”. In: *Computers and Biomedical Research* 6.3 (1973), pp. 281–285. ISSN: 0010-4809. DOI: [https://doi.org/10.1016/0010-4809\(73\)90042-6](https://doi.org/10.1016/0010-4809(73)90042-6).
- [140] V. D’Andrea et al. “Optimum filter synthesis with DPLMS method for energy reconstruction”. In: *Eur. Phys. J. C* 83.2 (2023), p. 149. DOI: [10.1140/epjc/s10052-023-11299-z](https://doi.org/10.1140/epjc/s10052-023-11299-z). arXiv: [2209.09863](https://arxiv.org/abs/2209.09863) [[physics.ins-det](https://arxiv.org/abs/2209.09863)].

- [141] Nina Burlac. *Master Thesis: Towards a new approach for the Pulse Shape Discrimination in the Gerda experiment*. Oct. 2020. URL: <https://hdl.handle.net/20.500.12319/848>.
- [142] E. Gatti et al. “Digital Penalized LMS method for filter synthesis with arbitrary constraints and noise”. In: *Nuclear Instruments and Methods in Physics Research Section A: Accelerators, Spectrometers, Detectors and Associated Equipment* 523.1 (2004), pp. 167–185. ISSN: 0168-9002. DOI: <https://doi.org/10.1016/j.nima.2003.12.032>.
- [143] F.S. Goulding and D.A. Landis. “Ballistic deficit correction in semiconductor detector spectrometers”. In: *IEEE Transactions on Nuclear Science* 35.1 (1988), pp. 119–124. DOI: [10.1109/23.12687](https://doi.org/10.1109/23.12687).
- [144] Tommaso Comellato. “Inverted Coaxial Detectors for Legend”. PhD thesis. Munich, Tech. U., 2022. URL: <https://inspirehep.net/literature/2596814>.
- [145] V.D. Ashitkov et al. “New experimental limit on the ^{42}Ar content in the Earth’s atmosphere”. In: *Nuclear Instruments and Methods in Physics Research Section A: Accelerators, Spectrometers, Detectors and Associated Equipment* 416.1 (1998), pp. 179–181. ISSN: 0168-9002. DOI: [https://doi.org/10.1016/S0168-9002\(98\)00740-2](https://doi.org/10.1016/S0168-9002(98)00740-2).
- [146] V. D. Ashitkov et al. “Liquid argon ionization detector for double beta decay studies”. In: (Sept. 2003). DOI: <https://doi.org/10.48550/arXiv.nucl-ex/0309001>. arXiv: [nucl-ex/0309001](https://arxiv.org/abs/nucl-ex/0309001).
- [147] A. S. Barabash, R. R. Saakyan, and V. I. Umatov. “On concentration of ^{42}Ar in liquid argon”. In: *J. Phys. Conf. Ser.* 718.6 (2016), p. 062004. DOI: [10.1088/1742-6596/718/6/062004](https://doi.org/10.1088/1742-6596/718/6/062004).
- [148] M. Agostini et al. “The background in the $0\nu\beta\beta$ experiment GERDA”. In: *Eur. Phys. J. C* 74.4 (2014), p. 2764. DOI: [10.1140/epjc/s10052-014-2764-z](https://doi.org/10.1140/epjc/s10052-014-2764-z). arXiv: [1306.5084](https://arxiv.org/abs/1306.5084) [[physics.ins-det](https://arxiv.org/abs/1306.5084)].
- [149] M. Agostini et al. “Modeling of GERDA Phase II data”. In: *JHEP* 03 (2020), p. 139. DOI: [10.1007/JHEP03\(2020\)139](https://doi.org/10.1007/JHEP03(2020)139). arXiv: [1909.02522](https://arxiv.org/abs/1909.02522) [[nucl-ex](https://arxiv.org/abs/1909.02522)].
- [150] Matteo Agostini et al. “LArGe: active background suppression using argon scintillation for the Gerda $0\nu\beta\beta$ -experiment”. In: *European Physical Journal C* 75:506 (Oct. 2015). DOI: [10.1140/epjc/s10052-015-3681-5](https://doi.org/10.1140/epjc/s10052-015-3681-5).
- [151] M. Agostini et al. “Upgrade for Phase II of the Gerda experiment”. In: *Eur. Phys. J. C* 78.5 (2018), p. 388. DOI: [10.1140/epjc/s10052-018-5812-2](https://doi.org/10.1140/epjc/s10052-018-5812-2). arXiv: [1711.01452](https://arxiv.org/abs/1711.01452) [[physics.ins-det](https://arxiv.org/abs/1711.01452)].
- [152] J. Benziger et al. “The nylon scintillator containment vessels for the Borexino solar neutrino experiment”. In: *Nuclear Instruments and Methods in Physics Research Section A: Accelerators, Spectrometers, Detectors and Associated Equipment* 582.2 (2007), pp. 509–534. ISSN: 0168-9002. DOI: <https://doi.org/10.1016/j.nima.2007.08.176>.
- [153] G. Zuzel et al. “Ultra-traces of ^{226}Ra in nylon used in the Borexino solar neutrino experiment”. In: *Nuclear Instruments and Methods in Physics Research Section A: Accelerators, Spectrometers, Detectors and Associated Equipment* 498.1 (2003), pp. 240–255. ISSN: 0168-9002. DOI: [https://doi.org/10.1016/S0168-9002\(02\)01981-2](https://doi.org/10.1016/S0168-9002(02)01981-2).

- [154] M. Ibrahim Mirza. “Mitigation strategies for $^{42}\text{Ar}/^{42}\text{K}$ background reduction using encapsulation with ultra-pure plastic for the LEGEND experiment”. In: *AIP Conf. Proc.* 2908.1 (2023), p. 100006. DOI: [10.1063/5.0161061](https://doi.org/10.1063/5.0161061). arXiv: [2209.07598](https://arxiv.org/abs/2209.07598) [physics.ins-det].
- [155] P. Krause. “LAr detector performance”. In: *Talk at the LEGEND Collaboration Meeting* (Simon Fraser University, December 2023.).
- [156] Nuclear Data Services. *LiveChart of Nuclides*. URL: <https://www-nds.iaea.org/>.
- [157] S. Vinogradov et al. “Probability distribution and noise factor of solid state photomultiplier signals with cross-talk and afterpulsing”. In: *2009 IEEE Nuclear Science Symposium Conference Record (NSS/MIC)*. 2009, pp. 1496–1500. DOI: [10.1109/NSSMIC.2009.5402300](https://doi.org/10.1109/NSSMIC.2009.5402300).
- [158] J. Calvo et al. “Backgrounds and pulse shape discrimination in the ArDM liquid argon TPC”. In: *JCAP* 12 (2018), p. 011. DOI: [10.1088/1475-7516/2018/12/011](https://doi.org/10.1088/1475-7516/2018/12/011). arXiv: [1712.01932](https://arxiv.org/abs/1712.01932) [physics.ins-det].
- [159] W. H. Lippincott et al. “Scintillation time dependence and pulse shape discrimination in liquid argon”. In: *Phys. Rev. C* 78 (2008). [Erratum: *Phys.Rev.C* 81, 039901 (2010)], p. 035801. DOI: [10.1103/PhysRevC.81.039901](https://doi.org/10.1103/PhysRevC.81.039901). arXiv: [0801.1531](https://arxiv.org/abs/0801.1531) [nucl-ex].
- [160] G. Salamanna. “LAr veto FE electronics: hardware side”. In: *Talk at the LEGEND Collaboration Meeting* (Remote, October 2021.).
- [161] D. Renker. “Geiger-mode avalanche photodiodes, history, properties and problems”. In: *Nuclear Instruments and Methods in Physics Research Section A: Accelerators, Spectrometers, Detectors and Associated Equipment* 567.1 (2006). Proceedings of the 4th International Conference on New Developments in Photodetection, pp. 48–56. ISSN: 0168-9002. DOI: <https://doi.org/10.1016/j.nima.2006.05.060>.
- [162] Fabio Acerbi and Stefan Gundacker. “Understanding and simulating SiPMs”. In: *Nuclear Instruments and Methods in Physics Research Section A: Accelerators, Spectrometers, Detectors and Associated Equipment* 926 (2019). Silicon Photomultipliers: Technology, Characterisation and Applications, pp. 16–35. ISSN: 0168-9002. DOI: <https://doi.org/10.1016/j.nima.2018.11.118>.
- [163] F. Corsi et al. “Electrical Characterization of Silicon Photo-Multiplier Detectors for Optimal Front-End Design”. In: *2006 IEEE Nuclear Science Symposium Conference Record*. Vol. 2. 2006, pp. 1276–1280. DOI: [10.1109/NSSMIC.2006.356076](https://doi.org/10.1109/NSSMIC.2006.356076).